
Chapter 8: FLUID DISPENSING AND DISPERSION

Giann C. Yang, Ph.D.
National Institute of Standards and
Technology

David Keyser, Ph.D.
Naval Air Systems Command (retired)

TABLE OF CONTENTS

8.1	Introduction.....	722
8.1.1	Characteristics of Aircraft Engine Nacelle Fires.....	722
8.1.2	Summary of Suppressant Fluid Dynamics.....	723
8.1.3	Scope.....	724
8.2	Fluid Storage.....	725
8.3	Fluid Transport through Piping.....	726
8.3.1	Introduction.....	726
8.3.2	Previous Work.....	729
8.3.3	Base Code Selection.....	730
8.3.4	Code Development Work.....	732
8.3.5	Code Theory.....	733
8.3.6	Supporting Laboratory Data.....	753
8.3.7	Comparison of Code Predictions to Experimental Data.....	786
8.3.8	Assessment of Fluid Transport Model.....	804
8.4	Dynamics of Fluid Transport in Cluttered Spaces.....	805
8.4.1	Spray Transport past Generic Clutter Elements.....	805
8.4.2	Spray Interaction with Unheated and Heated Clutter Elements.....	809
8.4.3	Transport around Clutter and Recirculation Zones.....	821
8.4.4	Low Temperature Effects on Agent Dispersion.....	829
8.5	Modeling of Fluid Dispersion in a Nacelle.....	839
8.5.1	Background.....	839
8.5.2	CFD Models.....	839
8.5.3	Code Assessment Using Quarter-Scale Nacelle Tests and Simulations.....	847
8.5.4	Assessment of VULCAN Fire Suppression Sub-model.....	854
8.5.5	Assessment of VULCAN in Suppressant Distribution in a Full-Scale Nacelle.....	863
8.5.6	Assessment of VULCAN in Pool Fire Suppression in a Full-Scale Nacelle.....	868
8.6	Full-Scale Nacelle Fire Suppression Tests.....	871
8.6.1	Experimental Design.....	871
8.6.2	Test Facility.....	872
8.6.3	Test Matrices and Decision Tree.....	876
8.6.4	Actual Test Program.....	878
8.6.5	Instrumentation.....	879
8.6.6	Test Procedure.....	879

8.6.7 Test Results and Comparisons to Simulations	882
8.7 Improved Transport of Water to Fires	889
8.7.1 Background	889
8.7.2 Electrically Charged Water Mist.....	889
8.7.3 A Self-Atomizing Form of Water	909
8.8 Summary of Lessons Learned.....	916
8.9 References.....	918

8.1 INTRODUCTION

8.1.1 Characteristics of Aircraft Engine Nacelle Fires

Serious fires in aircraft engine nacelles, sufficient to terminate a mission, usually involve liquid fuel, either jet fuel or hydraulic fluid, supplied by a leak in its supply system. The primary types of fire are spray fires and pool fires. Fuel sprays occur when a pressurized line develops a relatively small opening, caused by battle or other damage, which results in a misting or atomized discharge of droplets. Fuel from larger openings in pressurized lines may flow over the hot surfaces and ignite there, or end up in pools below the engine contained by aircraft structure or other clutter. Typical ignition sources are electrical sparking and hot surfaces. Because aircraft engines normally produce and reject a lot of heat, the consequence is many and large hot surfaces on the outside of the engine. The air required to maintain combustion is furnished by flow from the atmosphere for which the original purpose is to cool the engine.

The most likely region for fires in engine nacelles is the long, narrow, annular space between the engine core and the outer aerodynamic skin. A large number of components are located within this region, resulting in a complex, cluttered geometry. The nacelle design typically includes ventilation airflow, either via an external scoop or other source, to both cool the nacelle and to avoid the build-up of flammable mixtures. In general, this engineered airflow has sufficient momentum to dominate the buoyancy produced by burning. The dynamics of a fire within an aircraft engine nacelle are typically dominated by the designed airflow.

Presently, aircraft survivability and suppression system proving tests are performed under conditions intended to replicate the nacelle airflow while the aircraft is in flight. Test fixtures, such as the Aircraft Engine Nacelle Fire Test Simulator (AEN) at Wright-Patterson Air Force Base (WPAFB) in Dayton, Ohio, have been constructed to represent variable geometries typical of aircraft nacelles. Extensive sets of experiments and live-fire tests with varying degrees of complex internal geometry have been conducted to evaluate the performance of suppression systems and new agents. These tests and experiments have provided significant insight into the essential features of successful systems and serve as the basis for present system acceptance. However, the results from these tests, particularly when fire extinguishment (as opposed to merely the concentration of agent) is the criterion, are often difficult to understand given the lack of a well-characterized flow field.

Adding to the difficulty in extinguishing fires in nacelles, especially in flight, is their cluttered interiors. These bluff bodies create many “flame-holders” regions with various sizes and shapes downstream of the recirculating zones into which the suppression agents have difficulty penetrating. In the case of pool fires resulting from flammable liquid accumulating at the bottom of the nacelle, one can encounter an unwanted situation where the pool fire is temporarily suppressed by an agent but rapidly flares up again

after the agent is exhausted from the nacelle. The re-ignition of the liquid pool is probably due to continuing fuel vapor generation from the pool and adjacent hot nacelle surfaces not being cooled below the ignition point of the fuel vapor as a result of the suppression action.

A phenomenon, termed *accelerated burning*, has been observed in a diversity of fire suppression tests and was witnessed in this test program as well. It resulted from slow injection of insufficient agent to suppress nacelle engine fires. The injection transient only served to facilitate mixing of fuel vapor and air for combustion. In these cases, the resulting fire could be more intense than if nothing had been done. This phenomenon has been studied by Hamins et al.¹

8.1.2 Summary of Suppressant Fluid Dynamics

Conventional fire suppression systems for aircraft engine nacelle protection typically consist of a pressure vessel, in which a liquid fire suppressant is stored and pressurized with an inert gas, such as nitrogen or carbon dioxide. The fire-suppressant is released remotely by a fast-opening valve upon the indication of fire. The pressurized agent is ejected into the piping manifold and is distributed to the locations in the nacelle, which have been selected by design and analysis for optimum delivery and dispersion of the agent in order to suppress any foreseen fire. A schematic of a fire suppressant system is shown in Figure 8-1.

The pressure vessel governs the initial conditions for agent discharge that affect the subsequent dispersion of the suppressant. The aspects of fluid storage in a pressure vessel are related to the determination of the thermodynamics state of the fluid in the bottle and the sizing of the bottle required to accommodate adequate amount of agent required for fire suppression without compromising the bottle's structural integrity.

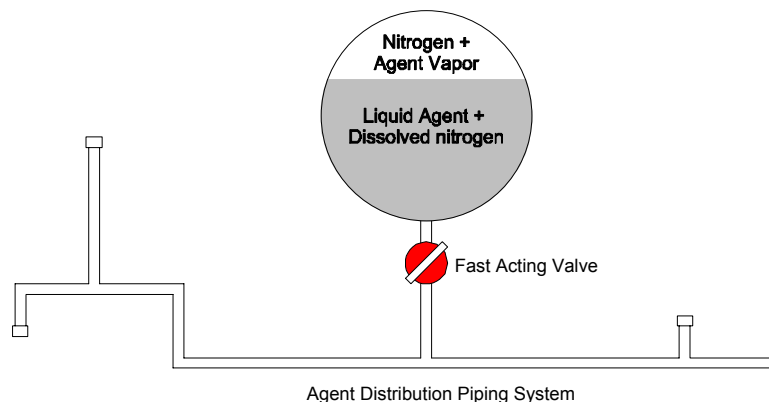


Figure 8-1. Schematic of Storage and Distribution System for Fire Suppression.

Once the valve is opened, the pressurized liquid agent is forced out into the distribution system (straight pipes, bends, tees, etc.), which may be at a temperature greater than the boiling point and at ambient pressure. This can cause a multi-component, two-phase flow, which is quite complicated to analyze and measure.

A gaseous suppressant can be easily dispersed throughout the protected space. If a superheated liquid agent is released, flashing will occur, which will greatly facilitate the agent dispersion. Halon 1301, with a boiling point of $-58\text{ }^{\circ}\text{C}$, is an example of such a fluid. Because of its flashing characteristics and rapid evaporation, the dispersion of halon 1301 in an enclosure, even cluttered with obstacles, is rapid and effective.

If the suppressant has a high normal boiling point and/or is released at temperatures below its normal boiling point, the liquid droplets formed at the discharge nozzle will persist as they flow through the nacelle. The actual droplet size distribution delivered to the fire will be different from the initial distribution at the discharge nozzle. After liquid droplets form, depending on the droplet number density and droplet ballistics (velocities and trajectories) and even before they arrive at the fire zone, droplet-droplet and droplet-surface interaction may happen in an aircraft engine nacelle due to its highly cluttered environment. These processes may alter the initial droplet size and velocity distributions significantly. The presence of high-speed airflow can also affect the droplet size and velocity distributions. If the dispersing spray encounters a solid obstacle, pooling, dripping, splitting, splashing, or shattering of the droplets will result. Dripping and pooling causes local retention of liquid on the nacelle bottom surface, cutting or splitting of the droplet due to impact at the edge of the surface may result in smaller droplets, and droplet splashing and shattering can generate smaller daughter or satellite droplets. The nacelle surface temperature also plays a role in the droplet-surface interaction.

8.1.3 Scope

The NGP determined that, following the discharge of a suppressant from the storage bottle, more needed to be understood about the behavior of the two-phase suppressant flow in the distribution plumbing and the subsequent dispersion of the suppressant from the plumbing outlets to the fire location through the cluttered environment in a nacelle. This chapter presents new understanding of and bases for improvements in the storage, the distribution, delivery, and dispersion of fire suppressants in an aircraft engine nacelle. Prior to the NGP, such a comprehensive approach to the study of fluid dispensing and dispersion for nacelle fire protection applications had never been attempted.

The two-phase distribution flow is discussed in detail in section 8.3. A two-phase computer code, based on a code widely used in the nuclear industries, was developed further for this application. The program was benchmarked against transient experimental data available in the literature, as well as experiments conducted in the NGP study.

The phenomena of liquid suppressant interacting with cluttered elements are discussed in section 8.4. In addition, the effects of liquid boiling point, storage bottle temperature, and nacelle and airflow temperatures on agent dispersion were examined using CF_3I as a surrogate.

Sections 8.5 and 8.6 focus on the study of agent dispersion in a nacelle using computer simulations and full-scale nacelle fire tests. Computational fluid dynamics (CFD) programs were used to simulate these processes, to aid the design of the experiment, to facilitate the formulation of the test matrices, and to predict the outcomes of fire-tests. CFD simulations provide detailed visualization of agent dispersion throughout the nacelle to optimize the locations and number of agent discharge nozzles needed for prototype fire suppression system designs. Agent concentration and agent interaction with probable flame loci can also be predicted to determine the appropriate amount of agent to be stored and the agent

injection duration. Such information leads to the design pressure for the storage bottle and design guidance for efficient agent deployment and provides a high degree of confidence in using simulation tools to guide fire protection system design for nacelles. These advances will also benefit other applications of complex geometry where flame extinguishment must be accomplished in time frames of the order of seconds or faster.

In section 8.7, two other potential strategies to facilitate fluid dispersion have been explored and will be discussed. One involves the use of an electrically charged, water-mist system, and the other examines a self-atomizing form of water employing CO₂ hydrates. Given the geometrical and physical constraints of a nacelle, these two techniques have not been proven to be promising for nacelle applications.

8.2 FLUID STORAGE

When the fire suppressant is a fluid, it will most likely be stored in a pressure vessel. In most applications, the release or discharge of the bottle content depends solely on the prevailing internal pressure within the bottle ullage. Yang and coworkers² have developed a methodology for predicting this pressure.

For a pure fluid, the ullage pressure will be the vapor pressure of the fluid at the prevailing temperature. If the applications are limited to room temperature or above, fluids with high vapor pressures at room temperature can be released at a moderate rate with adequate driving force within the bottle. However, the discharge can become problematic at very low temperatures where the vapor pressure becomes sub-atmospheric. The conventional way to alleviate this problem is to use a suppressant gas (*e.g.*, nitrogen) to enhance the ullage pressure above the vapor pressure of the fluid at room temperature. In this case, the ullage pressure is maintained at a relatively high level, even at low temperatures, to facilitate the discharge processes. An alternative way to address the low ullage pressure problem at low temperatures is to use the so-called hybrid system wherein an SPGG (solid propellant gas generator), upon activation, provides the pressure source to drive the fluid out of the bottle (see Chapter 9). The focus of this section is on a pure fluid pressurized with a suppressant gas.

The prevailing ullage pressure is critical to the discharge of the bottle content. The pressure can be derived from the thermodynamic state of the suppressant fluid with the pressurized gas under different ambient conditions. The myriad ambient conditions are the result of bottle location and in-flight or on-the-ground environments of an aircraft. The thermodynamic state of the fluid in the bottle not only determines the initial conditions for fluid agent discharge in case of a fire, but also provides data for bottle design in terms of its size and ability to withstand increased internal pressure at elevated temperature.

The ullage pressure in the bottle is a complex function of ambient temperature because of the temperature dependence of the fluid vapor pressure, the partial pressure of pressurized gas in the ullage, and the solubility of the pressurized gas in the fluid. For halon 1301, the bottle pressure-temperature relationship and the solubility of pressurized gas nitrogen in the agent have been well characterized. By contrast, such a relationship and solubility data are scarce or do not exist for many of the halon alternative fluids.

The thermodynamic state of the storage container can be determined by an appropriate equation of state applicable to mixtures (fluid and pressurized gas) with empirical binary interaction coefficients.³ Other thermodynamic frameworks have also been used.⁴ In the following, a brief discussion of the development of a computer code, named PROFISSY, in the Technology Development Program (TDP) to calculate the

thermodynamics state of the bottle will be presented. Detailed description of the code can be found in Yang et al.²

PROFISSY (acronym for PRoperties Of Fire Suppression Systems) was developed for the primary purpose of helping fire suppression bottle designers or users to obtain temperature-pressure characteristics of bottle contents. Simply put, given a vessel charged with agent and nitrogen at room temperature, one would like to know what the final vessel pressure will be when the vessel is at a different temperature. Only four pieces of input information are required to run the program: (1) agent mass, (2) vessel volume, (3) fill temperature, and (4) either nitrogen mass needed to pressurize the vessel, or the fill pressure of the vessel.

The program also predicts whether a liquid-full condition (i.e., the storage vessel is completely filled with liquid with no ullage) would occur at elevated temperatures for a given initial fill density, defined as the amount of liquid divided by the vessel volume. When the initial fill density is above the critical density of the fluid, a liquid-full condition will result due to the thermal expansion of the liquid, to the point that the vessel becomes completely filled as it is heated. A liquid-full condition is undesirable and must be avoided because the internal pressure of the vessel will rise sharply with temperature once a liquid-full condition has been reached.⁴ This could result in rupture of the vessel.

PROFISSY incorporates a thermodynamics model known as “extended corresponding states” (ECS).⁵ The central idea of extended corresponding states is that all points on the *PVT* (pressure-volume-temperature) surface of any fluid may be represented by scaling the *PVT* surface of a reference substance. These “scale factors” involve the critical properties of the fluid of interest and the reference fluid and may also be functions of temperature and density. The ECS model is a powerful tool, applicable to the entire range of fluid states, from dense liquid to dilute gas, as well as to the supercritical fluid regime. It may be used with only minimal information on a fluid: the critical point, the normal boiling point, and the molecular weight. Additional information on a fluid, such as vapor pressures, saturated liquid densities, and liquid viscosities can be used to refine the model predictions.

The current PROFISSY code, running on a PC, supports thermodynamics state calculations for halon 1301, FC-218, CF₃I, HFC-125, and HFC-227ea. Experimental data have been obtained to compare to the code predictions for these fluids.⁶ In general, the predictions were found to be within 10 % of the measurements.⁶ The code can be easily extended to include other fluid/nitrogen systems, if desired.

8.3 FLUID TRANSPORT THROUGH PIPING

8.3.1 Introduction

As stated above, the current halon delivery systems generally consist of a suppressant vessel connected to the delivery location by a piping network. Prior to the NGP, there was no publicly available simulation tool for transient, two-phase flow through a complex pipe system. There is a need to determine whether the existing piping system for halon 1301 can be used for a replacement agent. For the NGP, Tuzla and coworkers⁷ have developed a computer code for two-phase fire suppressant flow in a complex piping system.

Since halon and its potential replacement fluids are in a vapor state at standard pressure and temperature, at the discharge location the fluid will be a two-phase mixture of superheated liquid and vapor. Thus significant thermodynamic and thermal non-equilibrium can be expected between the phases. Also, due to the large pressure difference between upstream source vessel and downstream exit, continuous flashing is anticipated as the fluid travels through the piping, and two-phase critical (choked) flow can occur at various locations.

There has been some work conducted on modeling halon 1301 flows. In a 1988 summary of the state-of-the-art, DiNunno and Budnick⁸ indicated that most of the flow calculations were performed using proprietary methods. These methods were verified against standard NFPA procedures for calculations and by discharge testing in sealed tests. However, there were significant uncertainties in the calculations and also in extrapolation of test results to actual configurations.

Pitts et al.⁹ described a mathematical model for calculating the discharge of fire-suppressant fluids from a pressurized discharge tank across an orifice at the exit and showed that the transient pressure history in the discharge vessel calculated by the model compared reasonably well to data from experiments. Elliott et al.¹⁰ developed a computer program called HFLOW for predicting the discharge of halon 1301 from a discharge vessel through a piping system. The results of the program compared favorably to the results of experiments conducted with halon 1301 in several piping arrangements. The theoretical model was based on a homogeneous model of two-phase flow. Elliott et al.¹⁰ also modified an existing computer program called SOLA-LOOP,¹¹ which was originally written for steam-water flows, to be able to model halon 1301. This computer program was a non-equilibrium, non-homogeneous model of two-phase flow, using the drift flux approach to calculate slip between the phases. It was shown that this program, modified to account for halon 1301 properties, was able to capture the physics of the agent discharge more accurately than its predecessor.

The methods described by Yang et al.² and Elliott et al.¹⁰ appear to be the only methods available in the public domain for calculating performance of fire-suppressant fluid delivery systems. One way to develop a general, flexible computer program that would be able to model a variety of piping networks and handle several candidate fluids would be to extend this work by modifying these methods. Another approach is to take advantage of the advances in two-phase flow modeling that have taken place in the nuclear power industry, which have resulted in several computer codes available in the public domain. The development of the computer code described here followed the latter approach.

Hence, to predict the performance of the delivery system accurately, a computer code should be a transient two-phase code, which allows for phase non-equilibrium. The short delivery times require fairly high flows, which promote homogeneous two-phase flow, i.e., little slip. However, in imbalanced piping networks, with side tees and other fittings, some separated flow could occur (stratified flows, slug/plug flow, etc.). Hence, the code should be able to predict slip between phases and the corresponding effect on pressure drop. This can be especially important when separated flow encounters directional change, such as at a side tee. The ability to predict the transport of non-condensable gas is also important. The fluid, pressurized with a driver gas, is initially saturated with the gas. During the delivery, as the system depressurizes, the driver gas comes out of the solution and expands. This gas evolution phenomenon needs to be accounted for. One additional requirement is that the code should be useful for estimation of the transient hydrodynamic loads in the piping network. Thus, the momentum equations need to be sufficiently detailed to estimate the unbalanced force in piping sections between locations of elbows and other fittings.

A key technical approach in the present program was utilization of advancements made in other applications that deal with multi-phase flows. In particular, the highly sophisticated computer codes that have been developed for thermal-hydraulic analysis of nuclear power systems have all the characteristics required for analysis of fire suppressant systems. These include models that account for relative slip between liquid and vapor phases, thermodynamic non-equilibrium between the phases, changes in two-phase flow regimes, critical choke flows, and transport of non-condensable gases. Such codes are also structured for numerical analysis of fast transients, well capable of the transients anticipated for suppressant systems.

Since the fluids being considered for use in fire suppressant systems are different from the water/steam system of nuclear power systems, physical property packages need to be modified and expanded. Here again, the NGP leveraged existing technology by borrowing from existing property packages. Specifically, the REFPROP package, developed by NIST¹², covers many refrigerant fluids, including those that are potential candidates for the fire suppressant systems.

The effort contained an experimental task to obtain data needed to assess the code. The experimental program utilized a discharge loop using several proposed fire suppressants. Major flow parameters, which have not been measured heretofore, were successfully measured. These include measurements of instantaneous discharge flow rate, fluid temperature, and void fraction at various locations along a discharge pipe.

The program is based on a one-dimensional, two-fluid model of two-phase flow. In this model, separate conservation equations are written for the liquid and gas phases for mass, momentum, and energy. Constitutive relationships are specified for interphase transport of mass, momentum, and energy. Heat transfer between the fluid and passive structures such as pipe walls are modeled. The program also contains built-in models for wall friction and two-phase critical flow. The transport of non-condensable gas in the system, namely the nitrogen fill gas, as well as the nitrogen released from solution during agent discharge, is modeled via separate mass conservation equations, with constitutive relations to specify the rate of gas release. The conservation equations are solved using a semi-implicit numerical method, with user-supplied boundary and initial conditions.

The program was deliberately made flexible in terms of types of fluids and piping layout. The current version of the program allows the user to select any one of five fluids: water, halon 1301, CO₂, HFC-227ea or HFC-125. Modules are available in the program with which the user can model a delivery system, including one or more supply tanks and a combination of piping networks. The user can also model valves in the system, with specified valve opening times if needed.

The suppressant discharge is a highly transient process, generally lasting from less than a second to a few seconds. The program was benchmarked against transient experimental data available in the literature, as well as experiments conducted as a part of this project, on the discharge of HFC-227ea and HFC-125 in a specially prepared discharge loop. The present experiments lasted between 1.5 s to 6 s. In addition to transient system pressure at various points, these experiments also measured critical parameters, such as the transient mass discharge history, fluid temperature, and the void fraction near the exit. These are the first dynamic measurements of mass flow, fluid temperatures, and void fraction during suppression discharge. These new data allowed a more comprehensive assessment of the computer program than possible with previously available experimental data. The results of the assessment showed that the program is capable of predicting the performance of various delivery systems with several fluids.

Detailed description of the development of the computer code can be found in Tuzla et al.⁷, which comprises two volumes. The first volume provides a detailed description of the experimental work and discussion of the results. It also includes a brief description of the theory and numerical solution method, instructions for installation on a personal computer with the WINDOWS operating system, and instructions on preparation of the input needed to describe the system being analyzed. The second volume consists of three appendices: (a) an input manual for the computer program, (b) information on the experimental data, and (c) comparison of the present data to predictions of the computer program. A copy of the computer code can be found in the CD-ROM enclosed in that report.

8.3.2 Previous Work

To fully test the computer code developed in this research, comparisons of code predictions against experimental data were made. A literature survey was conducted to find possible sources for experimental data for transient two-phase flows. One widely referenced study is "The Marviken Tests," conducted using water/steam for the nuclear reactor industry and documented in the two reports.^{13,14} These tests used a liquid/vapor-filled vessel under high pressure and measured the vertical discharge characteristics as this system was released to atmospheric conditions. A similar test was carried out by Edwards and O'Brien¹⁵, but focused on the effects of a horizontal discharge. Even though the Marviken and Edwards tests were conducted with water/steam systems, they still provide some means for assessing portions of the code, which use mechanistic models for predicting non-homogeneous, non-equilibrium two-phase flows. These mechanistic models are fluid-independent and can be invoked for all fluids.

Three studies, which more closely reflect the intentions of the current study, have used fire suppressants as their test fluids, rather than water and steam. The work undertaken by Elliot et al.¹⁰ in 1984 includes both theoretical and experimental investigations. In this work, halon 1301 was used as the suppressant fluid. The tests discharged halon under nitrogen gas pre-pressure, resulting in flow of a liquid/vapor/non-condensable-gas mixture through a configuration of piping and an end nozzle. This study provides data on pressure decay as a function of time, allowing for the estimation of discharge flow rates, which are useful for accessing code predictions. This study also provides observations of experimental phenomena as the discharge proceeded. An example is the phenomenon of evolution of the dissolved nitrogen from the liquid halon, which causes an increase in the pressure of the discharge vessel and an increase in the driving force propelling the discharge of the fluid.

The most comprehensive tests conducted to this date were launched in the mid 1990s by the National Institute of Standards and Technology (Yang et al.² and Pitts et al.⁹). Their tests not only utilized halon 1301 as a test fluid, but also utilized HFC-125, HFC-227ea, and CF₃I. They conducted several experimental runs with each fluid, providing extensive data for various pipe configurations and operating conditions. Experiments with different initial fill volumes, pressures, and temperatures were performed to determine their effects on the two-phase system. Their findings provide important information about the characteristics of the two-phase transient flow as it discharges from the source vessel and through the piping. The pressure histograms from this earlier program are used as a benchmark in gauging the effectiveness of the code being developed in the current program.

These prior studies provided the beginning of an experimental database. However, there were no data on several key parameters important to computational code assessment. Primary among these is the instantaneous mass discharge rate and void fraction, both at the exit of the source vessel and at the exit of

the distribution pipe. Such parameters reflect the mechanisms of phase change (vaporization) and interfacial momentum transfer (slip velocity) that must be correctly modeled in the computer code. Without specific experimental measurements of such key parameters, it is impossible to fully assess the validity of any prediction. This is the reason why the current experimental program was structured to obtain a number of additional measurements, above and beyond the usual measurement of pressure decay.

Two-phase flow calculations require thermodynamic and transport properties of the fluid. These properties are required for single-phase liquid, for single-phase vapor, and for saturated vapor/liquid mixtures. The following thermodynamic properties are needed as functions of absolute pressure:

- Saturation temperature
- Specific heat for gas and liquid phases
- Thermal expansion coefficient for gas and liquid phases
- Isothermal compressibility for gas and liquid phases
- Specific volume for gas and liquid phases
- Specific entropy for gas and liquid phases

In addition, the following transport properties are also required for two-phase flow calculations:

- Dynamic viscosity for gas and liquid phases
- Thermal conductivity for gas and liquid phases
- Surface tension

Most fire suppressants are also used as refrigerants. The refrigerant property package REFPROP developed at NIST by Gallagher et al.¹² covers most of the fire suppressants. For example, it contains properties of halon 1301, and present fire suppressant candidate HFC-227ea. After evaluation, it was found that REFPROP was a suitable package for determining the properties required by the new code for two-phase flow calculations with suppressant fluids.

8.3.3 Base Code Selection

Desired Feature of the New Code

The base code was developed with some specific features in terms of its technical ability to model the basic phenomena of two-phase flows. In addition, user convenience and ease of development were also desirable features. The present development sought to include the following features in the new code.

Required features:

- Non-proprietary, publicly available
- Portable to various computer and operating systems
- Ease of development (well-documented, flexible architecture)

Desired features:

- Non-homogeneous two-phase flow accounting for relative slip between phases
- Non-equilibrium two-phase flow, allowing for metastable conditions during flashing
- Choking under single and two-phase conditions
- Non-condensable (dissolved gas) transport
- Multi-component mixtures (liquids, gases, powders)
- Flexible system modeling capability (choice of piping components and layout)
- Robust set of equations, for simulation of fast transient two-phase flows (for example, momentum equation to include frictional losses, energy equation to include dissipation)
- Demonstrated ability to model representative systems (assessment against experiments)
- Ease of application (user-friendly inputs)

There are other intangible features that have also been considered, such as the existence of an active user group, which would facilitate future modifications and developments.

Two-phase Codes Considered

The relevant codes are those used in the nuclear industry for loss-of-coolant accident analyses (LOCA). These codes address the major phenomena of interest (non-homogeneous, non-equilibrium two-phase flows, choking conditions, fast transients). The survey was limited to codes developed and available in the United States and consisted of RELAP5, RETRAN, TRAC-P, TRAC-B and GOTHIC. Codes developed in other countries that could be used (ATHLET, CATHARE) were not considered because easy access to these codes may not be available.

All these codes have many of the required and desirable features for the present application. They are all based on a two-fluid model of two-phase flow, with constitutive equations to specify the interfacial transport terms. Although some of them have multi-dimensional modeling capability, they are predominantly used in a one-dimensional mode. A brief history of these codes is presented below, with some relevant information:

RELAP5. The version examined of this code was RELAP5/MOD3, version 3.2, available since 1995, RELAP5/MOD3 Code Manual.^{16,17} This code was developed at the Idaho National Engineering and Environmental Laboratories (INEEL) under sponsorship of the U.S. Nuclear Regulatory Commission (USNRC). It is used for a variety of reactor accident analyses, including LOCA analyses, for a variety of types of reactors. It is also used in a variety of general thermal-hydraulic analyses in nuclear and non-nuclear systems. It is non-proprietary, and is publicly available, for a transmittal fee, from the USNRC. An active user group, including U.S. and international organizations, meets once a year. Information on user problems, error correction, etc. is transmitted to user group members once every three months.

RETRAN. The version examined of this code was RETRAN-03, RETRAN-03 (1992).¹⁸ This code was developed by Computer Simulations and Analysis, Inc., under sponsorship of the Electric Power Research Institute (EPRI). It is used primarily for analyses of reactor systems, with focus on the primary cooling system, and usually for non-LOCA scenarios. It is proprietary, and can be obtained from EPRI,

with license fees and user group membership fees. The user group, including U.S. and international organizations, is active and meets regularly.

TRAC-P. The examined version of this code was TRAC-PF1/MOD2, TRAC-PF1/MOD2 Code (1992).¹⁹ It was developed by the Los Alamos National Laboratory (LANL) under USNRC sponsorship. It is used primarily for LOCA analysis of pressurized water reactors. It is non-proprietary and can be obtained, for a transmittal fee, from the USNRC. There are a relatively small number of users and no regular user group meetings.

TRAC-B. The version examined of this code was TRAC-BF1/MOD1, TRAC-BF1/MOD1 Code (1992)²⁰ and TRAC-BF1/MOD1 Models (1992).²¹ It was developed by INEEL under USNRC sponsorship. It is used for accident analyses of boiling water reactors. It is non-proprietary and can be obtained from the USNRC for a transmittal fee. The user group is active and meets regularly.

GOTHIC. The version examined of this code was GOTHIC version 5.0, GOTHIC Containment Analysis Package Version 5.0 (1995).²² It was developed by Numerical Applications, Inc., under EPRI sponsorship. It is used primarily for analysis of reactor containments. It was developed from the COBRA series of codes originally developed at the Pacific Northwest Laboratory under USNRC sponsorship. The original COBRA series of codes are non-proprietary, but were not maintained by the USNRC after the mid-1980's, and are now difficult to obtain. The GOTHIC code is proprietary and can be obtained from EPRI for license fees and user membership fees. The user group is active and meets regularly.

Code Selected

The documentation for each of the candidate codes was reviewed. It was concluded that all the codes listed above have many of the required and desirable features, but none have all of them. The RELAP5 code (MOD3, version 3.2) had more of the required and desirable features than the other codes. In addition, the code had been adapted previously for operation with a fluid other than water, and the code architecture to accomplish this was available in the latest version of the code. This was especially helpful for insertion of new property packages for suppressant fluids. In addition, significant operating and code development experience with RELAP5 had been accumulated, thus providing confidence that the program objectives could be met successfully with this code. Based on these characteristics, RELAP5/MOD3, version 3.2 was selected as the base code platform for the present development.

8.3.4 Code Development Work

Scope of Program

The FSP computer code, which was derived by modifying the RELAP5/MOD3.2 computer code, is referred to in this section as the base code or, sometimes, as RELAP5. A detailed description of the code, particularly the numerical solution method, is not given here because the base code has been documented extensively.^{16,17} Most of the RELAP5 documentation applies to the FSP code. Users interested in the details of the solution method should refer to that documentation.

The main modifications to the base code in developing the FSP code were:

1. **Fluid Properties:** The base code was based on water-steam systems. This was supplemented in the FSP code by using the REFPROP fluid properties package.¹² In this version of FSP, four fluids have been incorporated, halon 1301, CO₂, HFC-227ea, and HFC-125. Any of these alternate fluids can be selected by the user. Water properties, which were the default option in the base code, have not been removed, and hence water is also one of the fluid options in FSP.
2. **Constitutive Relationships:** The code requires specification of constitutive relationships, such as for the calculation of wall drag and interphase drag, to provide closure for the basic two-phase flow conservation equations used by the two-fluid model. In the base code, several of these relationships were based on experimental data from water-based systems and were uniquely applicable to these systems. These relationships were modified in FSP to be fluid-independent. The specific areas modified were the interphase drag models in vertical flow, and wall heat transfer models for critical heat flux and transition boiling.
3. **Release of Dissolved Gas:** The base code contained transport equations for non-condensable gas in the gas phase and also for a solute (boron) in the liquid phase. In FSP, these transport equations were modified. The noncondensable gas transport equation was modified to include a source term to account for release of dissolved gas. The boron transport equation was altered to reflect transport of dissolved gas as the solute instead of boron. A sink term was added to this equation for conserving the total amount of noncondensable gas in the system. This approach allowed modeling the release of gas anywhere in the system based on local conditions. New constitutive relations were added to represent the gas release rate. This requires specification of two additional parameters, a critical bubble radius for initiating the gas release, and a rate constant. These parameters have been implemented in FSP as user input variables.

The above major modifications were made to the base code to develop the FSP code. There were some additional minor modifications, primarily for making the code usable on PC-based computer platforms. This version of FSP runs on a WINDOWS 95/98 operating system. Installation and detailed code implementation instructions can be found in Tuzla et al.⁷

8.3.5 Code Theory

The base code, RELAP5, was originally written in Standard FORTRAN-77 to run on the UNIX Operating System, but had been adapted to other operating environments. The version of RELAP5 chosen for further development is generally considered to be machine-independent and portable to a variety of commonly used operating systems.

To run this program, the user generates an input file. This input file is essentially the description of the problem to be executed. It contains the geometrical description of the system under analysis, the necessary boundary and initial conditions, and other constraints imposed by the user, such as partition of the system into control volumes (nodalization), selection of particular code options and control of the time step used in the numerical solution.

During execution, FSP generates two files, an output file that can be read by the user, and a restart file written in binary format. The output file provides information at time intervals requested by the user in

the input file. The restart file contains all the information the code needs such that the user can restart the code to run for a longer time period, with or without additional changes to the problem description, and is also used for generating graphical output.

The RELAP5 code also contains many user-convenient features and special models, which were developed primarily for nuclear plant analyses, such as the definition of specific components in nuclear systems, and code models to capture the transient behavior of nuclear fuel rods. Some of these are useful for the intended application to fire suppressant fluids and fluid systems, and some are not. In the development of the FSP code, most of the existing features of RELAP5 were retained, although not necessarily useful in modeling fire suppressant delivery systems.

The description of the code presented here is a brief summary, intended to provide basic information for the user. The base code has been documented in great detail,^{16,17} and the user is referred to that documentation for additional information, particularly the numerical solution method.

Governing Equations

The thermal-hydraulic model solves eight field equations for eight primary variables as a function of time (t) and distance (x). The eight primary dependent variables are pressure (P), phasic specific internal energies (U_g, U_f), vapor volume fraction or void fraction (α_g), phasic velocities (v_g, v_f), noncondensable quality (X_n), and solute density (ρ_b). Note that the noncondensable quality is defined as the mass fraction of noncondensables in the gas phase, the remaining fraction being the mass fraction of fluid in the gas phase. Of these eight variables, six are state variables ($P, U_g, U_f, \alpha_g, X_n, \rho_b$) and two are velocities (v_g, v_f). The corresponding eight field equations are the conservation equations for mass, momentum and energy for each phase, and the conservation of mass for the noncondensables in the gas and liquid phases. The equations are described in detail in RELAP5-1, 1995. The simple forms of these equations are shown below, as one-dimensional area-averaged equations, on a per unit volume basis.

Conservation of Mass:

Gas Phase:

$$\frac{\partial}{\partial t}(\alpha_g \rho_g) + \frac{1}{A} \frac{\partial}{\partial x}(\alpha_g \rho_g v_g A) = \Gamma_g + \Gamma_N \quad (8-1)$$

Liquid Phase:

$$\frac{\partial}{\partial t}(\alpha_f \rho_f) + \frac{1}{A} \frac{\partial}{\partial x}(\alpha_f \rho_f v_f A) = \Gamma_f \quad (8-2)$$

The terms on the right hand side of Equation 8-1 are the interfacial vapor generation per unit volume, and the noncondensable gas released from solution per unit volume. The terms on the right hand side of Equation 8-2 are the corresponding terms for the liquid phase. For continuity across the interface, $\Gamma_g + \Gamma_f = 0$. The source term for noncondensable gas, Γ_N , which is the rate of dissolved gas release per unit volume, is treated similar to an external source term. Thus, there is no corresponding term in the liquid phase mass conservation equation. Essentially, this assumes that the liquid density is not affected by the presence of dissolved gas.

Conservation of Momentum:

Gas Phase:

$$\begin{aligned} \alpha_g \rho_g A \frac{\partial v_g}{\partial t} + \frac{1}{2} \alpha_g \rho_g A \frac{\partial v_g^2}{\partial x} = & -\alpha_g A \frac{\partial P}{\partial x} + \alpha_g \rho_g B_x A - (\alpha_g \rho_g A) FWG(v_g) \\ & + \Gamma_g A(v_{gf} - v_g) - \Gamma_N A v_g - (\alpha_g \rho_g A) FIG(v_g - v_f) \\ & - C \alpha_g \alpha_f \rho_m A \left[\frac{\partial(v_g - v_f)}{\partial t} + v_f \frac{\partial v_g}{\partial x} - v_g \frac{\partial v_f}{\partial x} \right] \end{aligned} \quad (8-3)$$

Liquid Phase:

$$\begin{aligned} \alpha_f \rho_f A \frac{\partial v_f}{\partial t} + \frac{1}{2} \alpha_f \rho_f A \frac{\partial v_f^2}{\partial x} = & -\alpha_f A \frac{\partial P}{\partial x} + \alpha_f \rho_f B_x A - (\alpha_f \rho_f A) FWF(v_f) \\ & + \Gamma_f A(v_{fl} - v_f) - (\alpha_f \rho_f A) FIF(v_f - v_g) \\ & - C \alpha_f \alpha_g \rho_m A \left[\frac{\partial(v_f - v_g)}{\partial t} + v_g \frac{\partial v_f}{\partial x} - v_f \frac{\partial v_g}{\partial x} \right] \end{aligned} \quad (8-4)$$

On the right hand side of Equation 8-3, the second term is the body force and the subsequent terms are the wall friction, momentum transfer due to mass transfer (from vapor generation as well as dissolved gas release), interfacial frictional drag and force due to virtual mass.

Conservation of Thermal Energy:

Gas Phase:

$$\begin{aligned} \frac{\partial}{\partial t} (\alpha_g \rho_g U_g) + \frac{1}{A} \frac{\partial}{\partial x} (\alpha_g \rho_g U_g v_g A) = & -P \frac{\partial \alpha_g}{\partial t} - \frac{P}{A} \frac{\partial}{\partial x} (\alpha_g v_g A) \\ & Q_{wg} + Q_{ig} + \Gamma_g h_g + \Gamma_N h_N - Q_{gf} + DISS_g \end{aligned} \quad (8-5)$$

Liquid Phase:

$$\begin{aligned} \frac{\partial}{\partial t} (\alpha_f \rho_f U_f) + \frac{1}{A} \frac{\partial}{\partial x} (\alpha_f \rho_f U_f v_f A) = & -P \frac{\partial \alpha_f}{\partial t} - \frac{P}{A} \frac{\partial}{\partial x} (\alpha_f v_f A) \\ & Q_{wf} + Q_{if} + \Gamma_f h_f + Q_{gf} + DISS_f \end{aligned} \quad (8-6)$$

On the right hand side of Equation 8-5, the third to last terms are the wall heat transfer, interfacial heat transfer, energy transfer due to mass transfer (vapor generation as well as release of dissolved gas), sensible heat due to presence of noncondensables, and dissipation.

Conservation of Mass for Noncondensables in Gas Phase:

$$\frac{\partial \alpha_g \rho_g X_n}{\partial t} + \frac{1}{A} \frac{\partial}{\partial x} (\alpha_g \rho_g X_n v_g A) = \Gamma_N \quad (8-7)$$

where

X_n = mass fraction of noncondensable gas in the gaseous phase

Γ_N = noncondensable gas generation rate

This equation conserves mass of noncondensables in the gas phase, and allows transport/distribution of the noncondensables along with the gas phase. It is assumed that the noncondensables are transported at the same velocity as the fluid in the gas phase, that they are in thermal equilibrium with the vapor, and that the properties of the gas phase are mixture properties of the vapor/noncondensable mixture. The sensible heat transfer terms due to the presence of noncondensables in the energy equations represent heat transfer at the noncondensable gas-liquid interface. This is necessary because the interfacial terms use saturation temperature based on the local vapor partial pressure.

Conservation of Mass for Noncondensables in Liquid Phase (Dissolved Gas):

$$\frac{\partial \rho_s}{\partial t} + \frac{1}{A} \frac{\partial}{\partial x} (\rho_s v_f A) = \Gamma_s \quad (8-8)$$

where

ρ_s = density of the dissolved nitrogen (solute), i.e., mass of dissolved nitrogen per unit volume

Γ_s = negative of mass rate of nitrogen released per unit volume, or solute generation rate

This equation provides the means to model the release of dissolved gas at any location based on local conditions. The gas release model itself is described in a subsequent section, along with the assumptions used in its implementation in the code.

In the base code, it is assumed that at the gas-liquid interface, there is no storage of mass, momentum or energy. In FSP, the dissolved gas release term is modeled similar to that for an external source. It is assumed separately that $\Gamma_g + \Gamma_f = 0$ (similar to the base code), and that $\Gamma_N + \Gamma_s = 0$. Summing Equations 8-3 and 8-4 provides a relationship between the interfacial drag terms FIG and FIF . Summing Equations 8-5 and 8-6 provides a relationship between the interfacial mass transfer and interfacial heat transfer. These are essentially the interface jump conditions needed for closure of the conservation equations. Note that in FSP, because of the way in which the dissolved gas release term has been treated, the conservation of mass, momentum and energy at the gas-liquid interface is only approximately satisfied. This is an inherent assumption in the code. The results of executing the code for typical FSP applications have not shown significant effects due to this approximation. If new applications show significant effects, this assumption would have to be re-visited.

To complete the equation set, several terms on the right hand side of the conservation equations need to be specified, such as FWG , FIG , Q_{wg} , and Q_{ig} . These are the constitutive relations, described in a subsequent section. Typically, these are based on mechanistic models and empirical correlations, and are written in terms of velocities, thermodynamic and transport properties, and the temperatures of the liquid and gas phases. Thus, additional relationships have to be defined to relate these to the primary dependent variables of the code.

Numerical Solution

To solve the above set of equations, the differential conservation equations are cast into a numerically convenient set of finite difference equations, using a staggered spatial mesh arrangement. In this method, mass and energy are conserved over a control volume while momentum is conserved over a cell bounded by the mass and energy cell centers. A semi-implicit method is used for time advancement, where the implicit terms are formulated to be linear in the dependent variables at the new time. Essentially, this requires specification of the partial derivatives of fluid density with respect to the primary dependent variables. Most of the source terms on the right hand side of the equations are also treated semi-implicitly. The noncondensable dissolved gas release term is treated explicitly.

Figure 8-2 shows the staggered mesh concept used in the numerical solution. In the method, scalar variables (pressure, internal energies and void fraction) are defined at the cell centers, at K , L , and so on. Vector quantities (velocities) are defined at the cell boundaries, at the junctions connecting the cells, at j , $j + 1$, and so on. In this method, to define the flux terms at the boundaries of the mass and energy conservation cells, the void fraction and fluid properties are “denoted” from the upstream cells. Similarly, to estimate friction losses needed in the momentum conservation, “volume velocities” are estimated at cell centers using an averaging procedure of the velocities at the junctions connecting to each cell. The documentation of the base code (RELAP5) provides a detailed description of the method.^{16,17} Here, it is noted that the user can access “junction properties” as well as “volume properties” in developing the input model and examining the output of the code.

The governing equations, together with the interface jump conditions, constitutive relations, thermodynamic and transport properties, and property derivatives, as a function of the primary dependent variables, form a closed set of equation. The code solves this set for the primary dependent variables as a function of time and spatial location. Details of derivation of the finite difference equations and the numerical solution method are described in the base code documentation.^{16,17}

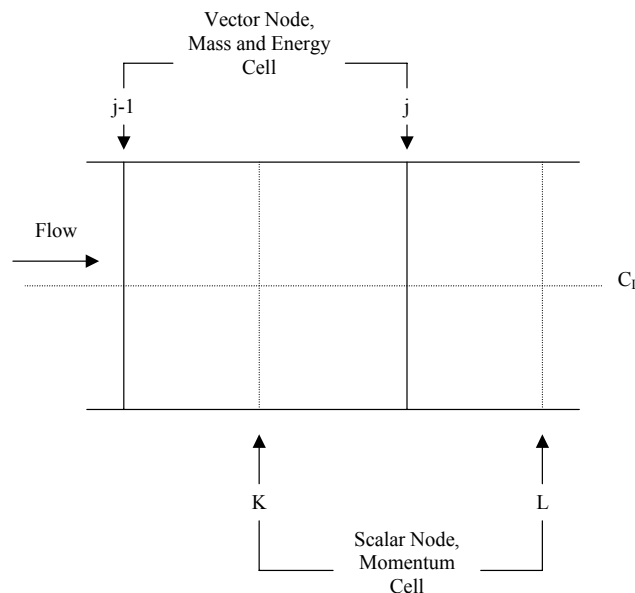


Figure 8-2. Staggered Mesh Numerical Method.

State Relationships and Fluid Properties

As discussed previously, the code uses five primary dependent state variables:

- P : total pressure
- α : gas phase volume fraction
- U_g : gas phase specific internal energy
- U_f : liquid phase specific internal energy
- X_n : mass fraction of noncondensable gas in the gas phase

All thermodynamic variables are expressed in terms of the above five state variables. In addition, several state derivatives are needed for the numerical scheme. Detailed descriptions of fluid property estimation and calculations of thermodynamic variables for the code can be found in Tuzla et al.⁷

Constitutive Models

The constitutive relations include models for defining two-phase flow regimes and flow-regime-related models for interphase drag and shear, the coefficient of virtual mass, wall friction, wall heat transfer, and interphase heat and mass transfer. Heat transfer regimes are defined and used for wall heat transfer. For the virtual mass, a formula based on the void fraction is used.

Note that while the FSP code contains models for wall heat transfer, these models have not been exercised or assessed with the various new fluids that have been implemented into the code. In addition, wall heat transfer is not expected to play a significant role in the analysis of typical suppressant delivery systems because of the short time period of the expected transient. If a user encounters a special application of FSP where wall heat transfer may need to be included in the model, the base code documentation contains the needed information.^{16,17}

The constitutive relations needed are for the terms: Γ_g , Γ_f , Γ_N , FWG , FWF , FIG , FIF , C , Q_{wg} , Q_{wf} , Q_{ig} , Q_{if} , Q_{gf} , $DISS_g$, and $DISS_f$. In general, these relationships are dependent on the thermodynamic state, void fraction, fluid properties and velocities. As shown in Figure 8-2, the thermodynamic state, void fraction and fluid properties are defined at volume centers, while the velocities are defined at the junctions. Fluid properties and the void fraction are “donored” to junctions, and volume velocities are estimated by momentum flux weighting of the velocities at the junctions that connect to each volume. It is convenient to use flow regimes to characterize the two-phase flow. This allows specifying a more mechanistic form to the various constitutive relations, which is desirable since the code is structured to handle various different fluids.

Four flow regime maps are included in the base code, but only two of these are relevant for applications of FSP. The other flow regime maps will not be encountered by the user and are not discussed here. The flow regime maps in FSP address flow regimes and transitions between flow regimes for horizontal flow and vertical flow.

The flow regime maps are based on the work of Taitel et al.²³ and Mishima and Ishii²⁴, who have developed flow regime classifications and mechanistic models to describe flow regime transitions.

However, some of their transition criteria are quite complex, and further simplification has been carried out in order to efficiently apply these criteria in the code. When wall heat transfer is not modeled, the flow regimes and the transition criteria are dependent on hydrodynamic conditions only. When wall heat transfer is modeled, there is a possibility that the wall may encounter the condition of critical heat flux (CHF). In the post-CHF condition, the wall will mostly not be wetted by the liquid. This alters the flow regime. To capture this effect, the code recognizes the effect of wall heat transfer explicitly, and if post-CHF conditions are indicated, a separate flow regime map is used to characterize the two-phase flow patterns. Again, note that the post-CHF regimes would be invoked only if the user models wall heat transfer, and the local fluid and wall conditions indicate post-CHF conditions. As discussed above, wall heat transfer is not expected to be required in most applications of the FSP code. Hence, these flow regimes are not described here, and the base code documentation contains detailed description, if needed.^{16,17}

The vertical flow regime map (for both up and down flow) is for volumes whose elevation angle ϕ is such that $45^\circ < |\phi| < 90^\circ$. This map is modeled as nine regimes – four for pre-CHF heat transfer, four for post-CHF heat transfer, and one for vertical stratification. As noted previously, the post-CHF regimes will not be encountered if wall heat transfer is not modeled by the user. The pre-CHF regimes are the same flow regimes as would exist if there was no wall heat transfer. For pre-CHF heat transfer, the regimes modeled are the bubbly, slug, annular mist, and mist-pre-CHF regimes.

The horizontal flow regime map is for volumes whose elevation angle ϕ is such that $0^\circ < |\phi| < 45^\circ$. This map does not distinguish between pre- and post-CHF regimes. Otherwise it is similar to the vertical flow regime map. The horizontal flow regime map consists of horizontally stratified, bubbly, slug, annular and mist-pre-CHF regimes.

In reviewing the base code, RELAP5/MOD3.2, it was found that most of the constitutive relations were structured to be reasonable for the fluids included in FSP. The only areas where correlations specific to water were used were in the computation of interphase drag in vertical flow, and in wall heat transfer. Thus only these calculations were modified. In the description presented below, the emphasis is on providing the user with basic information on what is contained in FSP. Details of the various models can be found in the base code documentation.^{16,17} Additional information is provided below in the specific areas where the base code was modified. The dissolved gas release model was developed especially for FSP, and so it is described in more detail than the other models.

Wall Friction

The relevant wall friction terms are *FWG* and *FWF* in the phasic momentum equations. Note that the wall friction force terms include only wall shear effects. Losses due to abrupt area change are calculated using mechanistic form loss models. Other losses due to elbows or complicated flow passage geometry are modeled using energy loss coefficients supplied by the user in the input for junction information.⁷ These terms are also directly used in computing the energy dissipation terms, $DISS_g$ and $DISS_f$ in the phasic thermal energy equations.

The approach was to first calculate an overall two-phase frictional pressure drop. This was done using a standard two-phase multiplier method (as shown in Wallis²⁵). The two-phase friction was then partitioned between the phases (Chisolm²⁶) to get the phasic wall friction components. A further adjustment was made to incorporate flow regime effects, using a wetted wall fraction. This provides a more physical

representation for certain regimes where it is clear that one phase would be more influenced by wall friction than the other, as in annular flow, where the wall is fully wetted by the liquid phase.

The model uses the hydraulic diameter and surface roughness data provided by the user for each volume. There is an option for the user to turn off wall friction altogether, but this is not recommended unless as a sensitivity study to debug results from a specific analysis.

Interphase Friction

The interphase friction (or drag) per unit volume in the phasic momentum equations is expressed in terms of a phasic interphase friction coefficient as:

$$F_{ig} = \alpha_g \rho_g FIG (v_g - v_f) \quad (8-9)$$

and

$$F_{if} = \alpha_f \rho_f FIF (v_g - v_f) \quad (8-10)$$

The magnitude of the interphase drag force per unit volume on the liquid is assumed to be equal to that on the gas phase. This provides a relationship between *FIG* and *FIF*,

$$\alpha_g \rho_g FIG = \alpha_f \rho_f FIF \quad (8-11)$$

The interphase drag force per unit volume represents the interphase momentum transfer rate and is due to the difference between the phasic velocities. Thus, analogous to the transfer of heat or mass, it can be expressed as:

$$F_{i,gf} = F_i (v_g - v_f) \quad (8-12)$$

where F_i is a momentum conductance term, and can be expressed as:

$$F_i = A_{gf} B_{gf} \quad (8-13)$$

where A_{gf} is the interfacial area per unit volume, and B_{gf} is a momentum transfer coefficient.

The code uses the flow regime characterization to derive relationships for A_{gf} and B_{gf} in terms of fluid properties, flow geometry, phasic velocities and the void fraction. These are then related back to the terms *FIG* and *FIF* needed in the phasic momentum equations.

The base code, RELAP5/MOD3.2, uses mechanistic models for the above calculations, except for vertical flow in the pre-CHF regimes. In this case, the base code uses a correlation developed empirically from water data. In FSP, to make this independent of the fluid type, the empirical correlation (called the Drift Flux correlation or the EPRI correlation) has been replaced with the mechanistic models. The models are similar to what exists in the base code for the various flow regimes and therefore are not further described here. It is noted that for the calculation of interphase drag in vertical flow in FSP, the vertically stratified regime is not explicitly used. Vertical stratification is recognized primarily for the calculation of interphase heat and mass transfer.

In building the input file, there is a parameter, b , that allows the user to select an optional interphase drag modeling approach for rod bundles. In FSP, in addition to replacing the interphase drag models for

vertical flow, this option has been essentially de-activated. Thus choosing a value of 0 or 1 for this parameter will not have an effect. It is recommended that the user choose the default value, which is zero.

Interphase Heat and Mass Transfer

The interphase heat and mass transfer rates are related by the assumption that energy is not stored at the interface. It should be noted that the code separately recognizes interphase mass transfer in the bulk fluid and at an interface near the wall. This allows the code to mechanistically treat some special cases, such as subcooled boiling. In this case, there is a radial temperature gradient within the liquid, and boiling occurs near the wall, while there is condensation in the bulk fluid. Thus, the general treatment is:

$$\Gamma_g = \Gamma_{ig} + \Gamma_w \quad (8-14)$$

where Γ_w is computed by the wall heat transfer models. When wall heat transfer is not modeled, this term is zero. Γ_{ig} is computed from the heat transfer at the bulk interface. The interface is assumed to be at the saturation temperature. The heat transfer at the bulk interface is then:

$$Q_{ig} = H_{ig} (T^s - T_g) \quad (8-15)$$

$$Q_{if} = H_{if} (T^s - T_f) \quad (8-16)$$

$$Q_{ig} + Q_{if} + \Gamma_{ig} (h_g - h_f) = 0 \quad (8-17)$$

where h_g and h_f can be at saturation or at the value corresponding to the local pressure and temperature, depending on whether the process is one of boiling or condensation.

The terms H_{ig} and H_{if} are the interphase heat conductance terms and are conveniently modeled as products of the interphase area per unit volume and the interphase heat transfer coefficient. These are in turn determined as a function of the flow regime, and modeled as a function of fluid properties, flow geometry, velocities and the void fraction.

Wall Heat Transfer

The total wall heat flux, q'' , is modeled as a sum of heat fluxes to the vapor and liquid phases:

$$q'' = h_g (T_w - T_{ref,g}) + h_f (T_w - T_{ref,f}) \quad (8-18)$$

where h_g and h_f are heat transfer coefficients to the gas and liquid phases respectively (per unit wall surface area), and $T_{ref,g}$ and $T_{ref,f}$ are gas and liquid reference temperatures. The reference temperatures can be the local gas or liquid temperature or the saturation temperature, depending on the correlation used for the heat transfer coefficient.

A heat transfer surface concept is used, based on the heat flux, wall temperature and saturation temperature, to decide the mode of heat transfer (such as convection to single phase liquid, bulk nucleate boiling, condensation). Correlations are used for the heat transfer coefficients in the various heat transfer regimes to compute the heat flux. The total heat flux is ensured to be continuous over the heat transfer-wall temperature surface, to avoid numerical difficulties as the heat transfer regimes go through transitions.

Also calculated is the portion of the wall heat flux (Q_{ig}^w and Q_{if}^w) that contributes directly to mass transfer. Then the interphase mass transfer due to wall heat transfer is calculated from:

$$Q_{ig}^w + Q_{if}^w + \Gamma_w (h_g - h_f) = 0 \quad (8-19)$$

where, as before, h_g and h_f can be either at saturation conditions or at the local pressure and temperature, depending on whether the process is boiling or condensation.

The base code, RELAP5/MOD3.2 contains generic models for the heat transfer coefficients in most of the heat transfer regimes that can be considered to be reasonably fluid-independent. In two areas, the correlations are more empirical and also based solely on water data. Hence, these have been modified in the FSP code. One area is the critical heat flux (CHF). The base code uses a table look-up procedure for calculating CHF, using data obtained for water at a variety of conditions. This was replaced in FSP by a simpler model, based on a modification to the Zuber correlation (Zuber et al.²⁷).

$$q_{CHF} = 1.31(0.96 - \alpha_g) \rho_g h_{fg} [\sigma g (\rho_f - \rho_g) / \rho_g^2]^{1/4} \quad (8-20)$$

Zuber's correlation has been shown to match CHF data for a variety of fluids under pool boiling conditions. The modification to Zuber's correlation is the term $(0.96 - \alpha_g)$ and has shown to match flow data with water and Freon. Note that this condition of CHF is normally one that is associated with hydrodynamic dryout of a heated surface. This is the type of CHF one may expect when wall heat transfer is modeled with only passive heat structures, such as typical pipe walls in fire-suppressant delivery systems. In implementing the above model in FSP, a lower limit of 1000 W/m² was imposed to prevent negative values, at high void fractions.

The other area modified is in the correlation for wetted area fraction used for computing post-CHF heat transfer. This correlation utilizes an exponential decay form to capture the decrease of wetted area fraction as the wall temperature increases. The decay constant was derived as a function of flow rate and void fraction, from water data. In FSP, the decay constant has been set to a fixed value. This is considered reasonable because this heat transfer regime is rarely encountered, and will provide continuity for the heat transfer surface if encountered.

Coefficient of Virtual Mass

The last term in the phasic momentum equations is the dynamic drag term due to virtual mass effects, also called the inertial drag force per unit volume. In the base code, in the numerical solution procedure, the spatial dependence of the velocities in this term was neglected. Thus the term only includes the time-dependent portion. This was a compromise, because the spatial terms were dependent on the nodalization selected by the user to represent a particular system, and there was some user experience that suggested that this led to numerical errors. The main intent of this term is to capture sudden accelerating flows, and the time-dependent term provides that capability. The coefficient, C , in this term is called the coefficient of virtual mass. It is given as:

$$C = 0.5 (1 + 2\alpha_g) / (1 - \alpha_g) \quad \text{for } 0 \leq \alpha_g \leq 0.5$$

and,

$$C = 0.5 (3 - 2\alpha_g) / \alpha_g \quad \text{for } 0.5 \leq \alpha_g \leq 1$$

Release of Dissolved Gas

The liquid agent in the storage vessel is stored under pressure of a noncondensable gas (N_2). It is assumed that the agent has been stored for a long enough period for the liquid to be saturated with N_2 (equilibrium condition). At equilibrium, the concentration of dissolved N_2 in the liquid medium is proportional to the partial pressure of N_2 in the gaseous space above the liquid. This is Henry's law:

$$x_N^* = H P_N \quad (8-21)$$

where x_N^* is the equilibrium concentration (mole fraction of solute in solution), H is Henry's constant and P_N is the partial pressure of N_2 above the liquid. H is usually a function of temperature and the liquid type.

As the system is depressurized, nitrogen will come out of the solution since the partial pressure decreases. According to Henry's law, the corresponding concentration of nitrogen in the solution must also decrease. Hence the excess must be released. In a fast depressurization transient, the excess can still be in solution due to surface tension. Considering a micro-bubble of dissolved gas with radius r_c , the difference between the pressure inside and outside the bubble is given by

$$\Delta P_{NUC} = \frac{2\sigma}{r_c} \quad (8-22)$$

where σ is the surface tension. As the pressure outside decreases, the pressure difference builds up until a point where surface tension can no longer hold the bubble together, and the excess N_2 is then released. This initiation mechanism is similar to nucleate boiling, in which the liquid is superheated before boiling can occur. The radius of the micro-bubble can be empirically determined by observing the point at which N_2 release occurs. In this model, this radius is assumed known (user input). The release pressure is then given by

$$P_{rel} = P_i - \Delta P_{NUC} = P_i - \frac{2\sigma}{r_c} \quad (8-23)$$

where P_i is the initial system pressure.

The above determines the initiation of release. The rate of release is determined as follows. Henry's law determines the equilibrium concentration for given conditions. As the system is depressurized, the corresponding partial pressure decreases. The corresponding equilibrium concentration will be less. The solution is therefore at a state of non-equilibrium. The release is a means to achieve a new equilibrium. Thus, the release rate is postulated to be proportional to the difference between the actual concentration and the equilibrium concentration (dictated by Henry's law) as follows:

$$\Gamma_{rel} = \Gamma_0 (x_N - x_N^*) \quad (8-24)$$

where Γ_0 is some release coefficient, x_N is the actual concentration, and x_N^* is the equilibrium concentration as given by Henry's law. Thus

$$\Gamma_{rel} = \Gamma_0 (x_N - H P_N) \quad (8-25)$$

The release will be zero when the actual concentration approaches the equilibrium concentration, as it should be. The release model is similar to other transfer phenomena, such as heat transfer and mass transfer.

The model requires that users specify, as input, the parameters r_c and Γ_0 , and the initial pressure P_i and temperature T_i .

The numerical implementation of the release rate model poses a problem, since the partial pressure is not the local value, but the value above the liquid-gas interface. A compromise is made by using the local total pressure in place of the partial pressure in calculating the equilibrium concentration using Henry's law. This over-predicts the equilibrium concentration, and hence under-predicts the release rate. It may be compensated by using a larger release coefficient. Thus, the release rate is numerically implemented as, for the k^{th} volume:

$$\Gamma_{rel,k} = \Gamma_0 (x_{N,k} - H P_k) \quad (8-26)$$

HP_k is the mole fraction of N_2 in solution. To convert to mass of N_2 per unit mass of solvent, one gets

$$\text{Mass Fraction } N_2 = \frac{H P_k W_N}{(1 - H P_k) W_f} \quad (8-27)$$

where W_N is the molecular weight of nitrogen (28.0) and W_f is the molecular weight of the fluid. The actual concentration is related to the solute density as

$$x_{N,k} = \left(\frac{\rho_s}{\alpha_f \rho_f} \right)_k \quad (8-28)$$

The solute generation rate is therefore the negative of the release rate:

$$\Gamma_{s,k} = -\Gamma_{N,k} = -\Gamma_0 \left[\left(\frac{\rho_s}{\alpha_f \rho_f} \right)_k - \frac{H P_k W_N}{(1 - H P_k) W_f} \right] \quad (8-29)$$

The above is only valid if the local concentration is greater than the equilibrium concentration. Otherwise the release rate should be zero. Hence

$$\Gamma_{s,k} = \min(\Gamma_{s,k}, 0.0) \quad (8-30)$$

Also, the amount of release in one time step should not be more than the total amount dissolved in the volume. Thus the maximum release rate is given by

$$\Gamma_{rel,k,max} = \frac{\rho_s}{\Delta t} \quad (8-31)$$

where Δt is the current time step. Hence the final expression for the solute generation term is

$$\Gamma_{s,k} = \max \left\{ \min(\Gamma_{s,k}, 0.0), -\frac{\rho_s}{\Delta t} \right\} \quad (8-32)$$

The Henry's constant is estimated from the PROFISSY Code (see Yang et al.²) as follows. Assuming Henry's law to be valid, the equilibrium concentration is given by

$$x_N = H P_N \quad (8-33)$$

In PROFISSY, the concentration of nitrogen in the agent liquid (x_N , mole fraction) is calculated given the system pressure (P), temperature (T), total volume (V), and total agent mass (m_a). The partial pressure of nitrogen can be determined from

$$P_N = P - P_v \quad (8-34)$$

where P_v is the saturation pressure of the agent fluid at T . Table 8-1 lists the output from PROFISSY, and the calculation of H as described above. Three fluid systems are considered: HFC-227ea, HFC-125 and halon 1301. As can be seen, the solubility of nitrogen in all three agents is very similar, and Henry's constant can be correlated as a quadratic function of temperature, as shown in Figure 8-3. The analytical form of the correlation is given by

$$H = H_0 + C_1 T + C_2 T^2 \quad (8-35)$$

where H is in mol/Pa, and T is in K and $H_0 = 2.35 \times 10^{-7}$, $C_1 = -1.55 \times 10^{-9}$, and $C_2 = 2.96 \times 10^{-12}$

Table 8-1. PROFISSY Results for Henry's Constants.

	HFC-227ea/N ₂	Halon 1301/N ₂	HFC-125/N ₂
<i>T</i> (K)	<i>H</i> (mol/Pa)	<i>H</i> (mol/Pa)	<i>H</i> (mol/Pa)
190	n/a	4.70E-08	n/a
200	n/a	4.20E-08	n/a
210	n/s	3.87E-08	3.65E-08
220	3.77E-08	3.67E-08	3.80E-08
230	3.62E-08	3.59E-08	3.37E-08
240	3.52E-08	3.30E-08	3.37E-08
250	3.47E-08	3.45E-08	3.47E-08
260	3.30E-08	3.15E-08	3.41E-08
270	3.34E-08	3.27E-08	3.25E-08
280	3.29E-08	3.28E-08	3.48E-08
290	3.29E-08	3.22E-08	3.40E-08
300	3.36E-08	3.35E-08	3.76E-08
310	3.49E-08	3.74E-08	3.90E-08
320	3.58E-08	3.96E-08	4.45E-08
330	3.79E-08	4.88E-08	5.39E-08
340	4.15E-08	n/a	n/a
350	4.59E-08	n/a	n/a
360	5.42E-08	n/a	n/a

Figure 8-4 shows the calculated bottle pressure as a function of time for various release coefficients. The critical radius was specified at 7.5×10^{-9} m. The initial concentration was estimated as 0.02916 kg N₂/ kg liquid phase. This value is comparable to the reported initial concentration of Test 146 in Elliott et al.¹⁰ At about 0.1 s, as the pressure decreases to a value of about 4 MPa, there is a noticeable change in the rate of pressure decrease. This is the pressure at which gas begins to be released from the liquid, and experimental results generally indicate that this would happen at about the same pressure for a given fluid type and system configuration. As discussed earlier, this pressure is controlled by the value of the critical gas bubble radius, r_c , chosen by the user. The lower the value of r_c specified, the lower the pressure at which gas release would be initiated.

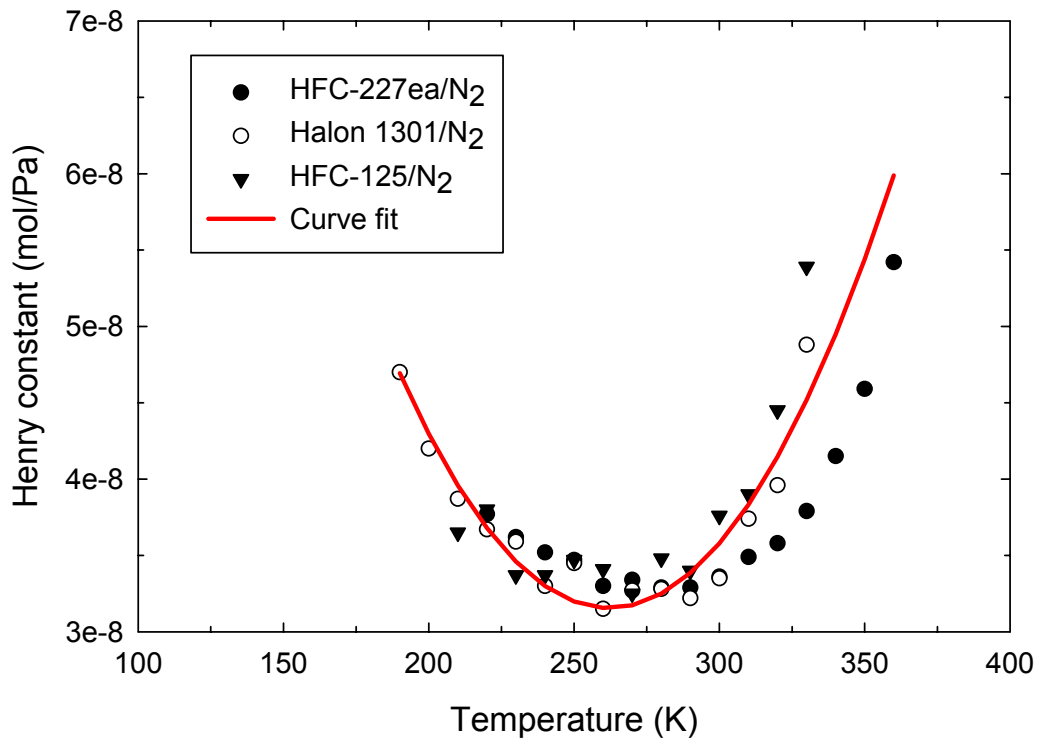


Figure 8-3. Curve Fit for Henry's Constant.

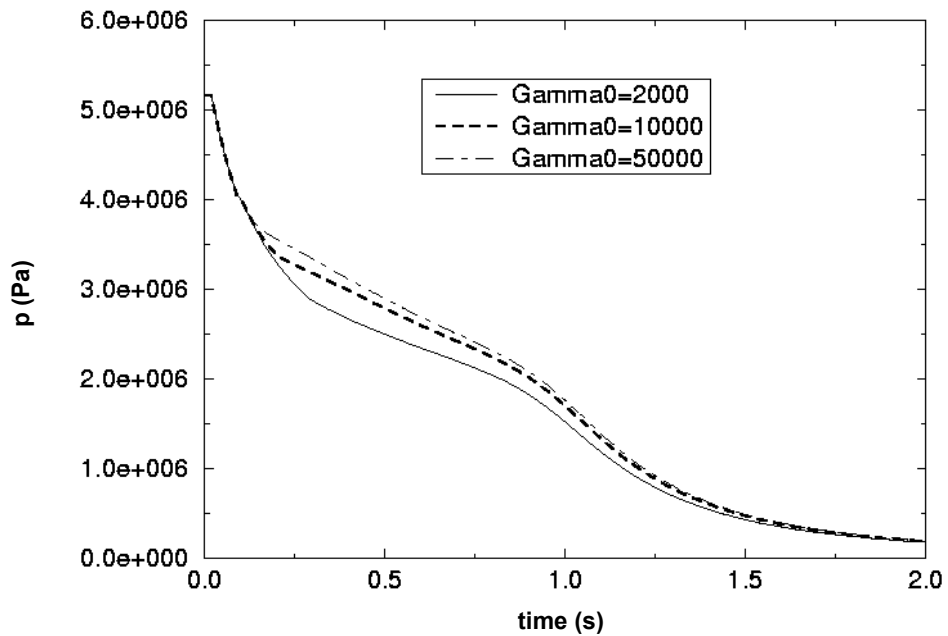


Figure 8-4. Effect of Release Coefficient on Calculated Pressure Response.

The value of Γ_0 controls the rate of gas release. At low values of Γ_0 , the rate of release is small, and the pressure continues to decrease monotonically below the pressure at which gas release was initiated. As the value of Γ_0 is increased, there is a noticeable decrease in the depressurization rate at the gas release pressure (at about 0.1 s). This is the expected trend. Test runs of the code indicate that this method of modeling the gas release works relatively smoothly, and the code appears to handle a wide range of release coefficients without numerical difficulty.

One of these sensitivity cases, corresponding to a Γ_0 of 10,000 kg/m³ s and an initial concentration of 0.02196 kg N₂/kg liquid, was used to further check out the model. Figure 8-5 compares the calculated pressure with experimental measurements. Figure 8-6 shows the void fraction responses for the various cells used to model the supply bottle. Volume 203-01, not shown in the figure, is at the top of the bottle, and Volume 203-10 is at the bottom. The figure shows a relatively smooth emptying of the bottle, with the void fractions in the lower cells increasing to 1.0 subsequent to the void fractions in the cells above them. The void fraction in the last cell, Volume 203-10, increases to 1.0 after all the other cells, at about 1.0 s. This represents the time in the calculation when the bottle is emptied.

This calculation was also used to check out other parameters. The solute concentration profiles showed smooth changes, following expected trends. A mass balance was carried out to ensure that the code conserved the mass of nitrogen, between the initial amount and the additional amount released from the liquid. Essentially, these checks ensured that the gas release model was implemented in the code as intended, and the mechanistic gas release model produced the expected trends. There is of course some uncertainty in how to specify the correct values for the parameters r_c and Γ_0 . However, as shown in other sections of this report, comparisons to experiments with different fluids and system configurations indicate reasonably good agreement between code calculations and experimental data, with these parameters varying over a relatively narrow range. This has been useful in arriving at a range of recommended values for these parameters. Further, from a design perspective, while variation of these parameters causes a noticeable variation in the initial pressure history, there is not much variation in the time required to empty the supply bottle. Hence it is believed that this gas release model, used with the range of recommended values for r_c and Γ_0 , would adequately serve the needs of a design engineer evaluating the performance of a suppressant delivery system.

Special Process Models

This section describes certain models in the code that simulate special processes. The user can select many of these processes via input. A detailed description of these process models can be found in the base code documentation.^{16,17} The information below is a brief summary, to provide some basic information and where appropriate, some user guidelines on the use of these models.

Choked Flow

Choking is defined as the condition where the mass flow rate becomes independent of the downstream conditions. Choking occurs because acoustic signals can no longer propagate upstream as the fluid velocity equals or exceeds the propagation velocity. In typical FSP applications, choking can occur at the bottle exit, as soon as the discharge begins, and also at the discharge location from the system. The choked flow model in FSP is by Trapp and Ransom²⁸ and is used to calculate the mass discharge from the

system. The model can also be used to predict the existence of and calculate choked flow at interior points in the system.

The user can select the choking model as a part of the junction control flag information in the input file. The user can select this option at all junctions. In fact, the default option will select the choked flow model. It is recommended, however, that the user only select this model at the system exit location(s) and at the junction representing the exit of the supply vessel. The model should be turned off at all other internal junctions. This is because the sonic velocity (propagation velocity) in two-phase flow can be a strong function of the void fraction, and the choked flow model imposes an external criterion on the code's normal numerical solution method. This can lead to difficulties in code execution and a drastic reduction in the computational time step.

Also note that the input for junctions allows the use of discharge coefficients for subcooled liquid, saturated fluid and single-phase vapor. Current assessment of the code against experiments suggests that best results are obtained by using a subcooled discharge coefficient of 1.0, a two-phase discharge coefficient of 0.8 to 0.9, and a single-phase vapor discharge coefficient equal to the two-phase discharge coefficient.

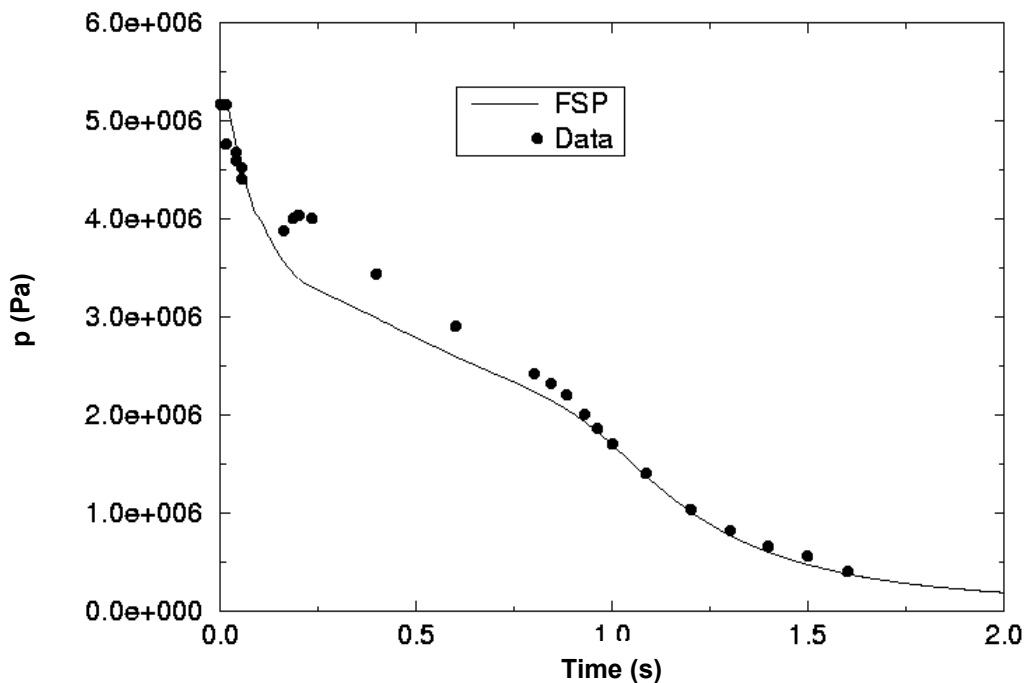


Figure 8-5. Comparison of Calculated and Measured Bottle Pressure for Test 146.

Horizontal Stratification and Entrainment

Flow at low velocity in a horizontal pipe can be stratified due to buoyancy forces. The horizontal flow regime map in the code contains a mechanistic model to predict when stratification occurs. When the flow is stratified, the area average pressures are affected by the nonuniform transverse distributions of the phases. The normal code equations are based on assuming uniform transverse pressure distribution. To account for the nonuniform pressure distribution, adjustments are made to the momentum equations to

consider area average pressures for the vapor and liquid phases, and the interfacial pressure between them. This model is always active in the code, but becomes significant only when the code's stratification criterion is met. The code then calculates a liquid level in the channel (circular pipe geometry is assumed) and uses this information to estimate the hydrostatic pressure in the transverse direction.

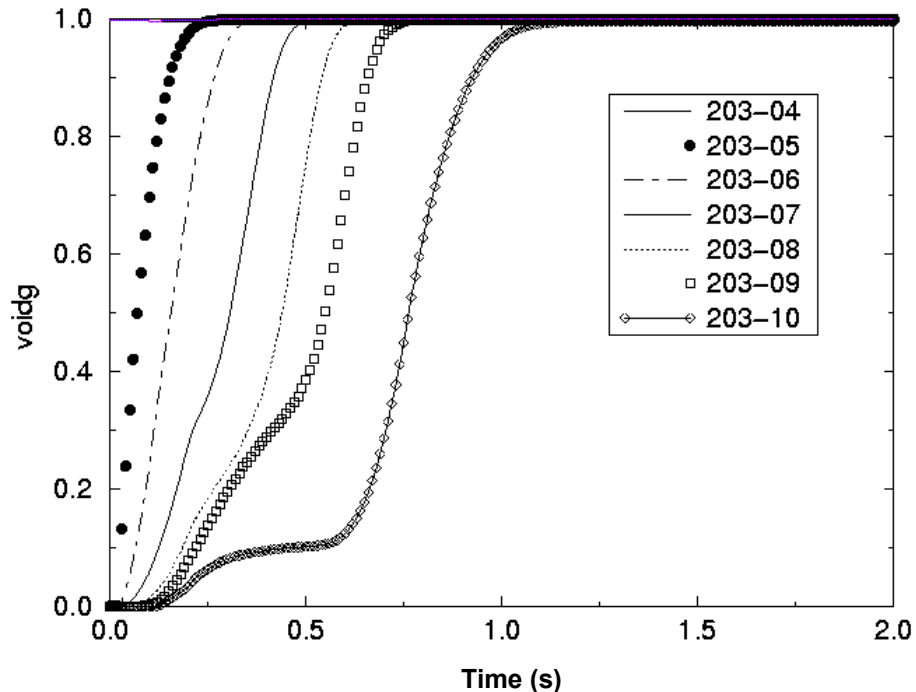


Figure 8-6. Void Fraction Responses in Lower Portion of Bottle.

Also, when the flow is stratified, the void fraction flowing in a junction may be different than the upstream volume void fraction. A typical example would be when there is an area contraction. With stratified conditions in the upstream volume, if the level is below the pipe centerline, the void fraction in the junction would be significantly higher than the upstream volume. If the level is above the pipe centerline, the junction void fraction would be lower than the upstream volume. In addition to the formation of a level and its effect, the vapor can entrain liquid through the junction, and similarly the liquid can pull through some gas. The code considers these possibilities, and adjusts the junction void fraction to be different than the upstream volume void fraction when the upstream volume is calculated to be stratified.

The user does not actively engage these models. It is part of the code's internal structure and will automatically be invoked as needed.

Abrupt Area Change

A general piping network system can contain sudden area changes and orifices. The code contains built-in models for the user to access in simulating these geometries. The basic hydrodynamic model in the code is formulated for slowly varying flow area. Hence, special models are needed when the flow area undergoes an abrupt change, such as at an orifice.

Basically, the user can select the abrupt area change option at any junction in the model, as a part of the junction control flag input information. The code will calculate the energy loss coefficients associated with the abrupt area change internally. In a case where the flow is going through a sudden contraction, the code will also internally compute the losses associated with the formation of a vena contracta. Along with selecting the abrupt area change option, if the user also enters form loss coefficients, these will be added to the internally calculated form losses.

User-Specified Form Losses

In the junction control flag information card, the user can specify a junction to be a smooth or abrupt area change junction. The user can also specify form loss coefficients at the junction. For standard geometries, and configurations such as elbows and tees, these form loss coefficients can be obtained from standard handbooks. If the user has frictional pressure drop data for a particular system at known flow rates, that can be used to back out form loss coefficients.

The user can also enter flow dependent form loss coefficients. Typically, the form losses would be a function of the Reynolds Number. The code input allows a standard form and the user has to enter the desired constants for the Reynolds Number dependence.

Cross Flow Junction

The code's numerical method is generally formulated using one-dimensional elements. However, there are applications where an approximate treatment of transverse flow can provide an improved physical simulation. The crossflow junction component provides this feature.

A typical place to use the crossflow junction would be in modeling a standard 90° tee. The crossflow junction would be used to model the connection to the branch line, as shown in Figure 8-7. In this case, the momentum flux in the side branch is assumed to be perpendicular to the main flow stream. Thus the mainstream momentum flux does not contribute to the crossflow momentum formulation. Essentially, in the crossflow junction formulation, there is no transport of axial direction momentum due to the flow in the transverse direction.

The user selects the crossflow junction option by specifying the appropriate connection code when describing the 'From' and 'To' volumes for a junction.

Component Models and Systems

The code contains a variety of generic components that are used to build system models. These include components such as Single Volume, Time-Dependent Volume, Single Junction, Pipe, Valve, etc. Most of these are self-explanatory. This section provides some additional information on building a system model and the use of some of the components and features.

Branch

There are several ways to simulate branching flows. Several single junctions can be connected to the exit of a single volume to simulate flow splits. A BRANCH component is also provided in the code. Essentially, this functions no differently than a single volume to which more than two junctions are

connected. Primarily, it is a user-convenience, which allows all the junction information to be entered along with the volume information in one component instead of using several separate components. A crossflow junction can be used to connect a branch component to another component. Two typical uses are in modeling branching flows in a one-dimensional branch, and a tee branch.

A one-dimensional branch is one where more than two normal junctions connect to a volume, and where it is assumed that multidimensional effects are small compared to system interaction effects. Typically, this would be used in branched flows that occur in headers or plena. Fluid entering a header and then splitting into several parallel paths would be modeled as a one-dimensional branch.

A tee branch is formed by the arrangement shown in Figure 8-7, where the crossflow junction was used. In this case, the Volume V_2 may be specified as a branch component, and the crossflow junction connecting to it could be defined by the appropriate connection code, described in the input manual in Tuzla et al.⁷ The tee connection could also be modeled without a crossflow junction, by using a branch component with normal junctions, as shown in Figure 8-8. This approach has the advantage that fewer volumes are used. The disadvantage is that if the tee is really a standard 90° tee, then it may not be the best representation of the physical process. In typical FSP applications, very little difference has been observed between the two approaches. Hence, either approach seems acceptable.

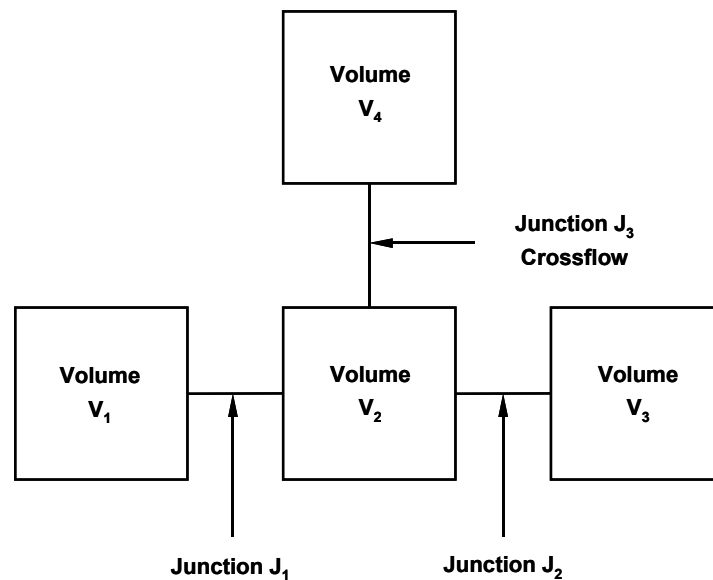


Figure 8-7. 90° Tee Model with Crossflow Junction.

Note that a volume with more than two junctions connected to it is treated by the code as a branch component, even if it has not been defined as such in the input. What this really means is that the volume velocity in this volume is determined as a momentum flux weighted average of the flows in the junctions connecting to it. Also, the volume cross-sectional area is apportioned between the various streams in proportion to the volumetric flow in these streams. The consequence is that, if one stream has a very high velocity, there would be excess error in conserving momentum (and mechanical energy) around this volume. One place where this has an impact is if one of the junctions connecting to the branch is the exit junction for the system and it is choked at a high velocity. To avoid this situation, it is recommended that the user allow some straight pipe length connected to all the junctions of a branch. It is also

recommended that when the BRANCH component is used, the junctions of the component use the abrupt area change option.

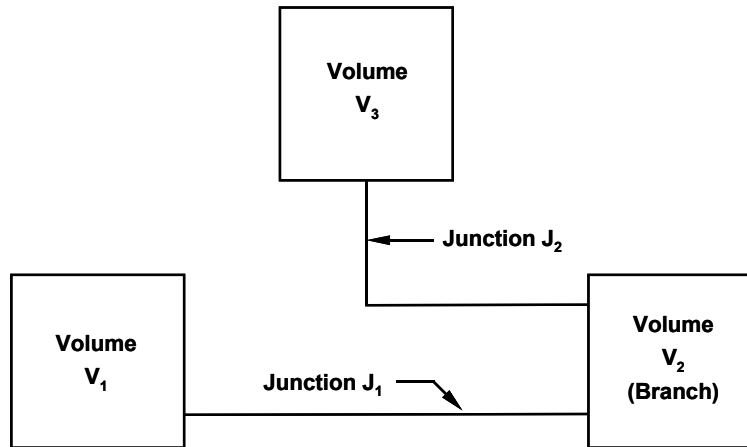


Figure 8-8. Tee Model with Normal Junctions.

Valves

Valves are quasi-steady models that are used to either specify an option in a system model or to simulate control mechanisms. They are essentially treated as single junctions and the input required to describe them is similar. There are two categories of valves, those that open and close instantly or those that open and close gradually. The base code contains several types of valves. Only two types are envisioned to be useful in modeling typical fire suppressant delivery systems, and these are described here.

A Trip Valve is one that is fully open or fully closed based on a trip setting. The opening or closing will occur in one time step following the trip signal. The trip signal can be structured to latch the valve in an open or closed position, if desired.

A Motor Valve has the ability to control the junction flow area as a function of time. The operation of this valve is controlled by two trips, one to open and one to close. A user-specified rate parameter controls the rate at which the valve area changes. The abrupt area change option is normally used with this component to allow the code to automatically compute the form loss coefficient as a function of the valve area.

Typical use of this component in FSP applications would be to describe the junction that connects the suppressant supply vessel to the piping system. The valve could be opened as fast as desired by the user to simulate the initiation of the discharge transient.

Trip Systems

The Trip System consists of the evaluation of logical statements. Each trip statement has a true or false result, and an associated variable, TIMEOF. This variable is the time in the transient at which the trip became true and has a value of -1.0 when the trip is false. This variable can be used to set time delays based on events during the transient. Within the code structure, the trip system only evaluates the logical statements (such as, is the transient time greater than 2.0 s?). The decision of what action is needed based

on the trip status resides within other models. In the above example, the trip system would assign a true or false value to a particular trip number depending on whether the transient time was less or greater than 2.0 s. If this trip number is invoked by a valve component, the valve models would decide whether to close or open the valve, at what rate, etc. Using the trip system is fairly self-explanatory, and directions are provided in Tuzla et al.⁷

Control Systems

The control system provides the capability to evaluate simultaneous algebraic and differential equations. This allows simulation of control systems typically used in hydrodynamic systems. Another use is to define auxiliary output quantities, which can then be extracted from the output or restart files as tables or plots.

In typical FSP applications, no complicated trip and control logic is required. Hence, control systems are primarily used to define auxiliary output variables. For example, enthalpy is not a normal code variable, and if it is needed for some reason, it can be computed using several control systems (such as the SUM and MULTIPLIER components) to calculate it from the internal energy, pressure and specific volume, which are all normal code variables. Another example would be if a user wanted to know the Froude Number at the system exit, for evaluating mixing characteristics in the discharge area. A variety of control systems are provided in Tuzla et al.⁷

Code Architecture

The FSP code was developed from the base code RELAP5/MOD3.2, which was written in FORTRAN 77 for a variety of 64-bit and 32-bit computers. In developing FSP from the base code, RELAP5/MOD3.2, the source code was obtained from the Idaho Engineering National Laboratory. This code was adaptable to other computing environments. The code was configured to work on a PC with WINDOWS 95 operating system and tested to ensure that the code options would function properly. The hardware chosen for installation was a laptop PC with a Pentium 233 MHz processor, 64 MB RAM and 3.2 GB hard drive. The compiler used was the DigitalTM Visual FORTRAN compiler (Standard Edition, Version 5.1) for WINDOWS 95 operating system. The coding is modular, using top-down structuring. The various models and procedures are isolated in separate subroutines. Detailed description of the top-level organization of the code, code installation and execution, input file processing, and graphics for output can be found in Tuzla et al.⁷

8.3.6 Supporting Laboratory Data

Experiments were performed to obtain data for several baseline fire suppressants and to establish a protocol for obtaining such data for any future candidate fluids. These data were then used in the assessment of the product code for simulating possible suppressant delivery systems. Descriptions of pertinent dimensions and design features of the test facility are provided below.

Experimental Test Facility

The test facility consists of a source vessel for the suppressant fluid, a quick opening discharge valve, a holding rack, a piping network, and a collection tank. This arrangement allows the system to be operated

as a closed loop to recycle the test fluid. A simple schematic is provided in Figure 8-9, showing the layout of the facility. The dimensions of this test system adhere as closely as possible to standard sizes used in present-day fire suppression systems.

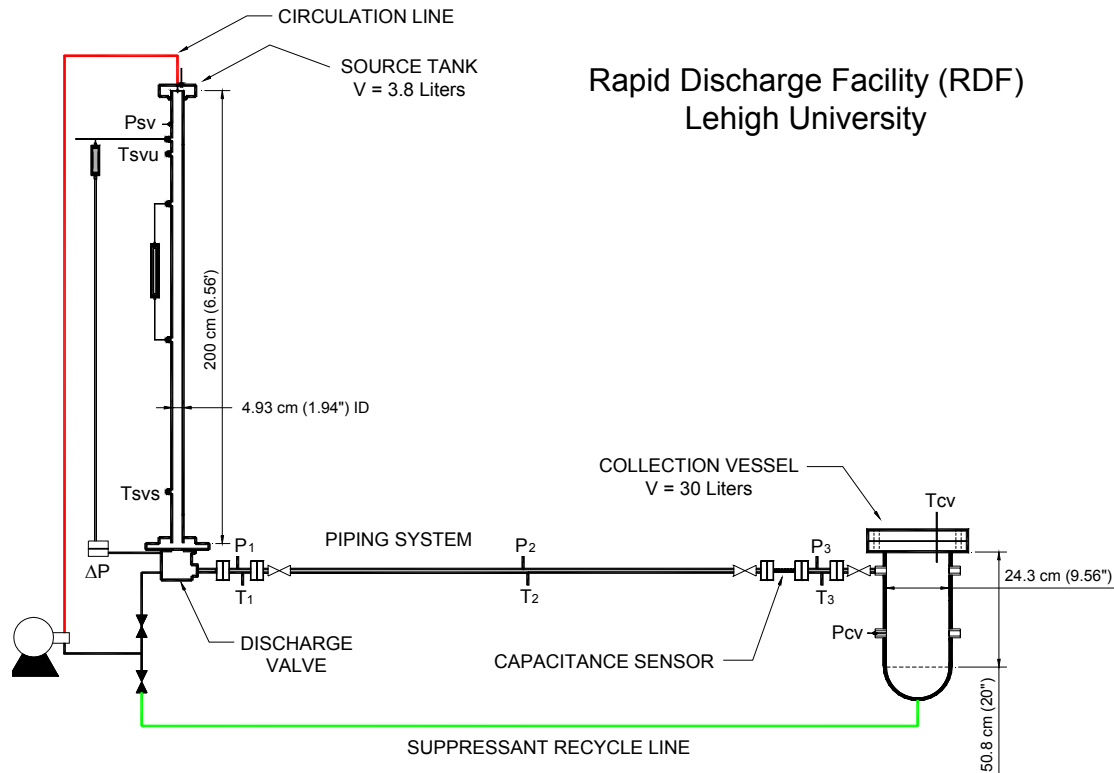


Figure 8-9. Schematic of Test Facility: Source Vessel, Discharge Piping, and Collection Vessel.

The source vessel, one of the main components of the facility, is shown in Figure 8-10. The source vessel has a total internal volume of 3.81 L and was initially charged with liquid to about 60 % of that volume. The source vessel was constructed from a 2 m long piece of 5.08 cm nominal diameter stainless steel pipe with an internal diameter of 4.93 cm and a wall thickness of 0.55 cm. Using a vessel of large length-diameter ratio improves the accuracy of measuring liquid inventory. A pressure difference associated with the static head of the liquid in the vessel is used to measure the liquid inventory in the vessel at any time during the experimental run. The long length, or height, of the source vessel provides a greater range of static head measurements, thus increasing the accuracy of determining the transient liquid inventory. This pipe was positioned vertically and capped at both ends by stainless steel pipe flanges approximately 2.54 cm thick. Two slip-on flanges with O-ring grooves for the pressure seals were welded to either end of the pipe so that the top and bottom plates could be bolted in place. The top plate has an identical outer diameter as the flanges, at 16.51 cm, and was tapped to allow for a mixing line inlet and a fill/relief line. The bottom plate has a larger diameter of 27.94 cm for the purpose of anchoring the vessel to the holding rack while minimizing any vibration or movement during operation. This plate was also tapped to allow the discharge valve to be screwed into place and sealed with a crushable, tempered aluminum gasket. Other features incorporated into the source vessel include pressure and temperature

ports, a liquid level gauge, a mixing line, and the differential pressure transducer with fluid transmission line for measurement of liquid inventory.

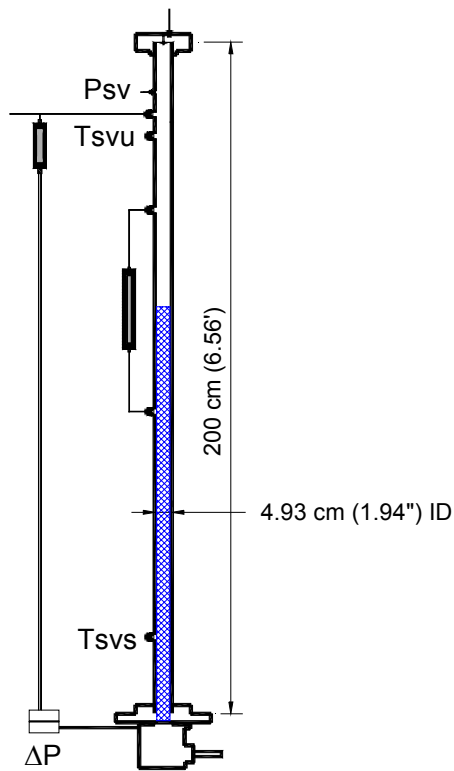


Figure 8-10. Schematic of Source Vessel Showing Mass Inventory Measurement.

Since tests required pressures up to (4.04 to 5.05) MPa in the source vessel, pressurization by nitrogen was employed. As shown in Figure 8-11, for HFC-227ea, the equilibrium vapor pressure of suppressant fluids only reaches about 0.505 MPa at room temperature, insufficient for the desired pressure without the additional partial pressure of an inert pressurization gas such as nitrogen. A potential problem with this method is that the total pressure in the vessel will not reach equilibrium until the liquid has become saturated with dissolved nitrogen. In order to expedite this process, a mixing system has been incorporated into the design, using a pump to recycle liquid suppressant from the bottom of the source vessel to a spray nozzle located in the vapor/gas space. By spraying small droplets of liquid through the nitrogen gas, the surface area of liquid in contact with nitrogen will increase, therefore increasing the rate at which nitrogen can be dissolved into the liquid.

Additional ports in the source vessel include an opening near the top, which serves as the connection to the nitrogen supply and as one leg of the transmission line for the differential pressure transducer. A liquid level gauge made of armored glass has also been attached to the middle section of the vessel to visually determine the liquid fill level in the vessel at the beginning of each experimental run. Also, there are two thermocouple ports for the vapor and liquid spaces and a pressure port in the vapor space. The last port is in the top plate, providing access for filling of the vessel and also serving as a connection for a safety pressure-relief device.

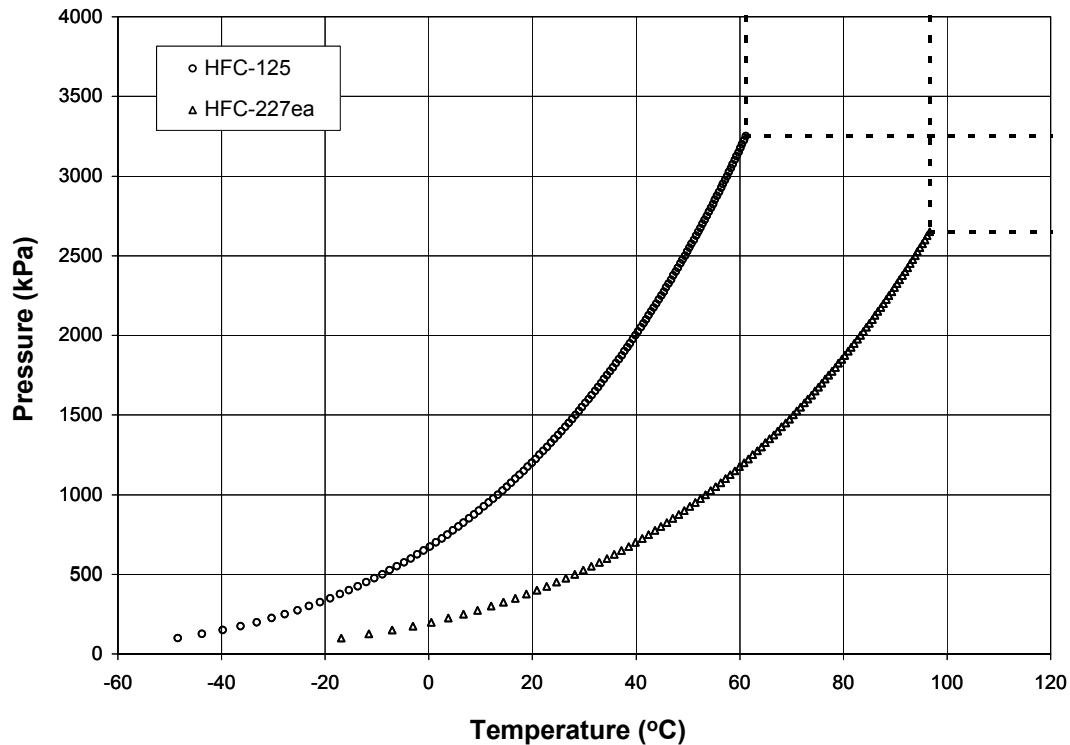


Figure 8-11. Pressure vs. Temperature Saturation Curve for HFC-227ea and HFC-125.

The next pertinent item in the design is the release mechanism of the source vessel, for initiating discharge of the test agent. A quick-opening plunger valve with an inlet diameter of 3.18 cm and an exit diameter of 4.45 cm was used for this purpose. This valve, shown in Figure 8-12, is a Model MV121KJ-2 valve made by Marotta Scientific Controls Inc. A feature of this valve is the use of the fluid pressure to drive the plunger upon command; thereby eliminating the need for springs or motors. To set or close the valve, the plunger is pushed up into its armed position and held in place by a small locking latch. Two O-rings are attached to the plunger to form a pressure seal along the valve casing. Pressure must then be provided on the inlet side of the valve for the valve to operate properly. To open the valve, an electrical charge provided by a 20V DC power source releases the latch, allowing the fluid pressure to rapidly drive open the plunger. This release is much faster than that of traditional solenoid valves, and is similar to that of a burst diaphragm or explosive-charge release, which is used in present-day suppression systems. The valve is connected to the 1/2-in discharge piping in the loop by a tapered transition piece. This transition incorporates a flange connection to permit access to the O-ring seals on the plunger for lubrication.

The piping in the test facility consists of 1.27 cm nominal diameter stainless steel pipe with an internal diameter of 1.39 cm and a wall thickness of 0.38 cm. There are five other pieces, including the adapter piece described above, which make up the discharge piping system. Two of these pieces are approximately 30.5 cm in length with flanges at either end to provide for easy disassembly. All the flanges are machined with an O-ring groove to provide an adequate seal against the high pressures experienced in the tests. These 30.5-cm sections will be used as access points at the beginning and end of the piping system, as indicated in Figure 8-13. They will also be the first and last locations of the pressure and temperature measurement ports. Ports for the pressure transducers and film thermocouples used for these measurements required special weld fittings in order to insure a complete pressure seal in

the loop. These fittings were specially designed to cause minimal disturbance to the flow, while allowing for the sensor to be as close to the flow as possible. See Figure 8-14 for a schematic diagram of these fittings.

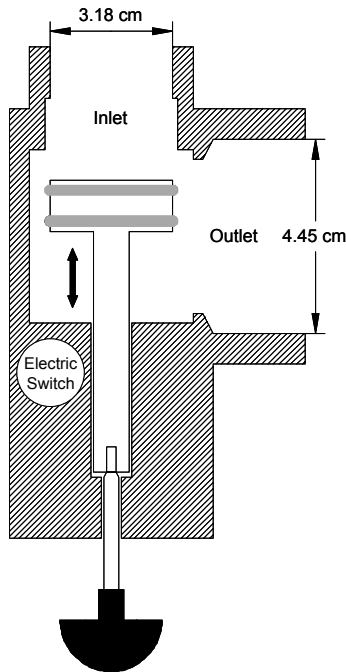


Figure 8-12. Schematic of a Marotta valve.

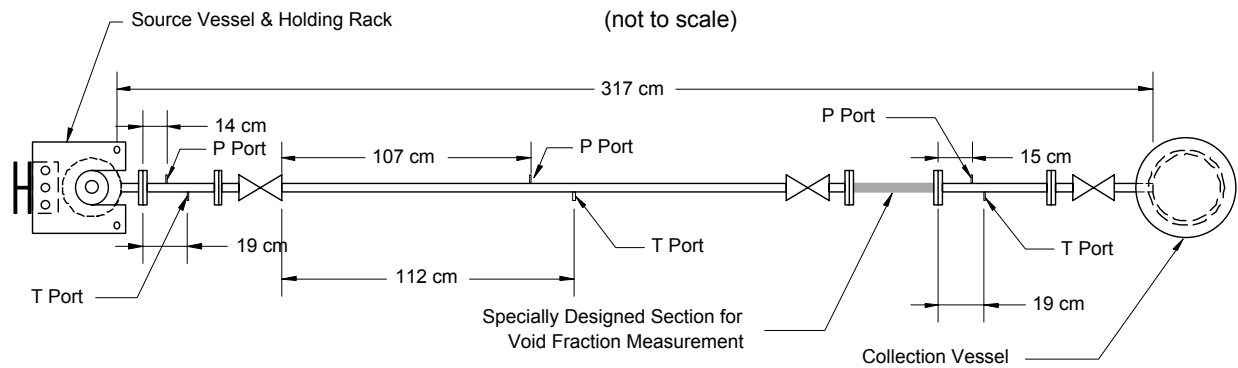


Figure 8-13. Top View of Test Facility; Schematic of Discharge Piping System.

The other two pieces in the piping system include a special section used for the void fraction measurement and a long middle section of pipe. The long middle section of pipe represents the distribution spool piece often found in fire-suppressant piping systems. Both ends are flanged and are capped by valves, allowing for the isolation of this section when dismantling. The middle piece will be tapped in the middle for temperature and pressure ports as described previously. This middle piece of long discharge piping allows for easy reconfiguration to different piping schemes (i.e., inclusion of tees or elbows). This whole piping system is then connected by a flange to the collection vessel, providing a closed flow path from the source vessel, through the piping system, to the collection vessel.

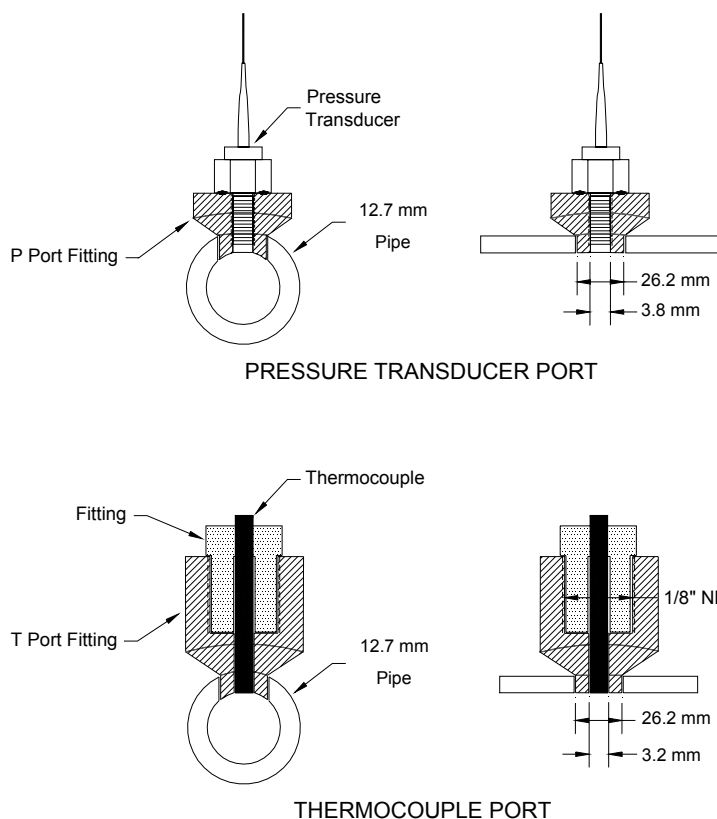


Figure 8-14. Schematic of Pressure Fittings for Temperature and Pressure Ports.

The collection vessel is designed to serve two purposes: to catch the test fluid for recycle and to enable monitoring of the transient discharge pressure during test runs. The collection vessel has an internal volume of approximately 30 L, chosen to limit the final pressure after discharge to less than 1.01 MPa to 1.212 MPa. This vessel is made of a 25.4 cm diameter stainless steel pipe with an internal diameter of 24.3 cm and a wall thickness of 1.50 cm. The bottom of the collection vessel is a hemispheric cap with a 1.27 cm port, to be used for emptying the contents. At the top end is a pair of 4.445 cm thick flanges sealed by an O-ring. The outside flange has access holes to allow for a cooling coil, a vacuum line, and a temperature measurement port. The cooling coil can carry either cold water or liquid nitrogen for the purpose of condensing the spent suppressant fluid for recycling. The vacuum line is connected to the top of the vessel for the purpose of relieving the excess pressure before the next run. The line is connected to a knock-back condenser to prevent a minimal amount of suppressant from escaping. Additional ports in the sides of the vessel provide connections for the piping system and a fast-response pressure transducer.

In anticipation of potentially large reaction forces during fluid discharge, a rugged framework was designed to support the test facility. As shown in Figure 8-15, a 20.3 cm I-beam, 305 cm high, was chosen to give a rigid backing for the source vessel while being heavy enough to dampen any vibrations exhibited during the test runs. This rack I-beam is directly bolted to the building structure for rigidity. The rack I-beam has three welded shelves for use in supporting the source vessel. The first is positioned just below the middle of the beam and is used to hold the source vessel from the bottom. Since this area experiences most of the forces during the discharge tests, the shelf in this area is bolted to the large flange at the bottom of the source vessel. This shelf is equipped with support legs for added stability. The next shelf is located near the top of the rack and anchors the top section of the source vessel by clamping to the 5.08 cm pipe. The last shelf, positioned lower down on the beam, is used to hold the mixing pump. The

I-beam is also equipped with bolt holes along its face in order to add support structures for the level gauges and mixing lines. As for the piping system, it is supported by a metal framework, which has provisions for clamping the pipe and preventing movement in both horizontal and vertical directions. The collection vessel is attached to a movable dolly to allow for opening of the piping system when access is necessary. To account for substantial forces associated with the fluid discharging into the vessel, the collection vessel is held in place by support braces attached to a building I-beam. A picture of this entire system is shown in Figure 8-16, where the source vessel, straight piping system, collection vessel, support structure and instrumentation can be seen.

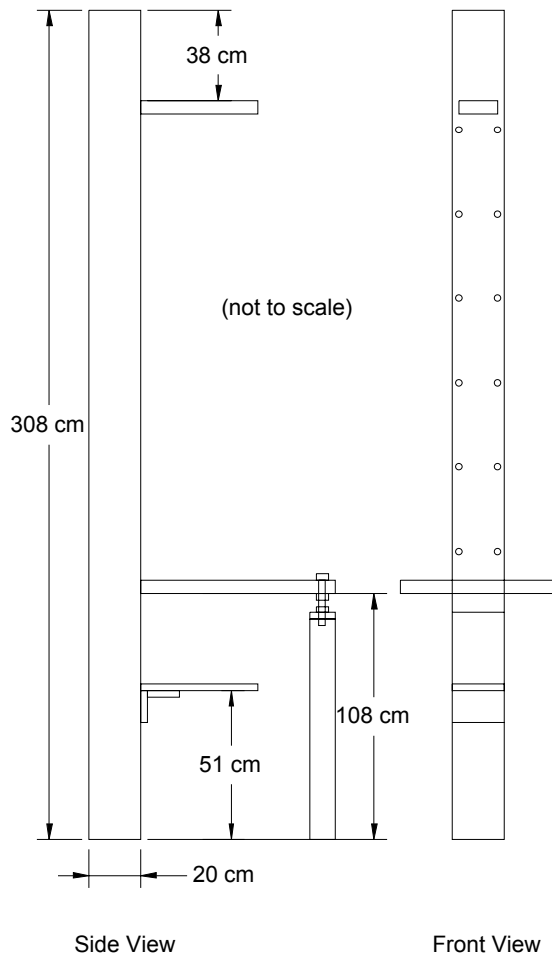


Figure 8-15. Schematic of Rack Used to Hold the Source Vessel.

Pressure Sensors

The test facility is equipped to measure instantaneous pressure readings in the source vessel, along the piping system, and in the collection vessel by means of fast response pressure transducers. Two types of transducers were used in the experiments conducted, the Entran Model EPX-V01 with a range of (0 to 6.87) MPa-g and the Validyne Model DP15 with varying ranges from (0 to 6.87) MPa-g. The Entran transducers were primarily used in the early runs when the temperature drop during operation was not a concern. The Validyne transducers were used for both pressure drop measurements and absolute pressure measurements. The Validyne transducers were used with a transmission fluid for speed of transmitting the pressure wave in the pressure drop readings and also for insulation when the temperature drop was

considerable, as in the HFC-125 tests. The Entran transducers have a diaphragm, which deflects according to the difference of the pressures experienced at its front and backsides, and provides an output through a strain gauge bridge located on the backside of the diaphragm. The Validyne transducers used a magnetically permeable diaphragm, which when deflected caused a magnetic reluctance, which was then interpreted by the inductance value of coils in the transducer body. In order to install these transducers at measurement locations, special fittings had to be designed and fabricated. It is desirable to locate the transducers as flush to the inside surface of the pipe as possible, in order to minimize disturbances to the flow. This was accomplished with the specially designed fittings shown in Figure 8-14. With these fittings welded into place on the pipe, the transducers can be screwed into the tapped hole, allowing an O-ring to seal against the high fluid pressures. Bench top experiments were conducted to determine whether the transducers had appropriate response times for the fast transient tests conducted. Both transducers were found to have response times at acceptable level of 140 ms for pressurization and 190 ms for depressurization when operating at 2.02 MPa to 3.03 MPa. The best test for the instrumentation was to view their performance in actual testing situations.

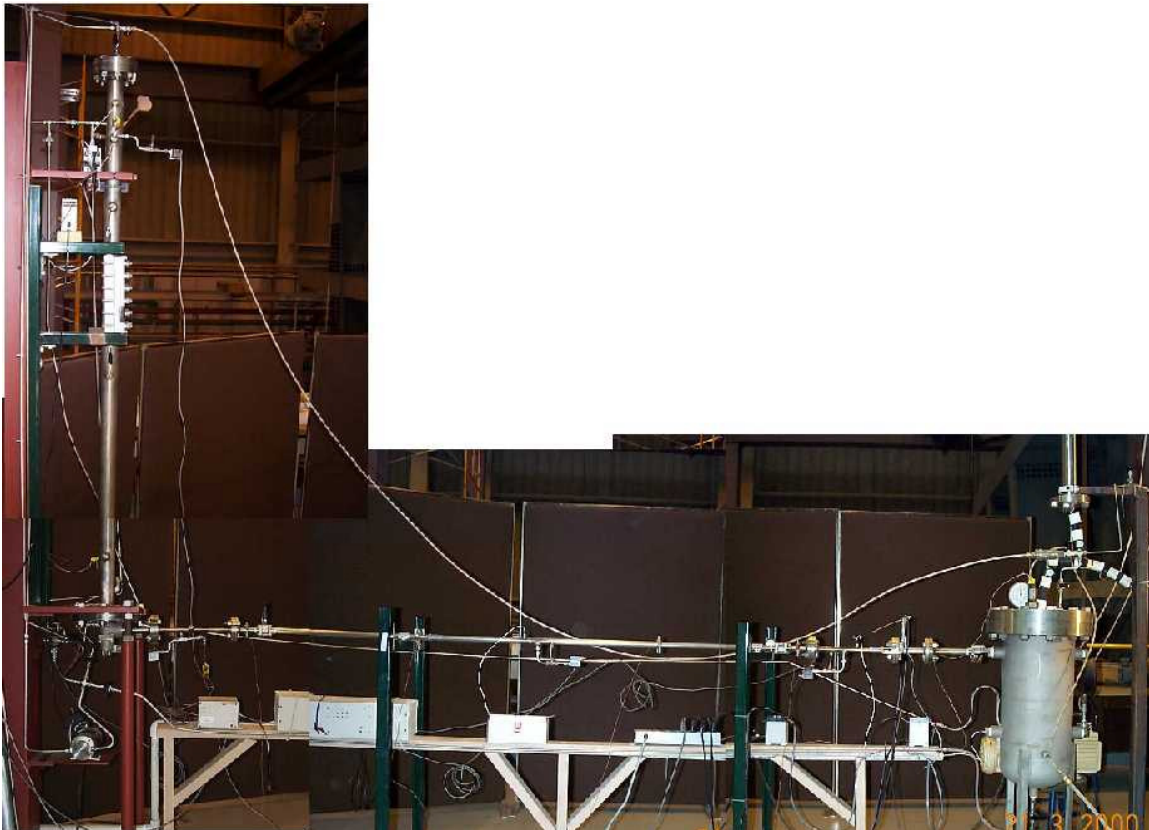


Figure 8-16. Picture of Test Facility: Source Vessel, Discharge Piping, Collection Vessel, Support Structure and Instrumentation.⁷

Figure 8-17 shows a typical output (Run #5) from the pressure transducers installed in the test facility. This run used HFC-227ea as a test fluid and was initially charged to a source vessel pressure of 4.22 MPa. As shown in the figure, the pressures in the source vessel, pipe, and collection vessel remained constant until the moment when the valve was actuated (time = 0 ms). Then the pressure in the source vessel dropped quickly while the pressures in the rest of the facility rose. This occurred until the pipe was filled

with fluid (time ≈ 200 ms) and then there was a steady decrease in all of the pressures until all of the fluid was discharged from the source vessel (time ≈ 1500 ms). At this point a small pressure increase or “bump” was prevalent in the piping pressure traces due to the exit of the remainder gas contents of the source vessel. A set of runs with similar initial conditions was also carried out to check the repeatability of the measurements and the reliability of the instrumentation. The operating conditions are shown in Table 8-2.

Table 8-2. Operating Condition for Repeatability Tests.

Run	Fill volume (mL)	Ambient temperature (°C)	Source vessel pressure (kPa)	Downstream pressure (kPa)
#3	2358	32	4180	720
#4	2370	29	4195	525
#5	2388	31	4220	720

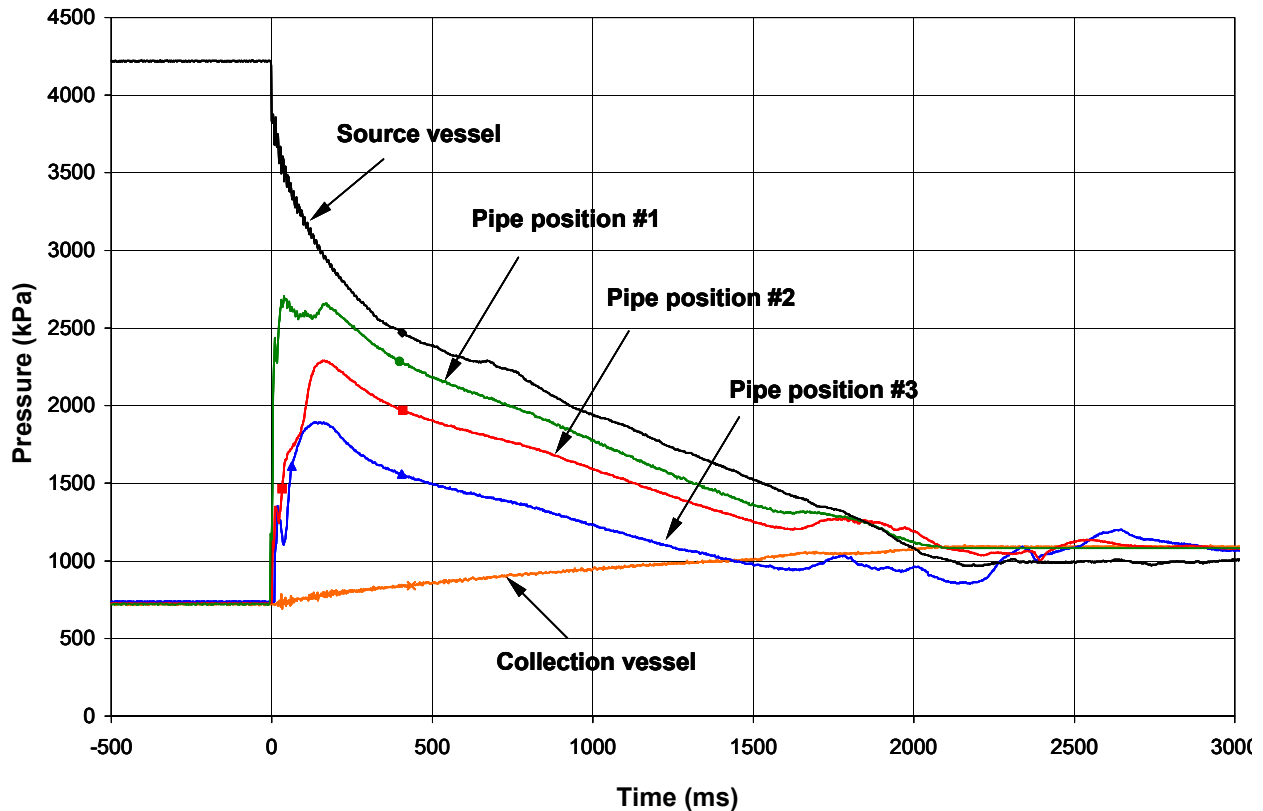


Figure 8-17. Pressure Traces for Experimental Run #5.

All the tests used HFC-227ea. The repeatability was very good as shown by Figure 8-18, which compares the source vessel pressure traces of the three experimental runs. The slight discrepancies are most likely caused by differences in the initial and environmental conditions and are believed to be not due to the instrumentation. The transducers did a good job in tracking the pressure fluctuations during the experimental runs.

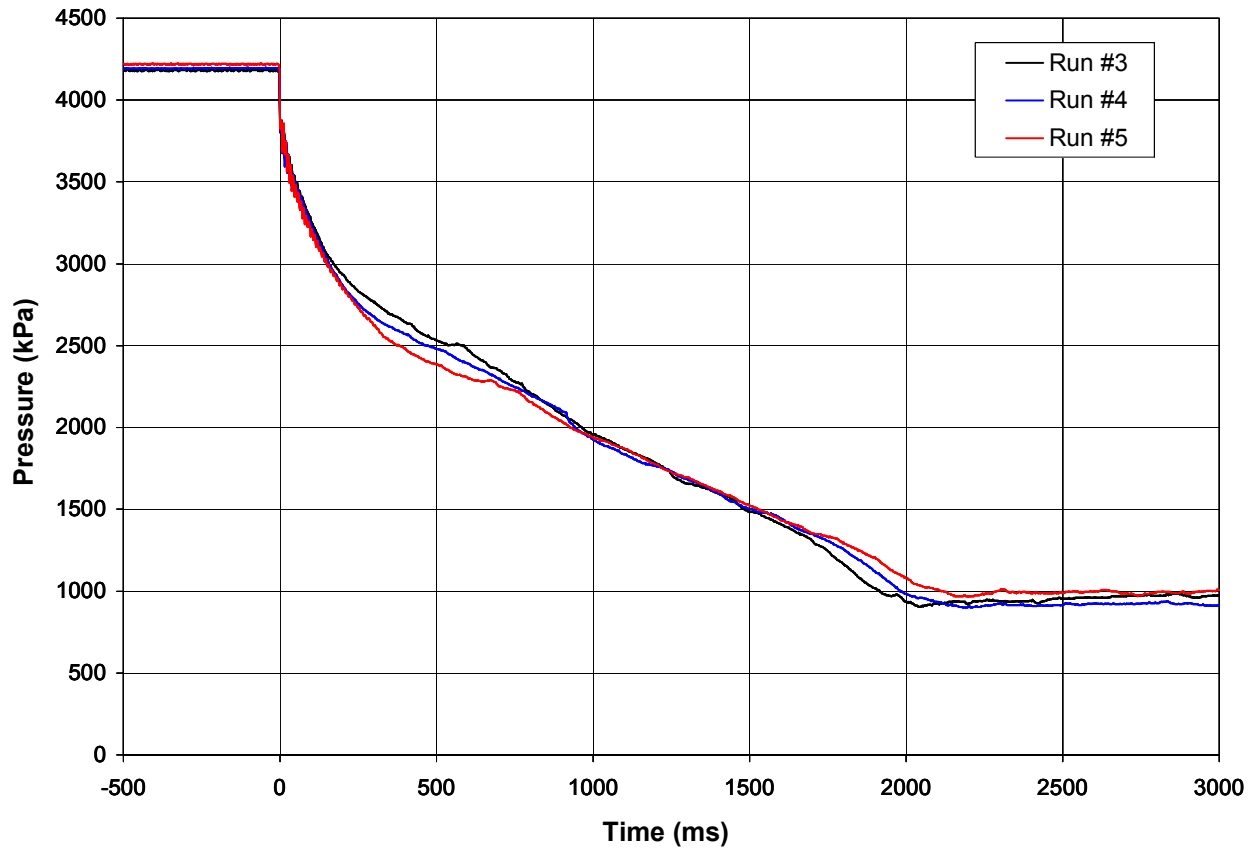


Figure 8-18. Repeatability of the Source Vessel Pressure Traces.

There was also a necessity to measure the pressure drop across particular sections of the piping system. While the absolute measurements at different locations allowed us to measure the variation of absolute pressure across the discharge pipe, there was also an interest in measuring pressure drops across fittings in order to determine frictional losses across these piping elements. Figure 8-19 and Figure 8-20 show the two other piping configurations tested in this study in addition to the straight pipe configuration. Validyne pressure transducers were connected on either side of the fittings to measure the distinct pressure drop associated with these fittings. This can be seen by the ports specifically designated to the fittings shown on the diagrams (i.e., PT2-PT3 across a 90° elbow). A typical output from this measurement is shown in Figure 8-21, where pressure drop versus time is displayed. This plot shows the pressure drop across a 90° elbow from Run #9 using HFC-227ea as a test fluid and an initial pressure of 3915 kPa. There is a notable pressure drop instantly as the fluid front passes through the elbow, which deteriorates as time passes. This continues until approximately 2300 ms when the last liquid is discharged and the remaining gas leaves the system, denoted by the sudden drop in pressure attributed to a reduction in the frictional component of pressure drop associated with gas flow over liquid flow. Similar plots were made for the pressure drop across capped tees, through tees and unions. Also, a comparison was done between the vertical branches of a through tee to study the effect of phasic composition on the separation of the flow. With these measurements, it was possible to successfully analyze the effects of different fittings on the pressure losses in the discharge piping.

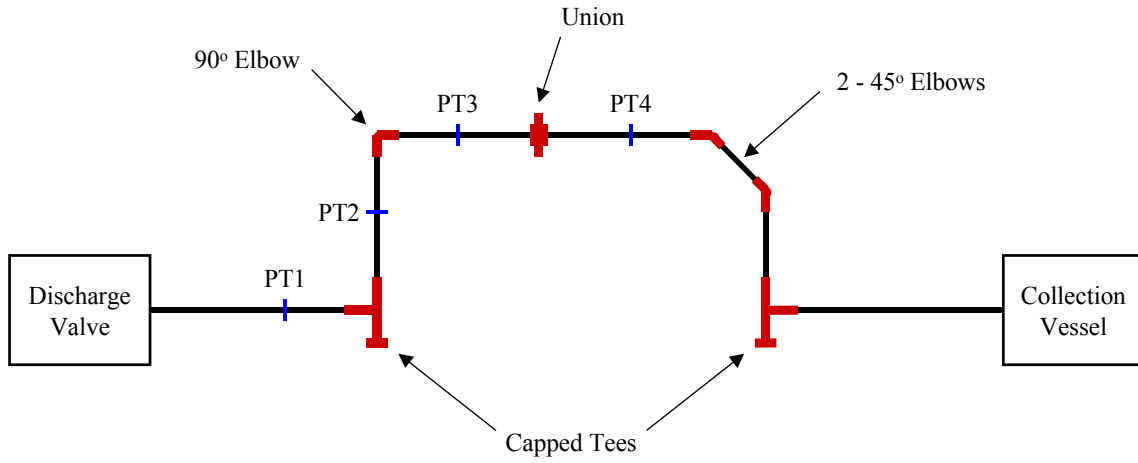


Figure 8-19. Schematic of Alternate Piping Configuration #1.

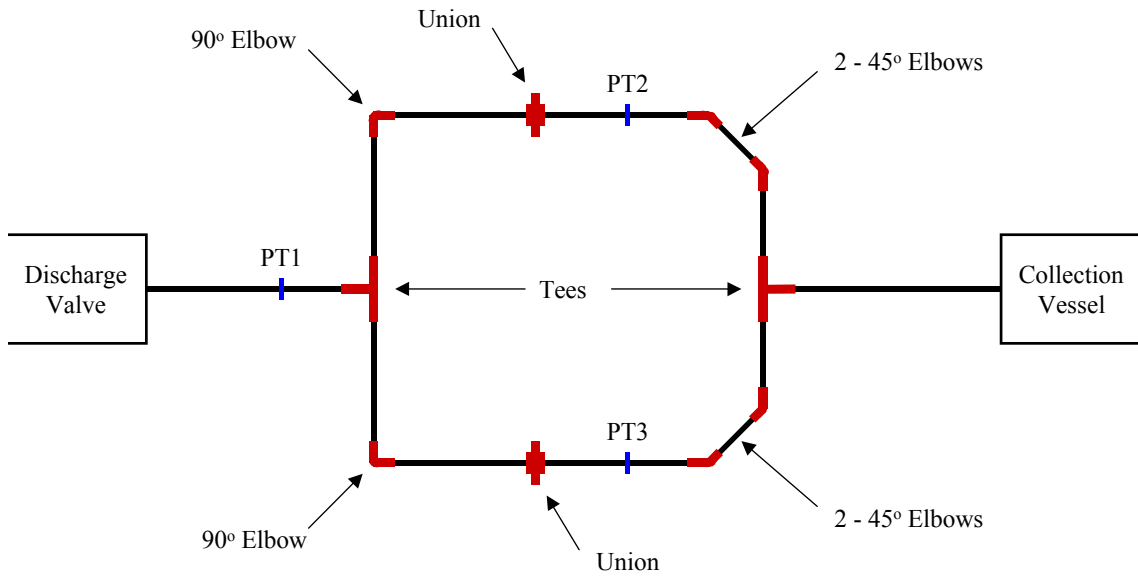


Figure 8-20. Schematic of Alternate Piping Configuration #2.

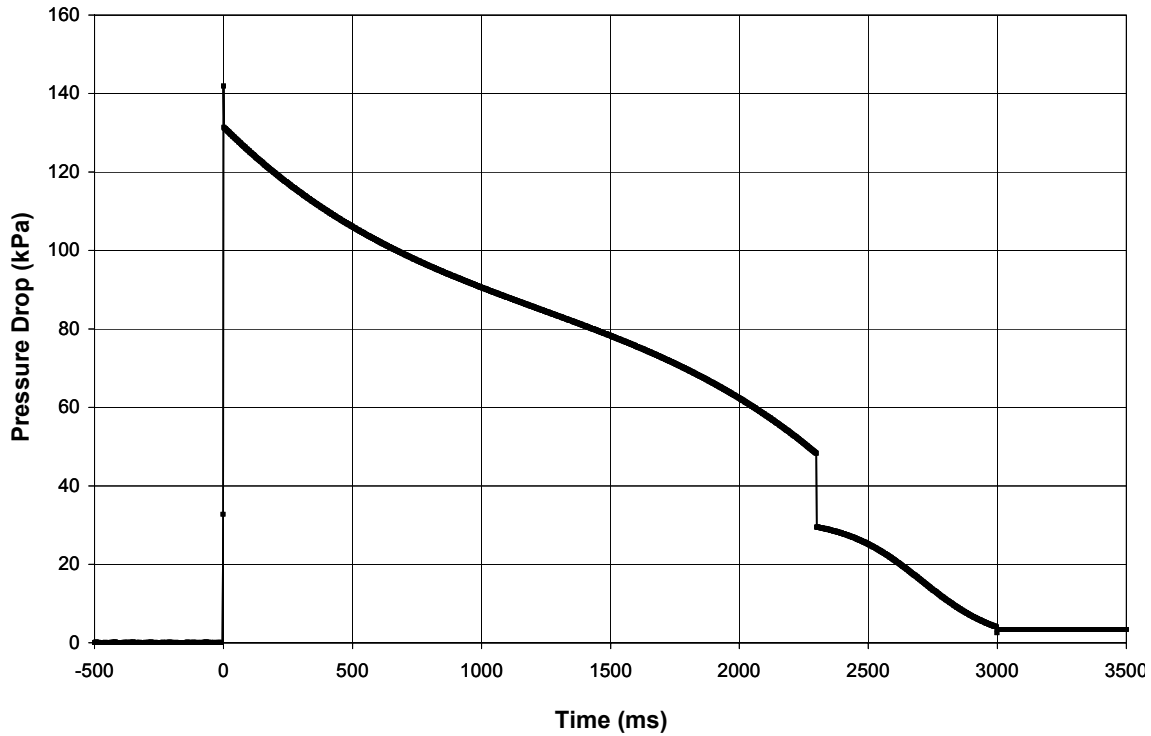


Figure 8-21. Transient pressure drop across a 90° elbow from Run #9.

Flow Rate Sensor

As mentioned previously, a key parameter to measure is the instantaneous mass flow rate of fluid during transient discharge from the source vessel. This has not been successfully measured in prior experiments due to its inherent difficulty. If fluid inventory in the source vessel could be measured as a function of time, then the rate of discharge would be given by the gradient of inventory versus time. Because of possible void generation in the liquid (due to gas evolution) and associated level swelling, observation of the liquid level does not provide an indication of fluid inventory. The approach is to measure the static head of fluid in the source vessel, as a dynamic function of time. Since frictional and kinetic terms are negligible in the overall momentum balance for conditions in the vessel, the fluid inventory in the vessel can be obtained directly from static head measurements:

$$M = \frac{A}{g} \Delta P \quad (8-36)$$

where M is the fluid inventory, A is the cross-sectional area of the vessel, g is gravitational acceleration, and ΔP is the pressure difference from the bottom to the top of the vessel (static head). The instantaneous rate of mass flow out of the vessel is then obtained from the time derivative:

$$\dot{m} = \frac{dM}{dt} = \frac{A}{g} \frac{d\Delta P}{dt} \quad (8-37)$$

In order to obtain the desired accuracy for the rate of mass flow, a precise measurement of ΔP is necessary. A Validyne Model DP15 differential pressure transducer was used to obtain this static head ΔP . As shown in Figure 8-10 and Figure 8-22, this transducer was connected to the vapor space and the liquid volume at the top and bottom of the source vessel, respectively. The transmission line connecting the vapor space to the liquid space was filled with a Meriam Red fluid with a specific gravity of 2.95 to maximize response time. The theory behind this was that the pressure signals would be transmitted to the transducer at the speed of sound in liquid, sufficiently fast to obtain dynamic data during suppressant discharge and much quicker than through a compressible gas volume. Therefore, the connections to the liquid and vapor spaces were made at the wall of the Marotta valve and the wall of the source vessel, respectively. This allowed for an almost flush-mounted differential pressure transducer with an excellent response time for measuring liquid inventory. Figure 8-22 shows a diagram of the setup for this differential pressure transducer. Note that it was attempted to fill the transmission line as close to the source vessel as possible, therefore reducing any pockets of fire suppressant vapor and making a more accurate measurement.

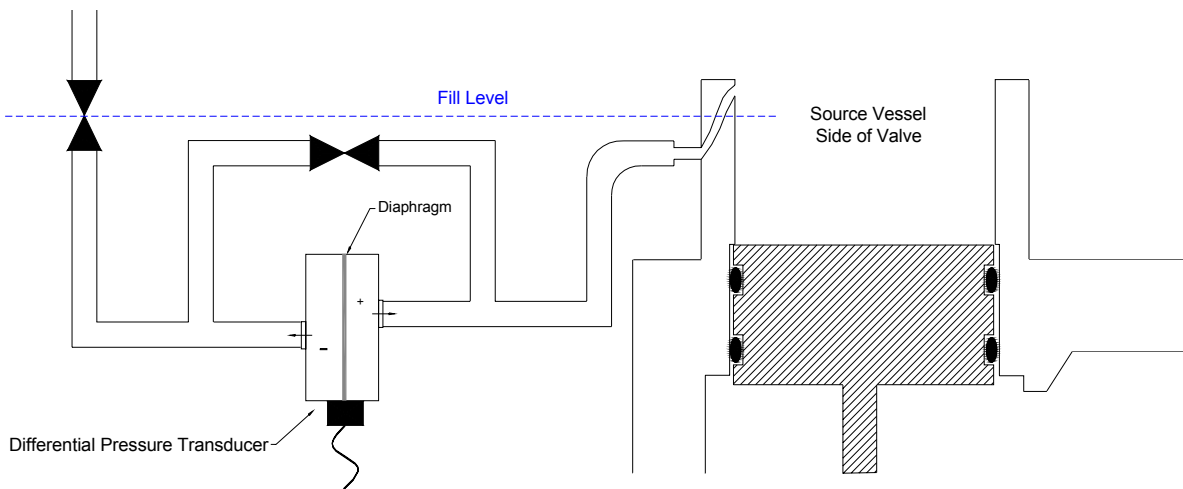


Figure 8-22. Diagram of Transducer Setup for Mass Inventory Measurement.

This technique worked very well, as shown in Figure 8-23, a plot of the cumulative mass leaving the source vessel versus time. This example shows the same experimental run described in the previous section. It shows that at the point when the valve was actuated, a quick release of test fluid left the source vessel and continued gradually until the source vessel was empty, at approximately 3.37 kg. This corresponded with the pressure drop in the source vessel shown in Figure 8-17 and with the end of the liquid flow and beginning of the gas flow at a time of ≈ 1500 ms. This is what one would expect; the fact that the pressure trace did not fluctuate very much indicated that there was a steady flow of fluid through the facility. Once again, this method for measuring the instantaneous liquid inventory gave excellent repeatability.

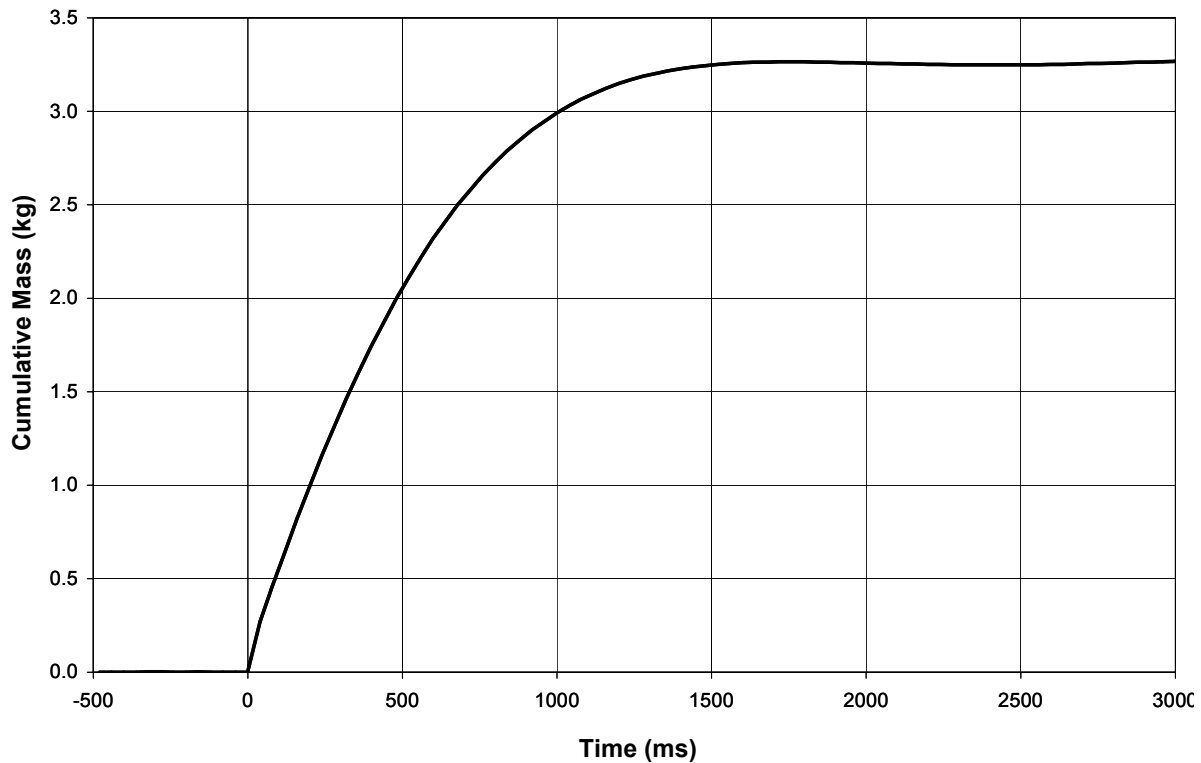


Figure 8-23. Transient Mass Inventory of Run #5.

Temperature Measurement Sensors

Fluid temperatures along the discharge pipe were measured using film thermocouples. It has been experimentally shown,²⁹ that this type of thermocouple can provide response times on the order of milliseconds. A schematic of the film thermocouple is shown in Figure 8-24. Since the hot junction of the thermocouple is comprised of the metallic film, it is essential to maintain a continuous electric conductive-path through that film. Two issues are involved: compatibility of the film material to the test fluid, and the erosive effects of the flow on the film. In past experiments, a metallo-organic paint was used to make the film at the tip of the thermocouple. This film worked well in experiments with high temperature steam and water. The same material was used for the junction film in the test series. A bench setup was prepared to test the thermocouple with this film junction. After forming the film, the thermocouple assembly was exposed to test liquids for durations of up to five minutes. Tests with the primary test fluid, HFC-227ea, indicated that the junction film holds up well to such exposure. No bench test for erosion of the film was attempted prior to the running of the test facility, due to the significant effort involved. It was found that the film held up for anywhere from 5-10 experimental runs before deterioration in the film deemed it necessary to remove the thermocouple from the facility and reapply the metallic film. The need for reapplication of the metallic film was determined by an increased fluctuation in the output signal of the thermocouple or in some cases a loss in the signal altogether. Many of the failures in the thermocouple were not attributed to the metallic film at all, but to the disintegration of the inner wiring of the thermocouple. This was most likely due to the vibration encountered in the test facility when the experimental runs were conducted and the tight seal on the thermocouple casing needed to hold the thermocouple in place during testing.

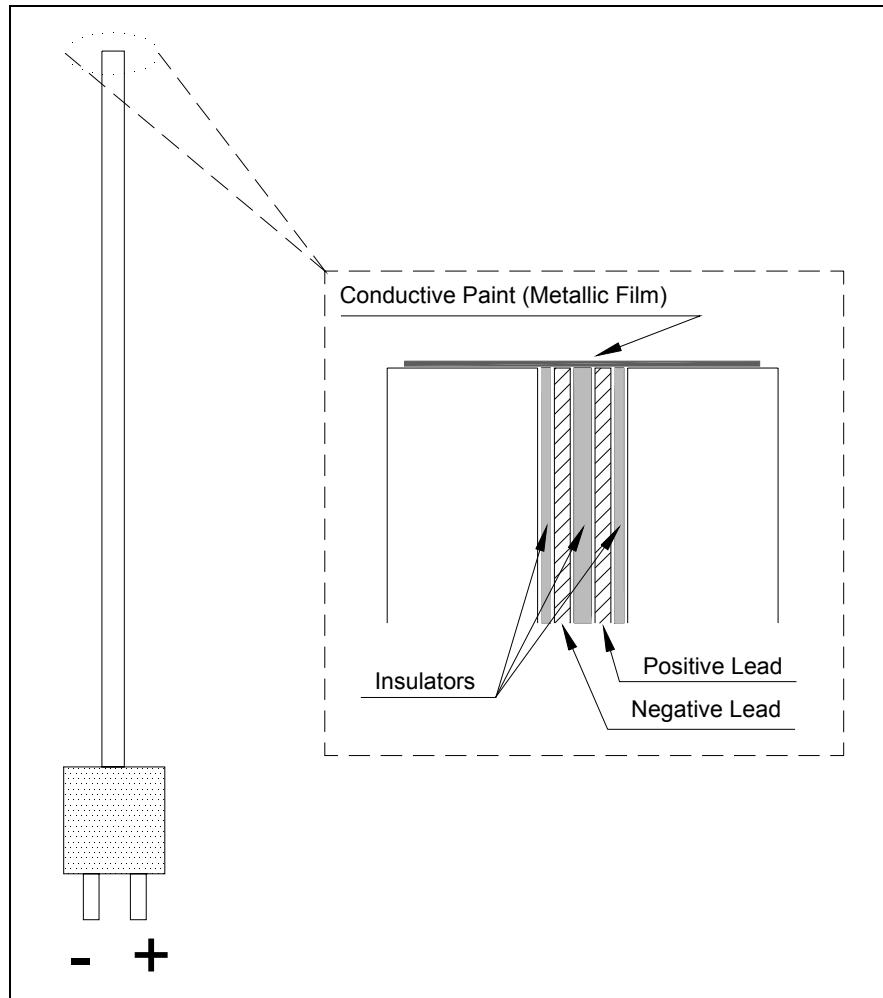


Figure 8-24. Schematic of Thermocouple Construction.

An example of a typical output from the four film thermocouples located throughout the test facility is shown in Figure 8-25. The top set of data is the signal from the film thermocouple located in the vapor space of the source vessel. The next three sets are from the film thermocouples in pipe positions #3, #2, and #1, respectively from top to bottom. This plot shows no significant temperature change in the vapor space, which is due to the fact that there was only a gas expansion involved in this region. While an adiabatic gas expansion from a volume of 1.5 L to 34 L should have resulted in a large decrease in temperature, this was not an adiabatic expansion due to the availability of a large heat sink in the stainless steel walls. With the considerable warming from the facility walls and the thermocouple's location at the top most portion of the entire facility, the only temperature drop experienced is minimal. As for the other set of thermocouple traces, it is believed the most significant reason for the difference in temperature drop along the pipe is also due to the warming effects.

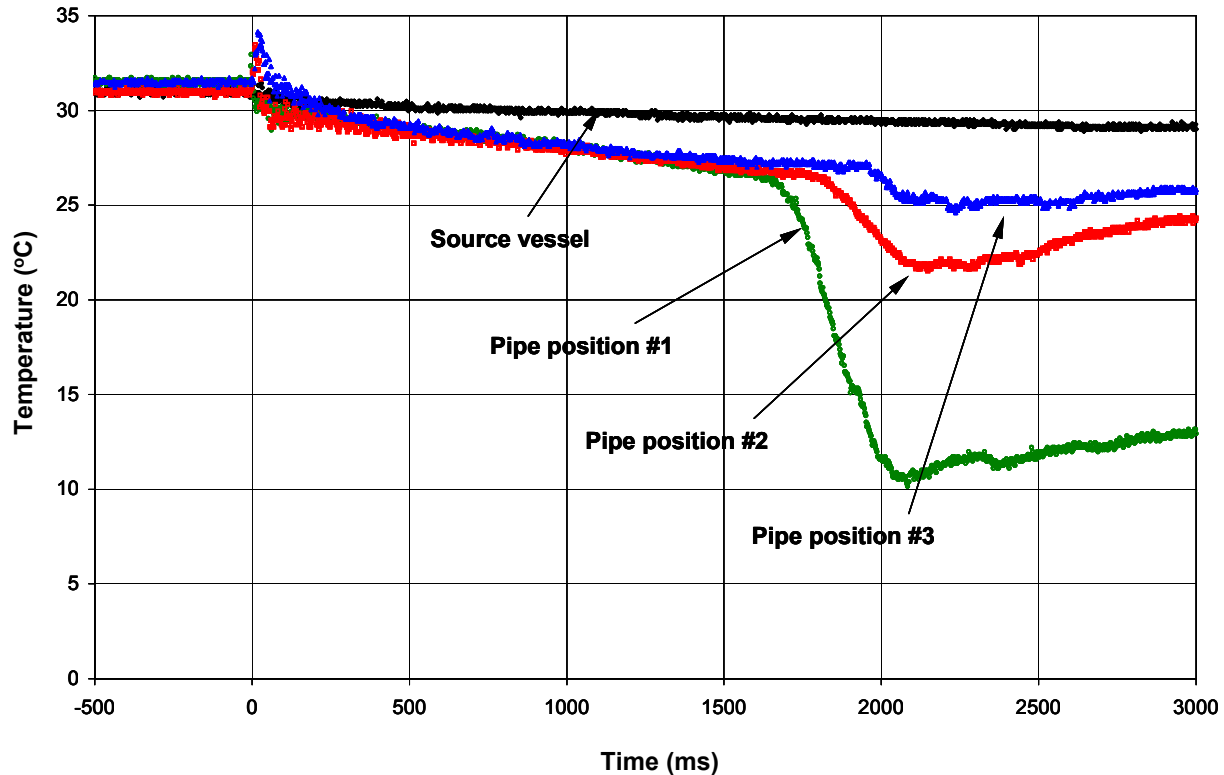


Figure 8-25. Transient Temperature Trace from Film Thermocouples of Run #5.

There were also two standard 0.79 mm diameter, shielded thermocouples in the source and collection vessels. Figure 8-26 shows a typical temperature trace from these thermocouples, again from Run #5. The two traces shown in this diagram are significantly different from each other. The collection vessel temperature does a quick dip and then warms back up to room temperature. This is due to the filling of the vessel with cold fluid, which is probably still going through the process of dissolution of nitrogen from liquid suppressant. Also, there is an energy loss associated with the phase change of the suppressant fluid as it goes from liquid in the pipe to gas in the collection vessel. This goes on until the collection vessel reaches the saturation pressure of the suppressant fluid, and then the vessel begins to heat up due to compression of the gas in the volume. On the other hand, the thermocouple located at the bottom of the source vessel initially does not change much since it is submersed in liquid suppressant. Then as the liquid in the source vessel runs out, it experiences the vaporization of the suppressant fluid on its surface and the expansion of the remaining gas in the system. To fully understand the complete picture of the changes of phase taking place in the experimental runs, a representation of the void in the facility is needed, which is described below.

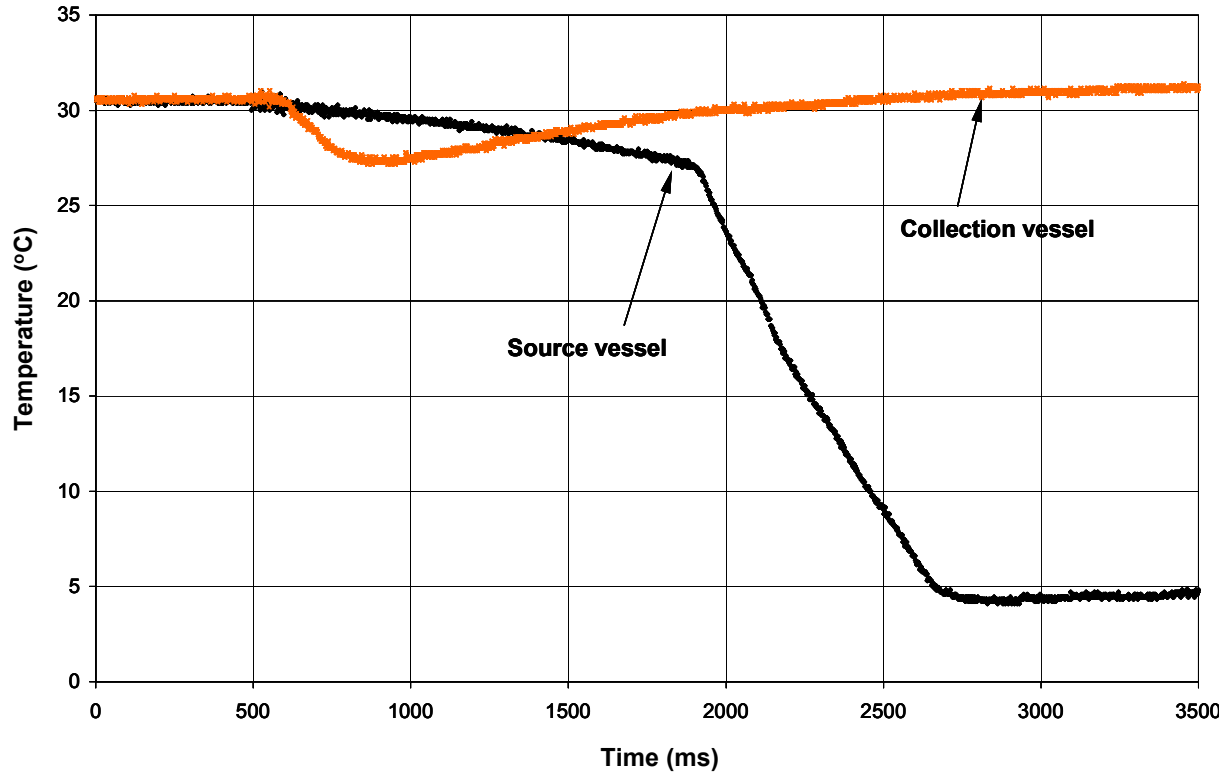


Figure 8-26. Transient Temperature Trace from Shielded Thermocouples of Run #5.

Void Fraction Sensor

One of the major flow variables for two-phase flow is the void fraction. Many flow parameters, such as thermodynamic quality, vapor and liquid mass fluxes, and transport properties of vapor and liquid affect the void fraction. In turn, the void fraction strongly affects pressure drop, holdup inventory, and flow rate for any given operating condition. Thus, it is desirable to experimentally measure the void fraction during the transient discharge of suppressant. Once again, this is a difficult measurement in two-phase flows and was not attempted in prior experiments of suppressant flow. In the present work, an attempt was made to measure the transient void fraction at the end of the discharge pipe. The desirable features of a sensor for void fraction are:

- No disturbance on flow
- Integrate the void fraction over the cross-section
- Fast response

Based on previous experience, a capacitance sensing method for this measurement was selected, in expectation that this method would satisfy all of the above desirable features.

A number of different capacitance probes were designed, fabricated, and bench tested. The final probe configuration is shown schematically in Figure 8-27. As indicated the probe consists of a positive electrode and a ground electrode, both placed on the outside surface of the discharge pipe. The section of the discharge pipe at this location needs to be electrically nonconductive to allow capacitance

measurements. For the purpose of these bench tests, a glass tube was used as the pipe material. The positive electrode is a strip of copper in contact with the outer surface of the pipe. The electrode span is as wide as the ID of the pipe. The ground electrode is placed on the opposing side of the pipe. When powered by a high-frequency voltage, this probe would measure an overall capacitance between the two electrodes, which includes the whole cross-section of the tube. This capacitance can then be calibrated to give the void fraction of the vapor/liquid mixture in the pipe. There is a guard electrode around the positive electrode to prevent/reduce stray capacitance.

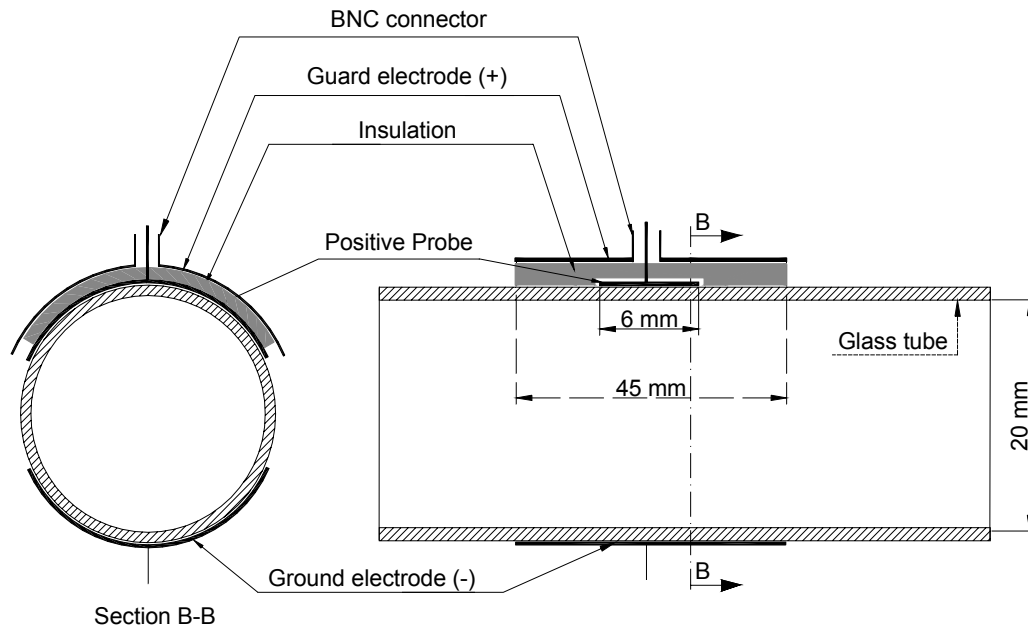


Figure 8-27. Schematic of Capacitance Probe for Bench Setup.

This probe was tested on a bench loop with water and HFC-134a. The schematic of the bench setup is shown in Figure 8-28. The test started with the glass tube filled with water. During the test, the tube was emptied from the bottom so that the liquid level receded with a constant speed. The recorded signal from the capacitance sensor was compiled as a voltage signal from the capacitance meter and then reduced into void fraction with a calibration using the signals associated with all liquid and all vapor. An example of the output from this test is shown in Figure 8-29. It is seen that initially the probe senses 100 % liquid in the tube. As the liquid level approaches the top edge of the sensor, the signal slowly starts to show some void in the sensing volume (edge effect). When the liquid level is within the sensing volume, the variation of measured void fraction is linear with liquid level. Again, there is an edge effect when the liquid level is close to the bottom edge of the sensing volume. Later, when the liquid level falls clear of the sensing volume, the probe senses all air in the tube. Despite the fact that the sensing area is guarded, there are some edge effects in the axial direction. The above test was repeated with HFC-134a under pressure and similar results were observed.

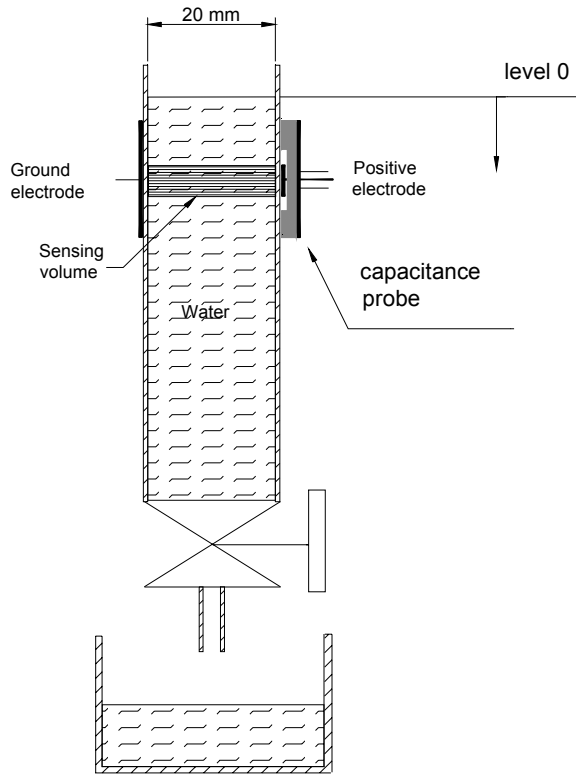


Figure 8-28. Bench Setup to Test Capacitance Sensor.

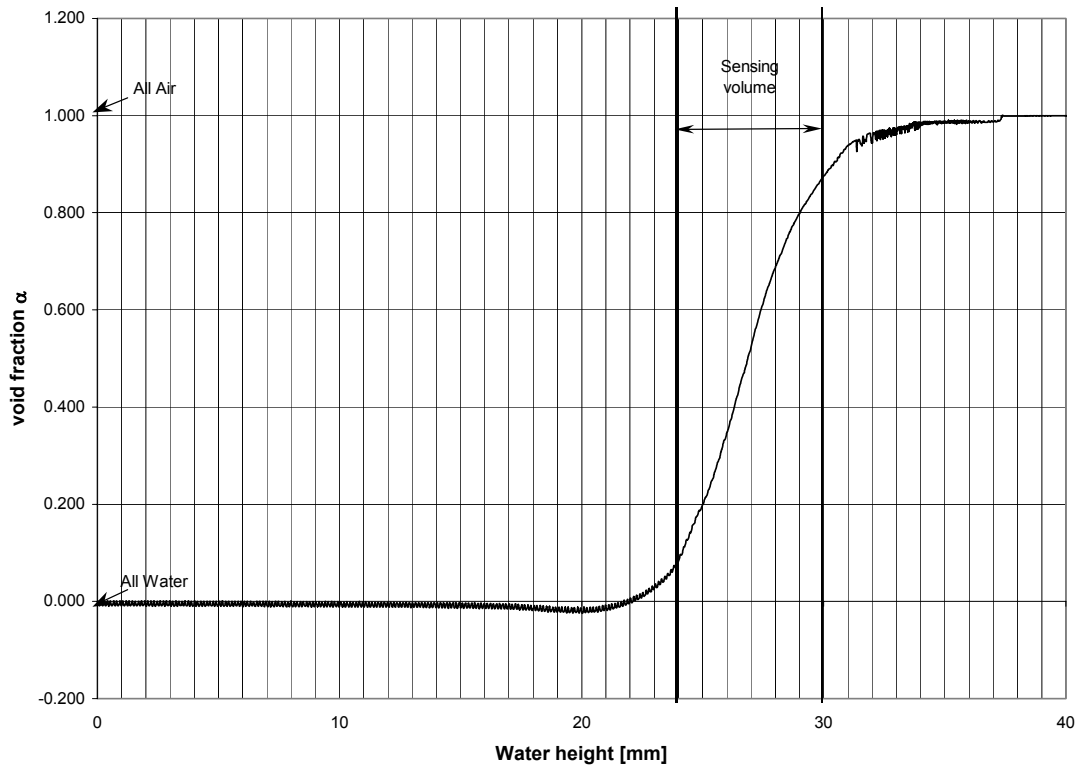


Figure 8-29. Void Fraction from Bench Tests of Capacitance Sensor.

The biggest problem with changing this design to fit the conditions experienced in the experimental test facility was to contain the higher pressures. In the previous bench examples, only low-pressure systems were dealt with and in the present application the system pressure was as high as 1250 kPa at the location of the void probe. The other difficulty was that an electrically conductive surface between the probe and the tested medium was not allowed. Due to these limitations, a design that would be constructed on the inner surface of the pipe was developed, as shown in Figure 8-30. There were three main pieces to this design; the first was the electrical plug welded to the metal pipe, which served as a pressure seal and as an electrical connection to the capacitance meter. The next two pieces were the guard and the probe separated by a small layer of insulation. To insure that these pieces were not washed away in the flow during the runs, they were covered in a thin layer of epoxy. This capacitance probe used the pipe wall as its ground creating an electrical field similar to the one shown in Figure 8-31.

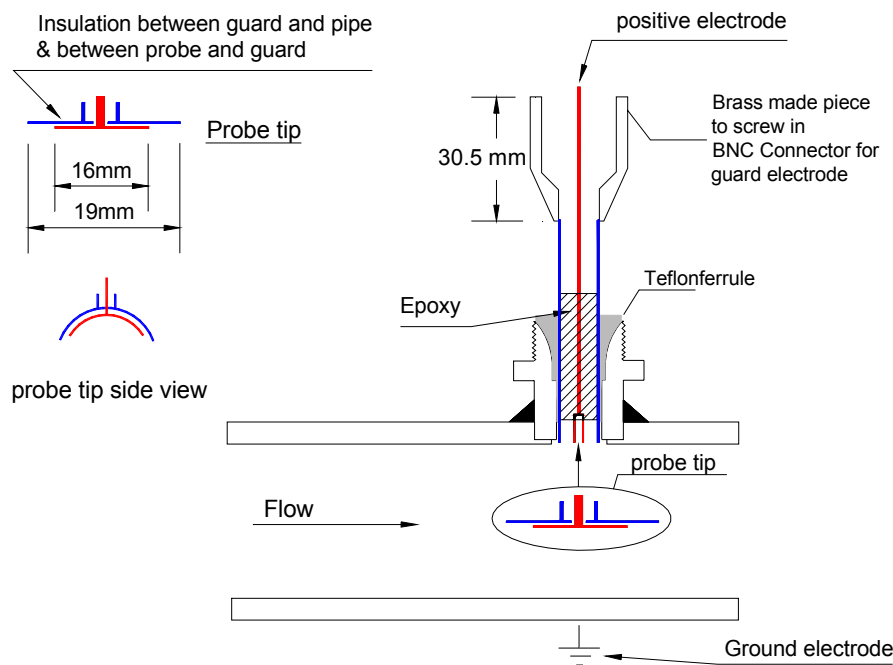
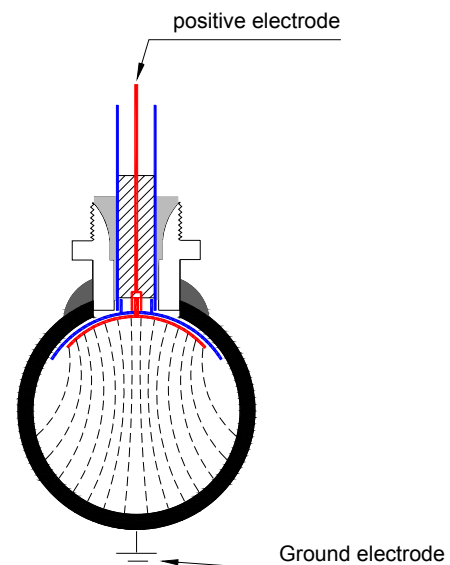


Figure 8-30.
Schematic of
Capacitance Probe for
Test Facility.

Figure 8-31. Cross-section of Capacitance
Setup Showing Electrical Field.



While the orientation of this design was horizontal as compared to vertical in the bench test setup, it was believed that the results were similar. An in situ calibration by filling the area with all liquid suppressant and then letting it run out so that only suppressant vapor remained was conducted.

An example of the final output of an actual experimental run is provided in Figure 8-32, where void fraction versus time for Run #5 is shown. The signal initially starts out at a void fraction of 1.0 (all vapor) and then shoots down to approximately 0.4 as the area is flooded with the transient flow of two-phase fluid. The signal fluctuates as the mixture of the two phases changes depending on the speed and location of the dissolution of the nitrogen from the liquid suppressant. As the flow slows down, so do the fluctuations in the capacitance signal, until the liquid runs out (time = 1700 ms), and the remaining gas is vented into the collection vessel, causing the signal to abruptly go back to the 1.0 region. The largest problem with the capacitance signal resulted from the static charge build up of the fast moving dispersed flow. It caused the signal to jump out of range and required a significant filtering effort to be conducted. This is also the reason for the offset in the final value at the end of the run. Despite these slight problems, it was felt that the capacitance probe design gave an excellent representation of the void fraction values experienced during the experimental runs.

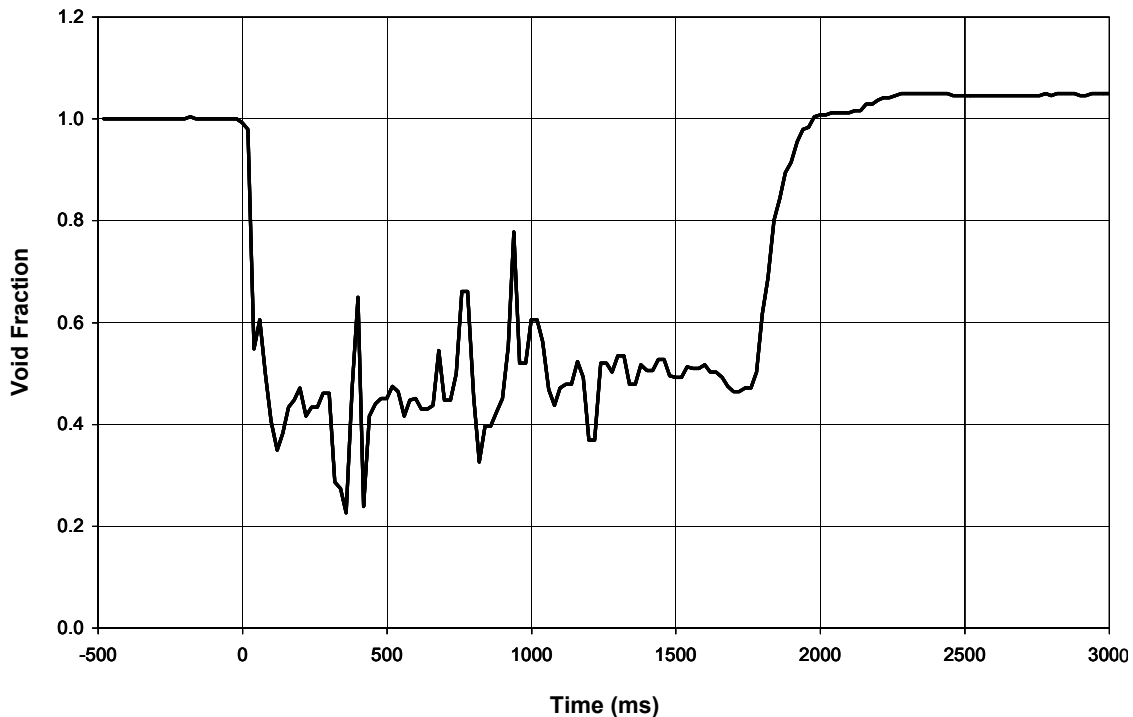


Figure 8-32. Transient Void Fraction of Run #5.

Test Matrix Performed in Study

After the completion of the test facility, it was necessary to choose the appropriate initial conditions in which to conduct the experimental runs. The main goal was to encompass a wide variety of test parameters while keeping the total number of runs at a minimum to lessen the wear on the instrumentation. Table 8-3 shows the experimental runs conducted in this study. HFC-227ea was used as

the primary test fluid since it was recommended at the time as the alternative fire suppressant with the best fire-retarding ability. HFC-125 was also used since it had been studied recently, and there was some test data that could be used for future comparison. In the preliminary experiments, water and carbon dioxide were used to test the new instrumentation after installation. For example, Run #19 used water as a test fluid and was undertaken to test the capacitance sensor and film thermocouple without exposing them to high pressure or a corrosive fluid. Run #18 also used water and had the intent of testing the mass flow sensor response and all of the thermocouples in the facility. In a similar manner, Runs #20 and #21, which used CO₂, were used to measure the response of the film thermocouples to a sudden drop of temperature as low as -40 °C, while also allowing us to gauge the error encountered by the pressure transducers at this temperature. These four runs utilized the straight pipe configuration in the test facility shown previously in Figure 8-13. The HFC-125 Runs (#14-#17) were conducted with only one objective, to test the influence of changing the source vessel pressure. The four runs were carried out at source vessel pressures varying from 2050 kPa to 5000 kPa. It must also be noted that any runs using source vessel pressures with initial conditions using low pressures were conducted at fill levels between 85 % and 90 %. This was done in an attempt to facilitate as much vaporization during the flow discharge as possible since the downstream pressure would remain at a lower pressure with the smaller amount of nitrogen gas available to expand.

The majority of the experimental runs used HFC-227ea as a test fluid and was broken into three main piping configuration groups. First, there were the tests using the straight pipe configuration. These tests had three different goals: (1) to test the repeatability of the instrumentation, (2) to observe the effect of changing the source vessel pressure, and (3) to determine the effect of a heat source or “hotspot” along the piping system. The repeatability Runs (#3 to #5) were conducted at an initial source vessel pressure of about 4.242 MPa. The result of the source vessel pressure trace is shown in Figure 8-18. While the “hotspot” Run (#7), was conducted at a similar starting pressure with a foot long section at 55 °C between the 2nd and 3rd instrumentation ports on the pipe, only one such run was needed since it was determined that a minimal effect resulted from the heat addition under such rapid transient conditions. The third goal was to observe the effect of varying the initial source vessel pressure from 2125 kPa to 4910 kPa (Runs #1 to #6). The second main piping configuration group used the piping configuration shown in Figure 8-19, where a vertical “U” turn was built into the piping system to allow the measurements of the effect of pipe fittings on the pressure loss in the system. The pressure drops across a capped tee, 90° elbow and union were measured with varying initial source vessel pressures from 2120 kPa to 4910 kPa in Run #8 to Run #10. The third piping configuration group used a complete vertical split as shown in Figure 8-20, where the tee was no longer capped but used to join two symmetric piping sections. The two sections were identical to the one used in the previous grouping although this time the pressure drop across the split was measured. A sensor was placed before the tee and after the 90° elbows on either arm of the split to test whether there was an effect from the splitting of the flow. These tests were also conducted at three varying initial source vessel pressures from 2140 kPa to 4910 kPa in Run #11 to Run #13. These tests examined the effects of changing the initial source vessel pressures, changing the test fluids, changing the piping configurations and the repeatability of the instrumentation.

A Typical Experimental Run

First the plunger in the Marotta valve is set into the closed position using the arming tool. Once the valve is closed, the next task is to recycle any fluid remaining in the collection vessel back to the source vessel using a magnetically driven centrifugal pump. If there is not enough test fluid in the collection vessel to

reach the desired initial fill level for the next run, then the recycle line is closed and a line to a fresh-supply tank above the test facility is opened, allowing the remaining liquid needed for the run to be pumped into the source vessel. Once this is accomplished, the supply line is closed and a circulation line is opened allowing the liquid at the bottom of the source vessel to be pumped to a spray nozzle at the top of the vessel. The spray nozzle then creates a fine mist of liquid to float through the vapor space of the vessel before joining the rest of the liquid. At this point, nitrogen gas is slowly added to the source vessel through a connection at the top of the vessel. The circulation pump is continuously run until the liquid is saturated with nitrogen. This is recognized by a constant pressure in the source vessel, which usually takes about 120 min. The circulation pump is then turned off, and the contents of the source vessel are allowed to settle and cool down to room temperature. The data acquisition system is initiated and run for 500 ms before the Marotta valve is actuated. This allows for the collection of the initial conditions of the system. Once the valve is actuated, the contents of the source vessel discharge through the Marotta valve into the piping system and finally collect in the collection vessel.

Table 8-3. Matrix of Experimental Runs Conducted.

Run #	Test Fluid	Piping Configuration	Fill Volume (mL)	P _{svo} (kPa)	P _{cvo} (kPa)	Temperature (°C)
1	HFC-227ea	Straight Pipe	3571	2125	10	32
2	HFC-227ea	Straight Pipe	2340	3235	635	33
3	HFC-227ea	Straight Pipe	2358	4180	720	32
4	HFC-227ea	Straight Pipe	2370	4195	525	29
5	HFC-227ea	Straight Pipe	2388	4220	720	31
6	HFC-227ea	Straight Pipe	2150	4910	715	31
7	HFC-227ea	Straight Pipe w/ Hotspot @ 55°C	2200	4230	710	27
8	HFC-227ea	Capped Tee (Config. #1)	3420	2120	125	21
9	HFC-227ea	Capped Tee (Config. #1)	2500	3915	575	24
10	HFC-227ea	Capped Tee (Config. #1)	2450	4910	615	25
11	HFC-227ea	Through Tee (Config. #2)	3507	2140	600	26
12	HFC-227ea	Through Tee (Config. #2)	2400	3935	655	24
13	HFC-227ea	Through Tee (Config. #2)	2460	4910	615	25
14	HFC-125	Straight Pipe	2900	2050	110	26
15	HFC-125	Straight Pipe	2363	3635	175	26
16	HFC-125	Straight Pipe	2400	4245	165	26
17	HFC-125	Straight Pipe	2467	5000	125	24
18	Water	Straight Pipe	3585	2875	120	28
19	Water	Straight Pipe	3100	4150	100	23
20	CO ₂	Straight Pipe	~1000	5215	100	20
21	CO ₂	Straight Pipe	~1000	5360	100	20

To fully understand the output from a single run, a typical experimental run (Run #5) will be examined in more detail. The pressure traces can be seen in Figure 8-17 where the traces go from the source vessel at the top, to the collection vessel at the bottom, and the pipe ports in the middle. Specifically, the black line (diamond) is the source vessel trace and the green (circle), red (square) and blue (triangle) traces are the first, second and third pipe positions, respectively, with the orange (cross) line being the trace for the collection vessel. Initially the source vessel is at 4220 kPa and the pressure downstream of the closed

valve is at 720 kPa. After the valve is opened, the pressure in the source vessel quickly drops as its contents fill the piping system, explaining the sudden rise in pressure there. At the point when the pipe is completely filled, ≈ 200 ms, there is a consistent drop in pressure as the fluid empties into the collection vessel. At ≈ 1600 ms, the fluid begins to run out and the flow in the system is predominately vapor. This quickly causes the entire system to equilibrate to the same ending pressure, ≈ 1100 kPa.

Not only can the pressure traces be followed for the discharge, but the temperature change also can be followed throughout the system. Figure 8-25 shows the output of the highly sensitive film thermocouples placed at the top of the source vessel in the vapor space and along the bottom of the piping system at the three port locations. The same color and symbol scheme is used as in the pressure traces with the source vessel being on top, followed by the third, second, and first pipe positions, respectively. There was little temperature change experienced in the fluid flow portion of the discharge since there was little flashing of the suppressant. The main temperature drop occurs at the point when the vapor discharge begins (≈ 1600 ms). This is due to the sudden expansion of the remaining nitrogen gas and falls as low as 10°C at the first pipe position. There are lesser temperature drops farther down the pipe due to the increased distance from the initial point of expansion and the warming of the vapor by the system walls. There were also two 0.79 mm shielded thermocouples placed in both the source vessel and collection vessel. The outputs of these are shown in Figure 8-26, where the black (diamond) symbols are for the bottom, fluid space of the source vessel, and the orange (cross) symbols are for the top, vapor space of the collection vessel. There is a small dip in the temperature of the collection vessel as the fluid initially reaches the large volume of the vessel and then it warms back up to room temperature rather quickly. As for the source vessel temperature, this thermocouple experiences a temperature drop due to the expansion of the gas that the film thermocouple in the vapor space did not. This is most likely due to the fact that the film thermocouple at the top of the vessel is in contact with stagnant gas and did not have enough time to sense its temperature, while the lower thermocouple experienced the shock of the quick expansion from the fast flowing gas.

The next insight derived from this study was provided by the differential pressure transducer, which measured the mass flow rate of the discharge. As seen in Figure 8-23, this instrumentation allowed for the measurement of the cumulative mass of liquid leaving the system. This provides a good estimate of how much liquid has left the source vessel and might possibly land on the desired destination, in this case, into the collection vessel. Ideally, one would have liked to locate such a sensor near the desired destination, but since an accurate, quick response method of measuring the collected fluid could not be developed, this seemed the most suitable alternative. Figure 8-23 verifies what has been already observed from the previous measurements of pressure and temperature. At first there is a primarily liquid flow, starting rapidly and slowly dying out as the inventory is relinquished to the piping system, until no liquid is left at ≈ 1600 ms. Along with this additional measurement to backup other assessments, the void fraction leaving the pipe was also measured by use of a capacitance sensor located at the end of the pipe. This instrument obtained an electrical signal, which pertained to a capacitance measurement of the flow passing through this section. This signal was then converted into a measurement of void fraction through a previous calibration where a value of 0.0 denotes all liquid flow and a value of 1.0 denotes all vapor flow with everything in the middle being a mixture of the two. Figure 8-32 shows the output from this sensor during the experimental run. Once again, the main liquid flow seems to end in the 1600 ms to 1800 ms range. The slight discrepancy between this measurement and the mass inventory measurement is most likely caused by the fact that they are on either ends of the pipe. This trace shows that at the beginning there is a flow of predominately liquid, void fraction of 0.4-0.2, which slowly rises to a more

consistent value of 0.5 until the liquid runs out and the value jumps back up to an all vapor level. There are many peaks in the trace due to the fact that the flow is highly turbulent at this period in the flow, with the phasic composition changing with the rate of nitrogen coming out of the solution. The flow slows down a little near the end, and the trace smoothes out until the end when there is no more flow. These four different methods of taking measurements indicate that the transport processes occurring during the rapid transient phase of the experimental runs can be adequately assessed. The detailed output of all of the experimental runs conducted in this study can be found in Appendix B of the report by Tuzla et al.⁷

Observations and Conclusions

The analysis of the full range of experiments conducted in this study provided many findings and observations. The most exciting developments in this study pertained to the previously unsuccessful measurements of mass flow, void fraction, and local temperature. The transient fluid inventory method gave excellent results, providing not only another check for the computer code developed in this work, but also an innovative technique currently unavailable in two-phase flow experiments. The void fraction measurement using a capacitance sensor has been used in other applications, but never in such a rapid-transient setting. In addition, most methods used in previous studies required the probe to extend out into the measured flow, which causes obstruction to the flow and obvious changes in the resulting flow characteristics. The current method provides a quick, accurate signal with minimal disturbance to the flow, resulting in the measurement of more realistic flow characteristics. Last, the film thermocouples used in this study also allowed measurements to be made without disturbing the fluid flow. In previous studies, thermocouples were always extended into the middle of the pipe in order to get the most accurate representation of the local temperatures, causing them to break and deflect the fluid as it flowed. These techniques had another shortcoming of not allowing a fast response due to the thermocouple sheathing. In the current case, only a paper-thin layer was present to shield the thermocouple junction from the flow while having no effect on the flow, due to their flush-mounted design. These techniques allowed this study to provide a more comprehensive data set for the computer code simulations to be tested against.

The experiments in this study primarily focused on the use of HFC-227ea as a test fluid. The first set of experimental runs examined the effect of changing the initial source vessel pressure on the flow characteristics through a straight, 12.7 mm nominal diameter pipe, see Figure 8-13. The main difference between these runs was the speed at which the source vessel discharged its contents into the piping system and hence, into the collection vessel. All the runs exhibited the same basic phenomena as seen in Figure 8-17: (1) a quick pressure drop as the pipe filled, (2) a continuous drop in the pressure as the source vessel discharged its remaining fluid, and (3) a slight pressure “bump” in the pressure measurements in the pipe due to the venting of the remaining gas and vapor in the source vessel. Similar behaviors are evident when examining the void fraction and mass flow measurements. The lowest void fraction is seen at the beginning of the runs (Figure 8-32) when the liquid content in the flow is the greatest. Near the end of the run, a marked increase in the void fraction is observed as more nitrogen comes out of solution causing it to rise. The corresponding mass flow measurement (Figure 8-23) shows the fastest discharge at the beginning of the run when the source vessel pressure is at its highest value, thus providing the greatest driving force. Once the pressure begins to wane, so does the flow, until it ends at the end of the liquid flow for the run.

The second set of experiments was conducted using an alternative piping system which contained tees, elbows, and a union as shown in Figure 8-19. The main goal for these runs was to measure the pressure

drop associated by adding specific pipe fittings into the piping network. As expected, the flow was significantly reduced by the pipe fittings, as shown in Figure 8-33. The comparison shows that Run #1 with the straight pipe finishes discharging its contents at approximately 4600 ms compared with Run #8 that used the piping layout containing two capped tees, a 90° elbow, a union and two 45° elbows, which finished at about 7500 ms. To study these pressure drop measurements, a comparison to literature values for non-compressible, turbulent flow through pipe fittings using the friction loss factor method was conducted. This method is based on the procedure where pipe fittings are set equal to equivalent lengths of pipe depending on the anticipated pressure drop associated with the fitting. In the experimental setup, the pressure ports used to measure the pressure drop across the fittings included not only the fitting but also some piping in between (see Figure 8-19). In each case the additional piping plus the fitting between the pressure ports was included in order to remain as accurate as possible. For example, the 90° elbows were made up of the pressure port then 5.08 centimeters of piping, then the elbow, then 7.62 more centimeters of piping and the final pressure port. Therefore, the designation, “90° elbow”, is actually the elbow plus 12.7 cm of piping. Predicted literature values were obtained by using the literature value for the friction loss factor, K , for the particular fitting and adding it to the calculated value for the additional piping, found by using Equation 8–38.

$$K = 4f_f \frac{L}{D} \quad (8-38)$$

where f_f is the friction factor of the pipe found by using a chart in the literature with the diameter and estimated roughness of the pipe, L and D are the length and diameter of the pipe, respectively. Once a total K is found for the fitting and additional piping, it can be used in Equation 8–39 to find the literature value for ΔP .

$$\Delta P = \frac{K \rho v^2}{2} \quad (8-39)$$

where ρ is the mixture density calculated using the experimental void fraction measurements, and v is the flow mixture velocity calculated from the experimental values of mass flow through the pipe and the mixture density.

Since the experiments took place under two-phase conditions, the mixture density was used in order to get as close to the actual conditions in the pipe as possible. The one drawback of this method was that the void fraction sensor was not located at the local position of the fitting, but at the end of the pipe so it might not be a precise representation of the void conditions at the fitting. For this reason and because the literature values for K were developed using liquid turbulent flow, a comparison to values using the liquid density and liquid velocity in place of the mixture density and mixture velocity was also included. See Table 8-4 for the detailed values of this comparison. As the comparison shows, there are some discrepancies between the literature and the experimental values, with the calculations using liquid density being in reasonable agreement. In order to compare whether the mixture or the liquid density is best used when calculating the literature value for ΔP , the error has been provided in parentheses. This error was determined using the experimental value as the actual value. The experimental values for pressure, void fraction, density and velocity were taken in the middle of the runs, with Run #8 being from 1500 ms to 3500 ms and Runs #9 and #10 being from 500 ms to 1500 ms. Some of the possible reasons for the discrepancies in the comparison between the calculations using the liquid density and those using the mixture density may be:

1. The phasic composition of the flow at the particular time during the run. For example, at the beginning of the run there is a large amount of liquid flowing, but there is also a large quantity of nitrogen degassing, so it is hard to tell how this will effect the calculations.
2. The capped tee is near the beginning of the piping layout, while the void sensor that is used for the calculation of the mixture density is at the end.
3. The fact that the literature value for the union is actually considered as if the fitting is just a section of straight pipe. In theory, this should be the case since the union when assembled should not interfere with the flow, but there are still ridges from the male and female sections connecting on the inside of the union, possibly causing disturbances to the flow.
4. The role of the two-phase flow in the experiments. An assumption made when modeling two-phase flow through pipe fittings is that the differences from single-phase liquid flow are marginal, but this may not be the case. The void fraction may play a large part in the pressure drop experienced through a pipe fitting since it will influence the flow conditions through the fitting.

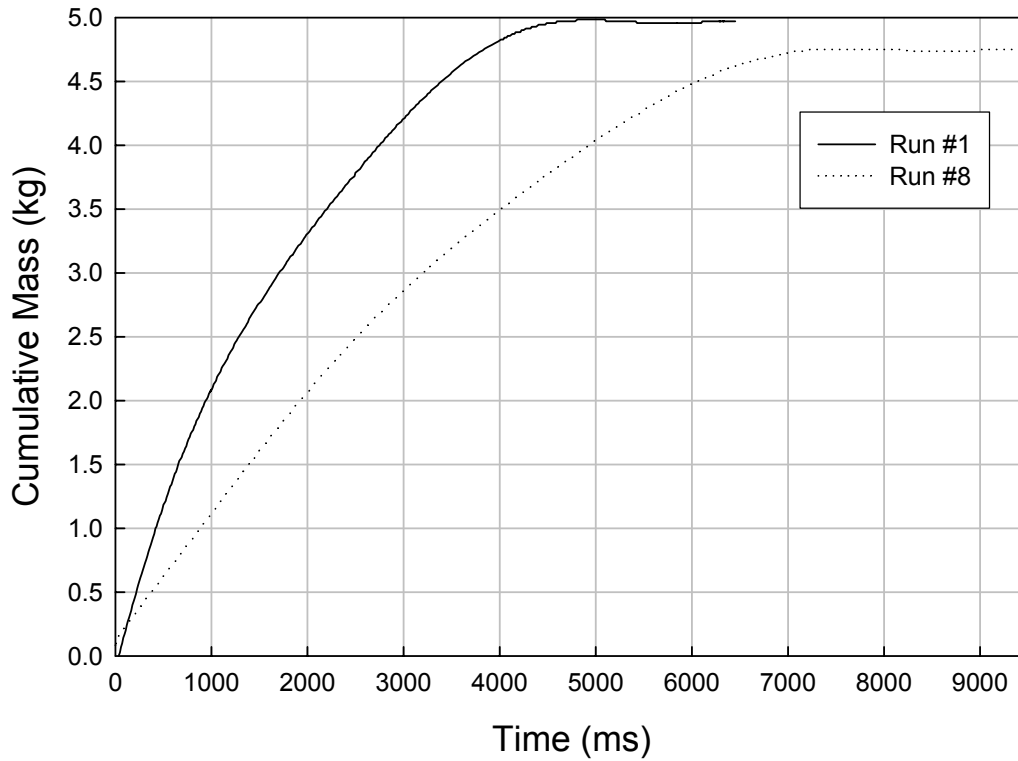


Figure 8-33. Cumulative Mass as a Function of Time for Runs #1 and #8.

Overall, the liquid density yielded a better calculation than the mixture assumption with an average error of 47 % compared with 155 %. These findings suggests that the phasic composition of the flow through the fitting plays a major role in the pressure drop experienced at any instantaneous time during the discharge and that local flow characteristics will play a large role in determining the magnitude of the pressure drop.

Table 8-4. Comparison of Experimental Pressure Drop Values to Literature Values.

	Run #8	Run #9	Run #10
Initial source vessel pressure (kPa)	2120	3915	4910
Void fraction	0.649	0.507	0.485
Liquid density (kg/m ³)	1403.5	1392.8	1389.0
Mixture density (kg/m ³)	514.43	704.73	733.18
Velocity (m/sec)	3.446	9.007	7.630
90° Elbow			
Experimental ΔP (kPa)	9900	27800	36000
Literature value ΔP (mixture ρ) (kPa)	21594 (118 %)	106073 (282 %)	72775 (102 %)
Literature value ΔP (liquid ρ) (kPa)	7915 (20 %)	53673 (93 %)	38414 (7 %)
Capped Tee			
Experimental ΔP (kPa)	11300	40400	62600
Literature value ΔP (mixture ρ) (kPa)	29778 (164 %)	195398 (384 %)	134059 (114 %)
Literature value ΔP (liquid ρ) (kPa)	14580 (29 %)	98871 (145 %)	70763 (13 %)
Union			
Experimental ΔP (kPa)	11100	31500	50400
Literature value ΔP (mixture ρ) (kPa)	17048 (54 %)	83742 (166 %)	57454 (14 %)
Literature value ΔP (liquid ρ) (kPa)	6248 (44 %)	42373 (35 %)	30327 (40 %)

The third set of experiments also used an alternative-piping configuration, which included a vertical split of the flow (see Figure 8-20). The goal of these runs was to examine whether there would be any difference in pressure drop between the two legs of the split. At slower flow velocities, separation of the flow may occur based on the flow regime of the discharge. For example, if the flow were stratified then all the liquid may flow through the bottom leg of the split and the entire vapor may travel through the top leg. This would be evident from the difference in pressure drop between the two legs since the vapor would have a much lower pressure drop than the liquid. In the experimental runs, no such trend was observed, as can be seen in Figure 8-34, which depicts the pressure drop across both legs after a vertical tee split. The plots for both the top and bottom branch are almost identical, which was the case for the entire tested pressure range of 2140 kPa to 4910 kPa. At these high velocities the flow is in the bubbly flow regime resulting in an even split between the two branches.

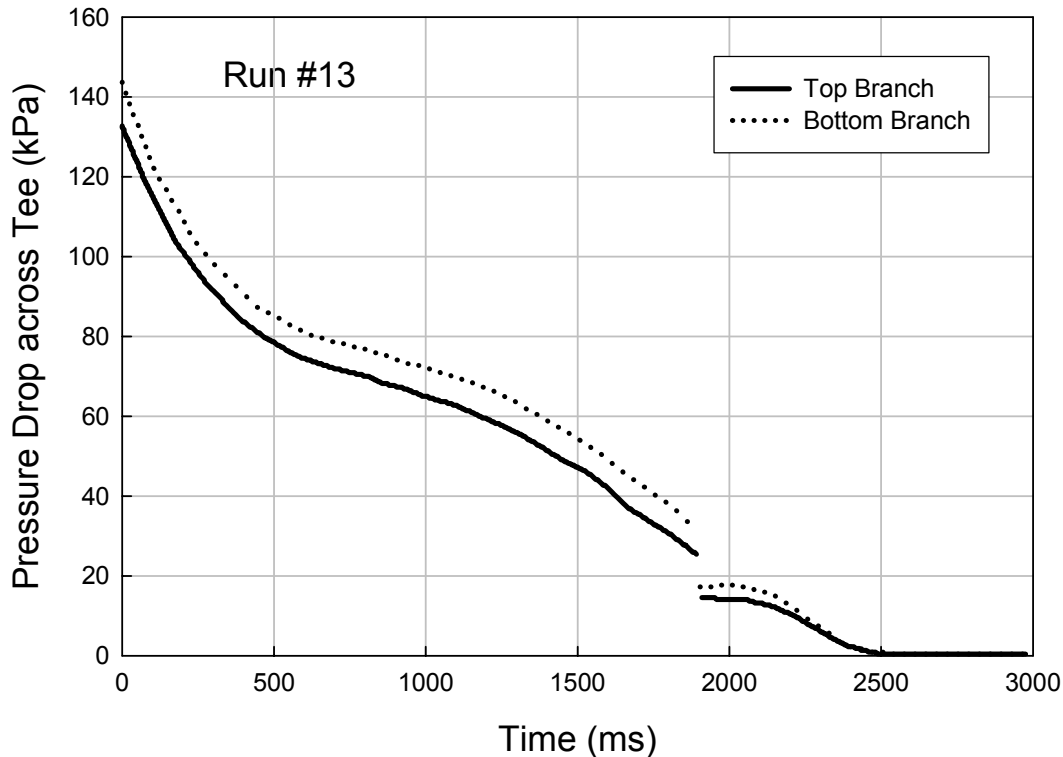


Figure 8-34. Pressure drops across top and bottom branch tees from Run #13.

The fourth set of experiments used the same piping configuration as the first set, the straight pipe, but the test fluid was changed to HFC-125. The main difference observed in these runs over the HFC-227ea runs was the drop in temperature as the liquid vaporized. If a comparison is made between Run #5 (HFC-227ea) and Run #16 (HFC-125), which have initial source vessel pressure within 5 kPa of each other, there is an undeniable difference in the temperature traces in the collection vessel.

As Figure 8-35 shows, the temperature in Run #5 only drops about 3 °C compared to a temperature drop of almost 35 °C in Run #16. The other temperature traces between these runs are similar. This may be due to the fact that the flow passes through the pipe at a fast rate with a high convective heat transfer coefficient, which causes the fluid to warm up. However, in the collection vessel, the volume/surface ratio is much larger and convective heat transfer to surface area is smaller. Although, it would have been beneficial to measure the temperature at the end of the pipe to justify this theory, it was unable to take this measurement due to a thermocouple failure. Once the liquid reaches the collection tank, it must vaporize to reach the saturation conditions in the collection vessel, causing a drop in temperature. These conditions did not significantly effect the other measurements near the end of the pipe for either fluid. For instance, for either fluid, the void fraction followed a similar trend as expected from the previous runs, it dropped off as the initial flow passed the sensor and then rose slowly until the liquid ran out, then it returned to the all vapor value, as shown in Figure 8-36 and Figure 8-37. During runs with both of these fluids, a noticeable pressure recovery due to the degassing of the nitrogen was not observed, which was seen in previous studies. Although, when examined closely, a sudden slow down in the pressure decay after the initial pressure drop was observed, which might indicate a slight recovery.

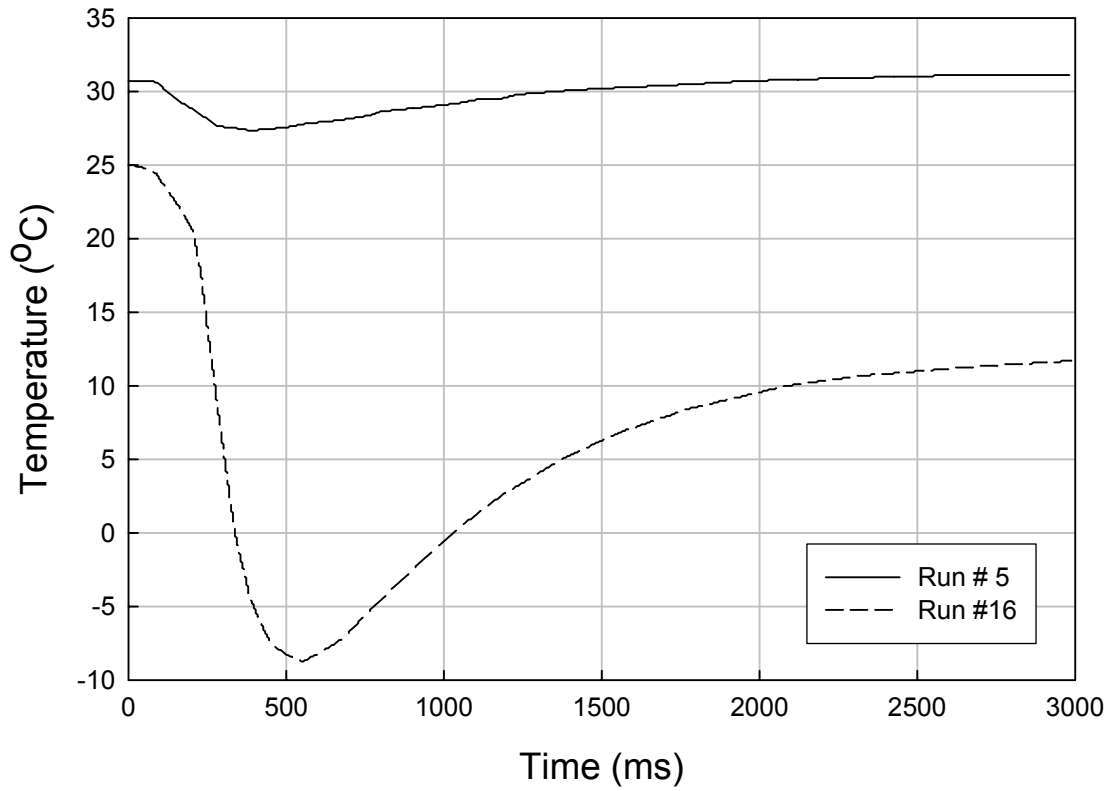


Figure 8-35. Comparison of Temperature Traces in the Collection Vessel from Runs #5 and #16.

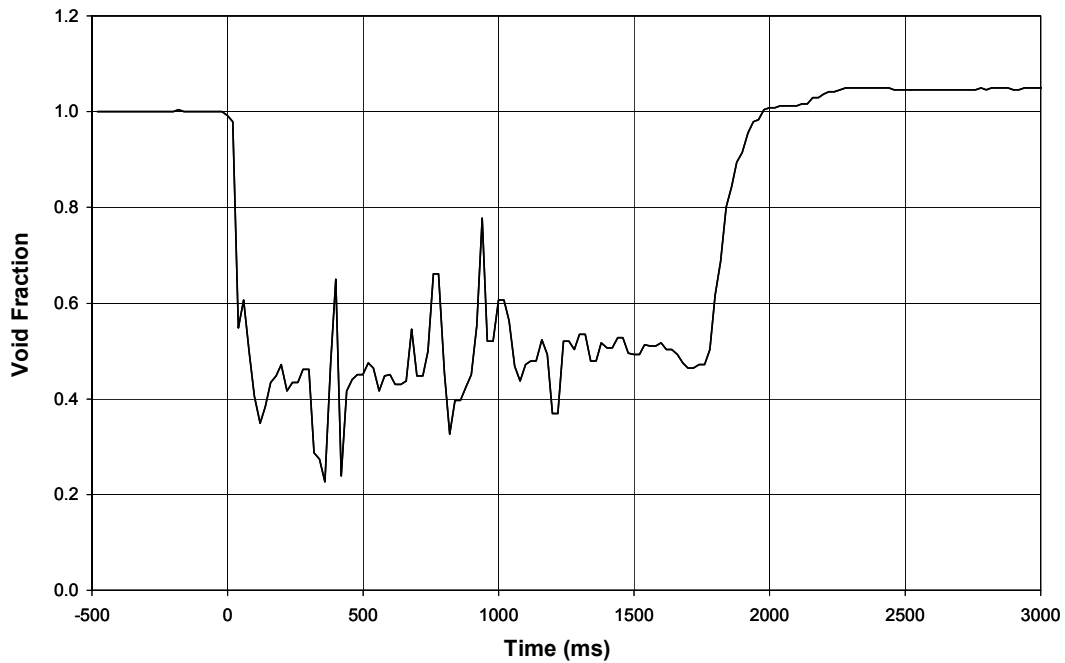


Figure 8-36. Void Fraction Measurements from Run #5.

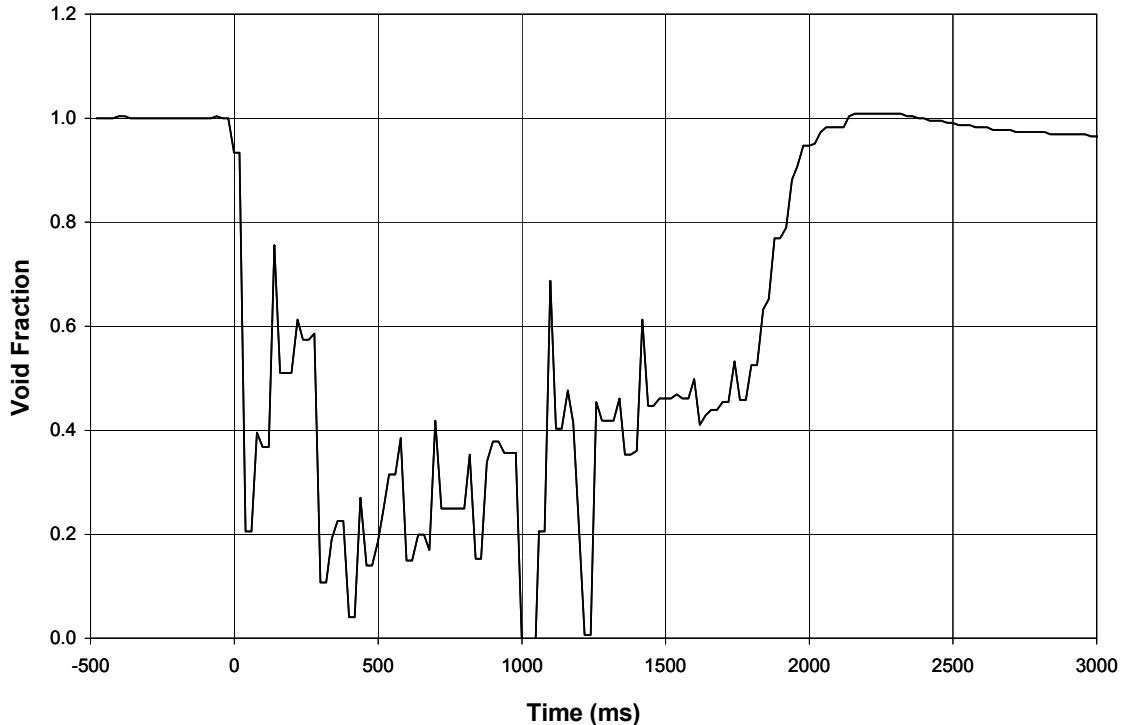


Figure 8-37. Void Fraction Measurements from Run #16.

This conclusion is supported by the fact that in the HFC-227ea runs there was a much smoother transition shown on the source vessel pressure trace between the initial pressure drop and the filling of the pipe. This can be seen best by once again comparing Runs #5 & #16, where there is a slight “bump” in the source vessel pressure trace at about 400 ms of Run #16, as shown in Figure 8-38 and Figure 8-39. The absence of a more pronounced pressure recovery due to the degassing of nitrogen can be accounted for by either of two reasons: the speed of the flow is too great for a noticeable increase in pressure from degassing to be observed at any one point, or the degassing took place so gradually over the run preventing any noticeable increase. It was unknown whether the degassing occurred at some point since the void fraction validated that a two-phase flow existed. However, it was certain that this was not due to vaporization since there was no temperature drop.

The last sets of runs were conducted during preliminary tests of the instrumentation after installation in the system. The first test using water, Run #18, allowed for testing the mass flow rate sensor. As can be seen in Figure 8-40, this test worked out very well and gave an excellent representation of the instantaneous mass inventory in the source vessel. This test also showed that the thermocouples could pick up quick drops in temperature, as shown in the pipe position 1 trace of the film thermocouple, which picked up the nitrogen expansion at the end of the run, as shown in Figure 8-41. The second test, Run #19, provided an excellent sample of the capabilities of the capacitance probe for measuring void fraction. Since there was no vaporization or dissolution of gas in this run, the void fraction should go from a value of 1.0 to 0.0 as the liquid flowed. This is exactly what was found at the beginning of the run until it stopped at precisely the same point as the temperature dropped, signifying the start of the nitrogen expansion through the system, as can be seen in Figure 8-42. The final set of experimental runs used carbon dioxide as a test fluid and was conducted with an open collection vessel to prevent a high pressure

at the end of the run. The goal of these tests was to get a grasp on the response time of the film thermocouples and what range of temperature drop they could collect. The thermocouples were able to pick up a quick drop in temperature of up to $-40\text{ }^{\circ}\text{C}$.

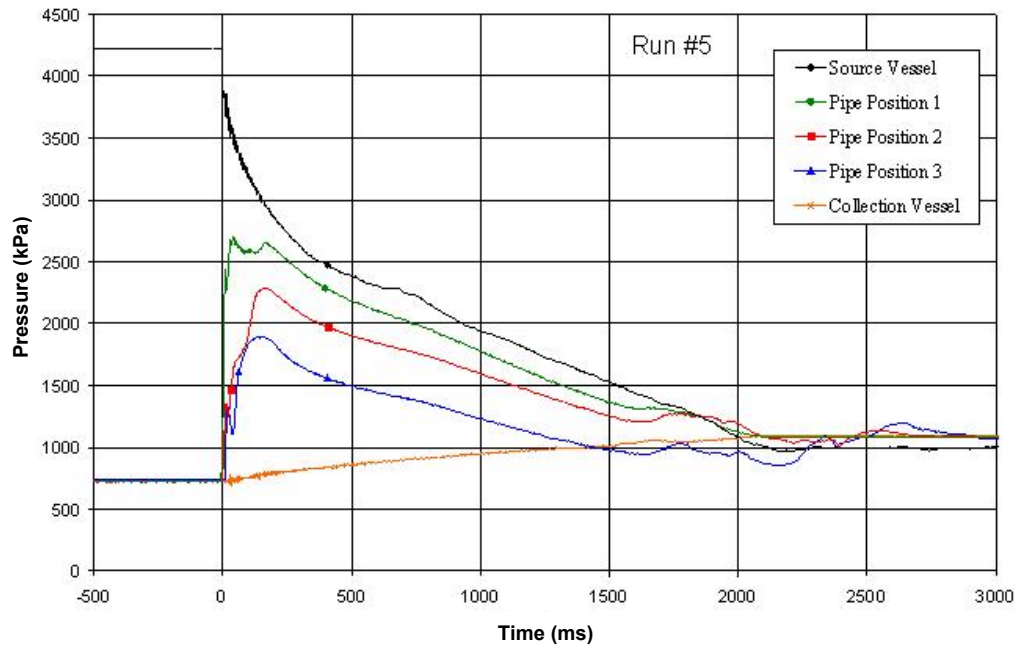


Figure 8-38. Pressure Traces from Run #5.

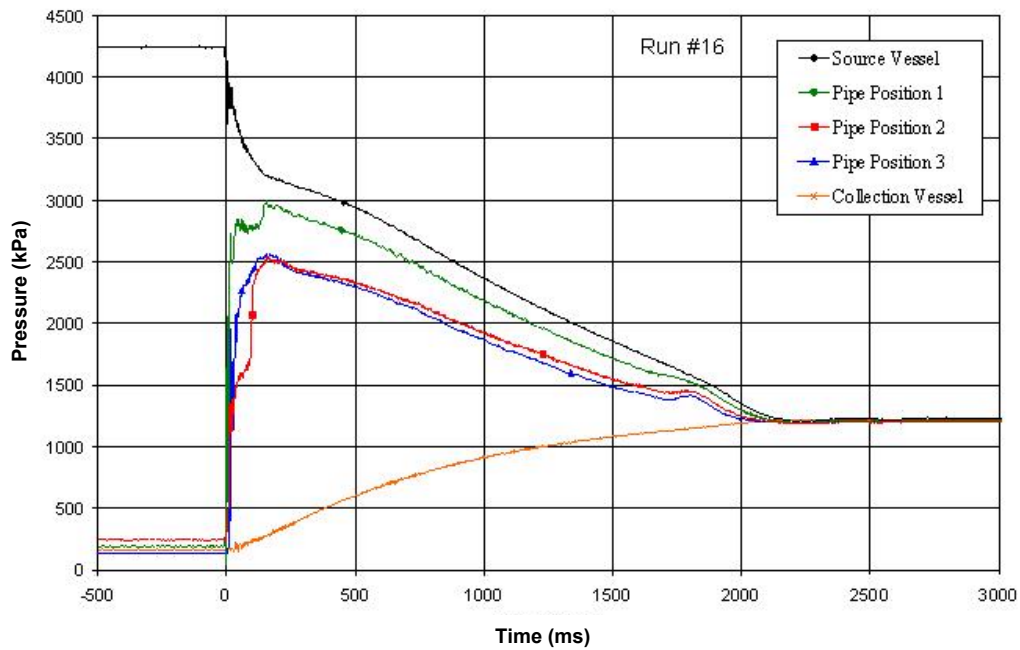


Figure 8-39. Pressure Traces from Run #16.

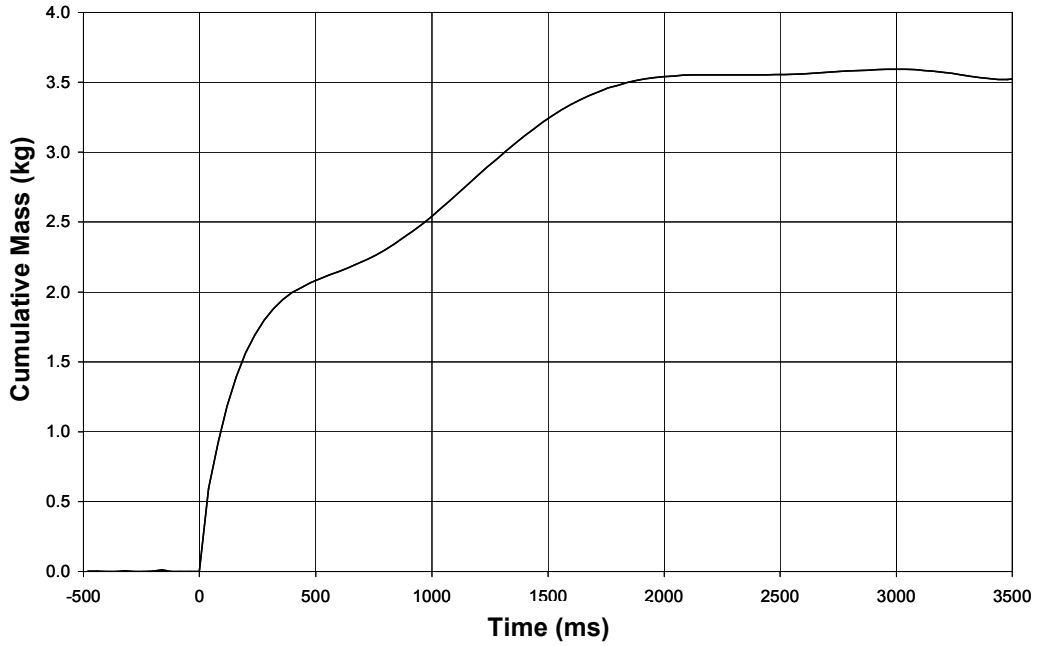


Figure 8-40. Mass Inventory in the Source Vessel from Run #18.

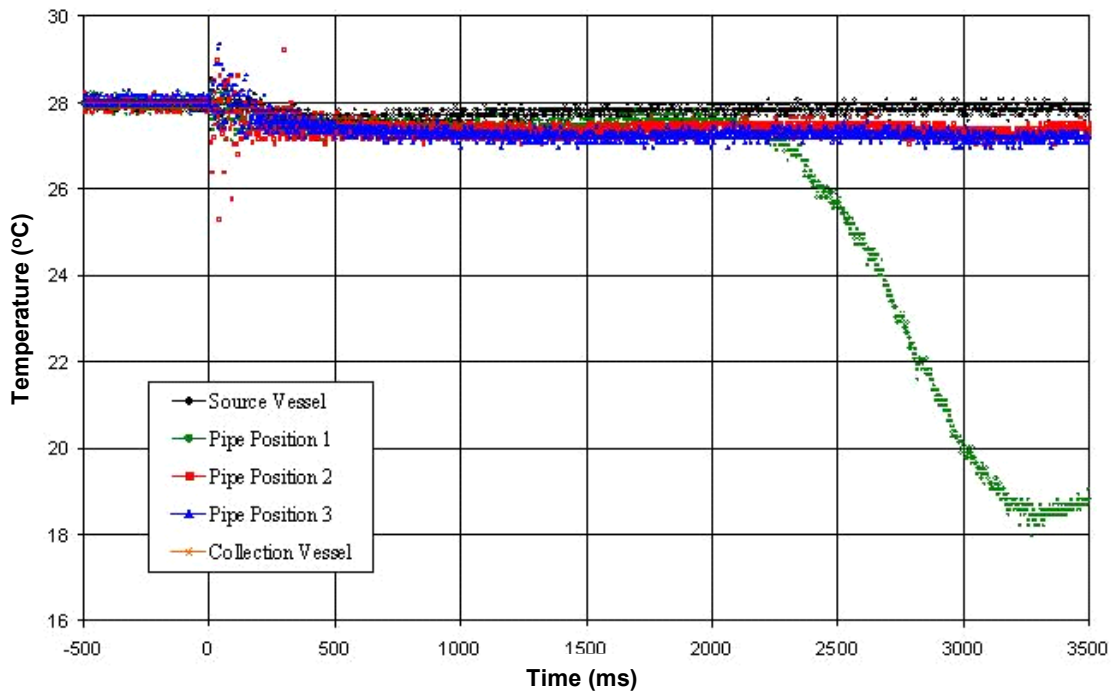


Figure 8-41. Temperature Traces at Various Positions from Run #18.

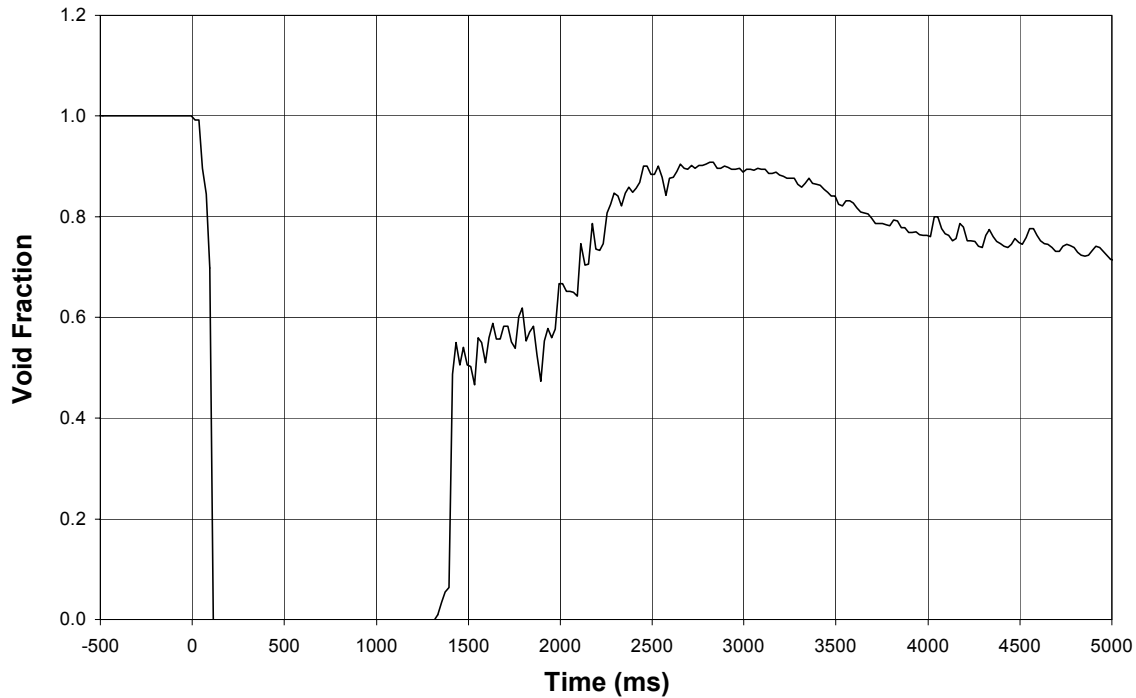


Figure 8-42. Void Fraction Measurements from Run #19.

8.3.7 Comparison of Code Predictions to Experimental Data

This section discusses some of the code assessments carried out against experiments. Early assessment of the FSP code was against halon 1301 discharge experiments reported by Elliott et al.¹⁰ These tests were carried out with three different system configurations. These included a bottle-nozzle arrangement, a bottle with straight pipe, and a bottle with a straight pipe branching to two separate exit legs. Test 146 from Elliott et al.¹⁰ was a bottle-nozzle arrangement. This test was used in early assessment of FSP for the gas release model. The other configurations tested by Elliott et al.¹⁰ were also simulated during various developmental stages of the code. The results generally showed good agreement between code calculations and experimental data. A re-assessment of the final code version against data from these configurations was not carried out. This was primarily because the tests were conducted with halon 1301, and the intent of code development was for alternate fluids. The expectation is that the final version of FSP would be able to simulate these tests quite well. Other experimental data on suppressant discharge through typical delivery systems have been compiled and reported by Yang et al.² and Pitts et al.⁹

This section presents the assessment of the code carried out against some of the experiments reported in Yang et al.² The experiments were conducted at NIST, and included a series of discharge tests using several agents (including halon 1301). The code was also assessed against current experiments carried out as a part of this code development project by examining several piping configurations, with HFC-227ea and with HFC-125. These experiments are particularly useful for code assessment because, in addition to the usual measurement of pressure, the experiments were able to estimate the mass flow rate of discharge, and also measured the void fraction near the pipe exit.

Code Assessment against NIST Test Data

The basic design of the NIST experimental apparatus consisted of a storage vessel (or pressure vessel), discharge piping, and a recovery tank. A nitrogen make-up tank was connected to the pressure vessel to simulate constant-head discharge if needed. The pressure vessel was fitted with a quick release valve at the bottom. Figure 8-43 shows the test apparatus. The data included vessel pressure and pressures at various locations along the discharge piping. Several discharge piping configurations were used. These included: (1) 3.5 m straight pipe discharge; (2) 3.5 m pipe with 90° bend; (3) 4.5 m pipe with 90° bend; (4) 3.5 m straight pipe with expansion from 9.5 mm ID to 15.9 mm ID; (5) 3.5 m straight pipe with contraction from 15.9 mm ID to 9.5 mm ID; and (6) 4.5 m, 15.9 mm ID tee configuration. Two pipe sizes were used for all configurations, unless otherwise stated, and these were 9.5 mm ID and 15.9 mm ID. The various configurations are shown in Figure 8-44.

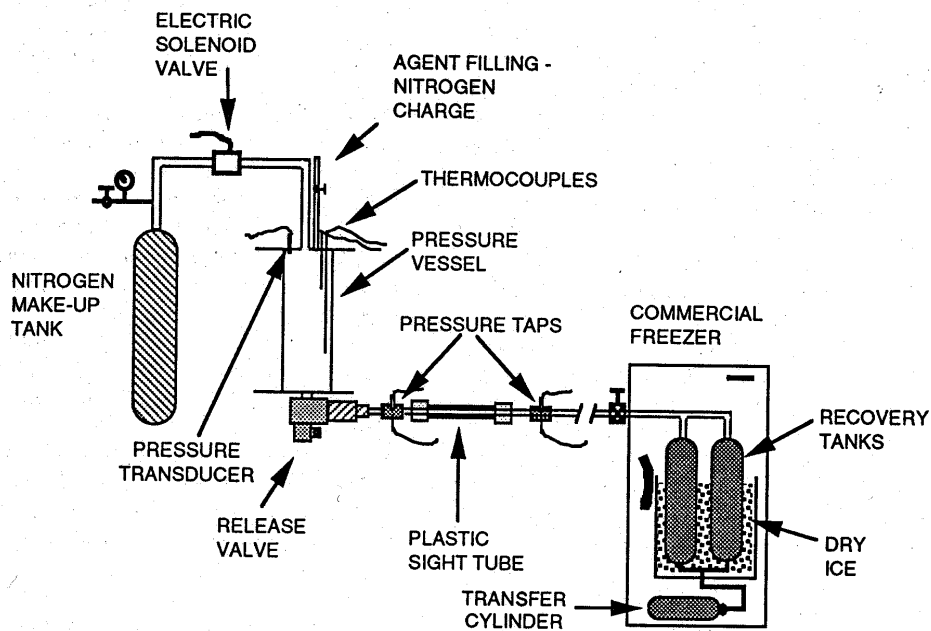


Figure 8-43. NIST Test Apparatus.²

Four agents were tested in these experiments. These were halon 1301, HFC-125, HFC-227ea and CF₃I. The assessment presented here is only for the HFC-227ea experiments. Table 8-5 lists the tests conducted with HFC-227ea. Note that the test identifier in the first column is actually the Figure Number in Appendix II of the NIST Report (Yang et al.²).

Four tests were simulated using FSP. These are Tests B-59, B-68, B-61, and B-60. Together they represent a variety of piping configurations. The results of the simulations are presented below.

A FSP input model for each discharge piping configuration was developed. The following geometrical information was obtained from Yang et al.²

Storage Vessel Volume:	$4.06 \times 10^{-3} \text{ m}^3$
Storage Vessel ID:	100 mm
Discharge Valve:	31.8 mm inlet to 44.5 mm exit
Discharge Valve Stroke:	order of 10 ms
Nitrogen Make-up Tank:	$88 \times 10^{-3} \text{ m}^3$
Nitrogen Charge Tubing:	19.1 mm ID
Nitrogen Solenoid Valve:	30 kPa pressure difference opening, stroke 50 ms
Discharge Piping Sizes:	9.5 mm and 15.9 mm ID
Discharge Piping Lengths:	3.5 m and 4.5 m
Recovery Tank Volume:	$15 \times 10^{-3} \text{ m}^3$

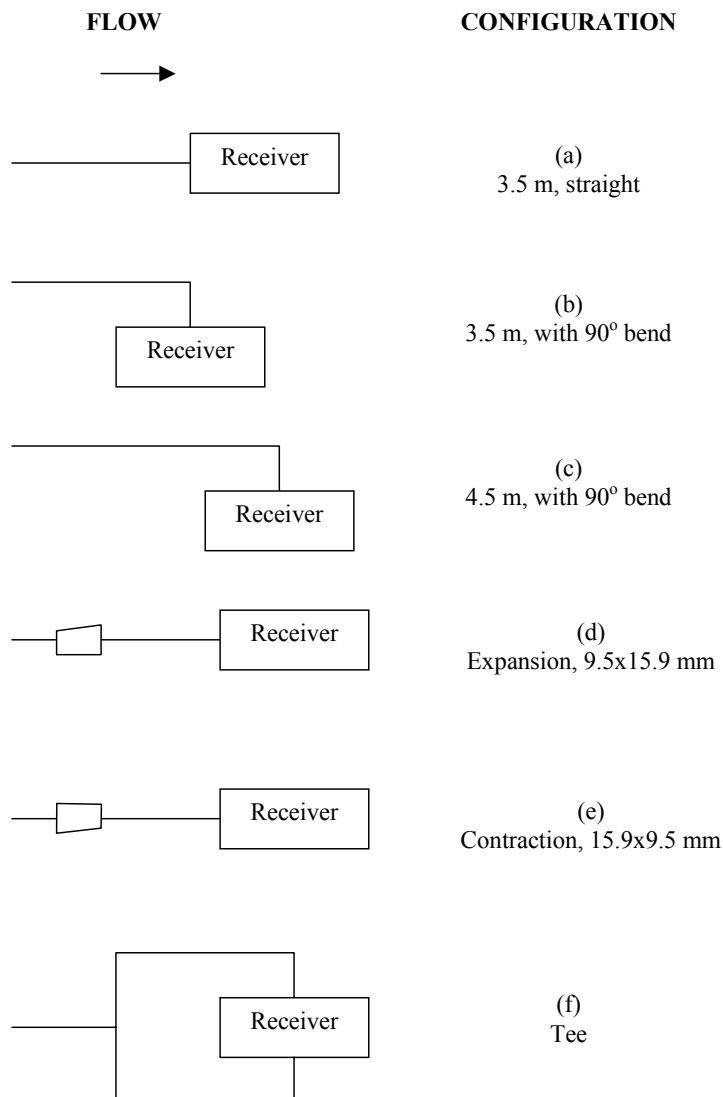


Figure 8-44. Piping Configurations for NIST Experiments.

Table 8-5. Test Matrix from NIST Experiments.

Test Identifier	Pressure (MPa)	Fill Volume (%)	Configuration
B-54	2.75	56.5	straight pipe, 9.5 mm ID, 3.5 m long
B-56	4.12	60.2	straight pipe, 9.5 mm ID, 3.5 m long
B-58	4.12	49.2	3.5 m, 90-deg bend, 9.5 mm ID
B-59	4.12	49.2	4.5 m, 90-deg bend, 9.5 mm ID
B-60	4.12	49.0	straight pipe with contraction
B-61	4.12	49.0	straight pipe with expansion
B-66	2.75	54.1	straight pipe, 15.9 mm ID, 3.5 m long
B-68	4.12	49.4	straight pipe, 15.9 mm ID, 3.5 m long
B-71	4.12	49.4	3.5m, 90-deg bend, 15.9 mm ID

The above information was used to develop the input models for FSP for each of the tests. The models are not described in detail or presented here. They were very similar, conceptually, to the sample problem described in detail in Tuzla et al.⁷ The supply vessel (called storage tank in these tests) and discharge piping were each modeled with PIPE components, with a VALVE component in between them, simulating the initiation of the discharge process. In modeling the discharge piping, junctions were located at the physical locations of area changes (contraction or expansion) and bends. Appropriate loss coefficients were entered to simulate the energy losses at these locations. Figure 8-45 shows the general FSP model used for these simulations.

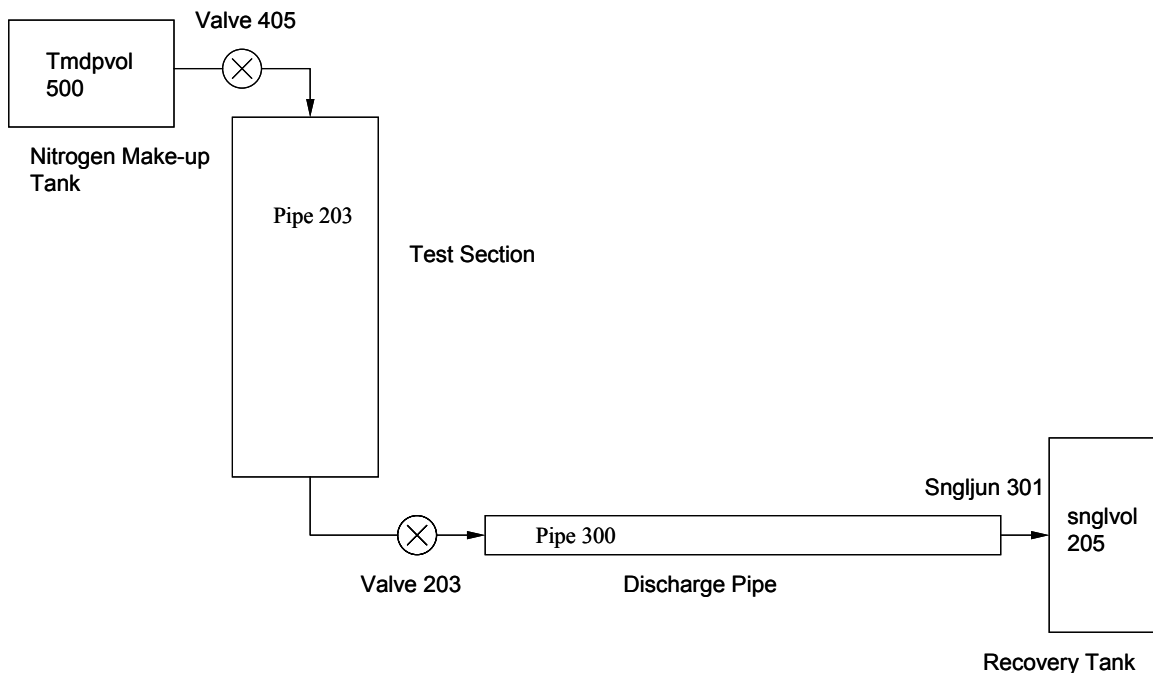


Figure 8-45. FSP Input Model.

These cases were all run with the value of r_c in the range of 7.5×10^{-9} m to 1.0×10^{-8} m. The discharge coefficients at the system exit were chosen as 1.0, 0.8 and 0.8 for the subcooled, two-phase, and single phase vapor conditions, respectively. The value of Γ_0 was set at 10,000 for the tests. Figure 8-46, Figure 8-47, Figure 8-48, and Figure 8-49 respectively show the calculated and measured pressure responses in the supply vessel, for Test B-59, B-68, B-61, and B-60. Not shown here are the pressure histories at various locations along the discharge piping. Generally, at these locations, the measured pressure would increase sharply as the discharge was initiated, and then decrease gradually as the fluid left the system. This trend was picked up by the code. Overall, the code picks up the qualitative trends in the pressure history. If the time for complete discharge of the agent is taken as the time at which the pressure drops to its lowest value, the code seems to calculate this generally within about 25 %. A better agreement between calculation and data could probably be obtained by varying r_c and Γ_0 . This has not been attempted here, primarily because there are inherent uncertainties in these parameters, and a code user would normally vary these parameters in design calculations to get conservative results for design purposes. Generally, a higher value of Γ_0 would release more dissolved gas earlier in the transient. This would generally delay the complete discharge of the bottle slightly. Users can utilize this information to develop conservative designs in applying the FSP code.

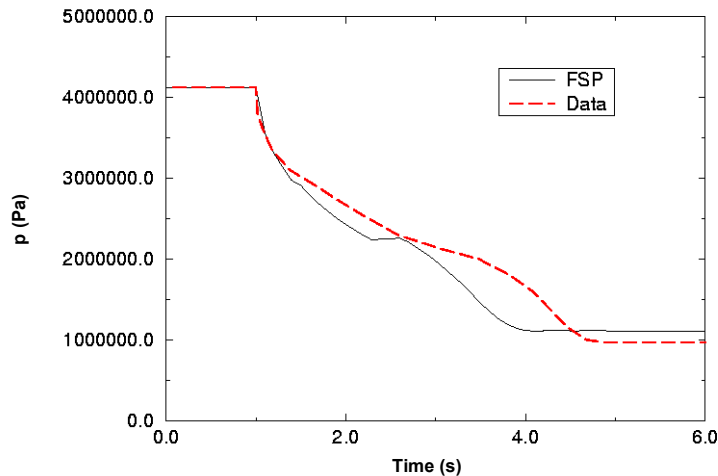
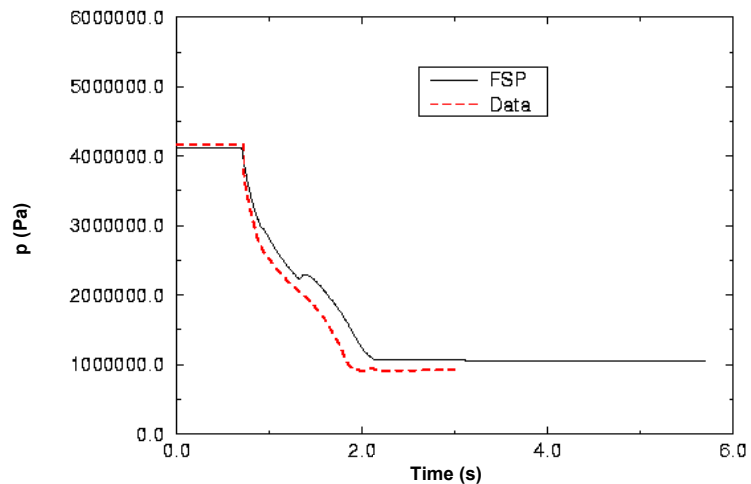


Figure 8-46. Comparison of Calculated and Measured Bottle Pressure for B-59.

Figure 8-47. Comparison of Calculated and Measured Bottle Pressure for B-68.



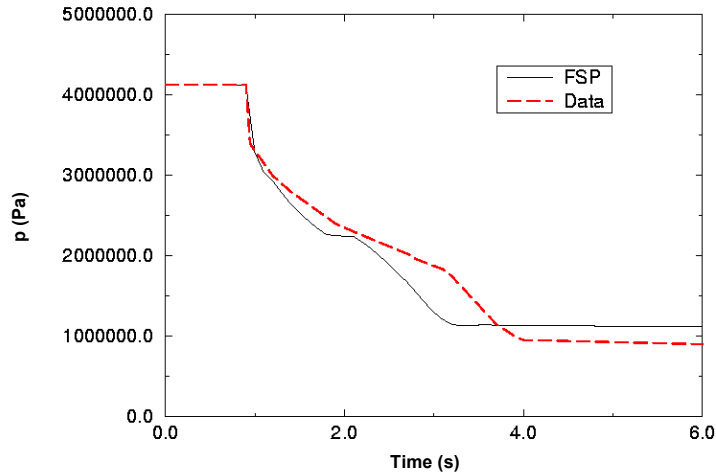
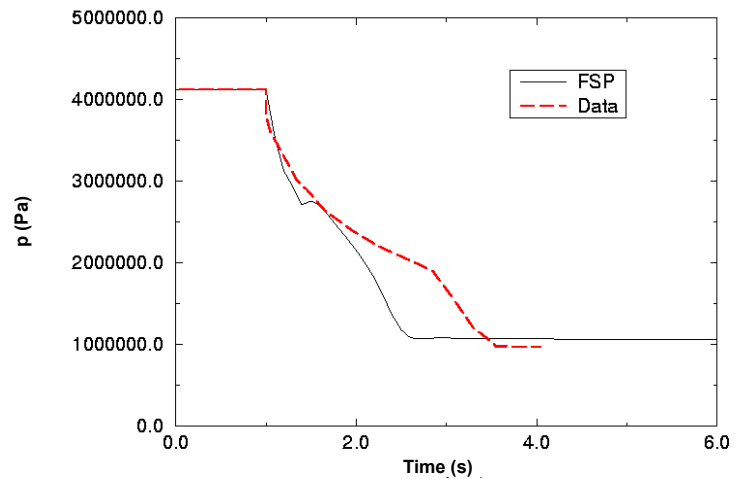


Figure 8-48. Comparison of Calculated and Measured Bottle Pressure for B-61.

Figure 8-49. Comparison of Calculated and Measured Bottle Pressure for B-60.



Code Assessment Against Current Test Data

In this section a detailed comparison of the computer code predictions and the experimental values for a rapid transient discharge of a suppressant flow will be examined. To fully test the code, all aspects of an actual suppressant discharge must be considered. For this reason, the current experimental data should be the benchmark for comparison since it includes the most extensive experimental data to date. This is due to the fact that data for local temperatures, void fraction, and mass flow rate which, were previously unavailable, were measured. In addition, extensive data for a number of different flow conditions and piping configurations have been obtained.

When using the computer code to make predictions, it was necessary to determine a few operating parameters to represent the operating conditions of a specific run. Some of these parameters are straightforward and pertinent to the piping configuration, such as diameters, lengths, etc., and operating conditions such as initial pressure, temperature, etc. However, some of these parameters are part of the modeling used in the code. One of these models is the gas dissolution model, as discussed above.

Dependent on the fluid used during the discharge, the gas dissolution model requires two constants: the critical bubble radius when nitrogen is released from the fluid and the release rate of nitrogen.

The critical radius can be found for a specific run by estimating when the release of nitrogen begins. This is the point near the beginning of the run when the pressure stops dropping rapidly, represented as a change in slope in the pressure trace. With this pressure and the surface tension of the fluid, a critical radius can be calculated as described earlier. After examining the first set of experimental Runs (#1-#7), it was determined that the value was in the range of 5 nm to 20 nm. The second parameter, the rate of degassing, was found to fall in the range from 1000-10,000, depending on the system. The last parameter that needs to be defined as input to the code is the discharge coefficient for choked flow conditions. Since the default is 1.0, it is expected that the value must be relatively close to this value.

For ease in use and consistency, it is desirable to choose one value for each of these parameters to run the computer code. To determine the appropriate values for these parameters, a sensitivity analysis of the effects of varying these parameters on the code's output was performed, and the results were compared with experimental data. The experimental Run #4 was used for this purpose. This run was chosen over the others because it was one of the repeatability tests and was in the range of typical suppressant discharge applications.

The first sensitivity study examined the effect of critical radius on the computer code output. To isolate the effect of changing this parameter, the values for the gas release rate and the discharge coefficients were kept constant at 1000 and 0.8, respectively. The calculations showed that a lower value for the critical radius caused the slope change in the source vessel pressure trace to occur later. Therefore, this parameter is important for determining when the gas begins to release from the liquid. By comparing the calculations using critical radii of 7.5 nm and 10 nm with the experimental results, as seen in Figure 8-50, a critical radius of 10 nm was chosen.

The second sensitivity study was to identify a value for the rate of nitrogen gas release, with the discharge coefficient and the critical radius kept constant at 0.8 and 7.5 nm, respectively. This rate influences the speed at which the nitrogen gas is released once the process begins, thus changing the shape of the pressure-time history. As shown in Figure 8-51, the pressure trend remains straight and uniform at lower gas release rates; however, there is a pressure recovery or "bump" in the trace at higher release rates. Based solely on the pressure-time history results, it is hard to determine the best value to use for this parameter so other output parameters from the calculations were examined. The void fraction results are shown in Figure 8-52, which indicates that average void fraction increases with the gas release rate parameter. This figure, the other does not, shows that a value just below 2500 kg/m³ s appears to be appropriate. Based on the observations from the above two figures, a gas release rate value of 2000 kg/m³ s was chosen.

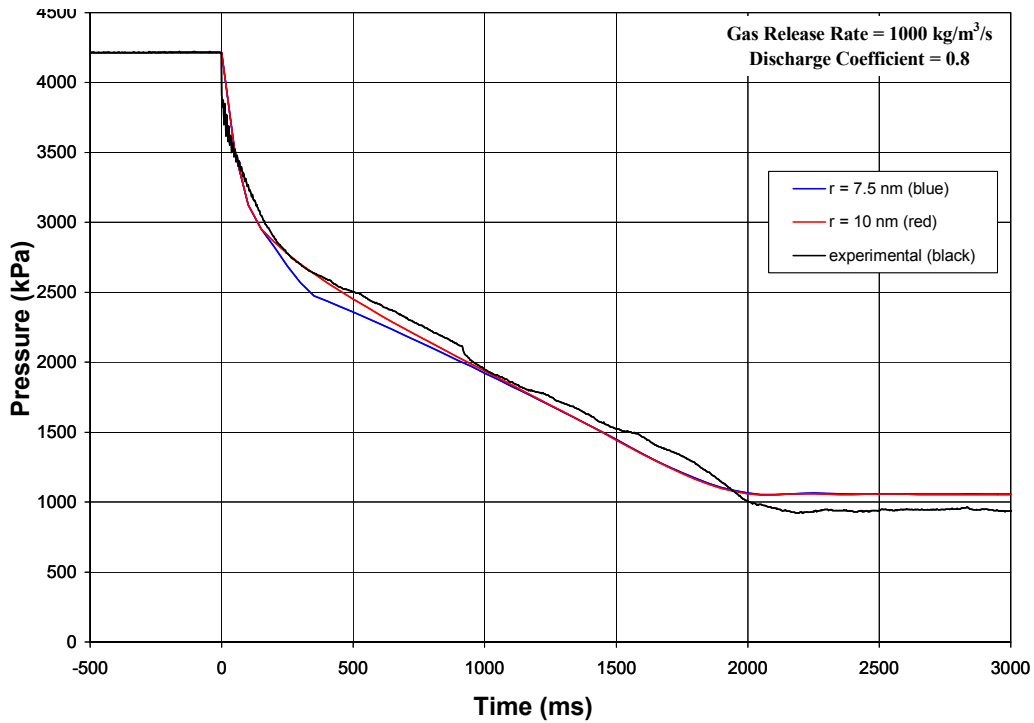


Figure 8-50. Comparison of Experimental and Predictive Source Vessel Pressure Data in Sensitivity Study on Critical Radius Value for Conditions of Run #4.

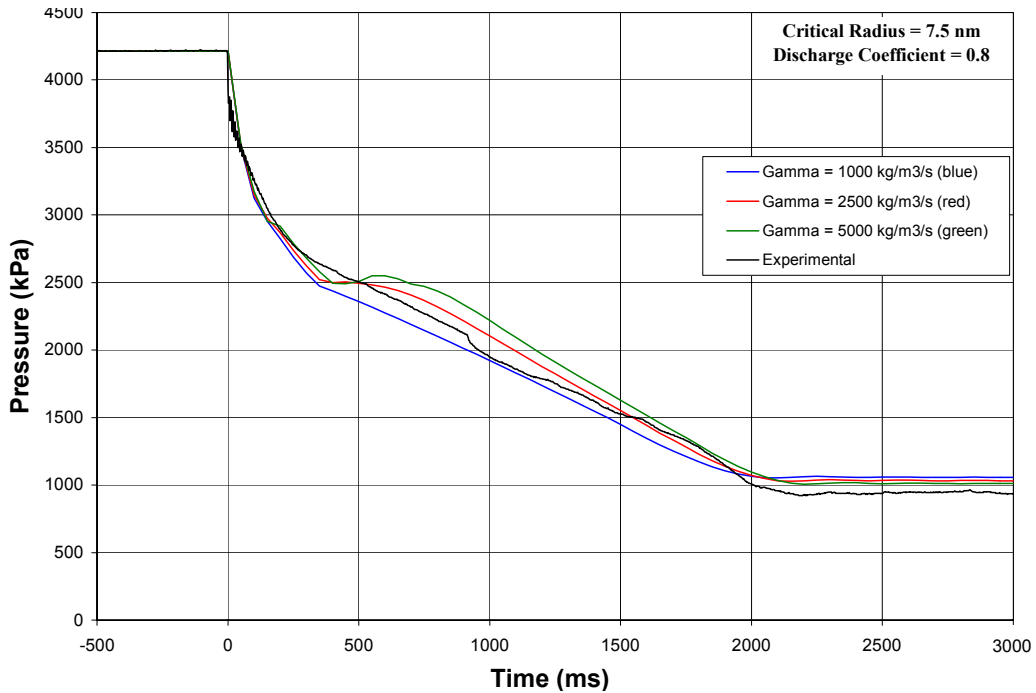


Figure 8-51. Comparison of Experimental and Predictive Source Vessel Pressure Data in Sensitivity Study on Gas Release Rate Value for Conditions of Run #4.

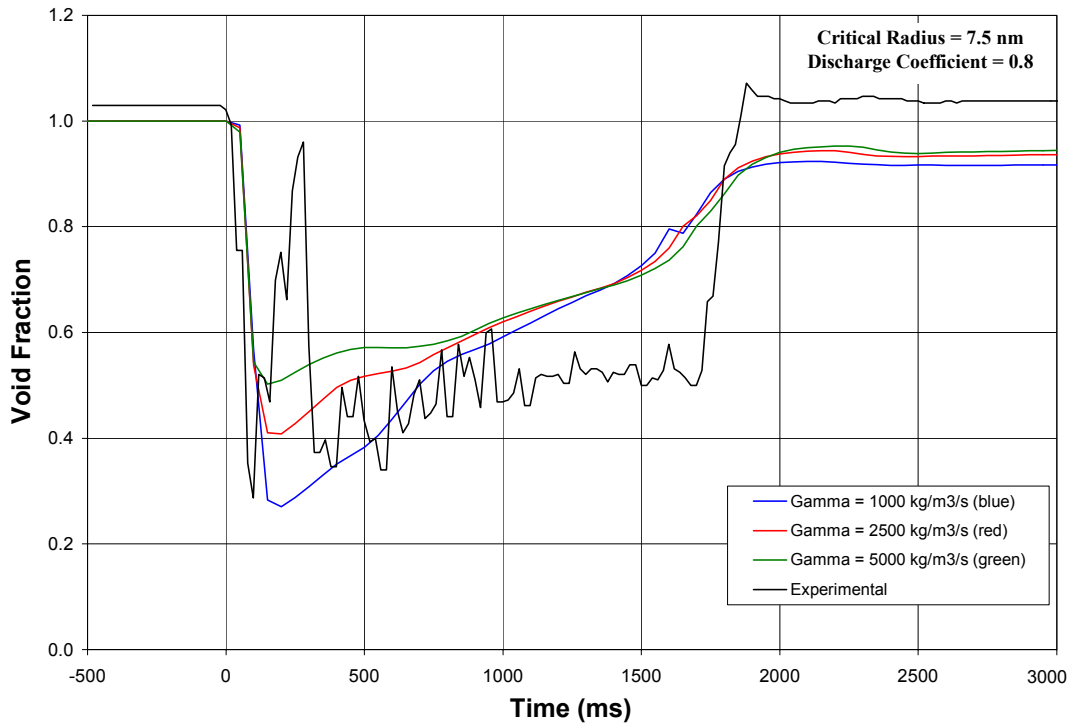


Figure 8-52. Comparison of Experimental and Predictive Void Fraction Data in Sensitivity Study on Gas Release Rate Value for Conditions of Run #4.

The last sensitivity analysis was to pick a value for the discharge coefficient. This parameter influences when and where choking occurs in the system. Values ranging from 0.75 to 1.15 were tried, and there were only negligible differences in the output. Therefore, it was decided to use a value of 0.9 for the discharge coefficient.

With all of the operating parameters chosen, a final comparison with the experimental data of Run #4 was conducted. The calculations show good agreement with the experimental results, as shown in Figure 8-53 and Figure 8-54.

In the following discussion, the focus is on comparing the computer code prediction with an entire experimental run (Run #5). The results for cumulative mass in the source vessel as a function of time are shown in Figure 8-55. The prediction agrees well with the experimental measurements. The only noticeable difference is the final mass value and the speed of the discharge represented by the different slope gradients. Even with these differences, the prediction gives an end-of-liquid flow at approximately 1800 ms compared to a measured time of 1600 ms in the experiment, a very good estimate of discharge time.

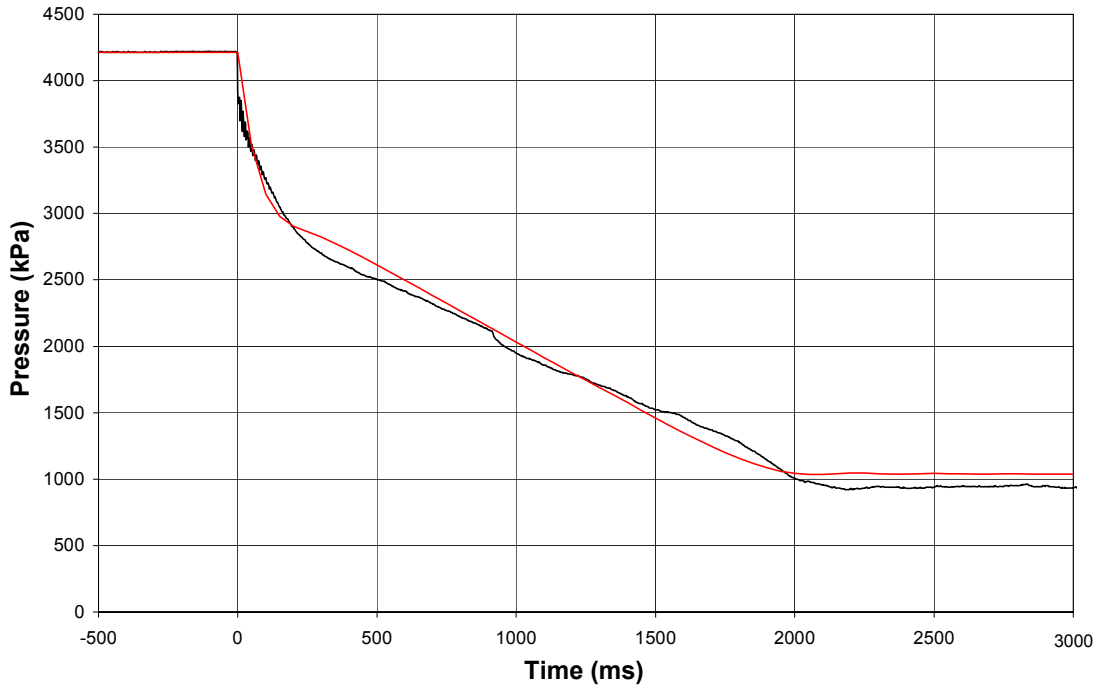


Figure 8-53. Comparison of Experimental (in black) and Predictive (in red) Pressure Data Using Final Values for Code Operating Parameters for Conditions of Run #4.

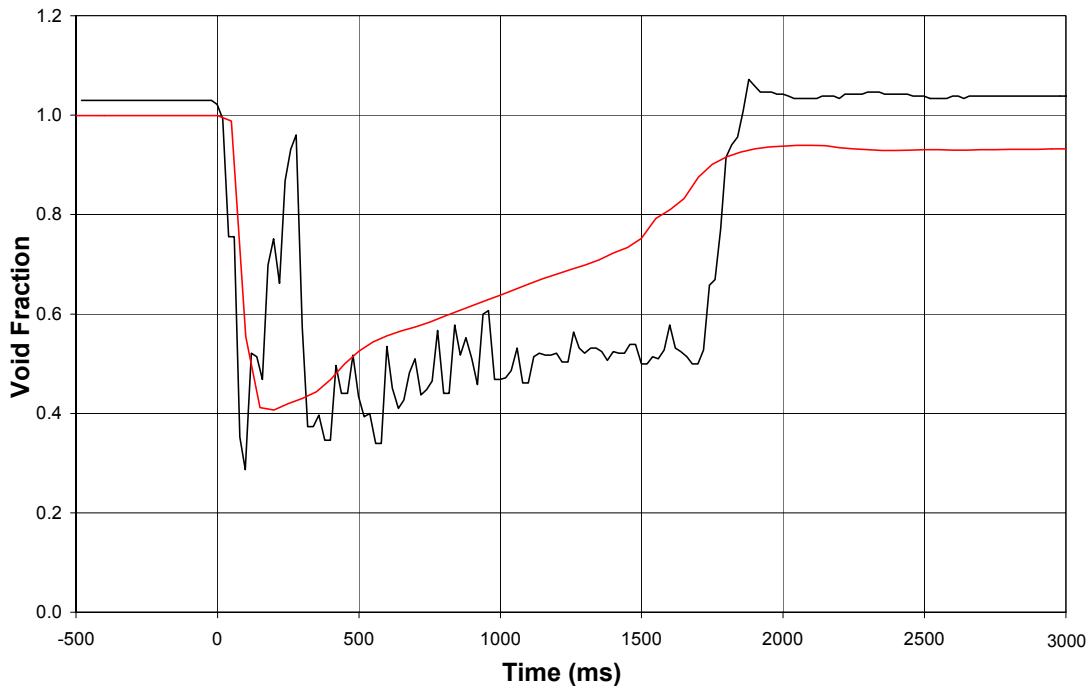


Figure 8-54. Comparison of Experimental (in black) and Predictive (in red) Void Fraction Data Using Final Values for Code Operating Parameters for Conditions of Run #4.

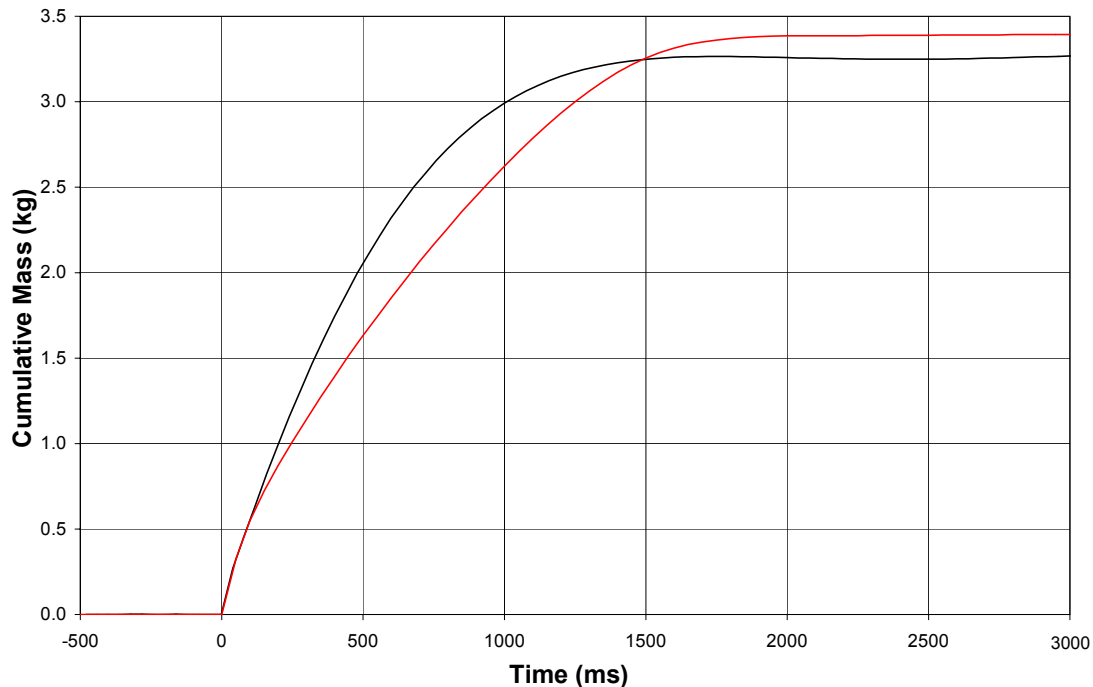


Figure 8-55. Comparison of Cumulative Mass for Experimental Run #5 (black) and Predictive Computer Code Data (red).

The next comparison examined is the void fraction experienced at the end of the piping system before the discharge reached the collection vessel. Again, the agreement between the prediction and experiment is good, as shown Figure 8-56. While the experiment was influenced by the local flow regime giving the output a fluctuating appearance, the prediction has a smooth trace due to the fact that the void fraction was calculated based on mass balance terms giving an average void fraction value for the amount of liquid and vapor present in the system. A similar trend can be seen in both, a sudden drop as the pipe is filled with liquid and then an increase as nitrogen comes out of solution and raises the average amount of gas in the flow until the run ends with no more liquid flowing. The only glaring difference is in the final value reached at the end of the run. The prediction never goes back to an all-vapor reading of 1.0, indicating that in the simulation there is still liquid present in the pipe. In a realistic situation, the liquid would eventually drain into the collection vessel since it is the lowest part of the system, but the prediction is finding this value through a mathematical simulation, so it may not account for this. Neglecting this problem, a good representation of the void fraction can be found using the prediction.

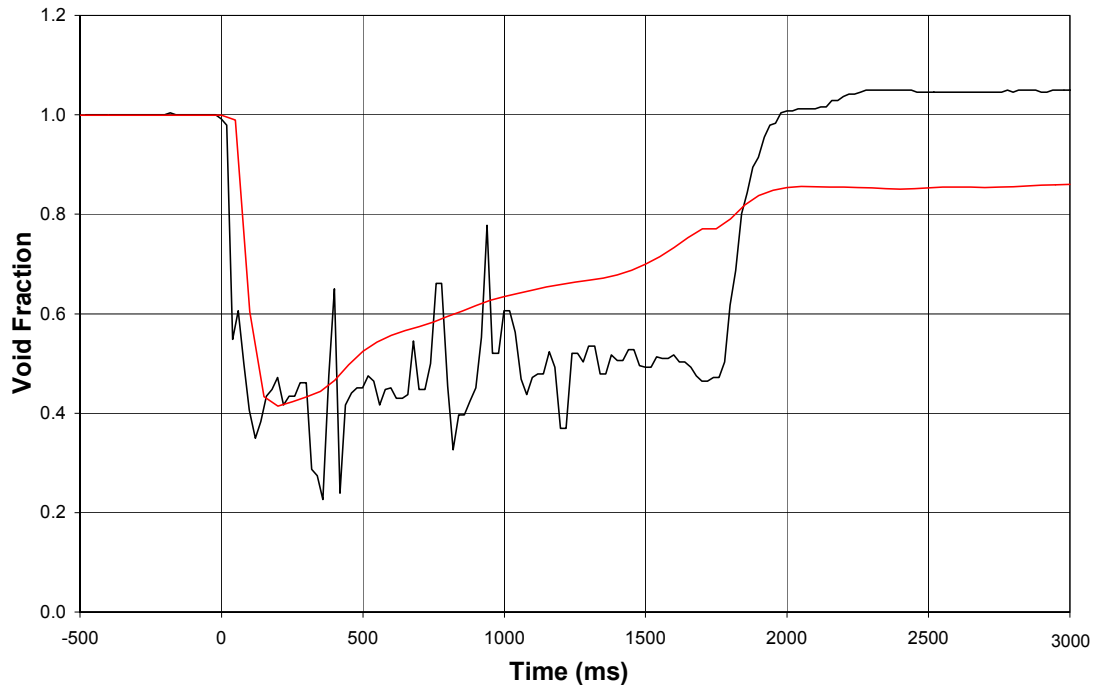


Figure 8-56. Comparison of Void Fraction for Experimental Run #5 (black) and Predictive Computer Code Data (red).

The most important comparison for this study is a comparison of the experimental and calculated pressure traces since pressure is what drives the discharge and delivers the suppressant to the fire. Figure 8-57, Figure 8-58, Figure 8-59, Figure 8-60, and Figure 8-61 show the prediction compared to the experiment for the pressures in the source vessel, at pipe position #1, at pipe position #2, at pipe position #3, and in the collection vessel, respectively. They all agree very well with the experimental data, with the only discrepancy being the final pressure at the end of the run. While the shape of the curves varies slightly, they all show the same trend and a similar slope as the pressure decreases during the discharge. This observation is most exciting since most of the experimental data available is in the form of pressure traces, allowing for the code to be more widely used in comparisons and in simulating the output of various system configurations.

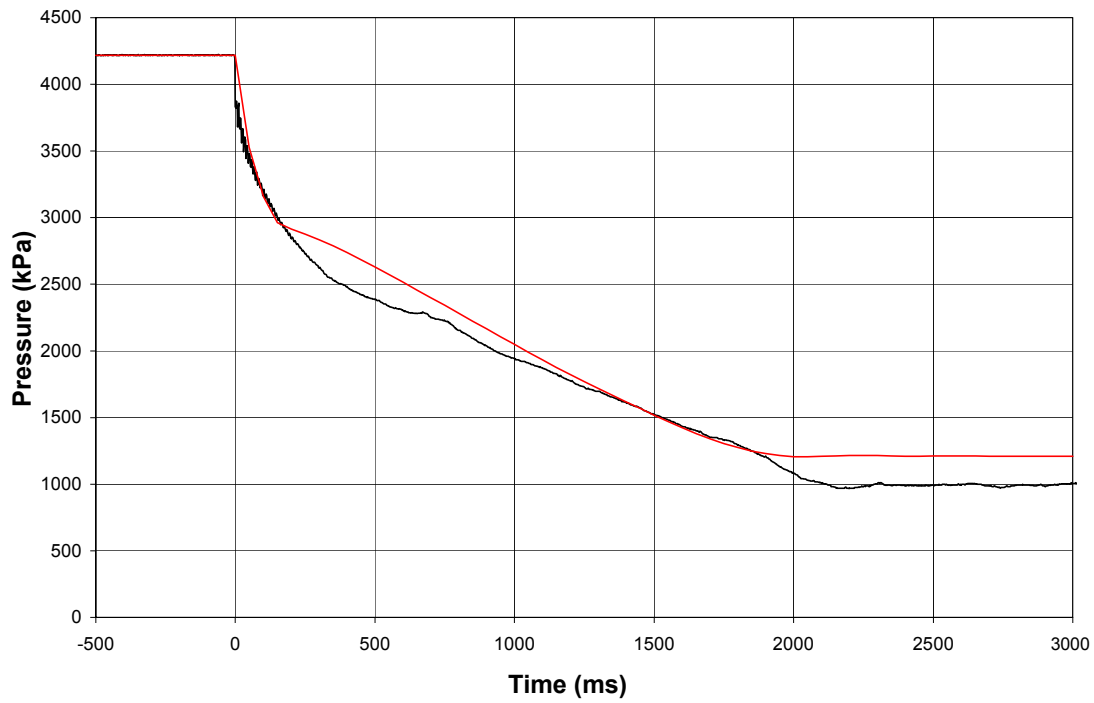


Figure 8-57. Comparison of Source Vessel Pressure for Experimental Run #5 (black) and Predictive Computer Code Data (red).

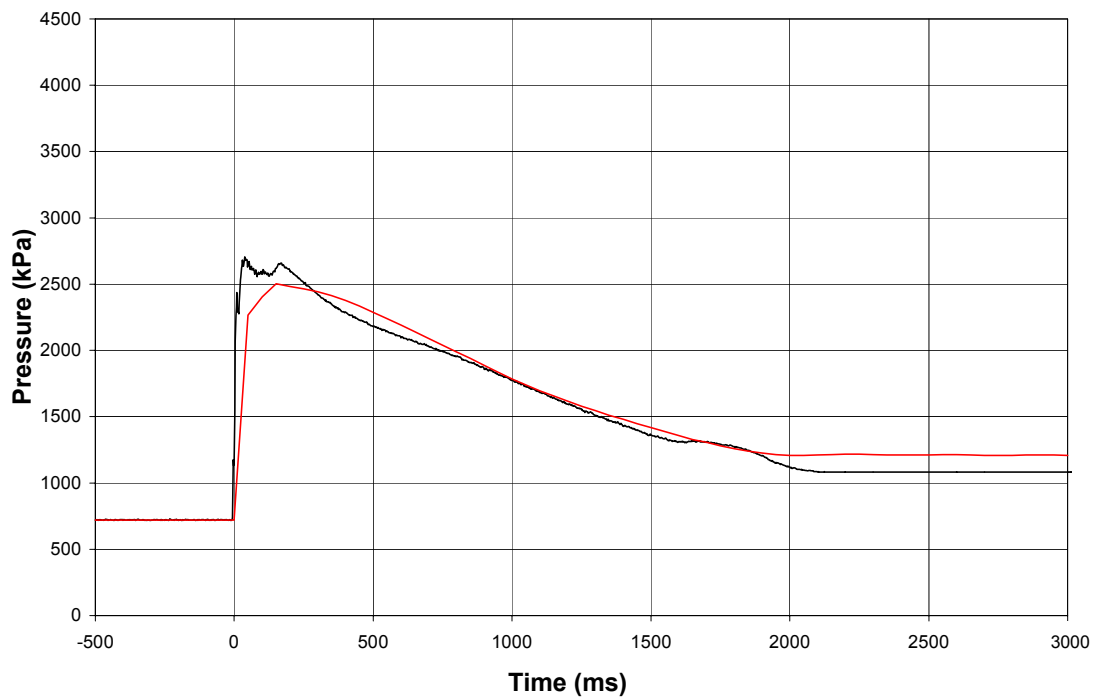


Figure 8-58. Comparison of Pipe Position #1 Pressure for Experimental Run #5 (black) and Predictive Computer Code Data (red).

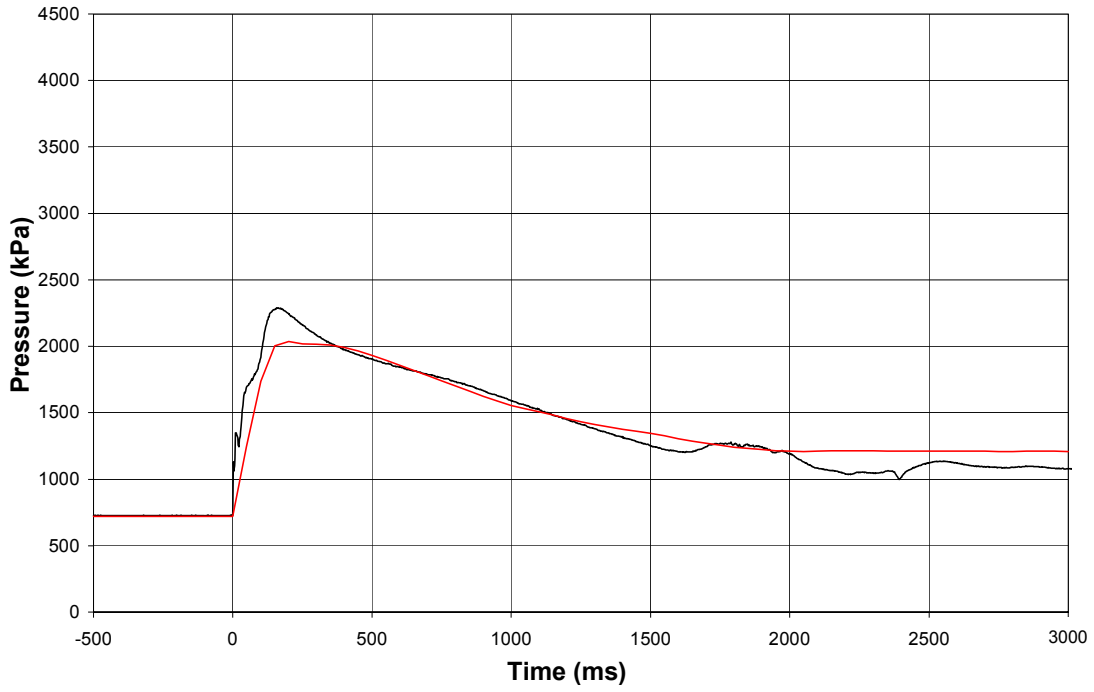


Figure 8-59. Comparison of Pipe Position #2 Pressure for Experimental Run #5 (black) and Predictive Computer Code Data (red).

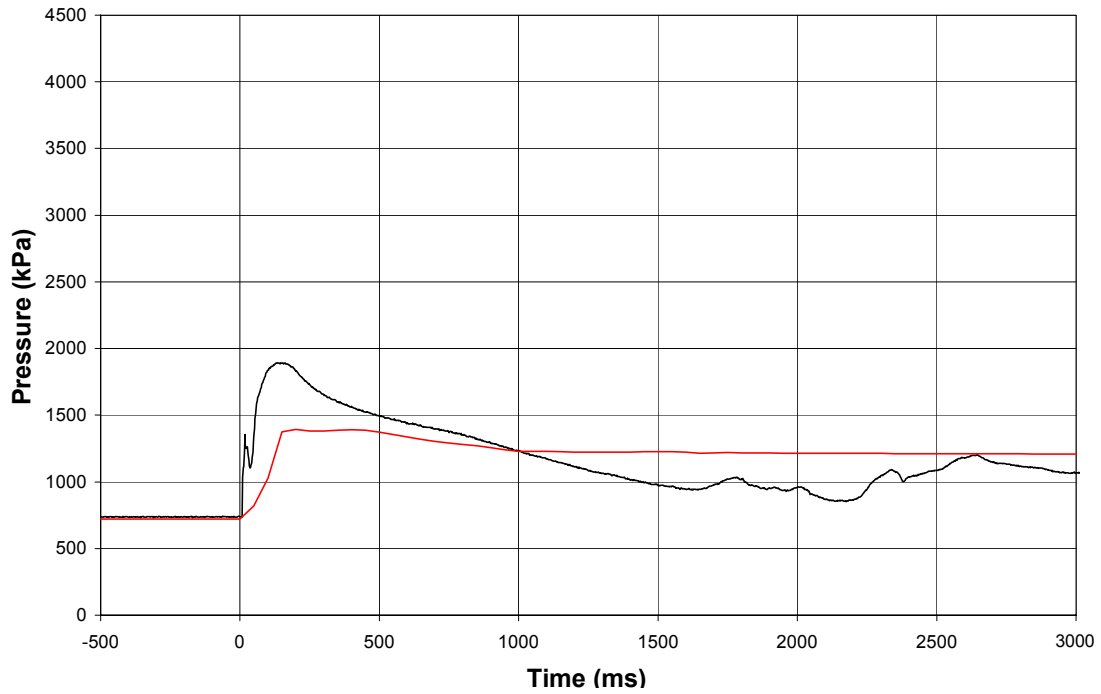


Figure 8-60. Comparison of Pipe Position #3 Pressure for Experimental Run #5 (black) and Predictive Computer Code Data (red).

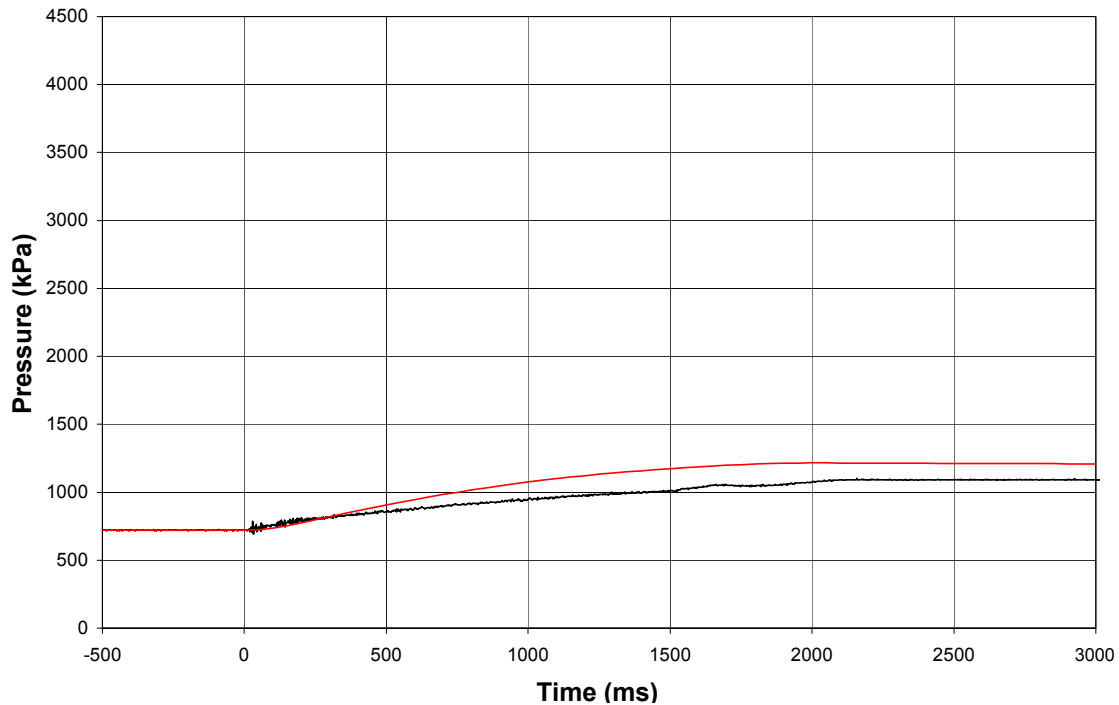


Figure 8-61. Comparison of Collection Vessel Pressure for Experimental Run #5 (black) and Predictive Computer Code Data (red).

While these comparisons were available with all of the runs conducted in this study, there were also special measurements made in some cases. For instance, experimental measurements of the pressure drop across different pipe fittings were conducted. While the prediction used a literature value for the friction loss factor associated with the fittings, comparison of the pressure drop across these fittings could still be made. This provides an indication of whether the literature values are accurate for a two-phase flow through different pipe configurations. Figure 8-62, Figure 8-63, and Figure 8-64 show the experimental data for Run #9 compared to the predicted data for the pressure drop across a capped tee, 90° elbow, and connecting union, respectively. This run used the simpler of the two alternative piping configurations (see Figure 8-19). The comparisons generally show reasonable agreement; however, the predicted pressure starts to fall earlier than the measurement. The experimental pressure trace exhibits a sudden drop when the liquid runs out at the initiation of the vapor/gas flow. Although the calculation does not predict a sudden drop in pressure at the end of the liquid flow, it shows an end of the run in the same general vicinity as the experimental trace, implying that it is most likely at the end of the liquid flow.

The last comparison made dealt with the temperature measurements. Since the predictive code does not consider heat transfer between the fluid and the piping, the only real temperature variation comes from any phase change in the system or any compression or expansion of the contents of the system. Specifically, degassing of the dissolved nitrogen and the adiabatic expansion of the nitrogen near the end of the run will be the main contributors. Because the code is not influenced by the ambient temperature of the system, it predicts a much lower temperature than the experimental measurements. The comparisons in this analysis are for experimental Run #16, which used HFC-125 as a test fluid. The largest temperature changes were experienced for this fluid.

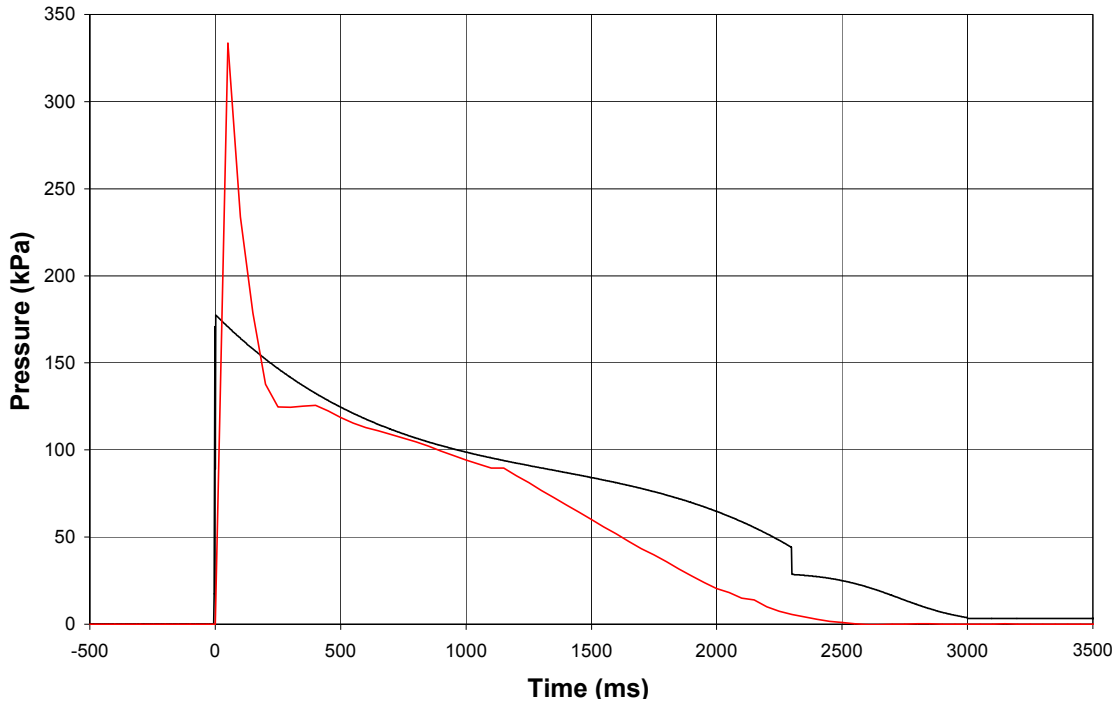


Figure 8-62. Comparison of Pressure Drop across a Capped Tee for Experimental Run #9 (black) and Predictive Computer Code Data (red).

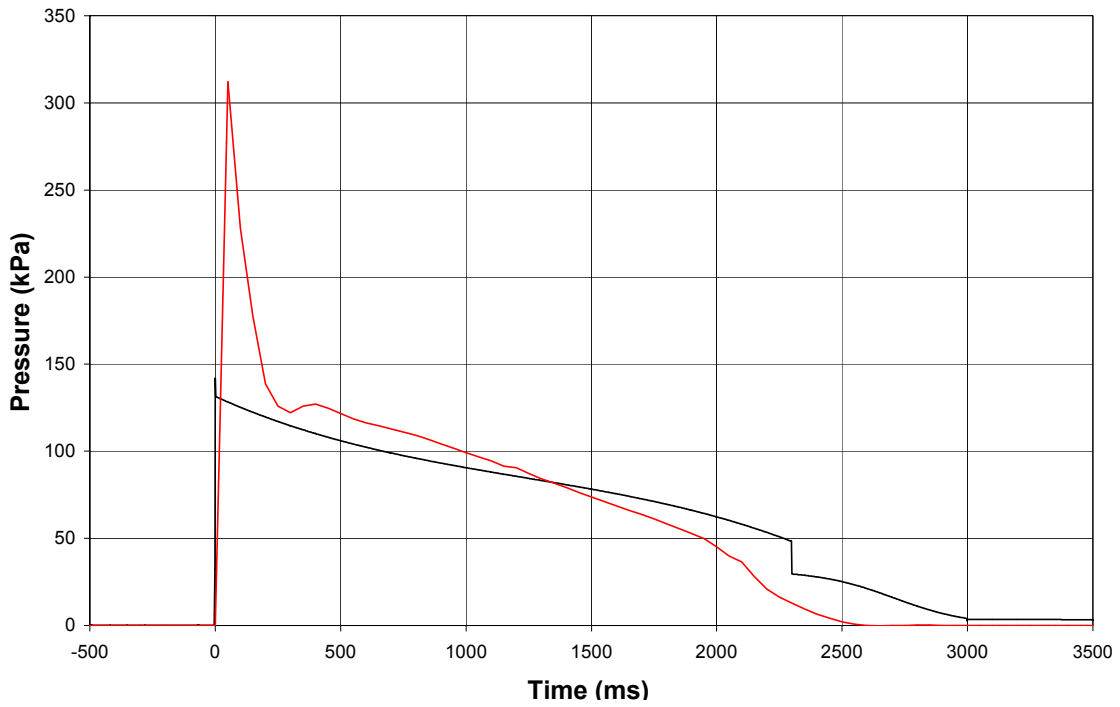


Figure 8-63. Comparison of Pressure Drop across a 90° Elbow for Experimental Run #9 (black) and Predictive Computer Code Data (red).

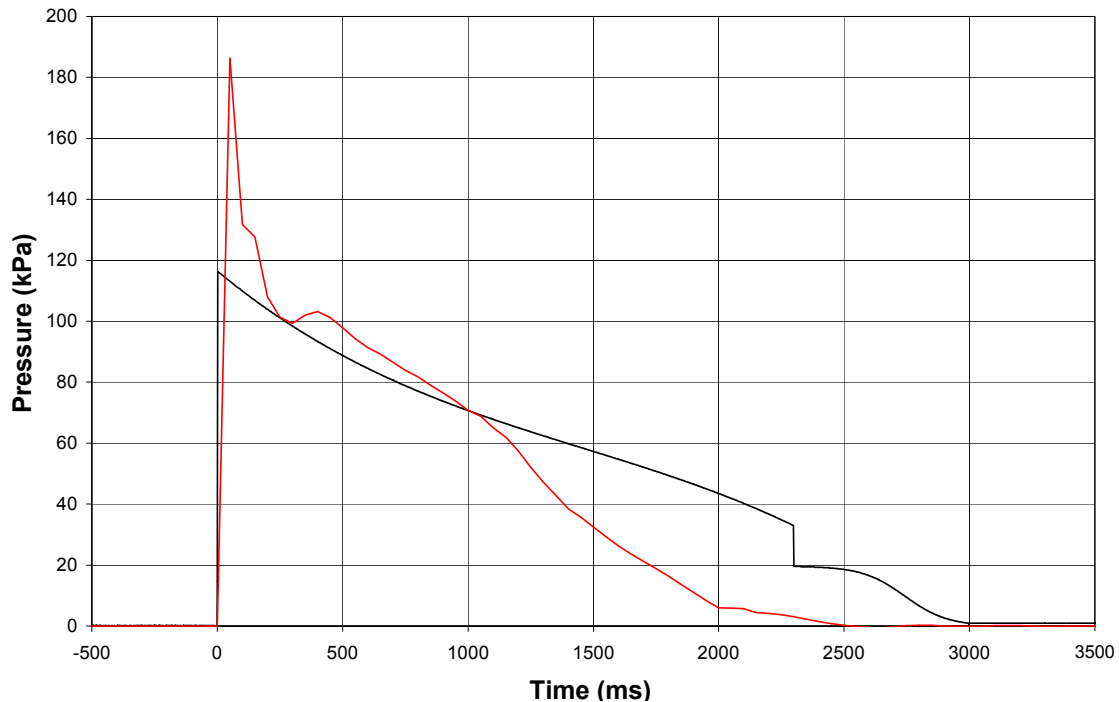


Figure 8-64. Comparison of Pressure Drop across a Union for Experimental Run #9 (black) and Predictive Computer Code Data (red).

In Figure 8-65, a comparison is made between the experimental measurements of the source vessel temperature using shielded thermocouple placed at the bottom of the vessel and immersed in the fluid and the fluid temperature predicted by the code. The trends in the predictions and measurements show good qualitative agreements. Figure 8-66 illustrates a temperature comparison between predictions and measurements for the pipe position #1 in the piping system. In this case, the differences between calculated and measured values are more pronounced than in the source vessel comparison. As expected, the heat transfer coefficient in the pipe is greater than anywhere else in the system, and the short-comings of excluding fluid-to-pipe heat transfer in the code are most noticeable in this region. A comparison of predicted and measured gas temperature in the collection vessel is shown in Figure 8-67. The initial temperature drop is due to the fact that the liquid is evaporating to raise the pressure to its saturation equilibrium value. This trend stops when the pressure rises high enough that there is no longer any need for the liquid to evaporate. Both the prediction and the experiment capture such trend in the temperature traces.

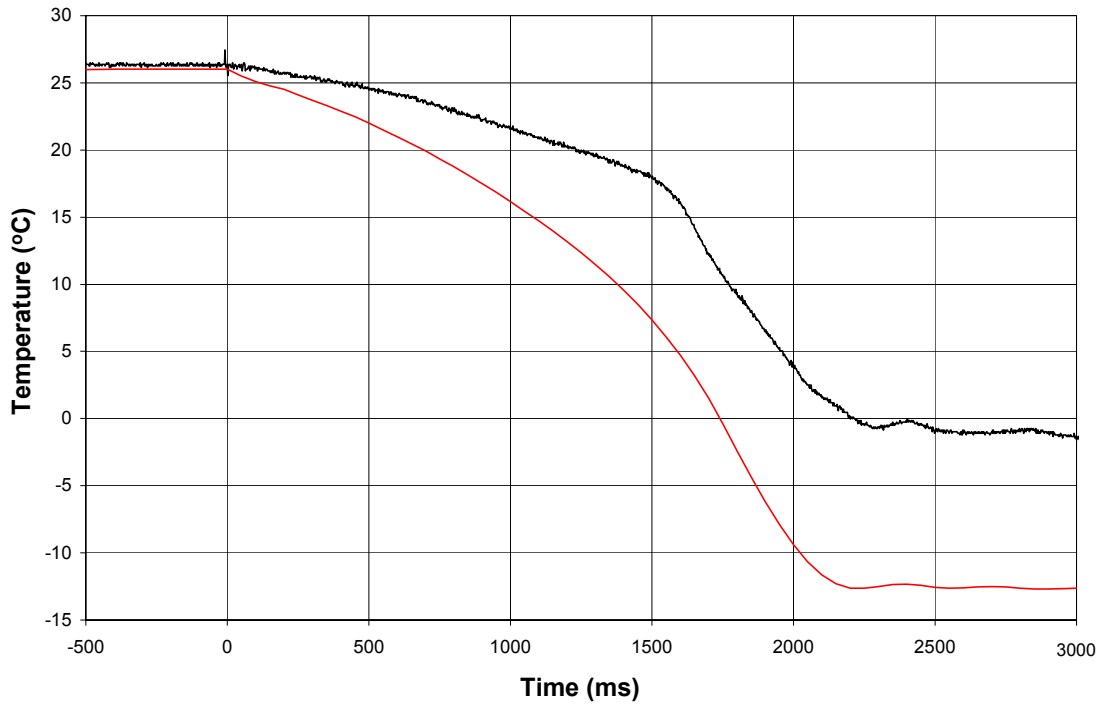


Figure 8-65. Comparison of Source Vessel Fluid Temperature for Experimental Run #16 (black) and Predictive Computer Code Data (red).

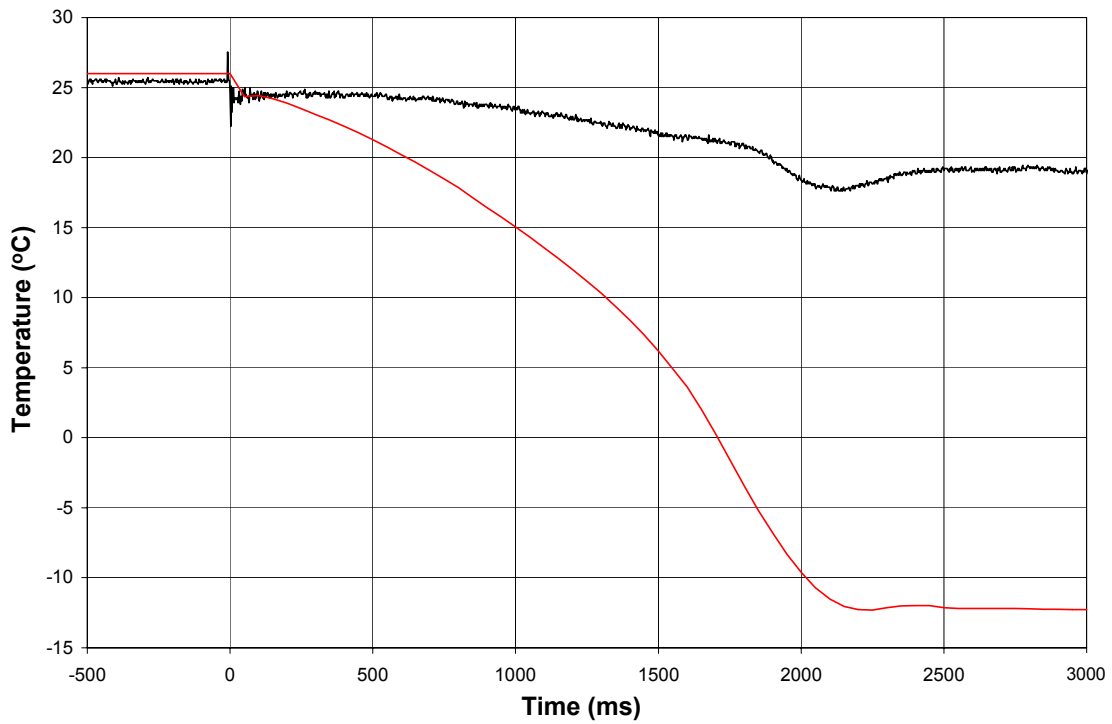


Figure 8-66. Comparison of Pipe Position #1 Fluid Temperature for Experimental Run #16 (black) and Predictive Computer Code Data (red).

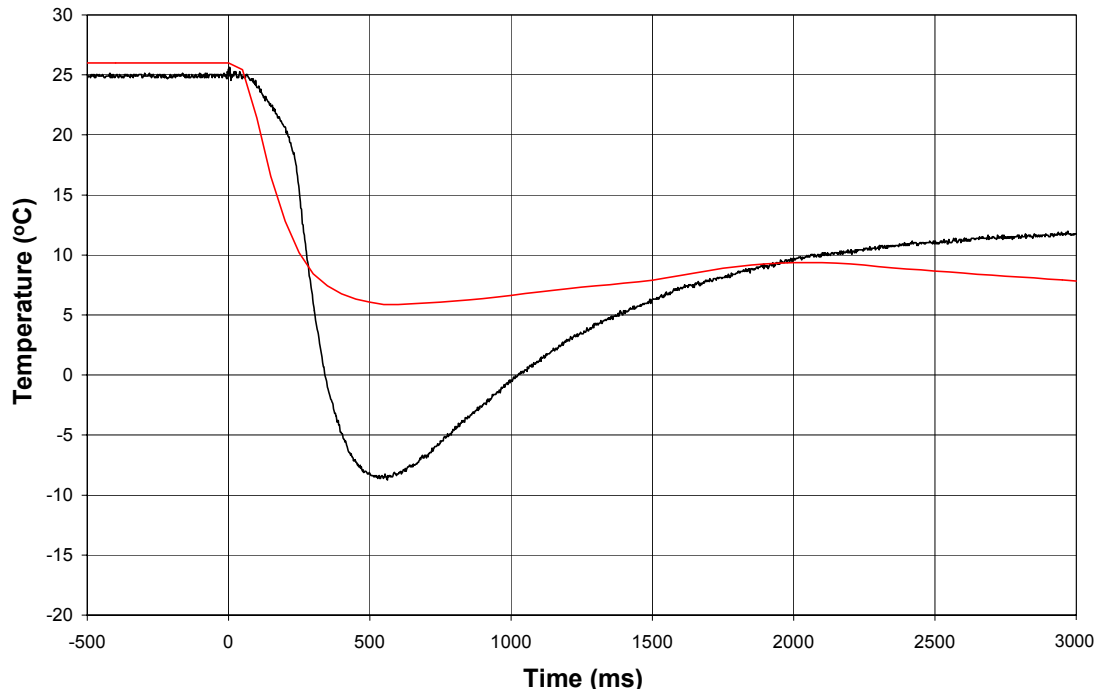


Figure 8-67. Comparison of Collection Vessel Gas Temperature for Experimental Run #16 (black) and Predictive Computer Code Data (red).

8.3.8 Assessment of Fluid Transport Model

Overall, comparisons between the predictions and the experimental runs generally show reasonable agreements. In most cases, the prediction gives good estimation of the physical characteristics of a two-phase flow in a model system. The code even handles two different test fluids with reasonable accuracy. It also predicted three different piping configurations well, demonstrating its versatility in modeling other potential systems. While these points support the code's robustness for use with suppressant systems, it must also be noted that there are a few limitations of the code. The most notable one is that the code would not always work for some initial conditions for a specific test fluid. This is most likely due to some limitation on the thermodynamics package. If this situation occurs, the user must slightly adjust the actual run condition in order to fall into a region of the thermodynamics package that will yield an output. For example, an error occurred before the program could complete the simulation for the experimental Run #5. However, changing the ambient temperature from 31 °C to 30 °C in the initial conditions enabled the simulation to completion. This was only a minor change, but it still made the simulation a bit cumbersome.

Another area that caused problems was to simulate low-pressure runs (2000 kPa to 2500 kPa, initial source vessel pressure). There were two problems which arose during these tests. The first was similar to the problem stated previously due to the thermodynamics package. These experimental runs (Runs #1 & #8) were conducted with low downstream pressures so that flashing could occur in the pipe directly after the start of the run and the actuation of the valve. The code would not accept these conditions to run the simulation due to the fact that it identified a non-equilibrium condition in the downstream areas. The downstream pressure had to be raised to a pressure closer to the saturation conditions of the test fluid in

order for the code to run. The other problem associated with these low-pressure test runs was the high fill level used in the source vessel. In experimental Runs #1, #8, #11, #14, and #18, a fill level of 80 % to 90 % was used to try and to reduce the amount of nitrogen present in the system. The hope was to keep the system pressure low enough to facilitate flashing of the suppressant during discharge. While the initial conditions did not cause the code to stop running with an error, it did provide unexpected results. For example, in Run #1, the total mass of test fluid (HFC-227ea) placed in the source vessel at the beginning of the run was about 4.9 kg. However, the code prediction never approached that value during the predicted discharge; it reached a final value of about 3.1 kg. It is unclear at this time why the code ran reasonably well with a fill level of about 60 %, instead of the test fill level of about 85 %. This problem would limit the applicability of the code to moderately fill conditions.

The last problem encountered executing the code was the high-pressure runs (4750 kPa to 5000 kPa, initial source vessel pressure). Once again, it was believed that the problem was caused by the properties package. The only way to get the code to run using these initial conditions was to lower the source vessel temperature considerably, while keeping the downstream temperature around the ambient value. Even then, the desired operating pressure could not always be reached. For example, in Run #6, the source vessel temperature was dropped from 31 °C to 2 °C with an initial source vessel pressure of 4860 kPa in place of 4910 kPa. In addition, the code tends to under-predict the total duration of discharge due most likely to the temperature dropping below the range of the thermodynamics package. Despite these observed problems, the code did a reasonable job in predicting the parameters (e.g., void fraction, mass inventory, etc.) for most runs with initial source vessel pressures from 3000 kPa to 4500 kPa and a fill level of about 65 %.

The FSP code can, in principle, be extended to include other candidate fluids that exhibit transient two-phase flow in piping system. The procedure outlined in Tuzla et al.⁷ for the incorporation of halon 1301, CO₂, HFC-227ea, and HFC-125 into FSP should be followed. In addition, a computational thermodynamic tool similar to REPROP or PROFISSY is needed to predict fluid properties for performing FSP calculations. Estimation of other input parameters like critical bubble radius and release rate of dissolved gas for the fluid of interest can be made through sensitivity analysis of these parameters in FSP calculations and comparison to experimental data.

8.4 DYNAMICS OF FLUID TRANSPORT IN CLUTTERED SPACES

8.4.1 Spray Transport Past Generic Clutter Elements

As discussed in Chapter 7, the NGP examined a wide range of potential candidates as alternatives to halon 1301. Should the transport of a chemical from the distribution plumbing to the fire site be inefficient, additional chemical (and the accordant larger storage bottle, piping, etc.) would be needed, an undesirable outcome. In particular, high boiling suppressants (which tend to have high heat extraction capacity) would be discharged in a liquid state, breaking into liquid droplets, and be entrained within the flow passing through the nacelle, impinging on various objects prior to reaching the fire zone. Since halon 1301 was so efficient, research into understanding the engine nacelle airflow offered little advantage. Today, however, a better understanding of the nacelle airflow and how it influences the spread of fires and fire extinguishing agents can have a large impact on the effectiveness of a halon replacement system. NGP research expanded the fundamental knowledge of spray interactions with

clutter (e.g., obstacles representing fuel and hydraulic lines, electrical wire bundles, etc.) to learn how well agents of low volatility might reach an unspecified downstream fire location.

Disimile and coworkers conducted experiments focusing on the ability of sprays to pass through a series of cylindrical obstacles, representing generic clutter, while moving in a turbulent coflow.³¹ Since only transport, and not flame extinguishment, was to be studied, water was used as the test fluid. A low-speed flow facility, with the test section air speed ranging up to 12.0 m/s, was modified for the current program. The major components of this facility include an inlet contraction, turbulence generator, test section, clutter section, and the return and separation plenum (Figure 8-68). The flow is from left to right. They collected three-dimensional velocity and diameter data at two locations downstream for nine combinations of clutter spacing and coflow airspeed.

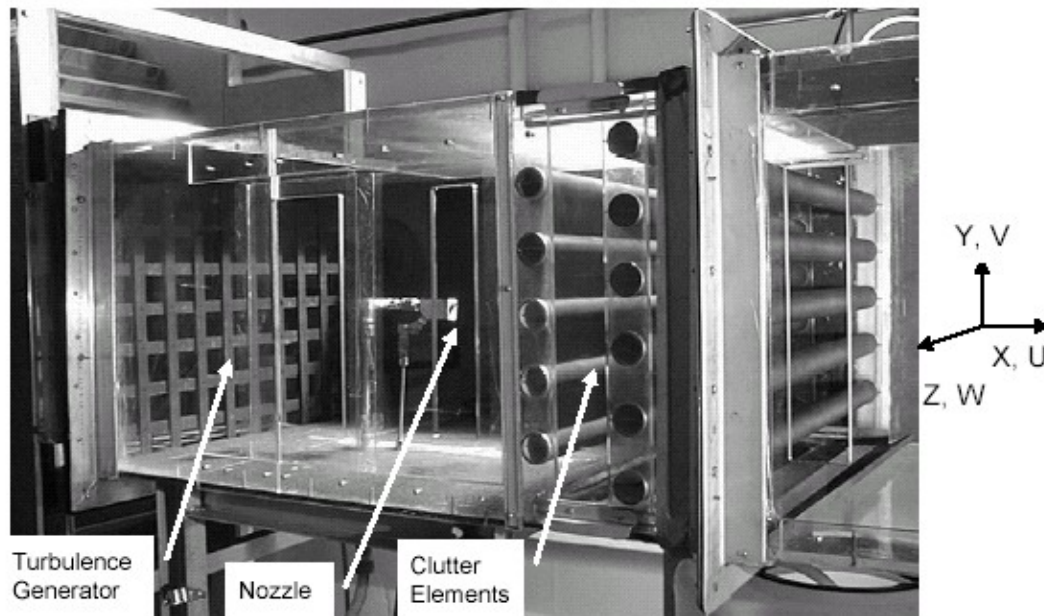


Figure 8-68. Zone A of the Test Section.

A large grid consisting of several 25.4 mm wide, 6.4 mm thick, sharp-edged flat steel slats, spanning the cross-sectional area of Zone A of the test section, was assembled in a checkerboard pattern with open cell dimension between the slats of 51 mm \times 51 mm. This grid is also visible in Figure 8-68. Velocity surveys using constant temperature anemometry were acquired downstream of the turbulence generator, at $x = 711.2 \text{ mm} \pm 0.8 \text{ mm}$. A wave-like distribution of the streamwise component of the mean velocity was observed, with velocities ranging from approximately 3.7 m/s to 5.0 m/s. Although general symmetry was observed, it appeared that the lower portion of the test section had a greater degree of unsteadiness. It is believed that the additional unsteadiness was a result of smoke generation supply tubes positioned at the entrance of the inlet contraction. In a similar manner, turbulent intensities were recorded and ranged between 10 % and 14 %.

The clutter package used in the current test series can be seen installed within Zone A of the test section (Figure 8-68). The clutter package consisted of 16 two-dimensional elements, spanning the width of the test section. These elements were cylindrical segments made from PVC. The elements had an outer

diameter D of $50.8 \text{ mm} \pm 0.8 \text{ mm}$ and were assembled to form three separate arrays with equally spaced rows of 5, 6, and 5 tube elements, separated vertically by $0.94 D$ between each cylindrical element. The streamwise spacing between each clutter array was variable, ranging in terms of element diameter, from $0.25 D$ to $2.00 D$ with an uncertainty of $\pm 0.06 D$.

The clutter arrangement was selected based on its geometric similarity to common elements found within aircraft engine nacelles. Many cylindrical elements fill the nacelle environment with various local densities. With the capability of varying the streamwise distance between each array of clutter elements in the chosen clutter package, the clutter densities found within larger aircraft engine nacelles was simulated.

A three-dimensional phase Doppler interferometer (PDI) was used to simultaneously acquire velocity components and the diameter of the liquid drops exiting the suppressant spray nozzle. Water and air are mixed by the dual fluid nozzle and travel toward the leading edge of the clutter package. The droplets not captured by the clutter package proceeded downstream, where their three-dimensional velocity and diameters were measured. The measurement volume of the PDI system was located at 2.0 and 5.5 clutter diameters downstream of the trailing edge of the clutter.

The spray nozzle water flow was set and maintained at $(17.1 \pm 0.4) \text{ L/min}$, with a corresponding nozzle water pressure of $(158 \pm 14) \text{ kPa}$. The water flow was monitored using a turbine type flowmeter positioned directly upstream of a pressure gage. The incoming air was regulated to a pressure of $(172 \pm 3) \text{ kPa}$. The test matrix consisted of 18 experimental conditions. This included 13 air speeds, five clutter densities, and two downstream measurement locations. Clutter package densities were varied by changes in the streamwise spacing between individual clutter arrays. Since the leading edge of the clutter package was fixed, changing the array spacing affected the location of the trailing edge of the last clutter element. Therefore, to maintain a fixed downstream location of the PDI measurement volume with respect to the trailing edge of the clutter, the PDI measurement volume had to be moved correspondingly.

To determine the volume of water transmitted through the clutter array as a function of the streamwise spacing of the clutter array and air speed, 13 air speeds were investigated ranging from 0.5 m/s to 6.5 m/s in increments of 0.5 m/s . To measure the volume of water passing through the clutter configuration accurately, a repeatable procedure for measuring the liquid water volume was followed. This included the water supply tanks being filled to the same initial starting volume of 303 L , the air speed and the nozzle air pressure set. A clock was then energized when the water pump was powered on such that the water flow through the nozzle was set to $(17.1 \pm 0.4) \text{ L/min}$. Water drops that wetted the clutter pooled on the individual elements and dripped down to a collection pan located beneath the clutter. Water droplets that passed through the clutter into Zone B were deposited within the return plenum. The volume of water collected directly under the clutter package was carefully measured, as was the water collected in the return plenum by using graduated containers.

Figure 8-69 shows the percentage of water recovered directly under the clutter package as a function of element spacing and air speed. The general trend of the data suggests that the volume of the liquid collected decreased with increasing air speed. In fact, above 4.5 m/s less than 5 % of the liquid was captured, and the differences between the five clutter densities converged. However, with the air speed set to 0.5 m/s , the amount of water collected under the clutter ranged from 61.25 % (at $0.25 D$ spacing) to 37.50 % (at $2.0 D$). As the spacing between the individual clutter rows was reduced, the amount of water

captured increased. Specifically, as the streamwise spacing was reduced from $2.0 D$ to $0.25 D$, the captured water increased to over 50 %.

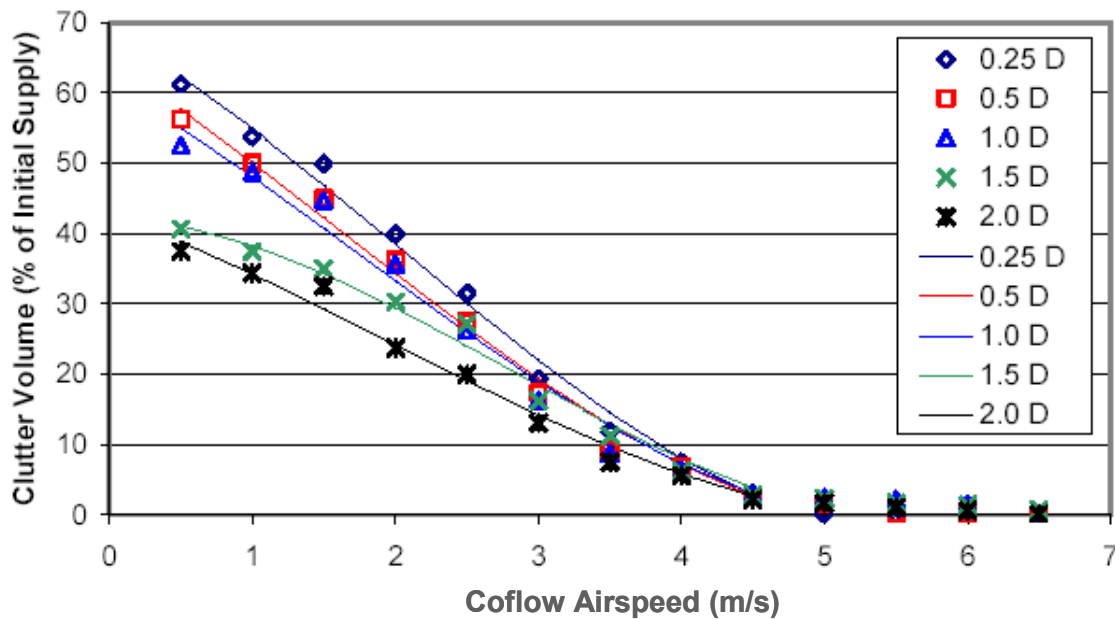


Figure 8-69. Clutter Recovery vs. Airspeed.

Likewise, Figure 8-70 indicates the amount of water collected in the return plenum as percent of the initial volume. All five clutter densities are represented in this figure. The volume collected in the plenum increases as the air speed increases. It can be seen that the volume recovered in the plenum approaches 100 % as the air speed increases.

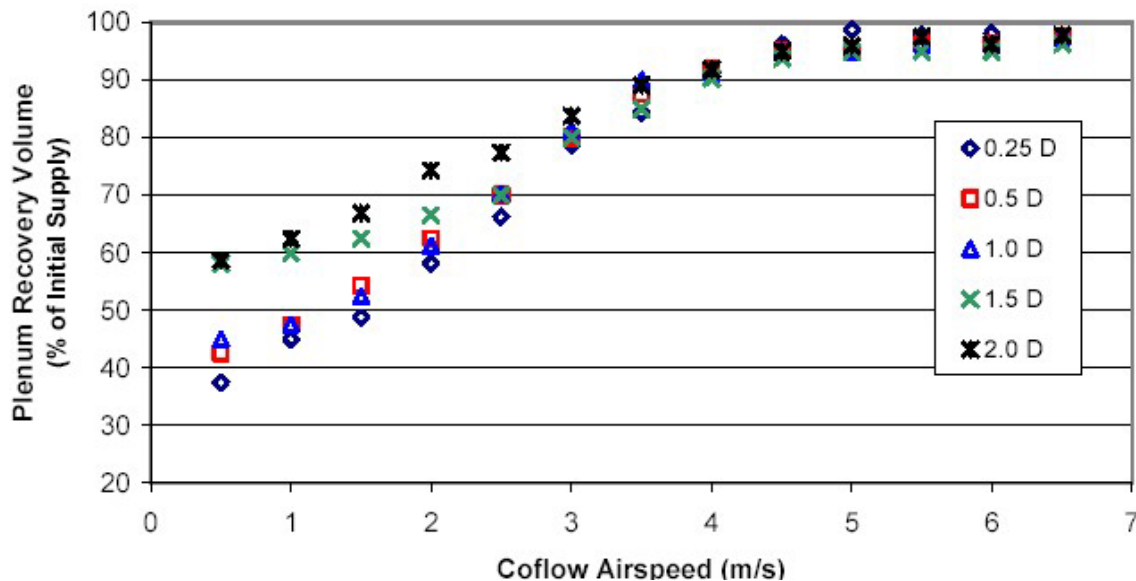


Figure 8-70. Plenum Recovery vs. Airspeed.

During the test evaluation of five clutter spacings and 13 air speeds, the percent of unaccounted water volume was determined. In all cases, the difference was random and less than 4 %. As a measure of repeatability, no less than 96 % of the total supply volume was recovered in the combined clutter and plenum return recovery tanks.

The results of these experiments clearly show the effect of cylindrical clutter elements on the transport of liquid droplets and provide benchmark data to develop first-generation computer models to aid in the design of fire suppression systems for aircraft engine nacelles. Although this work only addresses round elements of uniform size and distribution, it provides a framework to generate a database for examining the effects of different size, geometry, and density of clutter elements as well as different levels of turbulence on droplet transport for nacelle applications.

8.4.2 Spray Interaction with Unheated and Heated Clutter Elements

For the next level of understanding, Presser and coworkers injected liquid fire suppressants into a well-characterized, homogenous, turbulent flow field, and investigated the droplet transport processes under a variety of conditions, as well as the interaction of the spray with different obstacles.³² Also of interest was determining whether droplets rebounded and/or shattered off the surface of an obstacle.

The experimental arrangement is shown in Figure 8-71. The experiment was oriented horizontally to enable estimating the mass of liquid agent impinging on the obstacle, the mass that dripped off the obstacle, and the mass transported past the obstacle. This geometry also prevented liquid droplets downstream of the obstacle from falling back upstream into the oncoming stream.

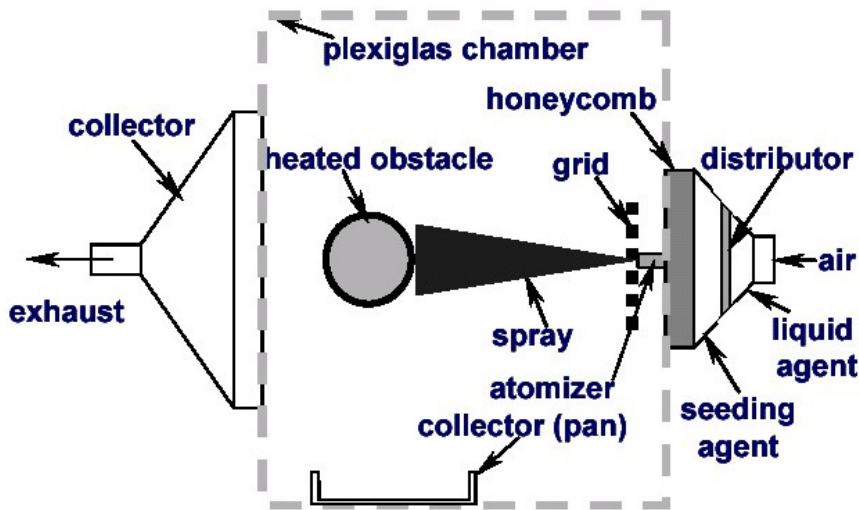


Figure 8-71. Heated Cylinder Test Section.

The initial agent was water and was supplied to the flow field with a 60° hollow-cone pressure-jet atomizer. In the octagon-shaped PMMA chamber, the front face supported the inlet passages for the liquid agent and air, and the back face supported the exhaust passage, which served to form a closed system with defined boundaries. A honeycomb layer was used to straighten the air flow, which was co-positioned around an injector for the agent. Grid-generated turbulence was imposed on the air stream by placing a square layer of wire mesh screen downstream of the honeycomb. For these experiments, the incoming air was directed entirely through a distributor plate with steel wool, circular cross-sectional area

of the honeycomb, and then through wire mesh screen (placed 25 mm downstream of the honeycomb), as shown in Figure 8-71. The face of the liquid atomizer was placed flush with the upstream side of the grid, and centered within one mesh cell so that the liquid spray would be unimpeded by the grid. The stepper-motor-driven traversing system translated the entire assembly, and permitted measurements of the flow field properties at selected locations downstream of the injector. Measurements included particle image velocimetry (PIV), PDI (to obtain spatial and temporal profiles of the size and velocity distributions), and visualization of the flow field. Measurements in the spray and flow field were carried out upstream and downstream of the obstacles.

Measurements were carried out with two obstacles, an aluminum cylinder and a more complex body-centered cube (BCC) arrangement of wooden spheres and connecting posts. (See Figure 8-72 and Figure 8-73, respectively.)

The cylinder had a diameter of 32 mm (305 mm in length), which was chosen because its diameter was larger than the integral length scale of turbulence. The cylinder was heated to study the effects of a heated surface on droplet vaporization and transport, as a droplet approached the heated surface. A hole was bored through the center for placement of a 250 W cartridge heater. The rod was also cut into two halves and 1 mm deep channels bored along one segment for placement of five K-type thermocouples. The thermocouples had an inconel sheath, ungrounded, and 0.8 mm in diameter (305 mm long). The thermocouples were placed in a cross pattern in the center of the rod (each separated by a distance along the surface of 6.4 mm, with the thermocouple junctions placed about 3.2 mm of the surface with bored holes at each location). The central thermocouple was used for temperature control of the heater, which was positioned behind the thermocouples.

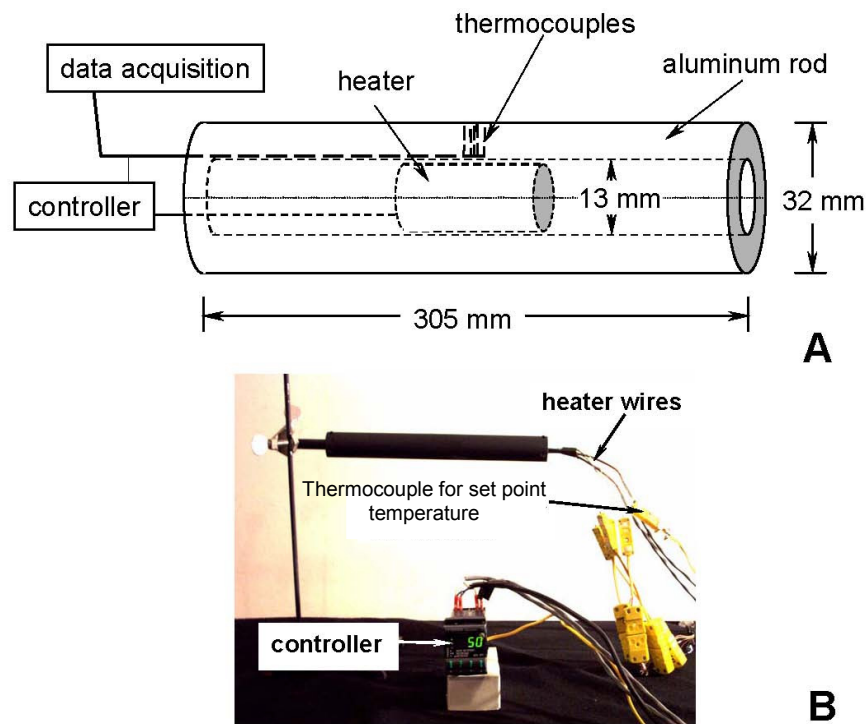


Figure 8-72. Heated Cylinder. (A) Schematic and (B) Front View.

The BCC was composed of nine wooden spheres with a nominal diameter of 28 mm, all interconnected with posts, as shown in Figure 8-73. The blockage ratio, or obstructed cross-sectional area for an equivalent area encompassing a face of the BCC, was about 64 %. The obstacles were placed nominally 182 mm downstream of the honeycomb, and centered with the atomizer centerline.

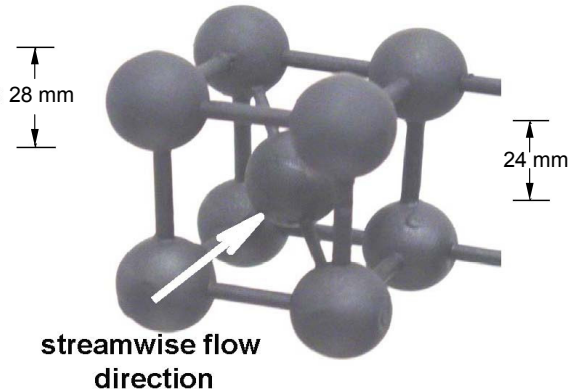
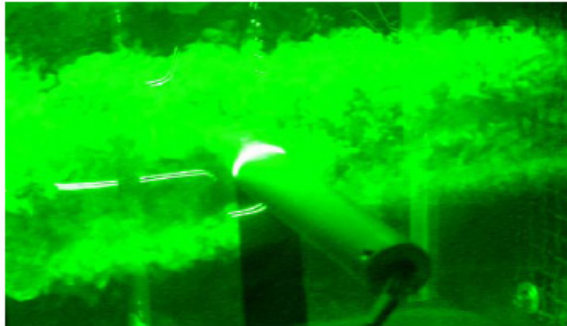


Figure 8-73. Body-centered Cube of Spheres.

PIV measurements were carried out in the droplet-laden, homogeneous turbulent flow over both the unheated and heated cylinder, and body-centered cube arrangement of spheres. Transport of both water droplets and seed particles was characterized upstream and downstream of these obstacles. Data were recorded for the cylinder at ambient temperature and after being heated to 150 °C to estimate the effects of the hot cylinder surface on droplet transport. The results indicated that smaller droplets were entrained into the recirculation region behind the cylinder while the larger droplets impacted the cylinder surface, accumulated and dripped off, and/or rebounded off the surface and dispersed radially outward into the free stream. The Weber number was too low to lead to droplet shattering. Significant spray cooling of the surface was observed for the heated cylinder, in addition to the presence of a vapor stream downstream of the cylinder along the shear layer region between the recirculation zone and free stream. Surface cooling that resulted from spray impingement was around 50 % of the preset cylinder temperature. For the BCC (with a blockage ratio of about 64 %), there was both transport of droplets and seed particles around and through the BCC, as well as significantly more liquid accumulation and dripping than for the cylinder.

The droplet-laden flow field over each obstacle was recorded with a digital movie camera at 9 frames/s. Examples of the observed droplet/particle transport processes are shown in Figure 8-74 for (a) seeded only and (b) droplet only flow over the unheated cylinder, and (c) combined droplet and seeded flow over the BCC. The seed was entrained in the turbulent flow field (see Figure 8-74A) and a relatively high concentration of particles was observed in the wake behind the cylinder. On the other hand, the droplets in the center of the spray were found to impinge on the surface of the cylinder while those droplets at larger radial positions were transported around or past the cylinder with an increased radial component of velocity (see Figure 8-74B). Few droplets were observed behind the cylinder in its wake. Droplets that impinged and wetted the cylinder surface dripped off at a rate of approximately one drop every 5 s. The transport of droplets through the BCC (see Figure 8-74C) was interesting in that both the spheres and connecting rods (that simulate cylinders) block the droplets, while the flow field traversing through the obstacle provided an unobstructed path for the entrained droplets. Dripping was observed from each sphere at a rate of approximately 1 droplet/s. If one assumes that droplets fall off each sphere at this rate, one can determine that this liquid represents approximately 4.5 % of the inlet water flow (assuming a

dripped droplet diameter of 8.5 μm , which was an estimated largest droplet size observed from digital movies). Although the BCC had more dripping of liquid than the cylinder, the major portion of the spray was still able to traverse the obstacle.



A Figure 8-74. Photographs of Seed/droplet-laden Flow Fields around Obstacles.

A: Unheated Cylinder; B: Heated Cylinder; C: Body-centered Cube of Spheres. Flow Direction is from Right to Left.

B

C

The above-mentioned laser sheet images indicated that dispersion of droplets/particles around the obstacle was dependent on its size. Comparison of the PIV velocity fields obtained with water droplets from the pressure-jet atomizer and 1 μm size seed particles formed from the fogging device also supported this finding. For example, the three components of droplet velocity for the flow over the unheated cylinder are presented in Figure 8-75. In this figure, three cases are presented that represent the flow with the seed only, both seed and spray, and spray only. The black circle represents the position and size of the cylinder. The black contour lines represent stream traces (i.e., direction) of the in-plane velocity vectors. Comparison of the two cases with spray to the seed-only case indicated that the recirculation zone was somewhat larger for the spray cases. Larger size droplets required a longer distance to interact with the turbulent flow field, reduce their higher momentum, and be entrained into the recirculation zone, if at all. The stream trace (contour lines) also showed an unexpected pattern behind the cylinder near the stagnation point. Instead of presenting closed loops that indicate a time-integrated recirculating pattern,

the contours appear to emanate from the stagnation region. One possible explanation is that there is a strong spanwise flow along the length of the cylinder. It appeared to be generated by the cylinder and may be related to the finite cylinder length (with an aspect ratio of about 10:1).

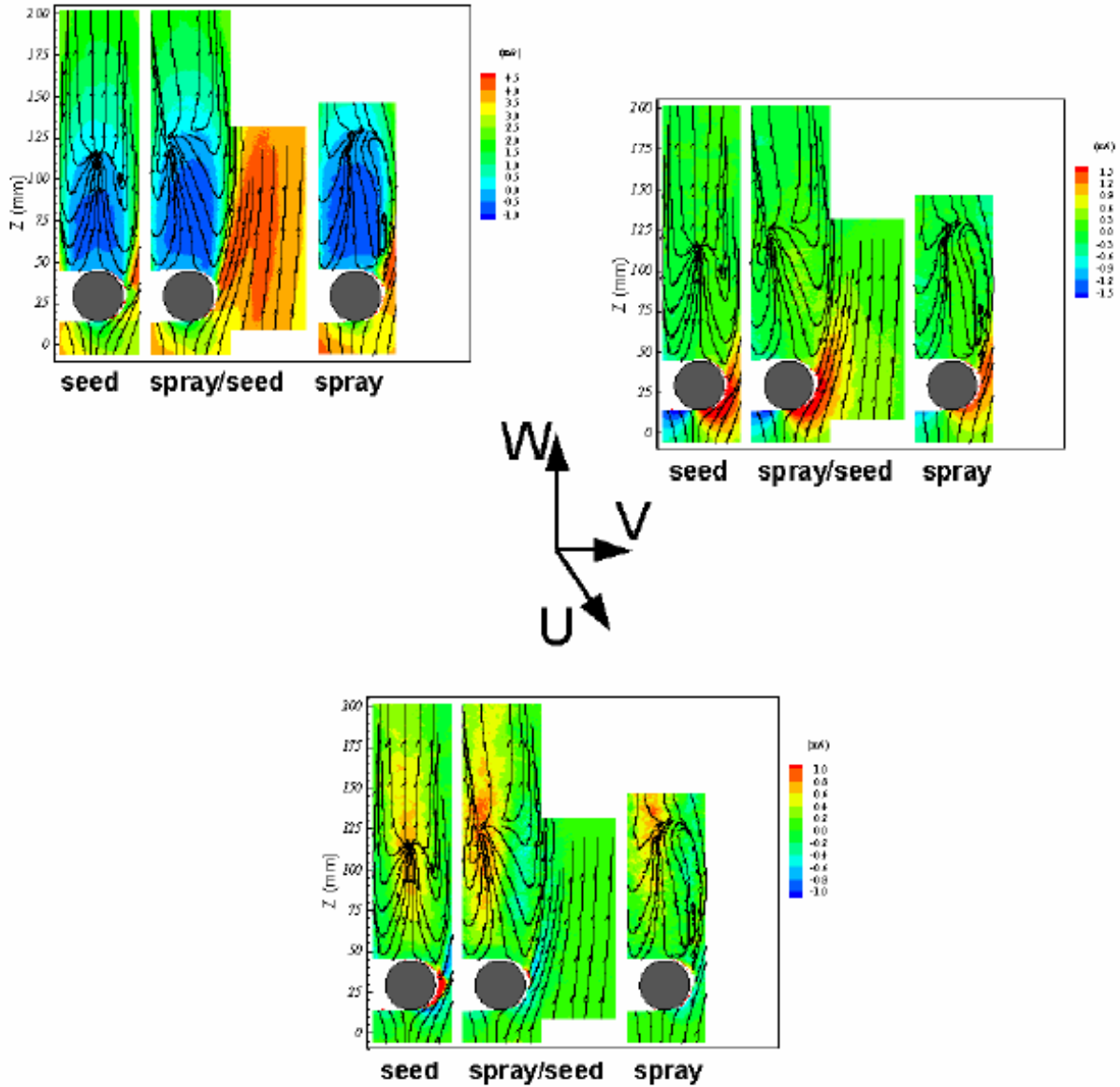


Figure 8-75. Variation of the Mean Streamwise and Cross-stream Velocities with Downstream Distance for the Unheated Cylinder. Contours are the Stream Traces of the In-plane Vectors Obtained from the Axial and Radial Components of Velocity.

Figure 8-76 presents the velocity field around the BCC for the combined spray/seed case. Although the configuration was more complicated, there were still similar features to the cylinder case. The flow accelerated around the spheres and there was reverse flow in the wake region. In addition, the presence of a cross-stream component of the flow was evident around the spheres. This cross flow may be a result of

the three-dimensional nature of the spheres and flow field, and the transport of entrained droplets and aerosol particles through convoluted pathways of this obstacle.

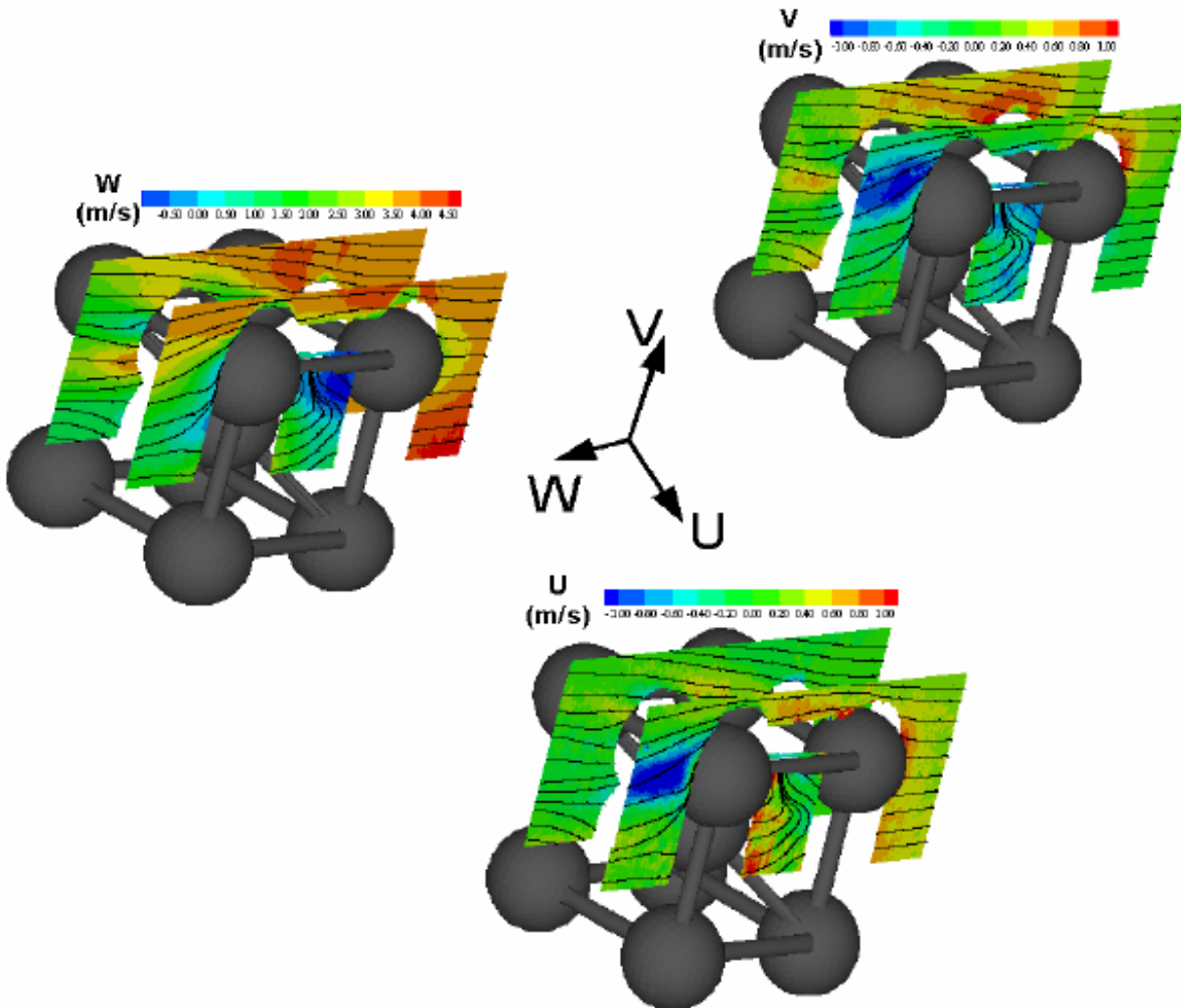


Figure 8-76. Variation of the Mean Streamwise and Cross-stream Velocities with Downstream Distance for the Body-centered Cube of Spheres. Contours are the Stream Traces of the In-plane Vectors Obtained from the Axial and Radial Components of Velocity.

Droplet Size and Velocity Distributions

The aforementioned results indicated that droplet surface impact, vaporization, and transport behind the cylinder were dependent on droplet size. Measurements of spatially and temporally resolved droplet size and velocity distributions in the upstream and downstream vicinity of the cylinder, using PDI, were needed. Three agents with different boiling points were examined: water (with a boiling point of 100 °C), HFE-7100 (with a boiling point of 61 °C) and HFE-7000 (with a boiling point of 34 °C). Several strategies may be used to detect size dependent effects in regions where droplets rebound or vaporize. For example, a droplet near the upstream surface of the cylinder with a negative streamwise velocity

(i.e., a droplet transported against the flow) would be indicative of a droplet rebounding off of the cylinder surface, and thus PDI would be used to obtain the associated droplet size. If the size distribution near the heated cylinder surface is devoid of relatively smaller size droplets, as compared to other locations away from the cylinder, then this result may be indicative of the effects of vaporization. These strategies were used in interpretation of the measurements.

Phase Doppler techniques involve creating an interference pattern in the region where two laser beams intersect, and results in a region consisting of alternating light and dark fringes. The region where the laser beams intersect is called the probe volume or sample volume. Due to the interference pattern, a droplet passing through the probe volume scatters light that exhibits an angular intensity distribution, which is characteristic of the size, refractive index, and velocity of the droplet. For a droplet with known refractive index, the size and velocity can be determined by analyzing the scattered light collected with several photomultiplier tubes (PMT). The PDI is a single-point (or spatially resolved) diagnostic instrument in that it obtains information about the spray at a single point in space. The PDI is also a single-particle instrument in that information is obtained for only one droplet at a time. This offers advantages over integrating techniques because the characteristics of a particular droplet (size, velocity, etc.) can be recorded and the data can be separated into classes (size classes, velocity classes) to further characterize the spray system.

The experiments were conducted using a two-component phase Doppler interferometer with a Real-time Signal Analyzer (RSA) available from TSI, Inc. A 5 W argon ion laser, operating in multi-line mode, was used as the illumination source. The blue (wavelength = 488 nm) and green (wavelength = 514.5 nm) lines of the argon ion laser were separated by beam conditioning optics, and focused by the transmitting optics to intersect and form the probe volume. The transmitting optics were coupled to the beam conditioning optics, using fiber optic cables to permit the transmitter to be located near the experiment. The front lens on the transmitter had a focal length of 500 mm. The green and blue beams had a beam separation distance of 39.9 mm and 40.2 mm, fringe spacing of 6.45 mm and 6.07 mm, and beam waist of 164 mm and 155 mm, respectively. Frequency shifting was set at 40 MHz. The receiver was located at a scattering angle of 30° measured from the direction of propagation of the laser beams. To accommodate the horizontal orientation of the experimental apparatus, the transmitter and receiver were positioned in a vertical plane, as shown in Figure 8-77. Due to the large size of the receiver, the transmitter was positioned with the laser beams angled at 30° to the cylinder, which required correction of the cross-stream velocity. The front lens on the receiver had a focal length of 1000 mm. The spacing for the three PMT detectors (A, B, and C) that were used to carry out the sizing measurements was 34.8 mm for detectors A and B, and 101 mm for detectors A and C. A 150 mm slit aperture was located within the receiver to limit the length of the probe volume.

The measurements were carried out at several radial (R , cross-stream) positions and over a range of axial (Z , streamwise) positions upstream and downstream of the cylinder. Figure 8-78 illustrates the measurement grid that was used and the location of the cylinder relative to the grid mesh. Measurements were carried out from approximately 50 mm upstream of the cylinder to a downstream position of 100 mm. An increment of 2.5 mm was used for $-25.4 \text{ mm} < Z < 38.1 \text{ mm}$, and an increment of 12.7 mm for all other axial positions. In the radial direction, measurements were carried out in increments of 5 mm from 0 mm to 20 mm in the upper hemisphere (i.e., in the positive radial direction). Data were not obtained immediately downstream of the cylinder (i.e., for $\approx 25 \text{ mm} < Z < 14.6 \text{ mm}$) because the signals were too low to detect any droplets.

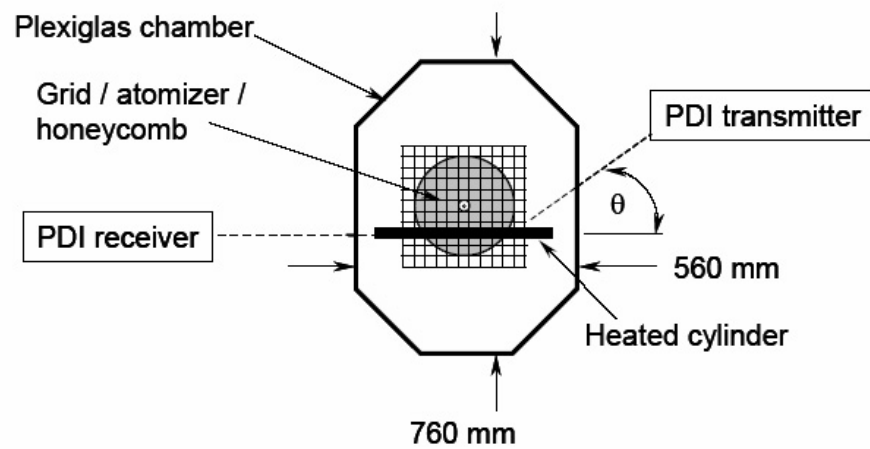
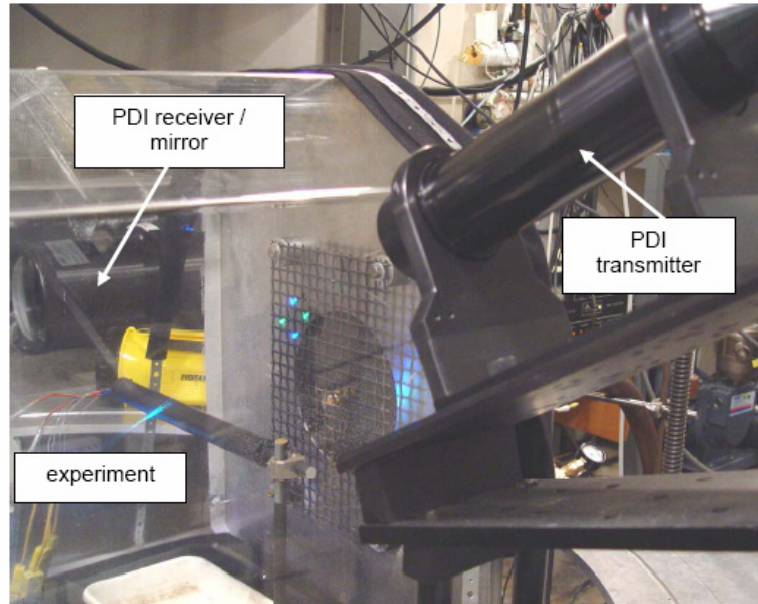


Figure 8-77. View and Schematic of the Experimental Arrangement with the Laser from the Phase Doppler Interferometry System.

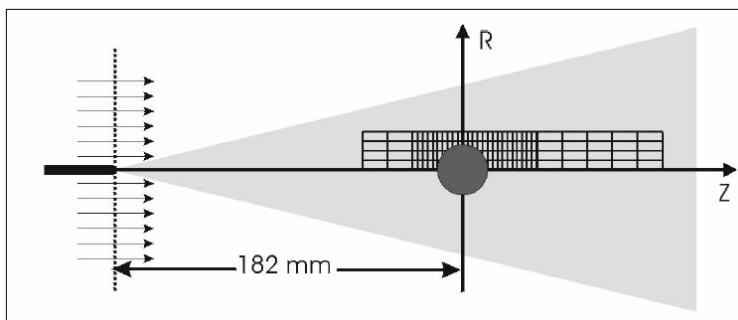


Figure 8-78. Schematic of the Measurement Grid around the Cylinder.

The droplet-laden flow field over both the unheated and heated obstacle was recorded with a high-resolution digital camera (providing both still-images and movies at 9 frames/s). Droplets were observed in the center of the spray impinging on the surface of the cylinder and dripping off at the bottom of the cylinder, while those droplets at larger radial positions were transported around the cylinder. Movies obtained with a high-speed digital camera at 1000 frames per second indicated that many impinging droplets rebounded off the surface and into the free stream. More rebounding droplets were observed when the air velocity was zero. Few larger size droplets were observed behind the cylinder in its wake, but were abundant with the smaller size aerosol seeds that were introduced to the flow through the air stream. There was no evidence of secondary breakup of the droplets, which was expected because the Weber number was much smaller than the critical value for droplet shattering.

When the cylinder was heated to 150 °C (i.e., well above the boiling point of water), the droplet-laden flow over the cylinder appeared to be similar to the unheated case except along the shear layer downstream of the cylinder. In this region, as mentioned earlier, a vapor layer formed which was presumed to be the result of vaporization of the liquid that wets the hot surface. It was expected that vaporization of liquid near the cylinder surface may influence locally the transport of droplets behind the cylinder by vaporizing the smaller size droplets, and thus was a focus of this segment of the investigation.

A solid-cone nozzle was used to increase the number of droplets impinging on the cylinder surface (a hollow-cone atomizer was used earlier with PIV measurements). It was observed that drippings off the cylinder occurred at a rate of approximately 6.5 mL/min for the unheated cylinder, while there was no dripping for the heated cylinder due to droplet vaporization. It was also observed by the PDI laser beam intensity that the concentration of droplets behind the cylinder was significantly reduced. For the heated cylinder, the cylinder surface temperature varied significantly with time after the spray was introduced to the flow field. However, it is unknown at this time whether these changes are attributable to time-varying changes in the response time of the cylinder heater during droplet impingement, or to some other systemic issue.

The PDI was used to provide information on: (1) droplets rebounding off the upstream face of the cylinder, (2) vaporization of droplets near the heated cylinder, (3) droplet sizes entrained into the recirculation region behind the cylinder, and (4) the effect of agent boiling point on droplet transport. The unheated cylinder results for the Sauter mean diameter (D_{32}) and droplet mean streamwise component of velocity (U) are presented in Figure 8-79. The rectangle located on the abscissa at an axial position of $Z \cong \pm 14.6$ mm represents the location of the cylinder. The gap in the data for the radial positions $R = 0, 5$ mm, and 10 mm indicates the presence of the cylinder. For Figure 8-79A, the general trends were: (1) a decrease in mean size on the downstream side of the cylinder, as compared to the upstream side, and (2) an increase in mean size with increasing radial distance from the central plane of the cylinder. The latter was indicative of the presence of more smaller size droplets near the center of the spray, as exemplified by the results obtained at the upstream axial position of $Z = -50$ mm, which was attributed to the design characteristics of the atomizer. For the droplet mean streamwise velocity (Figure 8-79B), the values increased with decreasing radial position at the upstream position of $Z = -50$ mm. These higher velocities correlate with the smaller droplet mean size near the center of the spray. As droplets approach the upstream surface of the cylinder, there is a decrease in the streamwise velocity component and an increase in the cross-stream component. There is an increase in the droplet streamwise velocity over the cylinder for $R = 15$ mm, and 20 mm, which is also characteristic of the accelerated flow over the cylinder, as described earlier. At locations near the upstream surface of the cylinder, negative values for the

streamwise velocity are detected (see Figure 8-80), which may be indicative of droplets rebounding off the surface. However, positive values of velocity are obtained for the abundance of droplets, which indicates that these impinging droplets either adhere to the cylinder surface or rebound at an angle that maintains their momentum in the downstream direction over the cylinder. Note that the symbols in Figure 8-80 are sized according to the actual droplet diameter.

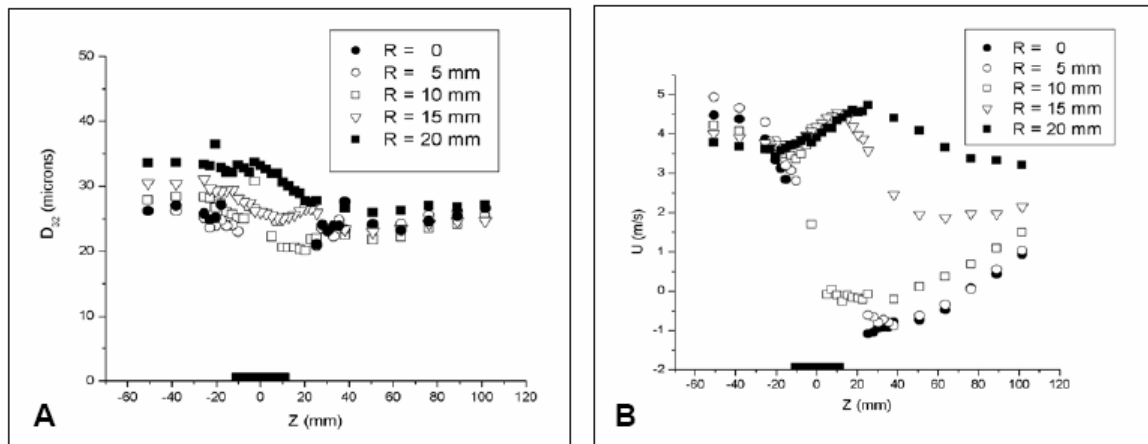


Figure 8-79. Variation of Water Droplet (A) Sauter Mean Diameter and (B) Mean Streamwise Velocity with Streamwise Position at Different Cross-stream Positions for the Unheated Cylinder.

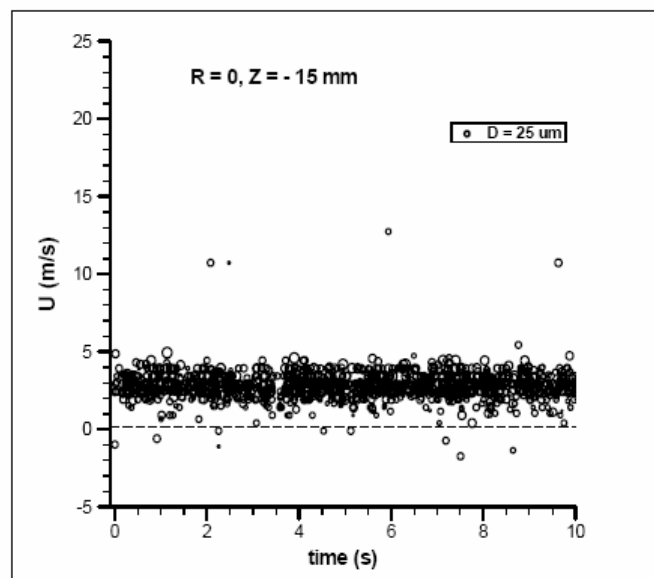


Figure 8-80. Variation of the Streamwise Velocity with Time upstream of the Unheated Cylinder at $Z = -15$ mm and along the Centerline.

The droplet streamwise velocities decrease and become negative values for $R = 0, 5$ mm, and 10 mm on the downstream side of the cylinder, which is indicative of the presence of a recirculation zone and the entrainment of these droplets into this zone. Although the magnitude of the droplet mean streamwise velocity downstream of the cylinder is negative, indicating the presence of a recirculation region, it is clear that the mean is representative of a distribution of velocities and associated droplet sizes. This point is highlighted in Figure 8-81, which presents the droplet streamwise velocity with respect to droplet interarrival time into the probe volume at two points downstream of the cylinder within the recirculation region. One measurement location along the centerline, at $Z = 25$ mm (see Figure 8-81A), represents a measurement close to the cylinder, while the other, at $Z = 76$ mm (see Figure 8-81B), represents a location near the downstream edge of the recirculation pattern. The results for $Z = 25$ mm indicate that many droplets are recirculated upstream toward the cylinder (because $U < 0$), as expected, but also indicate that several droplets at this location are transported in the downstream direction (i.e., $U > 0$). One can speculate that these latter droplets either originate in the recirculation zone or are transported around the cylinder surface and penetrate directly into the recirculation region. In addition, the droplet size does not provide additional information since the size for these droplets varies between $5 \mu\text{m}$ and $30 \mu\text{m}$, and this range is similar to that for the size distribution for the entire population for this measurement. In a similar vane, the results in Figure 8-81B indicate that the abundance of droplets are transported in the downstream direction at this point (i.e., for $U > 0$). However, a few droplets are entrained into the recirculation region (i.e., for $U < 0$).

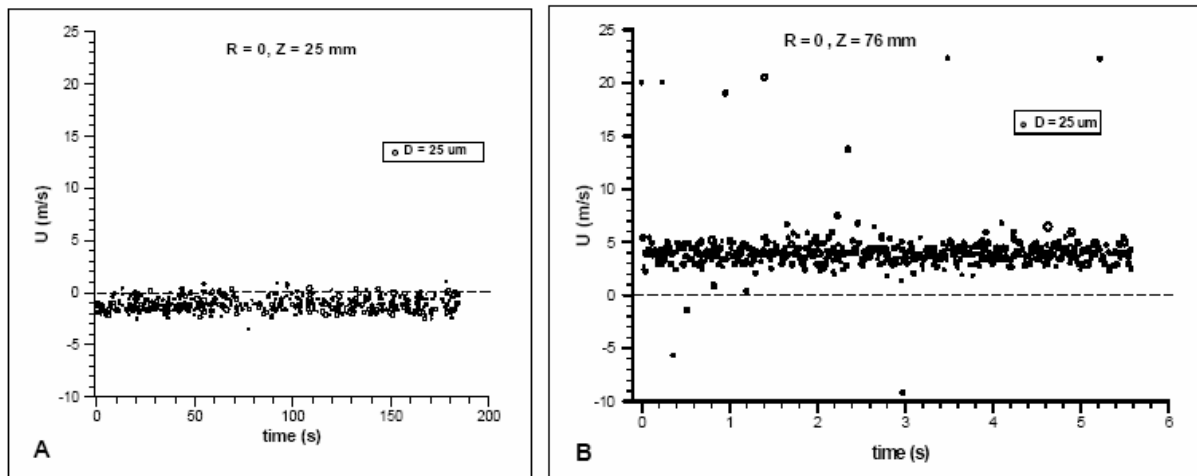


Figure 8-81. Variation of the Streamwise Velocity with Time at Two Streamwise Positions of (A) $Z = 25$ mm and (B) $Z = 76$ mm along the Centerline, downstream of the Unheated Cylinder within the Recirculation Region.

Comparison of results for the unheated and heated cylinders indicates consistently that the value of D_{32} are smaller for the heated case as the droplets are transported past the cylinder surface. The droplet streamwise and cross-stream components of velocity are also lower for the heated case. The unheated and heated results are compared in Figure 8-82 for D_{32} and U at $R = 20$ mm. The decrease in the values of both D_{32} and U for the heated case indicates that droplet vaporization does not result in the complete removal of the smaller size droplets from the distribution, but instead a decrease in the size of all droplets

(which results in an overall decrease in both the mean size and velocity). In fact, the droplet size distributions illustrate clearly the shift of the entire distribution to smaller sizes for the heated cylinder.

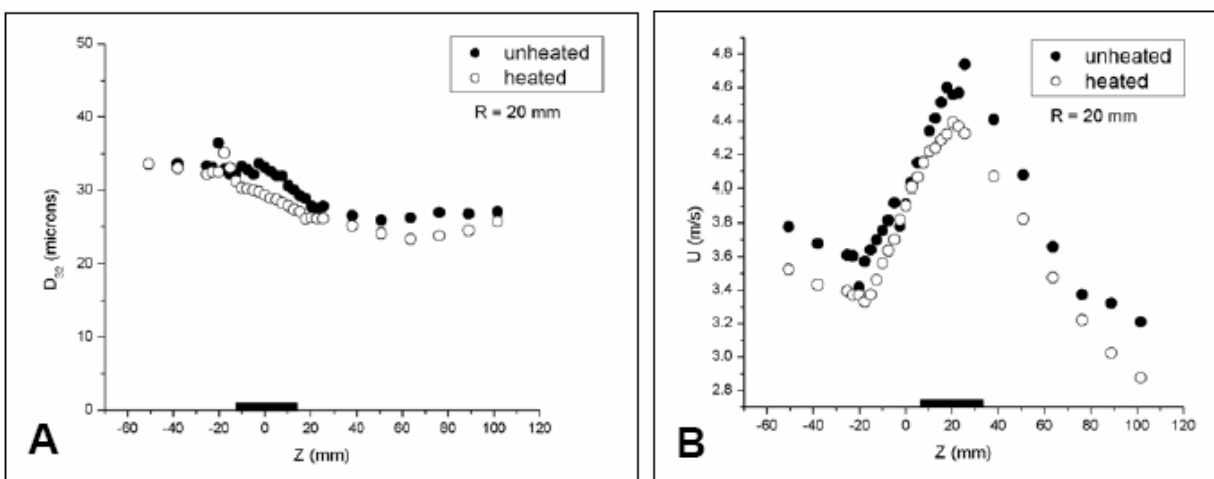


Figure 8-82. Variation of Water Droplet (A) Sauter Mean Diameter and (B) Mean Streamwise Velocity for the Unheated (22 °C) and Heated (150 °C) Cylinders.

Droplets with lower boiling points (i.e., the HFE agents as compared to water) were observed to vaporize more readily, resulting in vaporization of droplets before reaching the obstacle, and the absence of dripping off the cylinder surface. Comparison of results for the three agents indicates that droplet size increases and velocity decreases with increasing agent boiling point. Figure 8-83 presents a comparison of the droplet mean size and streamwise velocity with streamwise position for the three agents at $R = 20$ mm. The size distribution for each agent is also found to shift to larger sizes for increasing agent boiling point.

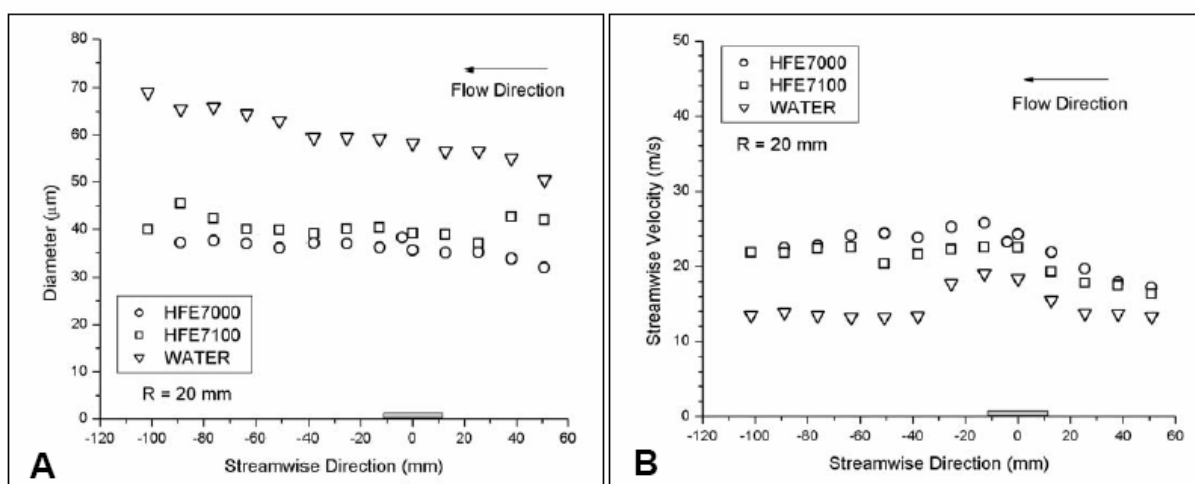


Figure 8-83. Comparison of the Droplet (A) Mean Size and (B) Streamwise Velocity for the Three Agents.

This study shows the effects of agent thermophysical properties on droplet transport processes through clutter elements. Other parameters, such as initial droplet size and velocity distributions, initial droplet number density, clutter surface temperature, and geometry of clutter elements, also govern droplet interaction with clutter elements and droplet transport through the elements. All these factors together with the nacelle airflow and potential fire location need to be considered when designing a fire suppression system using a liquid fire suppressant for nacelle applications.

8.4.3 Transport around Clutter and Recirculation Zones

There is a dearth of data of flow around basic bluff-body shapes immersed in the low speed, turbulent free streams characteristic of engine nacelles. Therefore, wind tunnel models of basic shapes were manufactured and tested in a high-turbulence, low-speed wind tunnel.³³ The data were analyzed to obtain mean velocities, turbulence intensities, and drag coefficients. In addition, the data time history was analyzed to gage the Strouhal number of the bluff-body wake. The data from these tests were used to develop and validate a sub-grid-scale CFD model to account for the effects of small objects in the engine bay that are difficult to resolve using a CFD mesh.

Circular cylinders (single and in tandem), spheres (single and tandem), a simulated wire bundle, a structural rib, and a cubic arrangement of spheres with cylindrical connectors were tested from 1 m/s to 10 m/s in a free-stream turbulence intensity of approximately 10 %. A circular cylinder was also tested in laminar flow at a turbulence intensity of 0.6 % for comparison with published data. Drag measurements were estimated using a momentum deficit approach.

Experimental Setup

The tests were conducted in the low-speed, high-turbulence wind tunnel located at the United States Naval Academy (USNA). The test facility is an open jet wind tunnel powered by three 3.73 kW motors and has a speed range from 0 m/s to 18 m/s. A turbulence grid, consisting of 5 cm (2 inch) PVC plumbing pipe, was installed at the jet exit and a 0.99 m long by 0.69 m high by 0.18 m wide extension was added to condition the flow downstream of the turbulence grid. Empty test section tests found that the flow had average turbulence intensities across the test section of 9.78 %, 9.32 %, and 9.65 %. Test section flow non-uniformities of 0.16 m/s, 0.08 m/s, and 0.02 m/s were measured at average free stream velocities of 10.21 m/s, 5.08 m/s, and 1.19 m/s, respectively. The wind tunnel free stream velocity was analyzed in the absence of the turbulence grid also and found to have a test section flow non-uniformity of 0.03 m/s at a velocity of 9.87 m/s. The turbulence intensity across the “clean” test section averaged 0.58 %.

The clutter models were placed at the jet exit (Figure 8-84 and Figure 8-85), and a thermal anemometry probe was traversed upstream one model diameter from the leading edge of the model and one, three, and six model diameters downstream from the trailing edge of the model. Various shaped models were tested.

Table 8-6 gives details of the models and test conditions. The cylinder models were manufactured from PVC or copper pipe. Representative surfaces of the pipe material were measured and found to have a surface finish 0.4 μm , rms.

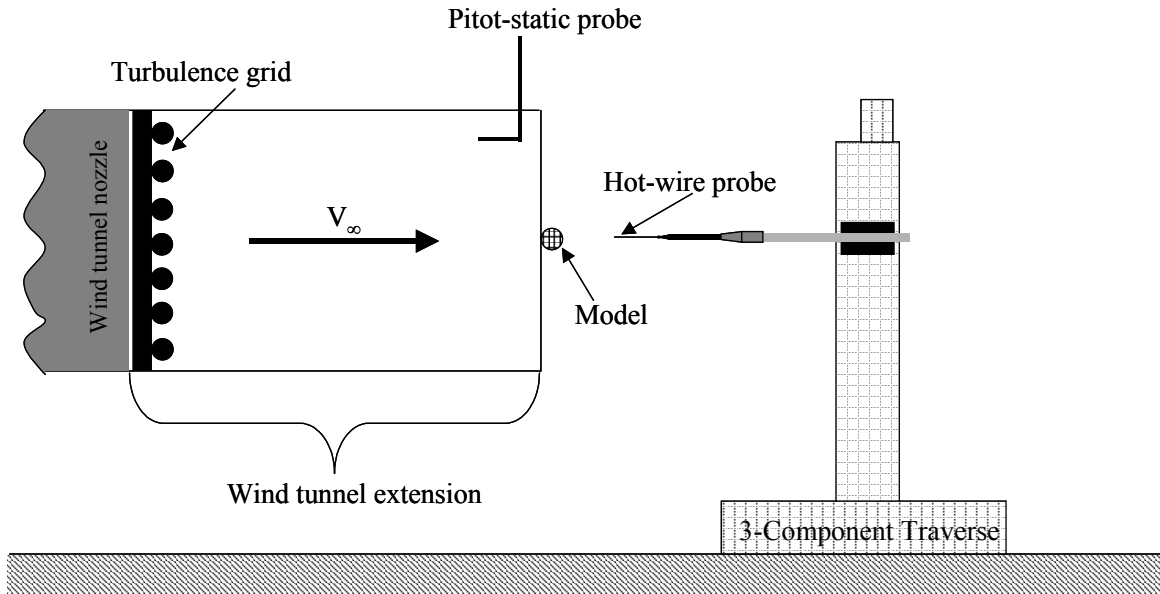


Figure 8-84. USNA Wind Tunnel Schematic.



Figure 8-85. Low-speed, High-turbulence, Open Jet USNA Wind Tunnel.

Table 8-6. Model Geometry and Test Conditions.

Type	Diameter (mm)	Velocity (m/s)	Reynolds Number	Material	Laminar	Turbulent	Spacing	Model Location from Ceiling (mm)
Empty TS	N/A	10, 5, 1	NA	N/A	× (10 m/s)	×		306.8 (297.3 laminar)
Cylinder	48.4	10 5 1	32600 16200 3250	PVC	×	×		297.3
Cylinder	28.8	10 5 1	19550 9800 2200	Copper		×		318.4
Cylinder	9.6	10 5 1	6400 3200 760	Copper		×		323.9
Tandem cylinder	28.8	5	9800	Copper		×	1 <i>d</i>	277.8
Sphere	50.8	5	16900	Wood		×		342.9 (CL)
Tandem sphere	50.8	5	16900	Wood		×	1 <i>d</i>	342.9 (CL)
Rib	38.1	5	12800	Aluminum		×		Tunnel floor
Wire bundle	47.6 (9.5 mm wire)	10	32000	Wire around PVC		×		306.4
Cube	63.5 (25.4 mm spheres)	5	12800	Wood		×		342.9 (CL)

Wire Bundle Model

This model was created using approximately 1.3 cm diameter wires secured around a 2.54 cm PVC pipe, see Figure 8-86. The outer diameter of the wire bundle is roughly equivalent to the large cylinder model. The mean velocity and turbulence intensity data were little affected by a 1 in 24 rotation of the wire bundle model. In comparison to the large cylinder data, the wake of the wire bundle model had a greater velocity deficit and an increase in the turbulence intensity.

Tandem Medium Cylinder Model

The tandem cylinder model, seen in Figure 8-87, was tested, and the results were compared to those from the medium cylinder model at 5 m/s. The tandem medium cylinder model had a significantly wider wake and more of a velocity decrement. The turbulence intensity of the tandem medium cylinder model was higher than the medium cylinder model turbulence intensity. Tandem cylinder drag (and correspondingly, the shed wake) is very much dependent upon the spacing between the cylinders. The

data depicted is for a cylinder spacing of one diameter. New data may prove to be markedly different for another cylinder spacing.

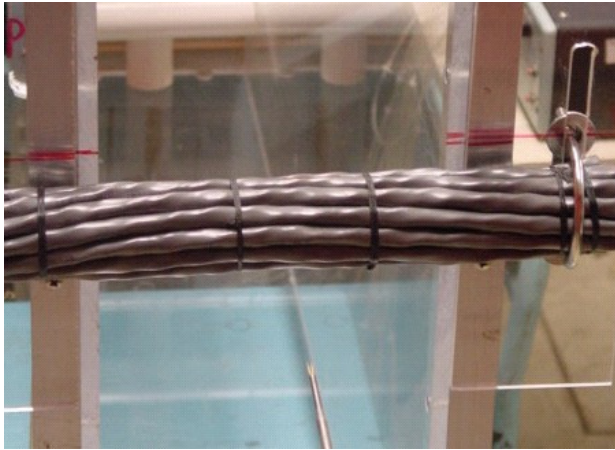
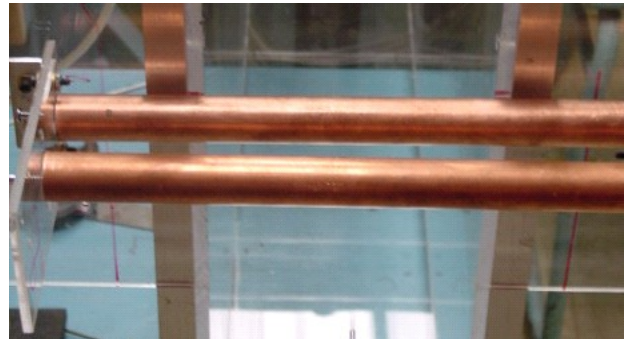


Figure 8-86. Photograph of the Wire Bundle Model.

Figure 8-87. Photograph of the Tandem Medium Cylinder Model.



Sphere Model

To obtain an accurate assessment of the drag coefficient, horizontal traverses were accomplished for all of the three-dimensional models (sphere, tandem sphere, and cube). For each location, six traverses (three horizontal and three vertical) were obtained. In general, the sphere exhibited a smaller wake with less turbulence intensity as compared to a similar sized two-dimensional cylinder at a similar Reynolds number. The effect of the model wake on the flow quickly dissipated downstream of the model, approaching the free stream tunnel conditions.

Tandem Sphere Model

This model was compared to the sphere model; the tandem sphere model had a wider wake but less of a velocity deficit immediately behind the model. However, the tandem sphere model had a slightly greater velocity deficit farther downstream. Turbulence intensity levels were less than the single sphere model immediately downstream but were slightly more at the farther downstream location.

Cube Model

A cube arrangement of spheres with connecting rods, as shown in Figure 8-88 was meant to simulate the many porous, three-dimensional objects found in an engine bay. The mean velocity and turbulence intensity were measured at different upstream and downstream traverse locations at a free stream velocity of 5 m/s. Unlike the sphere data, the wake of the cube was not seen to dissipate as quickly at the downstream traverse locations. In addition, the wake immediately downstream was wider but with a smaller velocity deficit than seen for the sphere. Turbulence intensity immediately aft of the cube was noticeably less than that of the sphere. However, the turbulence intensity of the cube far downstream was noticeably higher than the sphere's.

Rib Model

A representative aircraft rib, affixed to a flat plate was tested to determine mean velocity and turbulence intensity data. Limited data were also obtained on the flat plate alone. As expected, there is a sizeable velocity deficit seen near the flat plate and behind the rib. Recovery to the free stream velocity is delayed as the vertical traverse location moves downstream. The turbulence intensity data is chaotic near the flat plate and behind the rib. Recovery to the free stream turbulence intensity is delayed.

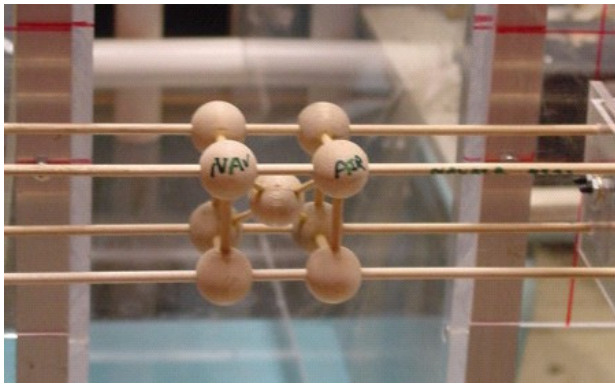


Figure 8-88. Photograph of the Cube Model.

Drag Estimates

The drag coefficient estimates are presented in Table 8-7 along with the uncertainty estimates. In general, the models in a turbulent free stream had lower values of drag coefficient compared to the published values for similar models in a low-turbulence free stream. The analysis used the velocity data and takes into account the wind tunnel velocity jet dissipation, effects of the walls and jet boundaries, and momentum losses vertically as well as horizontally. The present tests and historical data yielded similar drag coefficient values for a cylinder in low turbulence flow (1.23 for the present test, 1.20 from the literature). The estimate for the tandem sphere data in a “clean” flow field was estimated from Hoerner³⁴ assuming the models to be flat disks. The estimate for the cube in a “clean” flow field was based on a porous model composed of spheres and rods, weighted by area. Analyzing data with a similar amount of scatter^{35, 36} for a circular cylinder and applying the same uncertainty/bias estimates yielded an uncertainty of 13.2 % at 95 % confidence.

Table 8-7. Summary of Drag Coefficients.

Model Type	C_D (present test)	Velocity (m/s)	95 % Confidence (%)	C_D (published; low turbulence)	Reynolds Number	Size (mm)
Large cylinder	0.555	9.540	8.4	1.20	30812	48.41
Large cylinder	0.792	4.731	11.3	1.20	15279	48.41
Large cylinder	1.130	1.012	10.8	1.00	3268	48.41
Cylinder low turbulence	1.228	9.534	7.1	1.20	30793	48.41
Medium cylinder	1.040	9.237	8.2	1.20	17611	28.80
Medium cylinder	0.858	4.618	8.6	1.06	8804	28.80
Medium cylinder	1.084	1.089	12.6	1.00	2077	28.80
Tandem medium cylinder	0.939	4.630	11.3	1.06	8826	28.80
Small cylinder	0.368	9.556	8.4	1.04	6089	9.55
Small cylinder	0.444	4.825	9.0	1.00	3074	9.55
Small cylinder	0.635	1.128	9.5	1.30	719	9.55
Sphere	0.467	4.950	26.8	0.47	16775	50.80
Tandem sphere	0.703	4.907	8.9	0.71	16633	50.80
Rib	0.921	5.086	15.9	1.30	12930	38.10
Wire bundle	1.039	9.334	8.6	1.14	29662	47.63
Cube	0.242	4.531	15.9	0.28	19195	63.50

Generally, for a given Reynolds number, the smaller the size of the model, the lower the drag coefficient. For the small cylinder, the drag coefficient was found to be significantly lower than for the large and medium cylinders at a roughly equivalent Reynolds number. Although the length of the wind tunnel extension was thought sufficient to ensure that the generated turbulence was well-mixed, perhaps the nature of the eddies created by the 5.08 cm diameter turbulence grids causes differences in the local flow field around the various models, thus causing a violation in the similarity parameter.

The wire bundle model was seen to have significantly higher drag (approaching the drag coefficient of the cylinder in low turbulence flow field) compared to a similar sized cylinder. This is a different trend than seen in a similar model in a low turbulence flow field. A wire bundle in a low turbulence flow field has been shown to decrease the drag coefficient compared to a smooth cylinder of the same diameter.

The tandem sphere had nearly double the drag coefficient of the single sphere model. For each estimate, the same frontal area was used in the drag coefficient calculations. In a similar manner, the same frontal area was used for estimating the drag coefficients for the medium cylinder and tandem medium cylinder.

Strouhal Number

The algorithm to determine the power spectrum density (PSD) was based on the method by Welch.³⁷ The data were segmented into windows to allow eight averages. No data overlapping was employed, and a Hanning filter was used with a window length the same size as the data segments. The mean was eliminated from the PSD calculations and a 95 % confidence criterion was used to gage the PSD assessment.

Table 8-8 gives the frequency and Strouhal number resolution. The Strouhal number is a dimensionless characteristic of vortex-shedding off bluff bodies, such as clutter. This shedding of vortices downstream affects the mixing of agent into the recirculation regions as well as the major downstream flows. In cases where a comparison of models needed to be consistent (e.g., a medium cylinder model and the tandem medium cylinder model), the analysis was performed over the same data record length.

Table 8-8. Frequency and Strouhal Number Resolution.

Model Type	Reynolds Number	Velocity (m/s)	Δf (Hz)	ΔSt
Large cylinder	32,605	10.0126	8.492	0.041
Large cylinder	16,208	4.9936	4.069	0.039
Large cylinder	3,253	1.0000	1.424	0.069
Medium cylinder	19,553	10.0157	10.851	0.031
Medium cylinder	9,826	4.9664	21.701	0.126
Medium cylinder	2,175	1.1070	3.255	0.085
Small cylinder	6,395	9.9710	13.021	0.012
Small cylinder	3,193	4.9840	13.021	0.025
Cylinder-low turbulence	32,338	10.0126	11.182	0.054
Tandem medium cylinder	9,435	4.8953	21.701	0.128
Sphere	16,917	4.9866	8.492	0.087
Tandem sphere	17,426	5.0994	8.492	0.085
Wire bundle	32,019	10.0131	8.492	0.040
Cube	21,585	5.0647	4.069	0.051

To gage the coherence, the empty test section data were analyzed to determine the pulse frequency peaks in the tunnel. This was used as a guide to cull non-model frequencies from the spectrum. The Strouhal number corresponding to the dominant frequency is plotted against Reynolds number in Figure 8-89. It was found that the Strouhal number of the cylinder model in a low-turbulence flow field was lower, than that reported in the literature, 0.13 versus 0.19, (see Schlichting³⁶).

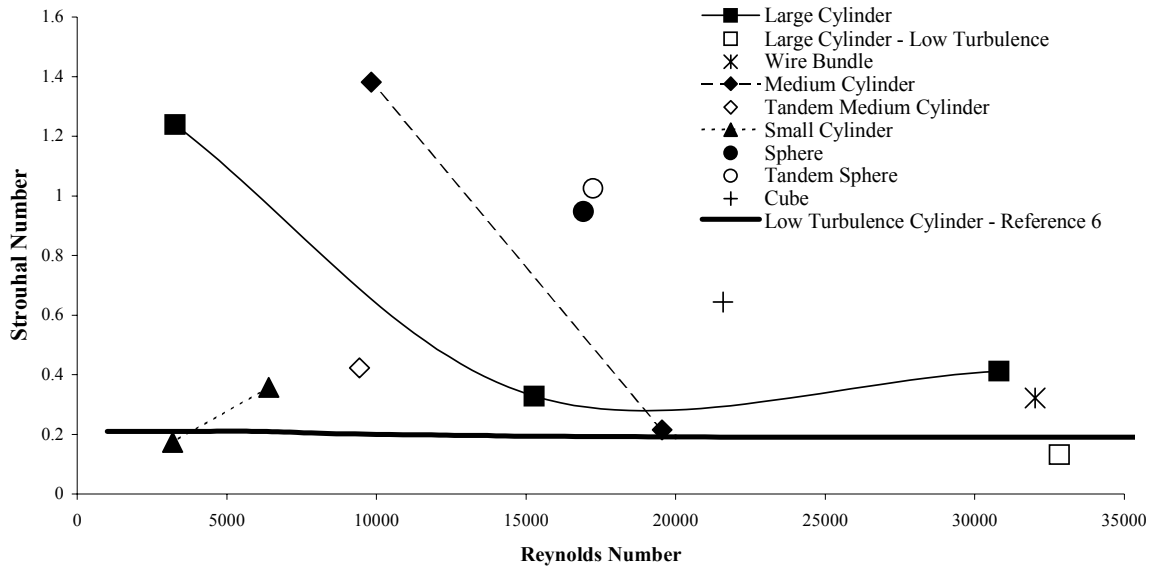


Figure 8-89. Strouhal Number versus Reynolds Number for the Various Tested Configurations.

It should be noted that model size had an effect on the Strouhal number. That is, the large circular cylinder at 1 m/s has the approximate Reynolds number of the small circular cylinder at 5 m/s. However, the Strouhal number was significantly different: 1.2 for the large cylinder at 1 m/s and 0.2 for the small cylinder at 5 m/s.

The fundamental frequency of the empty test section data was: 25.8 Hz ($St = 0.125, 0.074, \text{ and } 0.025$ based upon the large, medium, and small cylinder diameter, respectively) at 10 m/s, 17.3 Hz ($St = 0.167, 0.100, \text{ and } 0.033$ based upon the large, medium, and small cylinder diameter, respectively) at 5 m/s, and 8.7 Hz ($St = 0.419, 0.249, \text{ and } 0.083$ based upon the large, medium, and small cylinder diameter, respectively) at 10 m/s. The different flow fields most likely caused the differences in Strouhal numbers and drag coefficients.

The Strouhal numbers of the sphere and tandem sphere models were equal. However, there was a notable difference between the medium cylinder and tandem medium cylinder models. The wire bundle model was found to have a similar Strouhal number as the similarly sized cylinder. No dominant frequency was noted for the rib model. In general, the Strouhal number was higher for cylinders in a turbulent flow field compared to cylinders in low turbulence.

Summary and Implications

Fundamental measurements of mean velocity, turbulence intensity distributions, drag coefficient estimates, and wake shedding frequency were obtained for basic aerodynamic shapes. A limited comparison to data obtained for a circular cylinder in a low-turbulence flow field was also conducted. The results show that the wake structure behind a circular cylinder in a turbulent flow field was smaller compared to the same cylinder in low-turbulence flow. Turbulence intensity increased with decreasing Reynolds number. The drag coefficient estimates were generally lower than those obtained in low-

turbulence flow fields. Strouhal number variation with Reynolds number was generally higher for cylinders in a turbulent flow field, when compared to cylinders in low-turbulence. Model size was seen to affect the similarity parameters of the Strouhal number and Reynolds number due to differences in the shedding characteristics of the turbulence grid in the wind tunnel. The results also show higher turbulence intensity behind the bluff body when compared to the same configuration in a laminar flow field. Also, the drag coefficients for the same configuration were seen to be lower than those in a laminar flow. These latter two points imply that the clutter impedes the flow of agent and air less (proportionally) in a turbulent flow than in a laminar one and that the mixing of agent into the flow as a result of interacting with the clutter is less sensitive to Reynolds number than was expected. Subsequent testing, described below, indicates that clutter usually facilitates the mixing of agent in the protected space.

8.4.4 Low Temperature Effects on Agent Dispersion

Introduction

Should a fire suppressant be discharged into a sufficiently cold engine nacelle or dry bay, it is expected that some of the chemical will condense on the cold surfaces. Gravity would then lead to puddling of the condensate at a low point in the volume, and the agent would then volatilize at a rate determined by its vapor pressure at the local temperature and the local air flow. This behavior would necessitate the storage and distribution of additional suppressant, which would result in increased storage weight and volume, as well as a longer time to fire extinguishment. The cold temperature release finds its applications in the cold start of an engine in a cold environment or in high-altitude cruising conditions.

Yang and coworkers³⁸ conducted a series of tests in a simulated engine nacelle to verify this phenomenon and to estimate the magnitude of its impact. In these tests, the key variable was the difference between the boiling point of the suppressant and the ambient temperature in the nacelle. The temperature of the suppressant storage bottle was also treated as an independent variable.

For the NGP, a criterion for low temperature applications for a fire suppressant was set at $-40\text{ }^{\circ}\text{C}$. To study the effect of low temperature on agent dispersion, it was necessary to identify a surrogate agent that has a normal boiling point higher than the $-40\text{ }^{\circ}\text{C}$ minimum temperature criterion. Trifluoroiodomethane (CF_3I), which has been proposed as a potential replacement for halon 1301 in aircraft engine nacelle and dry bay fire protection applications,^{4,39} meets this criterion and was selected as a surrogate for the study. CF_3I has a normal boiling point of $-22\text{ }^{\circ}\text{C}$, which is almost $20\text{ }^{\circ}\text{C}$ higher than the $-40\text{ }^{\circ}\text{C}$ minimum temperature criterion. The dispersion of CF_3I into air at temperatures down to $-40\text{ }^{\circ}\text{C}$ may not be as effective as halon 1301, which has a normal boiling point of $-57.8\text{ }^{\circ}\text{C}$. In addition, CF_3I can be detected using UV absorption spectrometer, which was the available method for measuring temporal CF_3I concentration in this study. Table 8-9 lists some of the physical properties of CF_3I and CF_3Br .

Table 8-9. Selected Thermophysical Properties of CF_3I and CF_3Br .²

Agent	Molecular Weight (kg/mol)	T_b ($^{\circ}\text{C}$)	T_c ($^{\circ}\text{C}$)	P_c (MPa)	ρ_c (kg/m^3)	ΔH_v (kJ/kg)
CF_3I	0.196	-22.0	122.0	4.04	871	106
CF_3Br	0.149	-57.8	67.0	4.02	745	111

T_b is the normal boiling point; T_c is the critical temperature; P_c is the critical pressure; ρ_c is the critical density; ΔH_v is the latent heat of vaporization at T_b .

Although the release of CF_3I (at room temperature or chilled to about $-40\text{ }^\circ\text{C}$) into a fire compartment and an engine nacelle simulator at ambient room temperature has been examined,^{2,40} the discharge of cold CF_3I into a cold ambience has not been performed, or at least has not been documented in open literature. There is only one corporate internal report,⁴¹ which describes a study of the release of cold CF_3I into a well-mixed cold *enclosure* with no airflow. Careful examination of the data indicated some deterioration in the distribution of CF_3I within the enclosure when compared to room temperature conditions. To assure that there is no substantial deterioration in dispersion performance under cold temperature applications, discharge tests in an aircraft engine nacelle at temperatures below the agent boiling point are needed. The temperature of $-40\text{ }^\circ\text{C}$ was selected in this study because it was below the normal boiling point of CF_3I and was the lowest operating temperature for some of the equipment used in the experiments.

Experimental Apparatus (ELEFANT)

The experimental apparatus (called Extremely Low-temperature Environment For Aircraft Nacelle Testing) consisted of a simulated engine nacelle with baffles, an agent release port, four observation windows, and two measurement ports. Figure 8-90 is a schematic of the simulator. The annulus of the simulator had an inside diameter of 0.6 m and an outside diameter of 0.9 m, resulting in a cross-sectional area of 0.35 m^2 . The length (2 m) of the simulator was comparable to the distance between the agent injection port and the downstream end of a typical small engine nacelle. The baffle height was 0.075 m. The baffles were used to mimic a complicated flow path for the agent as in the case of a real nacelle. Two longitudinal ribs with the same height as the baffles were placed on the outer surface of the inner core of the nacelle between the inner forward and aft baffles. The ribs were used as barriers to the agent flowing circumferentially. The simulator was fabricated of 3.2 mm thick stainless-steel sheet metal.

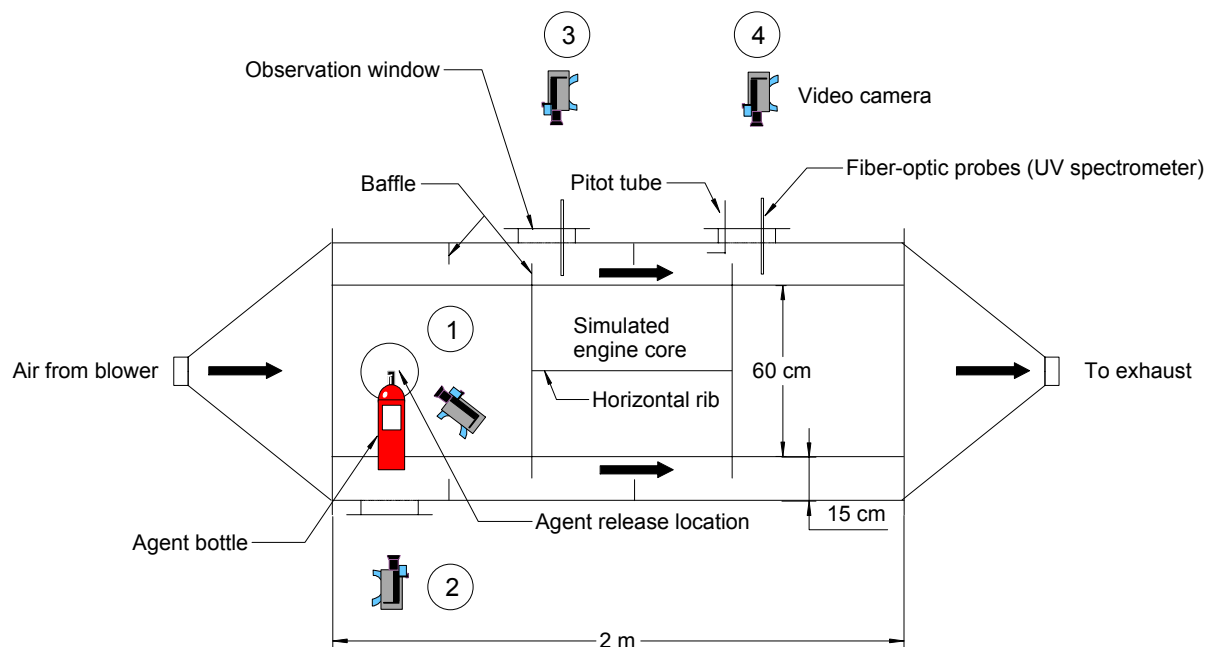


Figure 8-90. Schematic of the Test Fixture (ELEFANT).

A bottle with an internal volume of 2.36 L was used to store CF_3I for discharge. A fast-response static pressure transducer (uncertainty ± 10 kPa specified by the manufacturer) was mounted on the receiver bottle to monitor the pressure inside the bottle during filling and discharge. A K-type thermocouple (uncertainty ± 1 °C) was inserted into the bottle to record the temperature of the liquid agent before discharge. A quick-acting solenoid valve was used to release the agent. To tailor the agent discharge time (≈ 0.5 s), a reducer was placed at the valve exit. The agent was released through a vertical tee at the end of a short stainless-steel tubing (i.d. = 15.9 mm, o.d. = 19.1 mm) connected to the reducer. Four CCD cameras (30 frames/s) were used to observe the agent discharge behavior at the release port (Camera 1), at a location in the bottom of the simulator to observe any pooling of agent (Camera 2), and at the two concentration measurement locations (Cameras 3 and 4). A frequency-controlled, variable-speed blower provided airflow through the nacelle simulator. The maximum air speed at room temperature in the annulus, measured using a pitot tube, can reach 9.2 m/s.

To achieve an operating temperature of -40 °C, the entire facility was placed inside the U.S. Army environmental test chamber at Ft. Belvoir, and the cold discharge experiments were conducted inside the chamber. The chamber has an interior dimension of 2.74 m (H) \times 3.35 m (W) \times 3.66 m (L) and a 1.83 m \times 1.83 m sliding door. The lowest temperature attainable in the environmental test chamber is -54 °C. Discharge experiments in room temperature were also conducted inside the chamber with the refrigeration unit turned off to establish baselines for comparisons.

The experimental procedure involved the following steps. The receiver bottle was first immersed in dry ice and connected to the CF_3I supply bottle, which was placed on an electronic balance (uncertainty of ± 1 g) to monitor the amount of agent transferred to the receiver bottle. The dry ice was used to condense the CF_3I vapor in the receiver bottle. The supply bottle was slightly warmed using two 120 V floodlights to increase the vapor pressure to facilitate the transfer of CF_3I vapor to the receiver bottle. When the amount of agent in the receiver bottle reached the target mass, the bottle was then removed from the dry ice, warmed back to room temperature, and weighed on the electronic balance to determine the actual mass in the bottle. The receiver bottle was then pressurized with nitrogen to 4.12 MPa. Shaking the bottle intermittently and vigorously was required before the final equilibrium pressure was attained. The amount of nitrogen added was obtained by weighing the filled bottle. The bottle was now ready for the discharge experiments. For cold temperature conditions, the environmental test chamber and the receiver bottle were cooled down to approximately -40 °C before a test was commenced. Two contact K-type thermocouples were attached on the front and aft of the simulator external skin to monitor the ambient temperature of the chamber. In addition, a bare-beaded K-type thermocouple was placed in the annulus to measure the airflow temperature through the nacelle.

Given the simulated nacelle volume and airflow, the amount of agent required for a fixed injection period (< 0.5 s for typical nacelle applications) was estimated using the generic nacelle modeling results discussed in Hamins et al.⁶⁶ The agent bottle was charged with ≈ 1 kg of CF_3I and then pressurized with nitrogen to the desired pressure (4.21 MPa) at room temperature. Table 8-10 lists the experimental matrix. The airflow through the simulator was maintained at 1.5 kg/s \pm 0.1 kg/s (mean \pm standard deviation).

Table 8-10. Experimental Matrix.

Nominal Initial Conditions of Vessel	Nominal Conditions of Vessel Before Discharge	Nominal Conditions in the Simulator
22 °C and 4.12 MPa	-40 °C at prevailing <i>P</i>	-40 °C
22 °C and 4.12 MPa	22 °C and 4.12 MPa	22 °C (baseline)
22 °C and 4.12 MPa	22 °C and 4.12 MPa	-40 °C

The dispersion effectiveness of CF₃I was assessed based upon concentration measurements at the two locations inside the engine nacelle simulator (see Figure 8-90). The number of measurement locations could be easily increased; however, the intent of this work was not to address the certification process, which requires twelve measurement locations. The measurements were made using two Ocean Optics S2000 UV/VIS fiber-optic spectrometers. The optical components consisted of a deuterium/tungsten source, four (UV grade quartz) collimating lenses, and 300 μm diameter optical fibers. These were arranged to provide two measurement locations (coincident with Cameras 3 and 4) approximately 0.75 m apart along the direction of the airflow in the engine nacelle testing apparatus. A bifurcated fiber (1 m in length, coupled with a 5 m extension) was used to connect the source to a pair of collimating lenses secured by brackets to the Plexiglas® viewing windows located on the top of the apparatus. The source radiation emanating from each lens was transmitted over a 0.038 m optical path (perpendicular to the airflow) to an opposing set of collimating lenses connected by independent optical fibers (5 m in length) to the master and slave spectrometers. Although the manual indicated that these optical components should have a spectral range from 200 nm to 850 nm, very little throughput at wavelengths shorter than 250 nm was found.

The spectrometer settings used for the measurements in the nacelle testing apparatus were as follows. The spectrometers were triggered by an electronic timer. The integration time (analogous to the shutter speed) was set at 30 ms, and the pixel resolution of the analogue to digital converter (ADC) was set at 10, which amounts to a spectral resolution of only about 3 nm. With this configuration, it was able to achieve a data acquisition rate of approximately 12 single scan spectra (6 at each location) per second to capture the time dependent details of the agent discharge. An estimate of the uncertainty (one standard deviation) of the measurements was obtained by comparing results at these settings to more accurate values obtained after signal averaging 100 scans at the full resolution of the spectrometer (≈ 0.3 nm). Based on this analysis, the CF₃I partial pressures reported in this paper are accurate to ± 15 %.

The UV spectrometer was calibrated at 295 K using a quartz cell with an optical path length of 0.075 m. The cell was first evacuated to 1.33 Pa. Then, a fixed amount of CF₃I vapor was metered into the cell by monitoring the cell pressure. Spectra were taken using an integration time of 30 ms and a pixel resolution of 10. Figure 8-91 shows a typical CF₃I absorption spectrum at 295 K. Note that the peak absorbance for CF₃I centers around 270 nm. The calibration curve (at λ = 300 nm and 22 °C), which is a plot of absorbance (*A*) against concentration (*C*, molecules cm⁻³), is shown in Figure 8-92.

The Bouguer-Beer-Lambert law is expressed as

$$A(\lambda) = -\log \left[\frac{I(\lambda)}{I_o(\lambda)} \right] = \frac{C\sigma(\lambda, T)L}{2.303} \quad (8-40)$$

where $I(\lambda)$ and $I_o(\lambda)$ are the incident and transmitted intensities through the cell respectively, $\sigma(\lambda, T)$ is the absorption cross section (cm^2), L is the optical path length (cm), T is the temperature, and λ is the wavelength. Note that the absorption cross-section is a function of wavelength and temperature. Using the ideal gas law, Equation 8–41 gives the relationship between C and the partial pressure p (Pa) at 22 °C.

$$C = 2.44 \times 10^{14} p \quad (8-41)$$

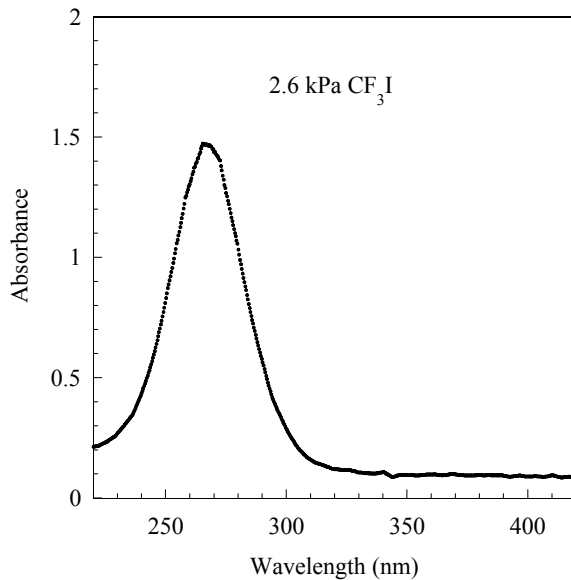


Figure 8-91. Absorption Spectrum of CF_3I .

From Equation 8–40, the absorption cross section can be obtained from the slope of the calibration curve. A linear regression line is fitted through the data points in Figure 8-92, and the absorption cross-section of CF_3I is $8.1 \times 10^{-20} \text{ cm}^2$, which is comparable to the value of $8.9 \times 10^{-20} \text{ cm}^2$ at $\lambda = 300 \text{ nm}$ and 22 °C to 27 °C in the literature.⁴² Since the calibration was performed at 22 °C, a correction for the temperature effect on the absorption cross section is necessary to obtain the CF_3I partial pressure at other prevailing temperature, using the following equation:⁴²

$$\sigma(\lambda, T) = \sigma(\lambda, 25 \text{ }^\circ\text{C}) \exp[B(\lambda)(T - 25)] \quad -63 \text{ }^\circ\text{C} < T < 27 \text{ }^\circ\text{C} \quad (8-42)$$

The concentration C of CF_3I at any temperature was calculated from the absorbance measurement using Equations 8–40 and 8–42. At 300 nm, $B = 4.876 \times 10^{-3} \text{ }^\circ\text{C}^{-1}$ from DeMore et al.⁴² The partial pressure of CF_3I was then obtained using the ideal gas law at the prevailing temperature. However, the temperature effect on the absorption cross section was found to be negligible in the concentration calculations.

An electronic timer was used to coordinate the experimental sequence of events. At $t = 0 \text{ s}$, a signal was sent from the timer to trigger the data acquisition system to record the pressure of the discharge bottle and the pitot tube output at a sampling rate of 200 Hz. At $t = 1 \text{ s}$, the timer initiated the two UV spectrometers, and at $t = 2 \text{ s}$, the solenoid valve was activated to discharge the CF_3I /nitrogen mixture from the bottle into the engine nacelle simulator.

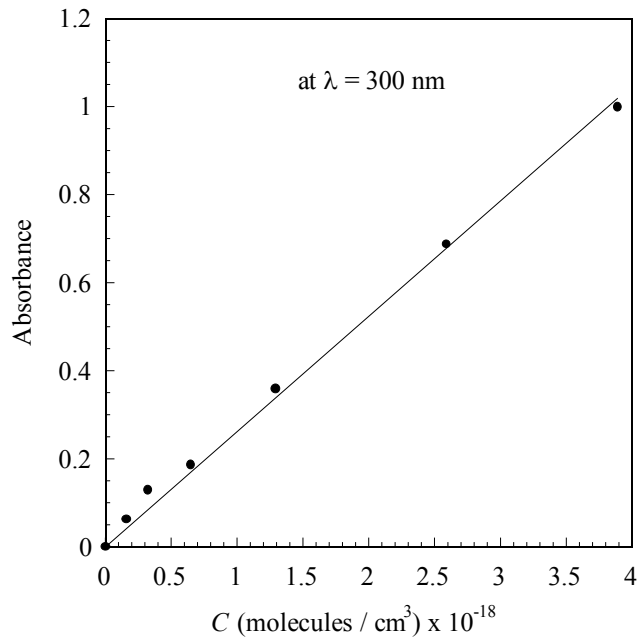


Figure 8-92. Calibration Curve at 300 nm.

Results and Discussion

Figure 8-93 shows the temporal variation of pressure inside the bottle during a typical discharge. The initial time ($t = 0$) corresponds to the time when the solenoid valve was opened. In the figure, the prevailing bottle pressure before discharge at ≈ -40 °C is much lower than that at room temperature. Due to the reduction in the initial bottle pressure, the discharge time (≈ 0.24 s) of the cold *liquid* agent is much longer than that (≈ 0.16 s) of the baseline case; the liquid discharge time corresponds to the transition point in the pressure *vs.* time curve.⁴³ The observations from Camera 1 also showed that the agent discharge time at ≈ -40 °C was longer than that at room temperature.

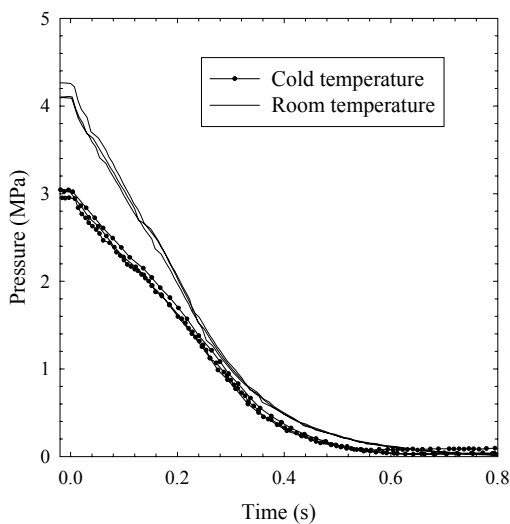


Figure 8-93. Variation of Bottle Pressure during Discharge at Room and Cold Temperatures.

When CF_3I was discharged at room temperature, the observations obtained from Camera 2 showed that a small amount of CF_3I pooled in the bottom of the simulator upon release, and the liquid CF_3I boiled off within 66 ms. When CF_3I was discharged at $-40\text{ }^\circ\text{C}$, a significant amount of liquid CF_3I pooled at the bottom of the nacelle upon release. The liquid CF_3I evaporated slowly and remained for many seconds ($> 60\text{ s}$) before complete evaporation. The observations from Cameras 3 and 4 showed that a cloud of CF_3I passed through the field of view of the cameras after agent discharge. The observations from Cameras 3 and 4 were qualitatively similar for the discharge of CF_3I at room temperature and $-40\text{ }^\circ\text{C}$.

The difference in pooling tendency described above can be explained as follows. Consider a 2.36 L container with 1 kg of CF_3I pressurized with nitrogen to 4.12 MPa at $22\text{ }^\circ\text{C}$. If the container is cooled down to $-40\text{ }^\circ\text{C}$ before release, the final pressure of the container is estimated to be 2.8 MPa using the computer code (PROFISSY).^{2,6} The code is based on the calculations of vapor-liquid phase equilibria using the extended corresponding-states principle. Assuming the discharge of the liquid agent from the container is an isentropic process from the initial container pressure to atmospheric pressure, the final states of the agent can be calculated using the computer code (FISSYCS)², which is a modified version of PROFISSY. Table 8-11 tabulates the calculated results for the two conditions. The liquid mole fraction (the percent of agent/nitrogen mixture still remaining in the liquid phase after the isentropic expansion process) is substantially higher at $-40\text{ }^\circ\text{C}$ than at $22\text{ }^\circ\text{C}$. Such a high liquid fraction should result in significant pooling upon agent release from the bottle. The combined effects of liquid pooling and slow evaporation at $-40\text{ }^\circ\text{C}$ will have an adverse impact on the subsequent dispersion of the agent/nitrogen mixture in the nacelle.

Table 8-11. Liquid Fraction of $\text{CF}_3\text{I}/\text{N}_2$ Mixture after Isentropic Expansion to 0.101 MPa.

Initial Conditions	Liquid Fraction (%)
$22\text{ }^\circ\text{C}$ at 4.12 MPa	70
$-40\text{ }^\circ\text{C}$ at 2.8 MPa	90

Although full CF_3I spectra were obtained in each test, a common practice used is to base concentration measurements on the wavelengths at the peak absorbance or its vicinity. The absorbance at 300 nm was used to obtain the CF_3I concentration because saturation of the detector at $\approx 280\text{ nm}$ was observed under certain test conditions. The concentration of CF_3I thus obtained is shown for both the room and cold temperature releases in Figure 8-94 and Figure 8-95 for the two measurement locations, respectively. The initial time ($t = 0$) in the figures corresponds to the initiation of the agent release. Although three runs were performed at each condition with similar observations, only a single run for each condition is shown in the figure for clarity. The arrival times of the agent at the two measurement locations were clearly captured in the figures. Some salient features are noted in the two figures.

For the room temperature release, an initial spike was observed at the forward measurement location. This was due to the presence of a two-phase (liquid droplet-laden) flow because the off-resonance spectral measurement at 500 nm also showed a peak at the same time. The two-phase flow was the result of break-up of the liquid core at the discharge port into droplets. The off-resonance extinction at 500 nm indicated that liquid CF_3I droplets were present for only a short period of time ($< 2\text{ s}$) immediately following the discharge. Therefore, it can be argued that the concentration measurements after the initial spike in Figure 8-94 was due largely to the CF_3I vapor, with minimal or negligible contribution from the droplets.

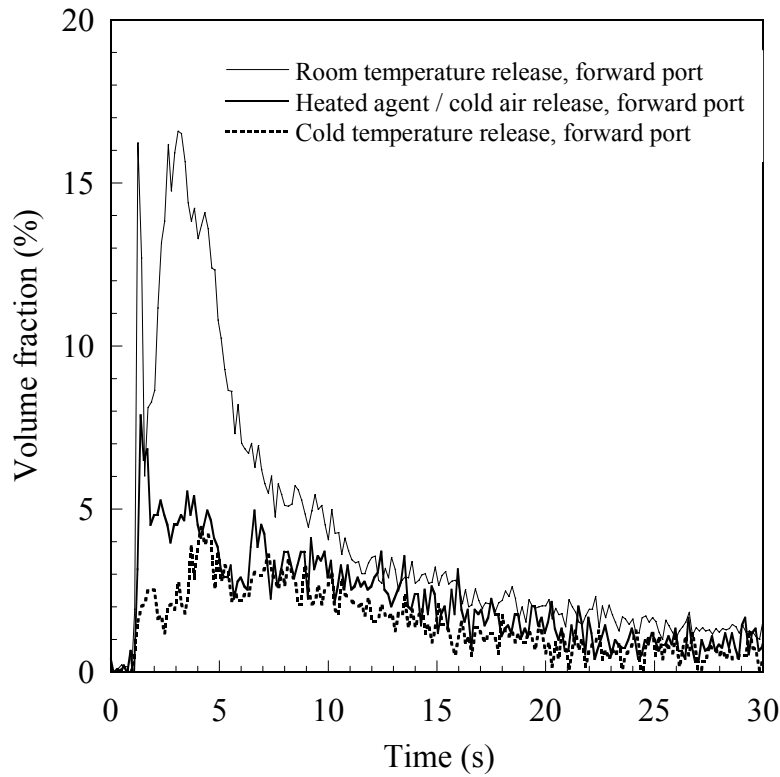
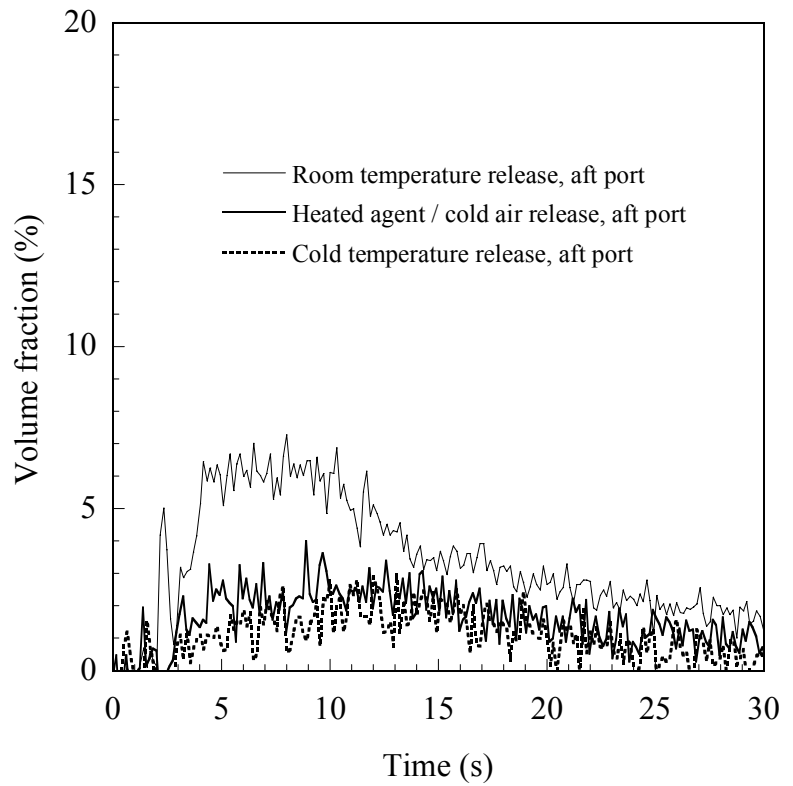


Figure 8-94. CF_3I Concentration Profiles at the Forward Port.

Figure 8-95. CF_3I Concentration Profiles at the Aft Port.



The off-resonance spectral measurement at 500 nm in the aft location indicated that no droplets were present. The absence of the droplets and the much lower CF_3I concentration (Figure 8-95) at this location indicated that the current nacelle simulator had indeed created a very challenging environment for agent dispersion, a condition which is generally true for a real engine nacelle. Furthermore, the generic nacelle model⁶⁶ provided a reasonable estimate of the amount of agent needed to achieve the required extinguishing concentration at two measurement locations in the current nacelle. Halon 1301 and CF_3I have similar heptane cup-burner extinguishing values, a volume fraction of 0.032 from Grosshandler et al.⁴ Assuming that the military specification for halon 1301 can be applied to CF_3I , the measurements in Figure 8-94 and Figure 8-95 suggest that a volume fraction of 0.06 can be attained over a duration of 0.5 s in both locations at room temperature.

For cold temperature release, the off-resonance spectral measurements at 500 nm did not indicate the initial presence of droplets at both forward and aft measurement locations. The absence of the droplets was due partly to the reduction in the initial bottle pressure (≈ 3 MPa vs. ≈ 4.1 MPa at room temperature), which would impart less momentum to the droplets upon the release of the agent. Droplets with less momentum were less likely to be transported to the two measurement locations. The combined effect of low bottle pressure and large liquid fraction in cold temperature release (see discussion above) might generate larger droplets as a result of poor atomization of the liquid core, thus hindering the ability of the droplets to follow the airflow. Similar to the room temperature release, the concentration at the forward location was higher than that at the aft. However, the difference was not as significant as in the case of room temperature release. The most important finding from this study was that there was a significant reduction in the agent concentration in the cold temperature release. At the forward measurement location, a reduction of a factor of almost 3 was observed at the peak concentration. At both locations, the agent concentration measurements were always *below* a volume fraction of 0.06.

One operational strategy to mitigate the poor dispersion of CF_3I for cold temperature applications has been proposed, namely, warming the bottle before being released into the cold ambience. Figure 8-94 and Figure 8-95 illustrate, respectively, the concentration measurements at the two locations in the nacelle simulator when the agent was released at ≈ 20 °C and the airflow through the nacelle was maintained at ≈ -40 °C. The concentration levels obtained under this condition were still much lower than those at room temperature; however, some improvement was clearly noted when compared to the results at cold temperature.

To further illustrate the potential of this approach, thermodynamic calculations were performed using PROFISSY, FISSYCS, and the same initial bottle conditions at room temperature. (1 kg of CF_3I in a 2.36 L bottle, pressurized with nitrogen to 4.12 MPa at 22 °C, see discussion above.) Note that in the following analysis, the heat transfer between the flashing spray and the nacelle surroundings was not considered. The calculations were performed as follows. First, a final state of the bottle was obtained using PROFISSY to simulate heating or cooling of the bottle. The state was then used as input for FISSYCS to obtain the amount of liquid fraction resulting from an isentropic process taking the fluid from the prevailing pressure to 0.101 MPa.

Figure 8-96 shows the calculated liquid fraction as a function of temperature. The liquid fraction decreases with increasing bottle temperature. However, there is a discontinuity at about 94 °C. At temperatures below the discontinuity temperature, the initial state is liquid-phase, the isentropic process results in a liquid-vapor system.

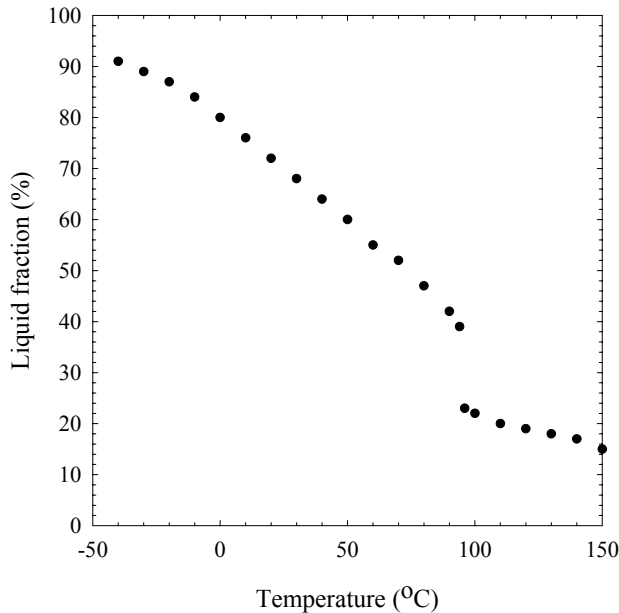


Figure 8-96. Calculated Liquid Fraction as a Function of Bottle Temperature.

At temperatures above the discontinuity temperature, PROFISSY predicted a single-phase gaseous state before the isentropic process. The discontinuity is the result of the occurrence of a two-phase system due to the isentropic process. If the strategy is to decrease the liquid fraction, heating the bottle up to a temperature before the discontinuity temperature is reached seems to be an option. Although heating the bottle above the discontinuity temperature appears to be a better choice from the figure, a dichotomy exists. On the one hand, the resulting liquid fraction is much lower than that at any temperature below the discontinuity temperature. On the other hand, the isentropic process inadvertently transforms a gaseous phase, which facilitates the dispersion of the agent, back to a liquid-vapor phase, which may hinder agent transport through cluttered space in the nacelle. However, system constraints (*e.g.*, bottle operating pressure and space) on a specific aircraft platform may ultimately limit the implementation of either approach because the bottle pressure is a function of temperature. Although the above argument provides some thermodynamic basis for examining the feasibility of heating the bottle to improve dispersion for cold temperature applications, the interaction of a flashing spray with cold nacelle surfaces may also play an important role in determining subsequent agent dispersion. Further experiments are needed to validate the concept.

The results from the two measurement locations in the nacelle have shown that the dispersion of CF_3I under this condition with the equipment and the discharge nozzle used is not very effective and there is substantial deterioration in agent concentration. If the military specification for halon 1301 extinguishing concentration can be applied to CF_3I (volume fraction of 0.06 for 0.5 s), the concentration levels at the two measurement locations in the nacelle never exceed the extinguishing concentration requirement. The situation worsens at the location further away from the agent injection port. If the extinguishing concentration for the nacelle is designed based on room-temperature test data, the measurements indicate that the dispersion and performance of the agent are likely to deteriorate when the agent is used at a temperature below its normal boiling point.

Implications

This study using CF_3I as a surrogate shows that the agent's normal boiling point and the prevailing bottle and nacelle conditions are critical to the agent dispersion processes for low temperature applications. Halon 1301 and HFC-125, with their respective normal boiling points lower than $-40\text{ }^\circ\text{C}$, will disperse efficiently. The benefit of a more efficient suppressant chemical with a high normal boiling point will be readily offset by the poor dispersion performance (puddling and slow evaporation) in a nacelle when the agent is expected to be used at temperatures below its normal boiling point. Heating the storage bottle before agent discharge could improve agent dispersion performance at low temperatures. For agents with high normal boiling points, nacelle fire suppression system design should not be solely based on the agent dispersion performance data obtained at room temperature, and low-temperature dispersion tests should also be conducted.

8.5 MODELING OF FLUID DISPERSION IN A NACELLE

8.5.1 Background

The focus of this research was to develop engineering models of flow, fire, and fire suppression and extinguishment in cluttered environments. These models will advance the fundamental knowledge of fire dynamics and suppression and provide a foundation for optimizing the distribution of suppressants for newly designed or retrofit fire safety systems in aircraft engine nacelles. This work was carried out in a joint, iterative computational/experimental approach to develop engineering subgrid models for use in integral CFD and fire field simulations. Models were developed using detailed CFD calculations performed at Sandia National Laboratories and discovery and validation experiments performed at Air Force and Naval laboratories. Only gaseous agents were investigated initially. The end goal was to provide computational tools to improve suppressant delivery and develop guidance to system designers.

8.5.2 CFD Models

During the course of the NGP, several CFD codes, which include VULCAN, CFD-ACE, Fire Prediction Model (FPM), and Fire Dynamics Simulator (FDS), have been assessed for use in modeling of fluid dispersion and fire suppression in aircraft engine nacelle environment. The simulation effort in this project focused mainly on the use of VULCAN because of its many newly developed sub-models specifically for aircraft engine nacelle applications.

Basic Features of VULCAN

VULCAN has been developed at Sandia National Laboratories (SNL) in collaboration with the SINTEF Foundation and the Norwegian University of Science and Technology. VULCAN is derived from the KAMELEON Fire model^{44, 45} and uses an extension of the SIMPLEC method of Patankar and Spalding⁴⁶ to solve the conservation equations on a structured, staggered, three-dimensional Cartesian, finite-difference grid. The brick mesh is employed to facilitate rapid solutions of radiative heat transfer. The ability to resolve the geometry of the system is only limited by the ability to construct the appropriate grid with the Cartesian grid generator available in VULCAN. First- and second-order upwind schemes can be used for the convective terms. Turbulence is modeled using a standard two-equation $k-\varepsilon$ model. The

VULCAN code has the capability of performing fire simulations, and the combustion simulation is based on Magnussen's Eddy Dissipation Concept (EDC) assuming infinitely fast combustion.⁴⁷ Models of soot generation and oxidation are also included.

The wide range of length-scales in reacting flows presents a significant modeling challenge. Where air flows are high enough that the flow is turbulent (as is typical in most terrestrial fire environments), fluid-mixing length-scales may span several decades from the geometric scale down to the Kolmogorov scales. Chemical length-scales may be even smaller, typically less than a millimeter. Because it is not possible to resolve the full range of dimensions, models of subgrid-scale processes are employed. Within the VULCAN fire-field model, the k - ϵ model is employed to predict the effect of turbulent fluctuations on the flow, and the EDC model predicts the chemical evolution using a collection of perfectly stirred reactors (PSR).

Modeling Fire Suppression

Combustion in VULCAN is modeled using the EDC that can be thought of as a distribution of PSRs that relate the fuel-consumption rate to the fluid-mixing rate, the latter obtained from turbulent time scales. The submodels within VULCAN assume that the fuel-air mixing rates scale with the inverse of the Kolmogorov time scale (τ_K). The actual mass rate of reactant mixing is proportional to τ_K and is also a function of the local mass fractions of reactants. In high-fidelity modeling of turbulent diffusion flames, the fluid time scales corresponding to extinction are found to be very close to the Kolmogorov time scales.⁴⁸ Conversion of reactants to products and the associated heat release occur at a rate determined by either the mixing rate or some maximum chemical rate that is a function of the composition. Fires are typically limited by mixing, but if the ratio of time scales is sufficiently small (fast mixing), then conversion of reactants to products and the associated heat release cannot proceed to completion. This results in a reduction in temperature leading to a reduction in chemical rates. Continued reduction in the mixing time relative to the chemical time leads to a state where no combustion is possible, and the flame is extinguished. The ratio between fluid and chemical mixing times is generally referred to as the Damköhler number. A suitable chemical time relevant to flame extinction can be defined as the value of PSR extinction time corresponding to a switch from combustion occurring to combustion being impossible, which is the chemical time scale representing the fastest possible chemical reaction rates. For Damköhler numbers smaller than a critical value, the flame will be extinguished. The critical Damköhler number that relates τ_K and the extinction time is not known *a priori* and is determined empirically by matching blow-off criteria for an ethane jet flame.⁴⁹ The suppression model takes advantage of this Damköhler number criterion by determining values corresponding to extinction from detailed chemical-kinetic calculations in the PSR configuration.

The chemical time scale is a function of the reactant mass or mole fractions, enthalpy, and pressure, assuming these reactants originate at ambient pressures and temperatures, neglecting enthalpy changes. While it is straightforward to make the chemical time scale a function of the enthalpy (and this has been done with the suppression model), the results then depend strongly on heat flux through walls, a quantity that is not well known for the experimental configurations. Two neglected thermal effects are of moderate significance: For JP-8 pool fires, the initial fuel vapor temperature is somewhat greater than ambient; this tends to reduce the chemical time scale. Radiative thermal losses and losses to the walls, while included in VULCAN, are neglected in the suppression model because the magnitude of these losses is dependent on the heat flux through the wall, which is unknown. Estimates indicate that heat losses to obstructions are significant here and tend to increase the chemical time scale.

Within VULCAN, chemical reactions are greatly simplified, reflecting the predominance of mixing processes in fires. This simplified treatment of kinetics is not necessarily sufficient for suppression predictions, and chemical time scales corresponding to the addition of suppressant are calculated off-line. These off-line calculations use the CHEMKIN PSR capability⁵⁰ with a detailed chemical mechanisms for iso-octane from Curran et al.,⁵¹ coupled with a mechanism for halogenated suppressants from Babushok et al.⁵² Chemical time scales have been obtained for iso-octane combustion in air with HFC-125, N₂, H₂O, CO₂ and CF₃Br, although only results with the first suppressant are described here. Chemical time scales relevant to suppression are obtained by conducting PSR simulations at successively shorter residence times until combustion is extinguished, thereby defining the extinction time. To facilitate use in CFD simulations, values for the extinction time are fitted to a suitable functional form as a function of the mole fraction of HFC-125 added to the inlet air. For iso-octane, the selected surrogate for JP-8, the curve fit is inverted to express the magnitude required to extinguish the mixture. Given the chemical time scale as a function of the fluid cell composition and the mixing rate based on the dissipation rate and viscosity (through the Kolmogorov time scale), the magnitude of the Damköhler number in that cell determines whether combustion takes place in that cell or not. In the numerical implementation, given τ_K in a fluid cell, the time required to extinguish the flame is obtained using a comparison with the HFC-125 mole fraction in the fluid cell to indicate whether suppression occurs. A similar approach was used by Byggstoyl and Magnussen for local quenching in the absence of suppressants.⁵³ A detailed description of the fire suppression model can be found in Hewson et al.⁵⁴

Subgrid Scale Clutter Model

The release and transport of an agent into an engine nacelle is sensitive to local geometrical features or “clutter” that is difficult to resolve numerically without using an excessively large CFD grid. Examples include wire bundles or hydraulic lines. Capturing these features in a grid will result in extremely small time steps for accurate numerical simulations of agent release and subsequent fire suppression. An alternative is to use a sub-grid scale (SGS) model to represent the macroscopic effects of these small features using reasonably sized CFD grid-cells. For agent dispersal in a cold flow environment, the macroscopic flow effects of sub-grid clutter cells must have two main effects. The first is to provide a momentum sink due to viscous and pressure drag forces. The second is to either increase or decrease the turbulent kinetic energy, depending on the local clutter size relative to the characteristic length-scale of turbulence. In general, if the size of the clutter is smaller than the turbulent length-scale, the turbulent kinetic energy will decrease, and vice versa. Regarding flame suppression, the clutter serves as either a mechanism for flame attachment or for local extinction depending on the local time scales of the heat transfer to the clutter and chemical kinetics for ignition.

Specifically, the effects of subgrid scale (SGS) clutter on the momentum and turbulent kinetic energy transport were developed with application to engine nacelles.^{55, 56} The modeling methodology was based on a two-phase averaging procedure introducing expressions that required SGS modeling. The SGS models were formulated using a combination of well-established constitutive relations borrowed from the porous media literature and classical relations for drag on bluff bodies. The modeling methodology was exercised for two classes of problems. The first was flow in a porous media for which the obstructions were relatively dense. For this problem, predictions using the SGS clutter model were compared to established correlations taken from the porous media literature. The second class of problems was a cylinder in cross-flow for which both detailed experimental measurements and detailed CFD calculations of velocity deficit and kinetic energy profiles were available. Results from the experimental

measurements revealed that the effect of upstream turbulence had a significant effect on the drag coefficient. Comparisons of the detailed CFD predictions to experimental measurements showed reasonable agreement for the mean and RMS streamwise velocity indicating that extracting phase-averaged quantities from the detailed computations, as part of future efforts, was a sound approach for determining unknown clutter model constants in a bluff body drag limit.

Basic Features of CFD-ACE

CFD-ACE, a commercial computational fluid dynamics model with a body-fitted coordinate grid, is a pressure-based commercial code^{57,58} that solves the Favre-averaged Navier-Stokes equations. The code uses a cell-centered control volume approach to discretizing the governing equations. It employs an iterative solution scheme in which the assembled equations for each dependent variable are solved sequentially and repeatedly to reduce errors to acceptably low values.

Various modeling options are available. In the present calculations, the governing equations were solved until a steady-state solution was reached. Heat transfer was not modeled. The code was applied using the incompressible option with a single fluid (air) and the k - ϵ turbulence model of Launder and Spalding⁵⁹ with wall functions. In addition, the k - ω turbulence model of Wilcox⁶⁰ and the Low Reynolds number k - ϵ turbulence model of Chien and Smith⁶¹ were used in sensitivity calculations. First-order upwind spatial differencing was used for the turbulence quantities and 90 % second-order upwind spatial differencing (with 10 % first order blend) was used for the velocity and density. The structured grid utilized a body-fitted coordinate system with multiple domains.

Basic Features of FPM

The Fire Prediction Model (FPM)⁶² simulates the events occurring during the penetration of a single ballistic threat into an aircraft and subsequent penetration of a fuel tank. The model describes the principal processes involved the initiation and sustainment of fires, or ullage explosions in a dry bay. The model runs on personal computers, and queries the user for specific information about the conditions to be analyzed. No off-line computations by the user are required; the model contains pre-determined threat, fluid, and target material data encompassing a wide range of conditions of interest. The FPM was designed specifically to provide a tool to examine dry bay fires and ullage explosions over a wide range of conditions rapidly and apply directly to the needs for live-fire testing predictions, planning, and post-test analysis; vulnerability estimates (probability of kill given a hit, $P_{k/h}$); and aircraft design guidelines. The simulation principally relies on basic physical principles which are supplemented by empirical data as needed. Study conditions that can be examined by the FPM are grouped into 9 categories and briefly described below.

Flammable Liquid Container Type The user can select an integral or non-integral tank or a liquid line.

Run Setup The run setup option allows the user to tailor the run to their needs. The user can select single-shot or parametric runs, specify the flow field cell size, and modify the time step to increase speed or accuracy.

Target Vehicle The FPM allows the user to specify either an air or ground target vehicle. Selections of threats, liquids, and target materials are restricted based on the vehicle selected.

Ignition Source The FPM simulates spray ignition by either a ballistic threat, hot surface, or electrical spark. Ignition by a hot surface can occur directly by sprayed droplet impinging directly onto the hot surface or indirectly as liquid vapor previously released into the bay is carried past the hot surface.

Ballistic Threat Four types of ballistic threats can be simulated by the FPM: Armor-Piercing Incendiary (API) projectiles, High Explosive Incendiary (HEI) projectiles, warhead or bomblet fragments, or shaped charges. Because the functioning of an API projectile can vary depending on impact conditions, four types of function can be simulated: complete, partial, slow burn, or delayed.

Flammable Liquid Seven flammable liquids can be selected by the user. Three military jet fuels (JP-4, JP-5, or JP-8, two different flash points) a diesel fuel (DF-2), or two military hydraulic fluids (MIL-H-5606 and MIL-H-83282) are available. In addition, the user is given the option to describe the characteristics of some liquid of interest, other than what is available.

Encounter Conditions The user may define a wide range of environmental conditions under which the simulation is to be run, including target altitude, fuel and ambient air temperatures, ventilation air velocity, external pressure, and target velocity. For altitudes above sea level, the model will compute ambient conditions using the standard atmosphere. External air pressures will be computed by the model based on the target surface and location impacted and orientation of the damage-hole to airflow.

Dry Bay Description The FPM provides the user with a large number of options and features to describe the dry bay. First, the dry bay dimensions and location are defined. The dry bay is assumed to be a rectangular parallelepiped. Other items needed to define the bay include wall material and thickness; internal clutter locations and dimensions; structural barrier locations, dimensions, and orientation; ventilation flow areas and locations; and the presence of an ECS duct. As part of the dry bay description, a fire-suppression system can be specified. The user has a wide range of options to describe the fire-suppression system. Ten agents can be selected, including both cooling and reactive agents. Next, the number, location, and type of injector can be specified. The type can be spherical (agent injected radially from location) or directional (agent injected in a specified direction). The duration of the agent injection and mass-rate of injection are also needed. Finally, the injection can be activated by an IR sensor or manually, at the user's discretion. The clutter option is sufficiently general to allow the user to shape the bay into various shapes and/or multiple compartments. If a hot surface is present within the bay, the clutter is used as the hot component, and the user can describe the hot surface by its location and temperature.

Impact Condition The FPM requires a description of the impact conditions, including threat impact velocity, threat approach direction, and point of impact on the target's surface. In addition, the model can simulate the threat function to be on the dry-bay surface or internal to the bay.

As part of this effort, the FPM was modified to allow ignition of a spray fire with a user-described ignition source, bypassing the ballistic-impact routines of the model. The approach used by the FPM to simulate a spray fire is known as a separated-flow (two phase) model. This approach treats the finite rates of exchange of mass, momentum, and energy between the liquid and gas phases. In general, there are three approaches to separated flow models, reflecting differences in simulating evaporating and combusting sprays. The FPM uses the discrete-droplet approach. In this approach, the entire spray is divided into many representative samples of discrete drops whose motion and transport through the flow-field are found using a Lagrangian formulation in determining the drop's history, and an Eulerian

formulation is used to solve the governing equations for the gas phase. It is assumed that the spray is dilute; i.e., although the droplets interact with the gas phase, they do not interact with each other. Thus, droplet collisions are ignored and empirical correlations for single droplets can be employed for interphase transport rates.

In two-phase models, the liquid droplet flow is divided into a finite number of classifications: Each drop class is assigned an initial diameter, velocity, direction, temperature, concentration, position, and time of injection. The temporal evolution of each class is then determined throughout the flow.

The FPM uses this approach, adapting it to the FPM dry-bay flow-field. In effect, the FPM tracks the position of each class of droplet, computing the vaporization for each class dependent on the droplet location and bay conditions at that location, and the model's flow-field computes the conservation equations. The position of a given group is calculated from:

$$\begin{aligned}x_p &= x_{p_o} + \int v_{p_x} dt \\y_p &= y_{p_o} + \int v_{p_y} dt \\z_p &= z_{p_o} + \int v_{p_z} dt\end{aligned}\quad (8-43)$$

The instantaneous velocity is determined by the solution of the equation of motion.

$$m \frac{dV}{dt} = -\frac{1}{2} C_d \rho A V^2 + mg \quad (8-44)$$

The standard drag coefficient for solid spheres is employed for sprays.

$$C_D = \begin{cases} \frac{24}{\text{Re}_{d_p}} \left[1 + \frac{\text{Re}_{d_p}^{2/3}}{6} \right] & \text{for } \text{Re}_{d_p} < 1000 \\ 0.44 & \text{for } \text{Re}_{d_p} > 1000 \end{cases} \quad (8-45)$$

The Reynolds number is defined as:

$$\text{Re}_{d_p} = \frac{d_p |v_p - v|}{\nu} \quad (8-46)$$

The simulation of the transport properties involved in fire involves the application of the conservation equations of mass, momentum, energy, and species for that system. These equations simply describe a balance of the net rate of inflow and outflow of some particular parameter, its rate of storage, and its rate of production and destruction within a volume. The FPM describes the motion of the fluid within the bay by the Eulerian approach where the composition, velocity, and state of the fluid everywhere in the bay occupied by the fluid at all instants are determined. To derive the Eulerian equations of motion, a stationary coordinate system is chosen and fluid is observed entering and exiting a volume of arbitrary shape and size. This control volume is found within the fluid and is at rest with respect to the coordinate system. In the FPM, the volume is a cube whose length is specified by the user.

The FPM uses a staggered grid concept where the scalar properties of pressure, temperature, mass, and species mass are determined at the cell center and fluid velocities are established at each cell edge in each coordinate direction.

Solutions are obtained on a numerical grid of elementary control volumes which fill the entire dry bay. This approach ensures local balances in the many small control volumes, subject only to the particular boundary conditions. To improve computational efficiency and reduce model run-time, the FPM utilizes a multi-cell, three-dimensional dual grid system; a diffusion and convection grid. Within the diffusion grid, the simulation of fire is performed by the solution of the conservation equations of mass, momentum, species, and energy. Because convective currents work over much larger scales than the processes of diffusion and combustion, the conservation of momentum (the convective mass and energy flow) is performed in the convective grid and results superimposed into the diffusion grid by the prorating the flow.

The mass-rate of change of chemical fire suppressant can occur by convection, depletion by chemical reaction, or injection into the bay. The FPM simulates both chemical and "cooling" types of agents. Cooling agents such as CO₂ and H₂O extinguish flame by the rapid introduction of mass into the combustion zone, which absorbs heat through changes of heat capacity and the heat of vaporization as described above. Chemical agents extinguish fires by the removal of free radicals throughout the combustion process, precluding complete combustion as well as providing some cooling effect.

The FPM treats the chemical reaction of fuel vapor, oxygen, and suppressant as a one-step, third-order reaction, as shown below.



where k is the specific reaction rate constant and follows the Arrhenius law

$$k = A \exp\left(\frac{E}{RT}\right) \quad (8-48)$$

Basic Features of FDS

Fire Dynamics Simulator (FDS), developed by NIST, is a CFD model of fire-driven fluid flow. The formulation of the equations and the numerical algorithm and a user's guide can be found in McGrattan et al.^{63,64} In conjunction with FDS, an OpenGL graphics program called Smokeview was also developed by NIST to visualize the numerical output generated by FDS. Smokeview performs this visualization by presenting animated, traced, particle flow, animated contour slices of computed gas variables, and animated surface data. Smokeview also presents contours and vector plots of static data anywhere within a scene at a fixed time. A detailed description of Smokeview can be found in Forney and McGrattan.⁶⁵

Since its first release in February 2000, about half of the applications of FDS have been for design of smoke-handling systems and sprinkler/detector activation studies. The other half consists of reconstructing residential and industrial fires. Throughout its development, FDS has been aimed at solving practical problems in fire-protection engineering, while at the same time providing a tool to study

fundamental fire-dynamics and combustion. Some of the major components and sub-models used in FDS are briefly described below.

Hydrodynamic Model FDS solves numerically a form of the Navier-Stokes equations appropriate for low-speed, thermally driven flow with an emphasis on smoke and heat transport from fires. The core algorithm is an explicit predictor-corrector scheme, second order accurate in space and time. Turbulence is treated by means of the Smagorinsky form of Large Eddy Simulation (LES). It is possible to perform a Direct Numerical Simulation (DNS) if the underlying numerical grid is fine enough. LES is the default mode of operation.

Multi-blocking This is a term used to describe the use of more than one rectangular mesh in a calculation. FDS calculations can prescribe more than one rectangular mesh to handle cases where the computational domain is not easily embedded within a single block.

Combustion Model For most applications, FDS uses a mixture-fraction model for combustion. The mixture fraction is a conserved scalar quantity that is defined as the fraction of gas at a given point in the flow-field that originated as fuel. The model assumes that combustion is controlled by mixing, and that the reaction of fuel and oxygen is infinitely fast. The mass-fractions of all of the major reactants and their products can be derived from the mixture by means of “state relations,” empirical expressions derived from a combination of simplified analysis and measurement.

Radiation Radiative heat transfer is included in the model via the solution of the radiation equation for a nonscattering gray gas, in some limited cases using a wide-band model. The equation is solved using a technique similar to finite-volume methods for convective transport, thus the name given to it is the “Finite Volume Method” (FVM). Using approximately 100 discrete angles, the finite-volume solver requires about 15 % of the total CPU time of a calculation, a modest cost given the complexity of radiative heat transfer. Water droplets absorb thermal radiation. This is important in cases involving mist sprinklers, but it also plays a role in all sprinkler cases. The absorption coefficients are based on Mie theory.

Geometry FDS approximates the governing equations on a rectilinear grid. The user prescribes rectangular obstructions that are forced to conform with the underlying grid.

Boundary Conditions All solid surfaces are assigned thermal boundary conditions, plus information about the burning behavior of the material. Usually, material properties are stored in a database and invoked by name. Heat and mass transfer to and from solid surfaces is usually handled with empirical correlations, although it is possible to compute directly the heat and mass transfer when performing a Direct Numerical Simulation (DNS).

Heat-Conduction through a Wall In early versions, heat that was conducted into a wall was lost to an infinite void. Now it is possible to transfer the heat from one room to another through a one-cell-thick wall.

Thin Walls It is possible to prescribe a thin sheet barrier to impede the flow. This is particularly useful when the underlying grid is coarse, or when the barrier is indeed very thin, like a window. However, FDS will reject obstructions that are too small relative to the numerical grid.

Suppression The suppression algorithm is a necessary adjustment to the mixture-fraction model of that prevents combustion from occurring in cool, oxygen-depleted environments. Recall that the basic mixture-fraction model assumes that fuel and oxygen burn when mixed. This is a good assumption in many fire scenarios, but when compartments become under-ventilated, or when agents are injected, the “mixed is burnt” model is not appropriate.

Initial Conditions It is possible to prescribe some non-trivial initial conditions. For example, certain parts of the domain can have temperatures different from ambient, and an initially constant flow-field can be prescribed.

8.5.3 Code Assessment Using Quarter-Scale Nacelle Tests and Simulations

To evaluate the fidelity of these CFD codes and their suitability for highly-cluttered engine nacelle applications, an initial exploratory effort was to investigate the flow field in a simplified, quarter-scale nacelle of typical shape. Calculations were performed using both the CFD-ACE and VULCAN codes. Flow conditions examined correspond to the same Reynolds numbers as test data from the full-scale nacelle simulator used by the 46th Test Wing of the United States Air Force (USAF). These flow conditions were examined using both models prior to fabrication of a test fixture. Based on the pre-test simulations, a quarter-scale test fixture was designed and fabricated for the purpose of obtaining spatially resolved measurements of velocity and turbulence intensity. Post-test calculations have been performed for comparison to the experimental results obtained from the quarter-scale test fixture. Because of geometric complexities, efforts to characterize the flow field in engine nacelles using computational fluid dynamics have been limited to simplified cases. Calculations performed to date include the analysis performed by Hamins et al.⁶⁶ of agent transport for the extensive set of tests performed in the Aircraft Engine Nacelle (AEN) test facility for the Halon Alternatives Research Program for Aircraft Engine Nacelles and Dry Bays. Marginal agreement between calculation results and experimental data was obtained. In some cases, opposite trends were observed in the calculations and experimental results. Additional calculations were performed by Lopez et al.⁶⁷ of a typical fighter nacelle geometry simulating agent release via solid propellant gas generator.

Quarter-scale experiments (to allow access of appropriate diagnostics guided by pre-test calculations) were performed at WPAFB.⁶⁸ Flow conditions were scaled to match the Reynolds numbers in the extensive set of experiments performed in the AEN facility as part of the Halon Alternatives Program. Calculations were performed and compared with experimental data at multiple cross sections within the flow field. The pre-test calculations assisted in the design and execution of the experiments required to gain the necessary knowledge for these kinds of flows. Then the post-test simulations, using both CFD-ACE and VULCAN, and the exact geometry and boundary conditions from the experiments compared CFD results with the experimental results.

The primary flow-field calculations used the CFD-ACE code because of its body-fitted coordinate features to represent smooth circular geometries. Although capable of simulating reacting flows, the CFD-ACE code does not contain models for radiative heat transfer, turbulent combustion, and soot production needed to simulate fires. These fire-physics models are included in VULCAN; however, the VULCAN model approximates the geometry by using a rectangular brick grid to facilitate the solution for radiation. Although many nacelle fire cases can be addressed without modeling the fire-physics, it is ultimately desirable to be able to represent the heat transfer from the fire and the fire-suppression effects,

such as the influence of turbulent flame strain combined with fuel/air mixtures. Both models have been applied in the pre-test and post-test calculations. The flow solution yielded by the approximate mesh used in the VULCAN code is compared with the results provided by the CFD-ACE modeling to quantify the effect of the Cartesian VULCAN mesh.

Simplified Nacelle Tests and Simulations

A photograph of the experimental test fixture is shown in Figure 8-97. The fuselage stations where experimental velocity data were obtained are shown in Figure 8-98.

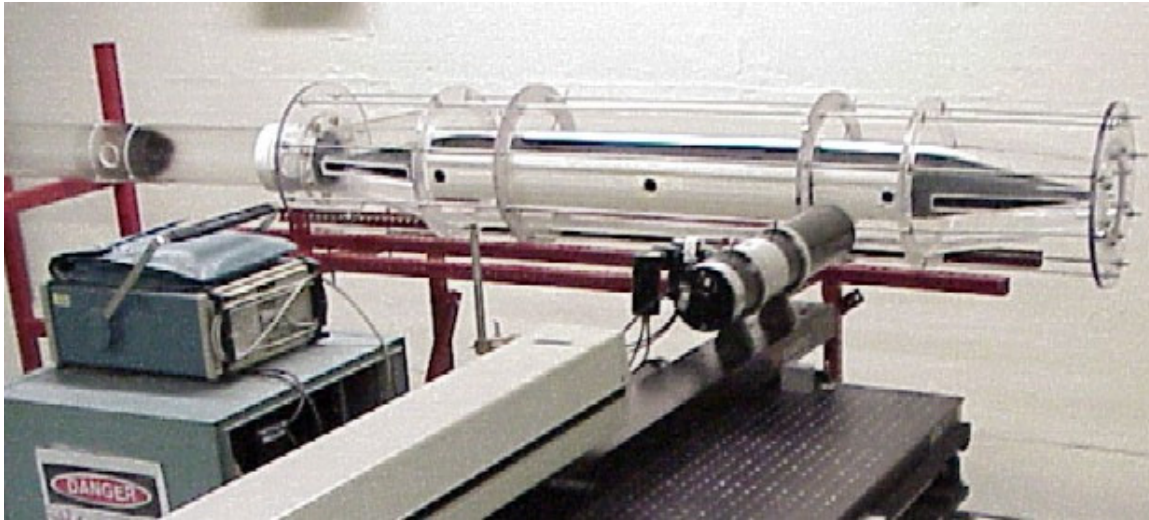


Figure 8-97. Photograph of the Quarter-Scale Nacelle Test Facility with LDV apparatus.

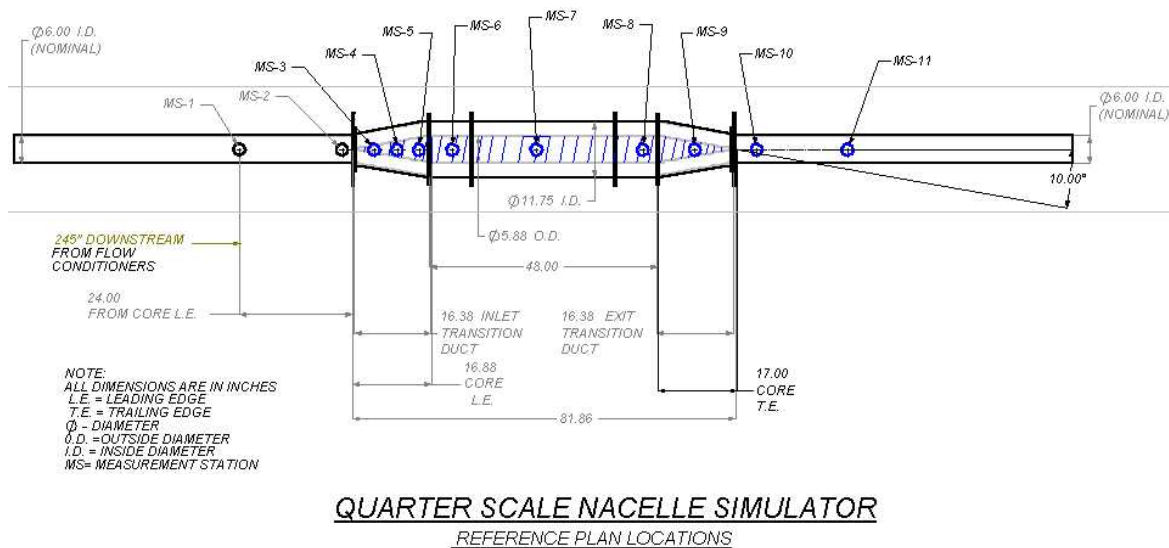


Figure 8-98. Measurement Stations in the Quarter-Scale Nacelle.

The CFD codes modeled the nacelle geometry starting at measurement station #1 (MS-1), where experimental data were used as an exact initial and boundary condition. The modeled geometry ended 10 pipe diameters downstream of the core region.

Upon entering the quarter scale nacelle, the flow undergoes a change from a pipe flow to an annular flow. This change in flow geometry is induced by a fluoropolymer cone, with a sharp leading edge centered within the nacelle. The cone is approximately 432 mm long and 149 mm at its base. The base of the cone is attached to the 149 mm teflon core which resides within the nacelle proper.

In the present simulator, the cone half-angle was machined at 10 degrees. As a result of the cone angle and transition duct wall offset, the flow is redirected away from the simulator centerline. This geometrical change occurs abruptly at the interface between the air supply duct and nacelle, and is therefore considered to be a sharp or discontinuous surface boundary.

Further, this divergence increases the flow cross-sectional area by a factor of approximately three. After passage through this transition duct the flow is abruptly redirected towards the simulator centerline by 10°. This occurs at a second discontinuity on both the inner surface (simulating the engine core) and outer surface. This next element, referred to as the nacelle proper is configured as an annular channel of constant spacing, H , between inner and outer surfaces – 74.7 mm. The nacelle proper extends downstream 1.22 m, approximately 16 H .

Exiting the nacelle proper the flow is redirected toward the simulator centerline through another 10-degree offset. This offset occurs at the entrance of a second cone, designated as the Exit Transition Duct (ETD). At the entrance of the ETD, the inner core of the nacelle proper undergoes a discrete transition back to a conical surface with a sharp trailing edge, thereby producing a transition from a converging annular channel back into a pipe flow.

Flow conditions upstream of the quarter-scale engine nacelle were determined by matching the Reynolds number (based on diameter) between the full-scale and quarter-scale nacelle simulators, for a specified mass flow. Air within the test range at ambient temperature and pressure was used to supply the flow facility in all tests. Supply air density was computed using the local temperature and pressure of the surrounding air resulted in a computed density of 1.2 kg/m³. From this density, a mass flow for the quarter-scale nacelle was determined to be approximately 0.344 kg/s. Assuming uniform flow, the average velocity within the 152.4 mm air supply tube was computed and estimated to be 15.7 m/s. Under these conditions the Reynolds number based on tube diameter, Re_D was estimated to be 172,000.

Velocity measurements were accomplished using both hot-wire anemometry and laser-Doppler velocimetry (LDV). Several hot-wire traverses were obtained to confirm that the air supplied to the simulator using an external blower was adequately conditioned. Verification of the flow conditioning section consisted of the acquisition of velocity data at the exit of the inlet supply tube with a typical hot-wire, nominally 4 microns in diameter and 1.25 mm-long, positioned normal to the mean flow. Velocity profiles were obtained by horizontally traversing across the tube diameter. Each velocity traverse consisted of measurements at 38 locations across the tube diameter. At each spatial location, 5000 samples were acquired from which a mean velocity and turbulence fluctuation level were computed. Once the supply airflow was considered to represent a fully-developed pipe flow, the simulator was attached to the inlet supply tube, and velocity traverses utilizing an LDV were initiated, which locations

or measurement stations were determined from prior simulations conducted by Sandia National Laboratories (SNL).

For VULCAN, the extreme length of the geometry created a grid with many computational cells (Figure 8-99). The final Cartesian grid consisted of 196 (X -direction) by 45 (Y -direction) by 45 (Z -direction) grid points for a total of 396,900 cells in the simulation. The cells in the cross-section were $0.007 \times 0.007 \text{ m}^2$, while the minimum cell length in the axial direction was 0.0085 m and varied along the pipe (refined in transition regions and stretched in the exit pipe and other straight sections). The simulation time was approximately 5 days utilizing a 250 MHz processor. The solution was converged such that all residuals were reduced 5 orders of magnitude.

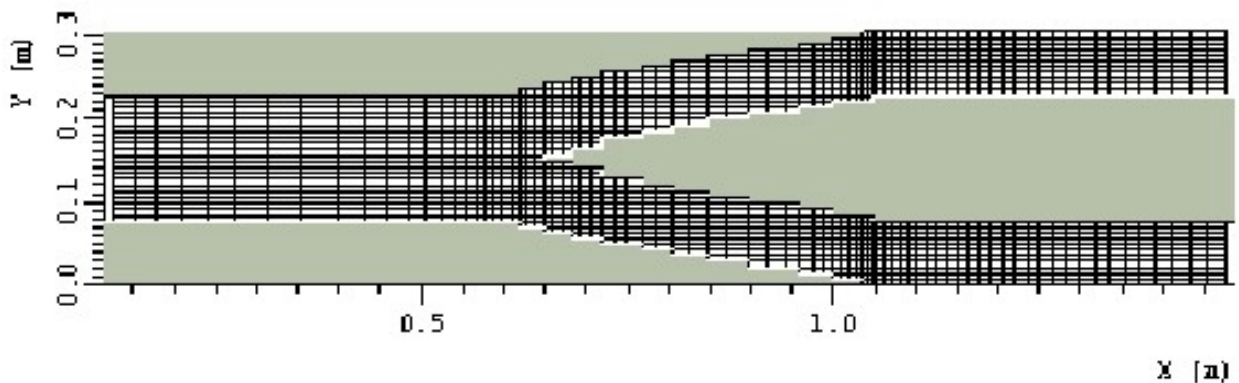


Figure 8-99. VULCAN Gridding for the Quarter-Scale Nacelle.

The computational grid used by CFD-ACE consisted of 301 axial (primary flow direction) points, 25 radial points, and 48 circumferential points, for a total of 361,200 grid points. Example slices from the grid are shown in Figure 8-100. Axial grid spacing in the annular (nacelle/core) region varied from 0.6 cm near the corners of the expansion/contraction regions to 1.8 cm in the middle section. Radial spacing was approximately 0.2 cm throughout the annulus. Circumferential spacing was constant at 7.5 degrees, which relates to arc dimensions of 2.0 cm at the maximum nacelle diameter to 1.0 cm at the maximum core diameter. In addition to the fine three-dimensional solution, a coarser mesh solution was obtained. The coarse mesh was generated by extracting every other grid point in all three directions from the fine mesh. The coarse mesh contained 151 axial points, 13 radial points, and 24 circumferential points, for a total of 47,112 grid points. In both cases, convergence was obtained such that all residuals of interest (velocity, pressure, turbulence) were reduced by more than 5 orders of magnitude. The fine mesh solution required 400 Mbytes of memory, 2200 iterations and 15 days computing time on a 250 MHz processor.

The boundary conditions used in the CFD simulations were carefully applied to represent the experimental conditions. In some cases, a slight deviation from the experimental conditions was necessary. The boundary conditions are fully discussed in Black et al.⁶⁹

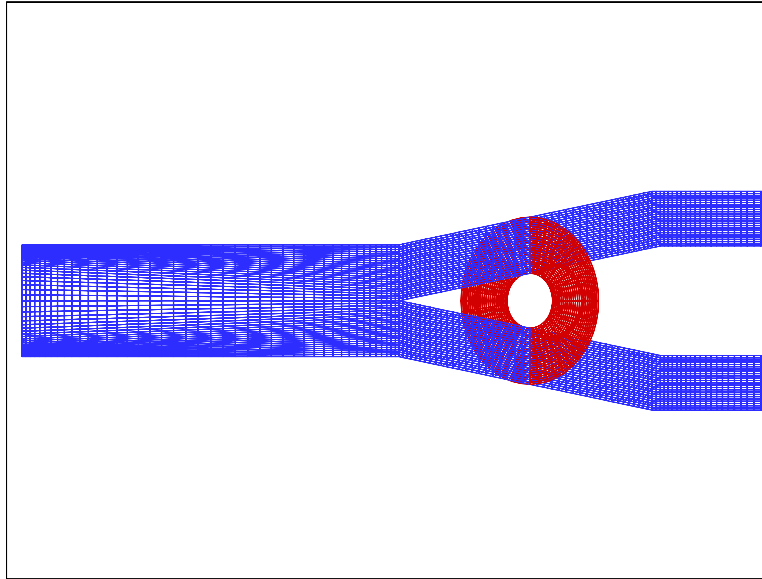


Figure 8-100. Section of the CFD-ACE Grid Used in the Simulation.

The data measured at the inlet (MS-1) showed a slight asymmetry in the velocity profile. It was not possible to use this asymmetric velocity profile as an inlet boundary condition in the calculations since only a radial profile was required. Instead, a logarithmic symmetrical profile was used to fit the data.

$$\frac{u}{u_{\max}} = \left(\frac{y}{R}\right)^{0.12} \tag{8-49}$$

The agreement with measured inlet profile is shown in Figure 8-101. In both cases, the maximum velocity is 20.07 m/s. Similar to the inlet velocity, the inlet turbulence intensity was also asymmetric. The simulations used a symmetric inlet turbulence intensity based on a parabolic curve fit of experimental data. This was accomplished by splitting the experimental data set at the midpoint, mirroring both sides across the centerline, and fitting a parabolic curve to these data in Figure 8-102. The resulting equation for the inlet turbulence intensity is shown on the plot as the solid curve.

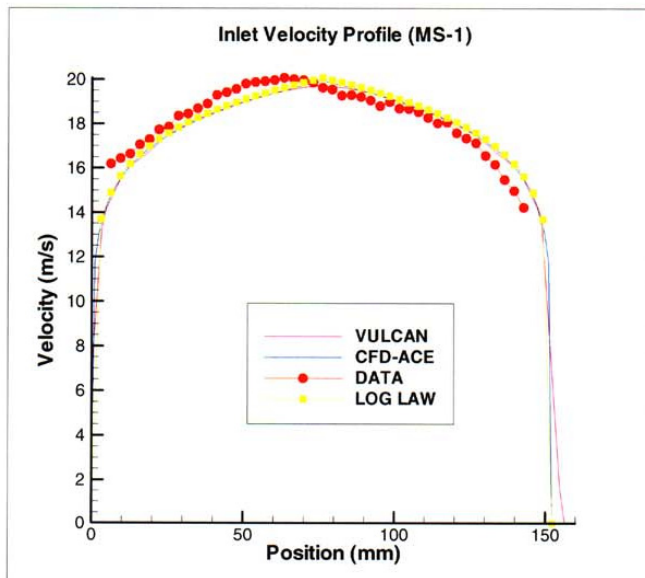


Figure 8-101. Inlet Velocity Profile.

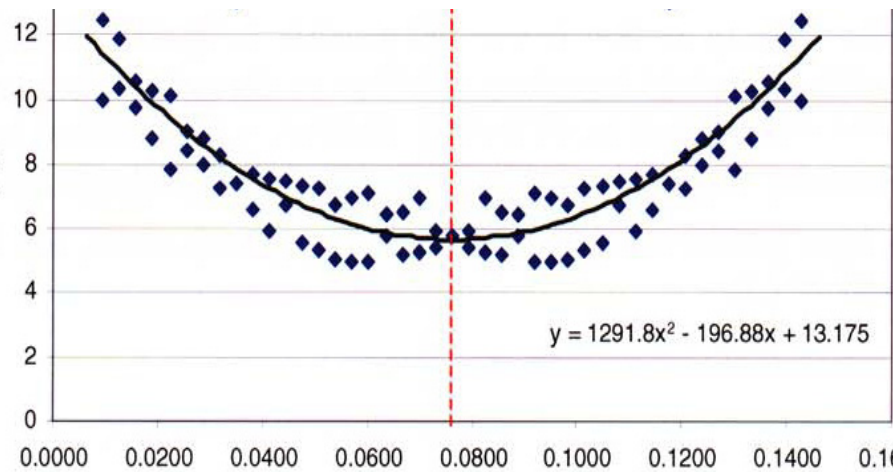


Figure 8-102. Inlet Turbulence Intensity Profile.

Comparison with Experimental Data

At the outlet of the nacelle geometry, constant pressure was specified using standard ambient conditions of 98,700 Pa and 293 K. The outlet was located 10 pipe diameters downstream from the nacelle's core. Along the surfaces of the core there was no surface roughness, and the temperature was likewise 293 K.

The experimental velocities at MS-4 are slightly larger than the CFD-ACE predictions and show oscillations near the nacelle wall and core wall (Figure 8-103). The VULCAN velocity predictions show a very narrow band of high velocity flow with rapid decreases in velocity away from the center of the channel because the VULCAN grid is not smooth along the angled walls and is blocking more of the flow. The experimental data shows poorer resolution near the walls. The experimental turbulence intensity values agree with the CFD predictions in the center of the channel but deviate near the walls.

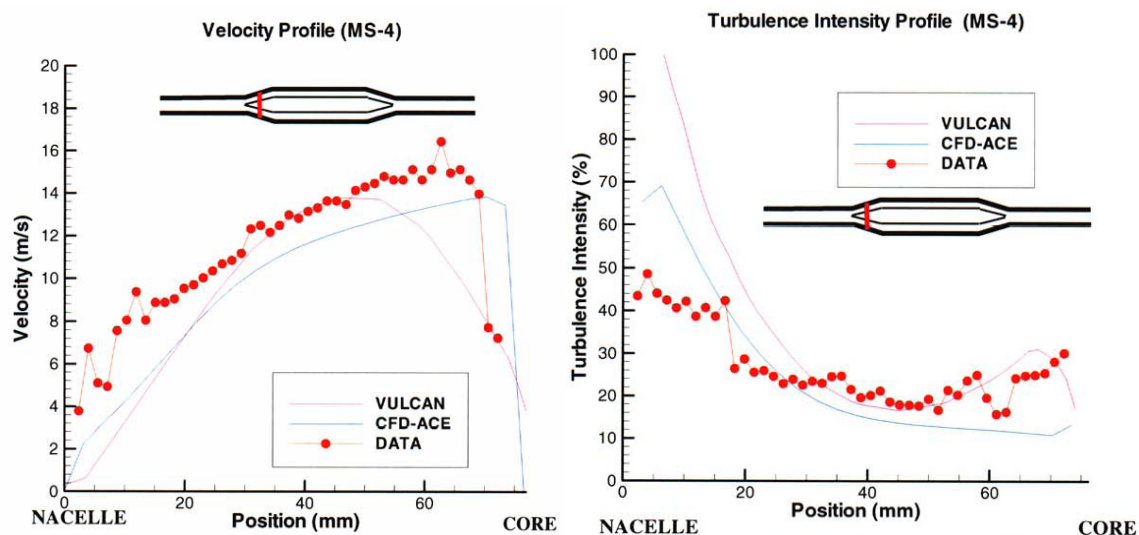


Figure 8-103. Velocity and Turbulence Intensity Profiles at Measurement Station 4.

The velocity predictions at MS-7 are in very good agreement with the experimental data, and the CFD predictions of turbulence intensities also show good agreement, with the data showing slightly larger turbulence intensity. It should be noted that the experimental data does not span the entire distance to the core (Figure 8-104).

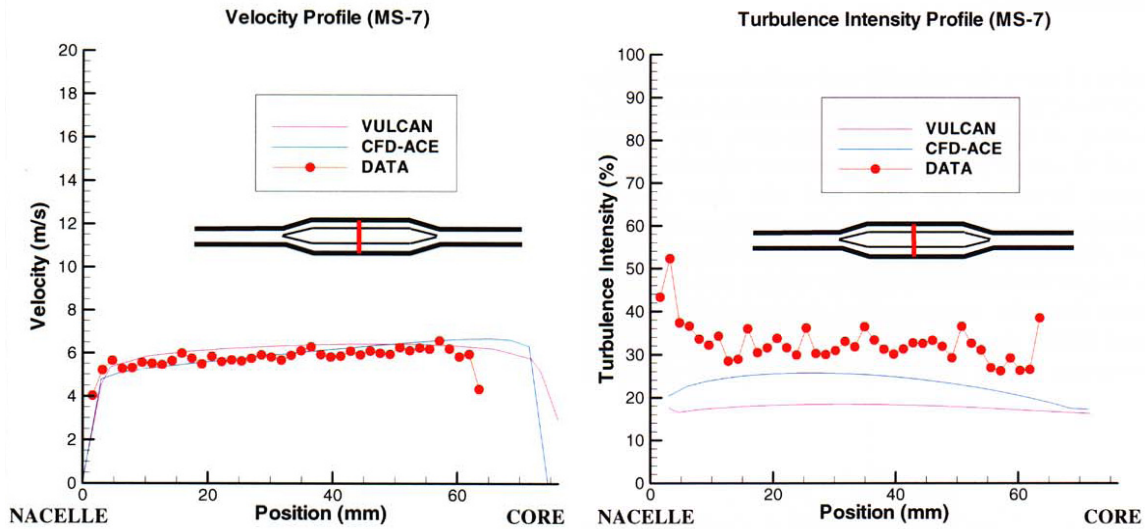


Figure 8-104. Velocity and Turbulence Intensity Profiles at Mid-nacelle.

The CFD-ACE velocity predictions shown in Figure 8-105 are in very good agreement with the experimental data, whereas, the VULCAN predictions show the flow slowing down near both the nacelle wall and the core wall and increasing in the center of the channel. This is caused by the stair-stepped grid along the angled walls which tend to squeeze the flow into center of the channel. Both CFD-ACE and VULCAN predict ~10 % lower turbulence intensity values than the experimental data, similar to the previous measurement plane (MS-8).

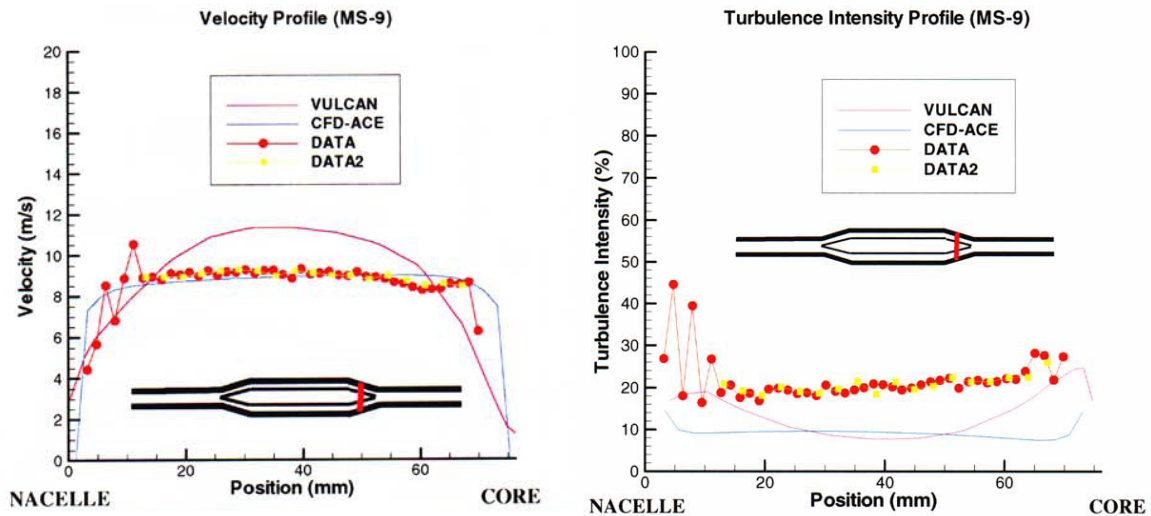


Figure 8-105. Comparison of Simulation and Experimental Data at the Exit Cone.

At the final measurement plane, MS-11, in the outlet pipe the predicted velocity profiles show the wake diminishing with increasing distance from the core, as shown in Figure 8-106. In addition, the measured turbulence intensity is considerably higher than CFD-ACE predicted, which is a constant turbulence intensity below 10 % for the majority of the flow across the pipe.

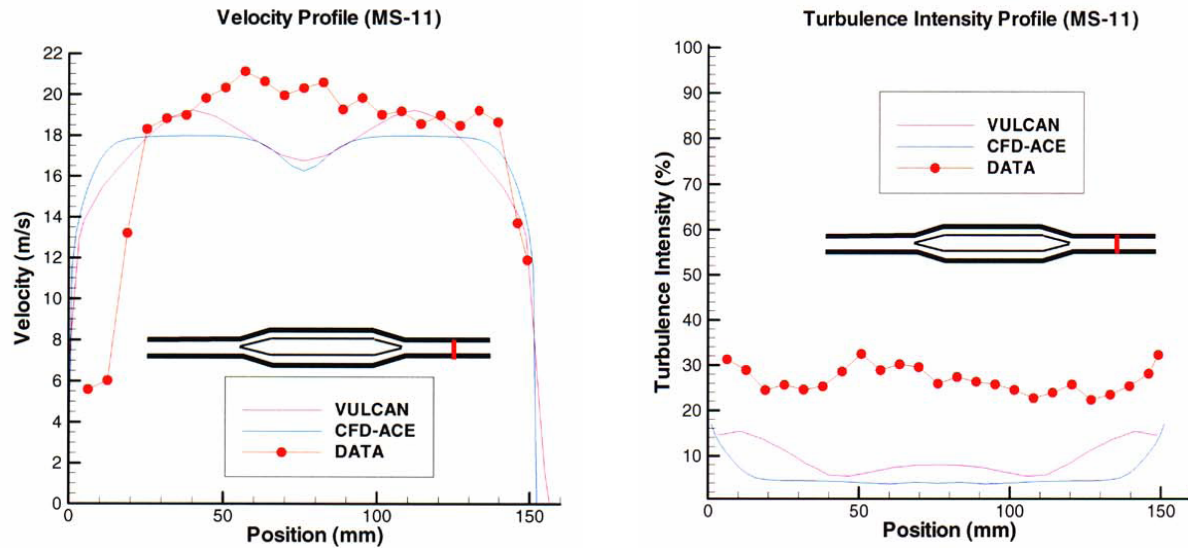


Figure 8-106. Velocity and Turbulence Intensity Profiles Flow in the Exit Pipe.

The comparisons of the numerical predictions with the experimental data, in general, showed good agreement with the velocity, and the turbulence intensity predictions also showed good agreement in the inlet pipe section and in the inlet transition section. However, the numerical predictions showed larger turbulence intensity near the corner region between the inlet transition duct and straight core section. Then, downstream the data consistently showed larger turbulence intensity at the remaining measurement planes, although the trends were similar. In addition, there were some differences between VULCAN and CFD-ACE results due to the Cartesian grid structure used by the VULCAN code. These differences mainly occurred in the inlet transition duct and the outlet transition duct where the walls are smoothly angled, but the grid is stepped. Also, the experimental data tended to show poorer resolution near the walls of the transition ducts because of the physical difficulties in measuring near these surfaces.

8.5.4 Assessment of VULCAN Fire Suppression Sub-model

The optimization of fire suppression systems in aircraft engine nacelle applications is made more challenging by the fact that clutter in the form of structural supports, wiring, piping, machinery and similar items can adversely affect the suppressant flow. Furthermore, recirculation zones that form on the downstream sides of clutter have been identified as favorable for flame stabilization.^{70,71,72} Of the various stabilized fires, liquid pool fires established behind obstructions such as structural ribs have been identified as some of the most challenging to suppress.^{70,71,72}

Flow obstructions can act as flame holders, stabilizing flames and making suppression difficult. Stabilization is aided by creating a recirculation region with relatively low dissipation rates, and thus large τ_k , and hot products. Suppression is made more difficult because it takes significantly more time for

suppressant to penetrate the recirculation zone than it takes for the suppressant to pass over an unobstructed flame. Hamins et al. and others^{66,75,73} have taken advantage of a simple mixing model in the form of the conservation equations for an unsteady PSR that predicts the suppression delay associated with the delay in mixing suppressant into a recirculation zone.⁵⁰ The model predicts that the mole fraction of suppressant in the recirculation zone varies as

$$X_{recirc} = X_{\infty} [1 - \exp(-t / \tau_{mix})] \quad (8-50)$$

where X_{∞} is the suppressant mole fraction outside the recirculation region and $\tau_{mix} \propto h / u^*$ is the mixing time, proportional to the quotient of the velocity past the recirculation zone and the recirculation zone thickness, here taken to be the step height, h . Takahashi et al.⁷⁴ measured the proportionality constant for their configuration to be $\tau_{mix} = 34.7(h / u^*)$ where u^* is explicitly given as the average of the mean flow velocity over the step and the mean flow without the step.

In this section, the efficacy of the VULCAN fire suppression sub-model for the suppression of pool fires stabilized behind obstructions was assessed. The suppression model was evaluated using measurements of the agent required to suppress a fire stabilized behind a rearward-facing step.⁷⁵ The CFD code was then used to indicate ways in which the arrangement of clutter within an environment resembling an aircraft engine nacelle may change suppressant requirements, suggesting potential design practices that might be confirmed with further experimental measurements.

For a CFD model to adequately predict suppression in the presence of obstructions, it will be important that the model can reasonably predict (1) the suppressant required to extinguish flames at a given fluid mixing rate, and (2) the rate of suppressant mixing into recirculation regions. To address these questions, simulations using the suppression model described above were conducted for JP-8 pool fires stabilized behind a backwards-facing step, and results are compared with measurements of Takahashi et al.⁷⁵ Those simulations for which there are experimental data available and that are involved in model evaluation are referred to as Case A1; see Table 8-12. All simulations denoted as Case A are conducted in a 154 mm by 154 mm square wind tunnel, 770 mm long, with a 64 mm tall backwards-facing step placed in front of a 150 mm by 150 mm JP-8 pool. Airflow through the wind tunnel was 10100 standard L/min, the turbulence level at the entrance was set to 6 % and the turbulent length scale, used to calculate the initial dissipation rate was set to 3 mm based on the turbulence generators employed in the experiments.

Table 8-12. Description of Simulations of Pool Fires Stabilized behind a Backwards-facing Step.

Case	Description	τ_{mix}
A1*	As in Takahashi et al. ⁷⁵ with the fuel being JP-8 and the suppressant being HFC-125.	0.23 s
A3	As in A1 but with a 42 mm rib on the upper wall collocated with the backwards-facing step.	0.15 s
A5	As in A1 but with a 42 mm rib on the upper wall 84 mm behind the backwards-facing step.	0.24 s
B1	22.5 cm high, 180 cm wide, and 180 cm long wind tunnel with 5 cm rib located 60 cm from entrance. A 45 cm long by 30 cm wide JP-8 pool was centered on the lower surface.	0.30 s
B2	As in B1 but with two 5 cm high longitudinal ribs each located 20 cm from the centerline.	0.30 s
C1	As in B1 but with the tunnel height reduced to 10 cm.	0.23 s
C2	As in B2 but with the tunnel height reduced to 10 cm.	0.23 s

*Used in model validation.

Figure 8-107 provides an overview of the simulation geometry, showing the location of the flame behind the step. Simulations were brought to a steady state with fires established, after which suppressant was injected, thoroughly mixed with the incoming air.

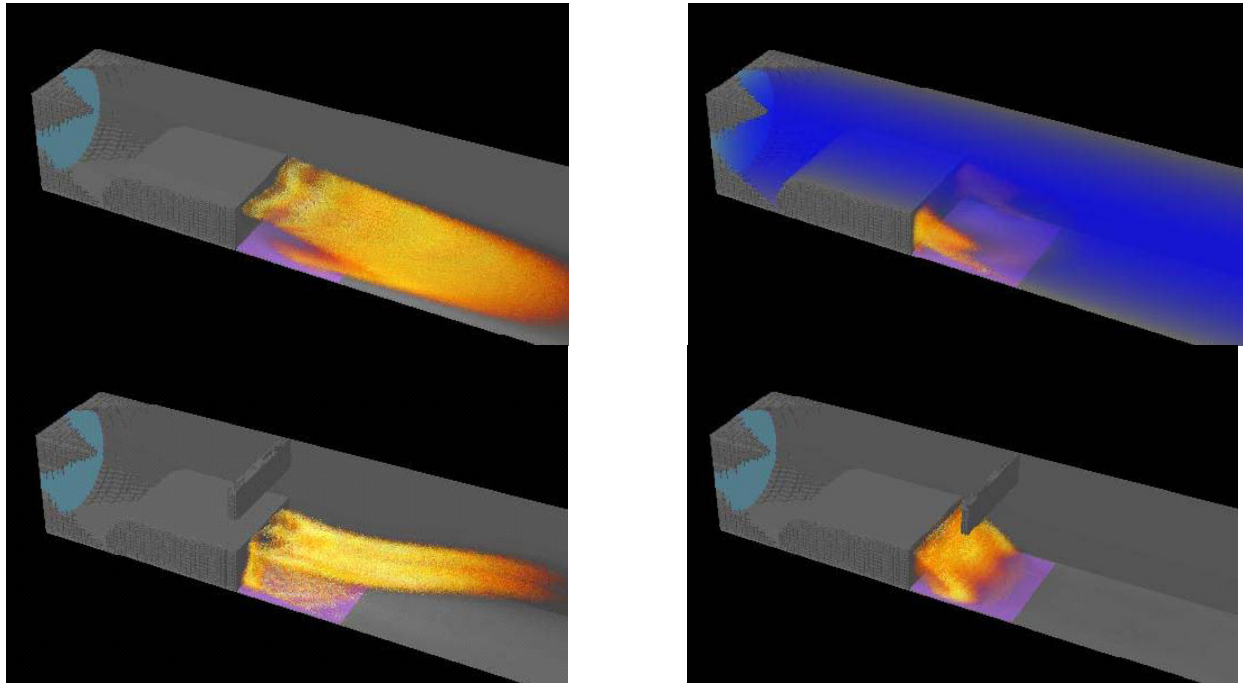


Figure 8-107. Ray Tracing Image of Case A1 before Agent Injection (top left) and 0.2 s after Injection of 10% HFC-125 (top right). Images of Case A3 (lower left) and A5 (lower right) before Agent Injection. The air/suppressant inlet is light blue, the pool is purple, the suppressant is deep blue, and the flame is orange to yellow.

Figure 8-108 shows the state along the wind tunnel centerline just prior to agent injection with the high temperature flame mainly located at the edge of the recirculation zone between the fuel and air. Fuel vaporization is determined by the rate of heat flux to the pool surface, moderated by an estimate of heat losses, for example to the porous plate through which the fuel passes. The flame location relative to the edge of the recirculation zone is somewhat sensitive to these heat losses. It was assumed that 40 % of the heat flux to the pool resulted in fuel vaporization. Greater heat losses result in reduced fuel vaporization, bringing the flame closer to the pool. This effect tends to increase the heat flux to the pool, partially offsetting the heat losses. The sensitivity to heat loss is not very large, but it is enough to move the flame in and out of the recirculation zone given 80 % to zero heat losses. Also shown in Figure 8-108 is a cross-section of the computational mesh, showing grid points clustered around the step to capture relevant details of the boundary layer in these regions. Grid sensitivity studies are in process, although refinement in regions around the step to date has not resulted in measurable differences in the results for Case A1. Injection of suppressant is conducted by keeping the air mass flow rate through the domain constant and increasing the total mass flow rate as required to inject the desired quantity of suppressant.

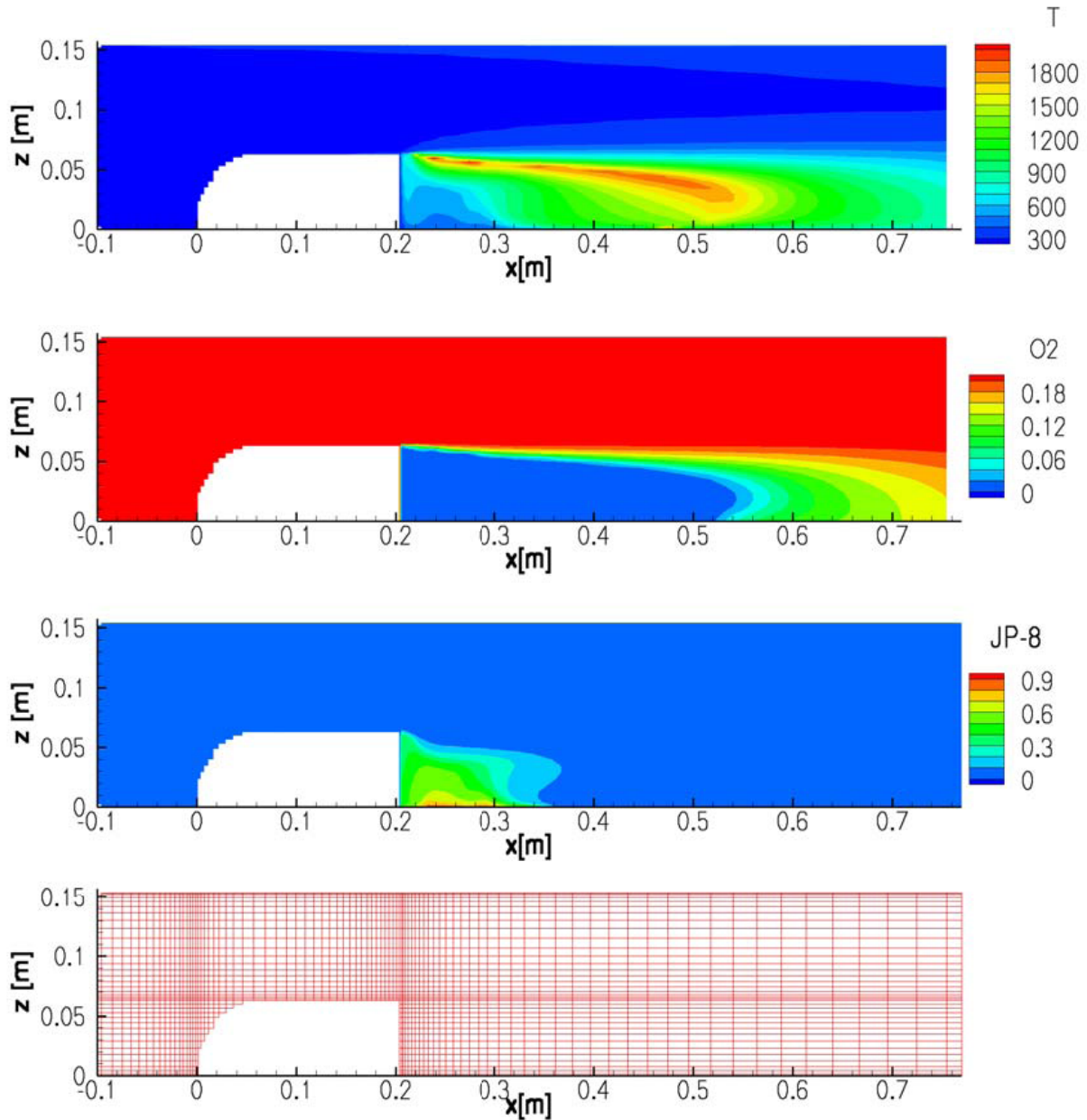


Figure 8-108. Centerline Contour Plots Showing (from top to bottom) the Temperature, Oxygen Mass Fraction, Fuel Mass Fraction and the Computational Grid for Case A1.

Rather than conduct a number of simulations for each suppressant mole fraction to determine the minimum injection time, as was done in the experiments, the suppressant was continually injected and the time to suppression was measured. Suppression was defined as the time at which the maximum temperature throughout the domain dropped below 1000 K. Figure 8-109(a) shows the evolution of the maximum temperature for various suppressant mole fractions. The selection of 1000 K as the temperature corresponding to suppression seems justified since the temperature rapidly drops around this point, and there is no evidence of tendency to reignite for temperatures below 1200 K. It is evident that an HFC-125 mole fraction of 0.075 is insufficient to suppress this flame, while 0.08 is sufficient.

Successively greater mole fractions lead to a monotonic reduction in the time required to suppress the flame. These results are summarized in Figure 8-109(b) where they are also compared with the results of Takahashi et al.⁷⁵

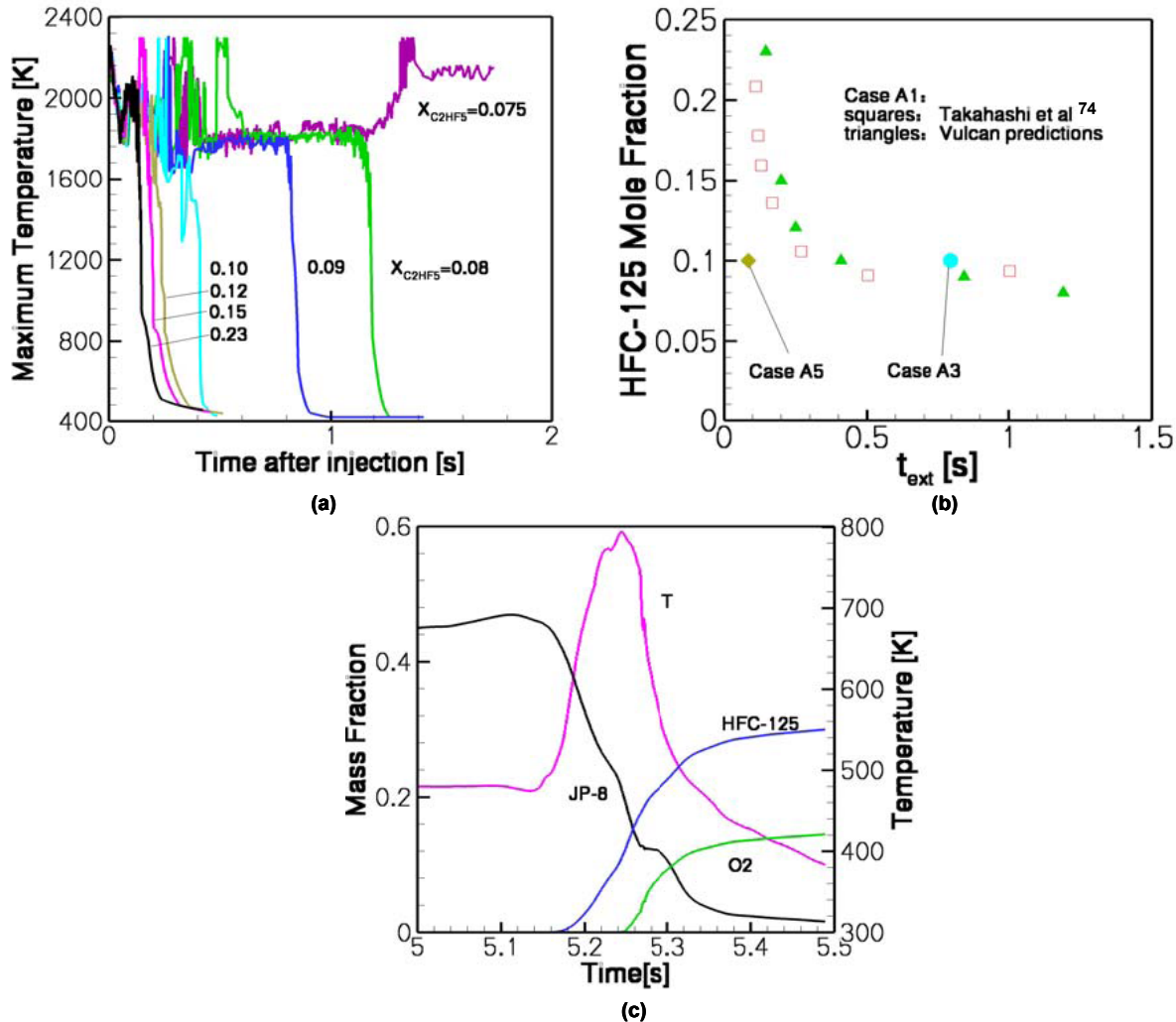


Figure 8-109. (a) Evolution of the Maximum Fluid Cell Temperature in the Domain for Case A1 for Various HFC-125 Mole Fractions. (b) Suppression Times as a Function of Added HFC-125 for Cases A1, A3 and A5. (c) Mass Fraction and Temperature Evolution in the Recirculation Zone (8 mm above pool and 8 mm behind step) for Case A1 with 10 % HFC-125 by Volume Injected at 5 s.

The maximum temperature shown in Figure 8-109(a) fluctuates greatly during the transient suppression process because of a combination of the refined grid and the delta-function nature of the EDC model: at certain instants of time the model treats a particular cell as almost entirely stoichiometric flame. This behavior occurs as the flame moves through the finely gridded region behind the step during the suppressant injection. While this behavior would not be observed when averaging over integral time or length scales, this can occur in the context of the EDC model when the cell thickness is comparable to the Kolmogorov scale as it is in the present grid at some locations. In fact, for better EDC model

applicability, it is desirable to coarsen the mesh, but high levels of grid refinement are used to reduce reliance on log-linear wall models in regions of adverse pressure gradients.

Figure 8-109(c) shows the local smoothness of the temperature evolution deep in the recirculation region along with major species. This figure and Figure 8-110 show key aspects of the suppression dynamics for the particular case A1 with 0.1 HFC-125 mole fraction. The suppressant rapidly flows over the top of the recirculation zone, but dilatation associated with combustion initially reduces recirculation behind the step. As the upper portions of the flame are suppressed (within the first 0.1 s) recirculation gradually increases, bringing suppressant in to extinguish regions that are still burning. As the fire suppression progresses, the flame is observed in Figure 8-109(c) and Figure 8-110 to move deeper into the recirculation zone as fuel vaporization is reduced and oxygen moves into the recirculation zone with the suppressant. It is found that an inner, secondary recirculation zone forms in the corner between the pool and the step into which some air is entrained, primarily from the sides, but into which suppressant penetration is exceedingly slow. With wall heat losses treated in the suppression model, this region is generally the last to be suppressed.

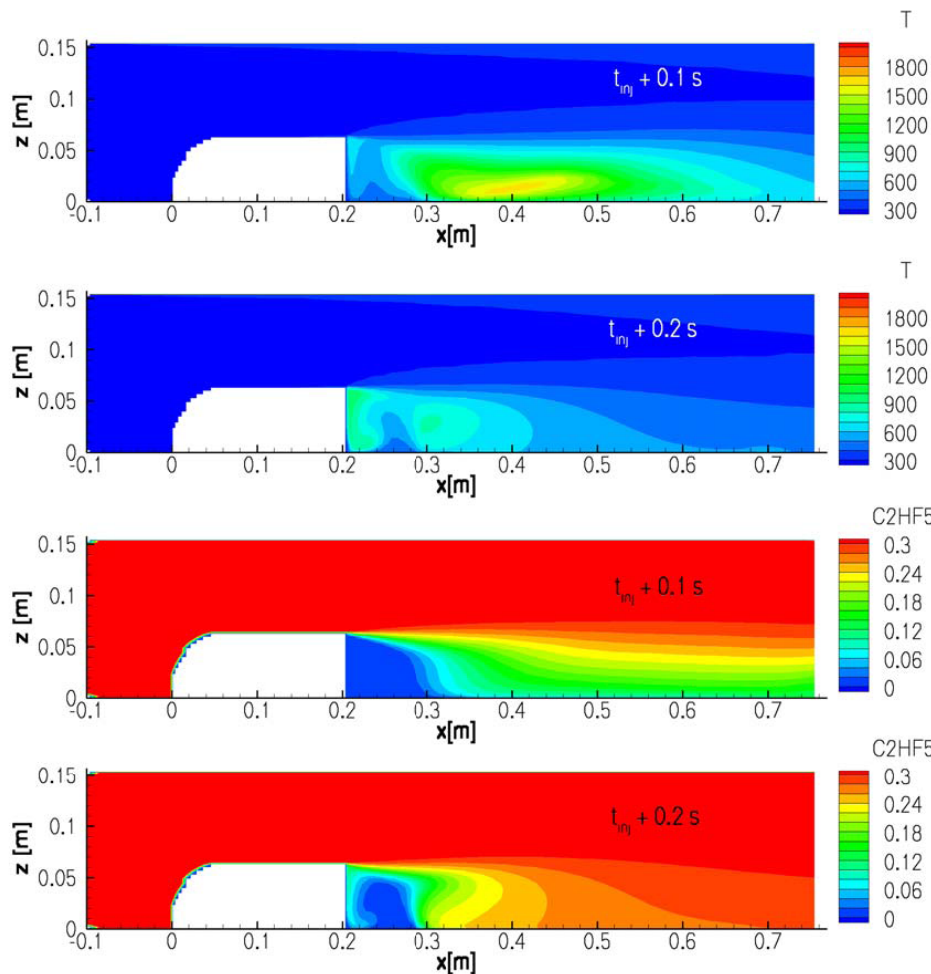


Figure 8-110.
Centerline Contour
Plots of Temperature
and HFC-125 Mass
Fraction at 0.1 s and
0.2 s after
Suppressant
Injection for Case A1
with 0.1 HFC-125
Mole Fraction
Injected.

Using the same basic configuration as the experiments conducted by Takahashi et al.,⁷⁵ simulations were conducted to investigate the effect of additional clutter, in the form of a small rib on the upper wall, opposite the backwards-facing step behind which the fire is stabilized. Specifically, a rib protruding from the upper surface with a height of 42 mm is located either directly above the end of the backward facing

step or two rib heights behind the back of the step; these configurations are denoted A3 and A5; the simulations are otherwise similar to those in A1. These scenarios reflect the existence of additional clutter on the side of a passage opposite the flame-stabilizing obstruction. Additional obstructions result in the acceleration of the flow over the step and past the fire. The correlation between flow velocities over obstructions and suppressant mixing rates^{66,73,74,75} would suggest that collocated obstructions would result in accelerated suppression. In Figure 8-109(b), suppression times are plotted for cases A3 and A5 with 10% HFC-125 suppressant in the free stream along with the results for Case A1 where there is no additional obstruction. The results are not completely intuitive: there is a strong reduction in suppression time for case A5 but no reduction and possibly an increase in suppression time for case A3. This trend goes against a simple implementation of Equation 8–50 that would suggest reduced suppression times in accordance with the changes of τ_{mix} in Table 8-12. Equation 8–50 would imply that case A3 should have the shortest suppression time while it is observed to have the longest.

The results for cases A3 and A5, relative to A1, can be explained by consideration of the pressure field, shown in Figure 8-111, that determines the extent of the recirculation regions.

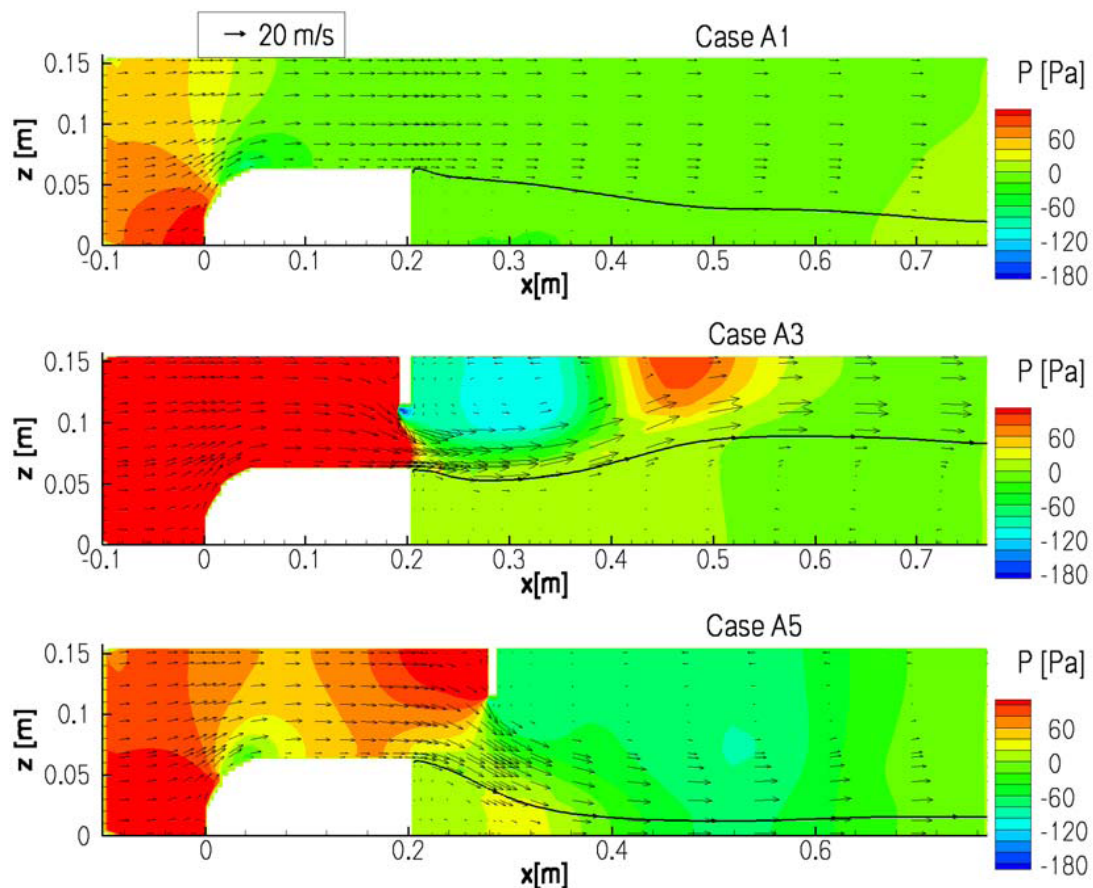


Figure 8-111. Centerline Pressure Contours and Velocity Vectors for Cases A1, A3 and A5 prior to Suppressant Injection. (Contour levels are equal for all panes and space at 2×10^6 Pa intervals. Solid lines represent streamline traces from just behind the corner of the step.)

Also shown in Figure 8-111 are velocity vectors and streamline traces from behind the corner of the step to provide rough indications of recirculation zone sizes. In case A3, flow past a flat plate oriented against the flow results in a greater pressure loss than flow over the backwards-facing step. The greater pressure loss tends to pull the mean flow upward, reducing the mixing in the lower recirculation zone where the fire is stabilized. Shifting the upper obstruction past the step results in significant reductions in the suppression time. This result occurs because the high-pressure region in front of the upper rib is coincident with the low-pressure region behind the backwards-facing step, accelerating the flow downward and increasing suppressant mixing into the recirculation zone. Thus, despite the fact that the area available for flow past the lower recirculation zone is greater and the velocity u^* correspondingly lower in Case A5 relative to Case A3, the suppression time is reduced because the flow is directed into the recirculation zone, thereby increasing mixing in the recirculation zone. The key result is that the suppression time is strongly dependent on recirculation zone size, and that multiple factors affect the recirculation zone size. Given a single obstruction, recirculation zone mixing is primarily dependent on h/u^* , but pressure gradients can change the effective recirculation zone thickness. Given this, recirculation region mixing times should be a function of h^*/u^* , where $h^* = h^*(h, \nabla p)$, indicating the dependence of the effective recirculation zone length scale on the pressure gradient. As is typical for separated flows, favorable (accelerating) pressure gradients reduce recirculation zone length scales while adverse pressure gradients have the opposite effect. Pressure drop past obstructions is related to the drag coefficient, and there is extensive literature on the subject that may be useful in identifying the magnitude of pressure changes across obstructions. It is noted here that the $k-\epsilon$ model is known to have limited success in adverse pressure-gradients, but the conclusions reached here are not dependent on the validity of the $k-\epsilon$ model. Rather, the conclusions depend on the relevance of pressure gradients in directing fluid flow, and on the result from dimensional analysis that mixing times can be related to μ and the characteristic scale of the recirculation zone.

The model validation experiments described above and others for studying fire suppression of obstruction-stabilized flames^{66,75} were conducted in roughly square wind tunnels. In certain applications such as aircraft engine nacelles, the width to height aspect ratio tends to be large. In preparation for studies of actual engine nacelle environments and to plan an additional series of experiments to be conducted at WPAFB by the USAF 46th Test Wing, a series of simulations using dimensions characteristic of the wind tunnel available at WPAFB and an F-18 engine nacelle were conducted. The characteristic dimensions identified are obstruction heights on the order of 5 cm in wide channels with heights on the order of 10 cm to 30 cm. The resulting series of simulations, cases B1, B2, C1 and C2 are summarized in Table 8-12. In each of these simulations, the inlet velocity was 5 m/s, the turbulence intensity was 10 % and the turbulent length scale was 0.025 m. Significantly, pool sizes are narrow relative to the channel width. Simulations indicate that dilatation from a pool fire behind a rib induces secondary recirculation regions that sweep the fire outward and along the rib transverse to the flow. Observation of these flow fields indicates that they may reduce the suppressant penetration into certain portions of the flame-stabilization region. However, within aircraft, structural supports and clutter are observed to be oriented in both transverse and longitudinal directions. The consequences of longitudinal (streamwise) ribs are examined by adding longitudinal ribs just outside of the pool (Cases B1 and C1 becoming Cases B2 and C2). It is observed that for both Cases B2 and C2 the longitudinal ribs do not prevent spread of the fire beyond the ribs, as shown in Figure 8-112. Mass fraction profiles in the recirculation zone indicate, however, that longitudinal ribs do affect the flow because rate of transport of agent is greater with ribs for Case B2 relative to B1 and for Case C2 relative to C1, shown in Figure 8-113(a). Further, the time to suppress the fire is reduced as shown in Figure 8-113(b). The result that

longitudinal ribs reduce the time required to suppress a fire suggest a series of experiments in high aspect ratio wind tunnels to evaluate their validity. If the experiments are consistent with the simulation results, then both the potential reduced suppression ability due to dilatation and the possibility that longitudinal clutter ameliorates it are considerations in system design.

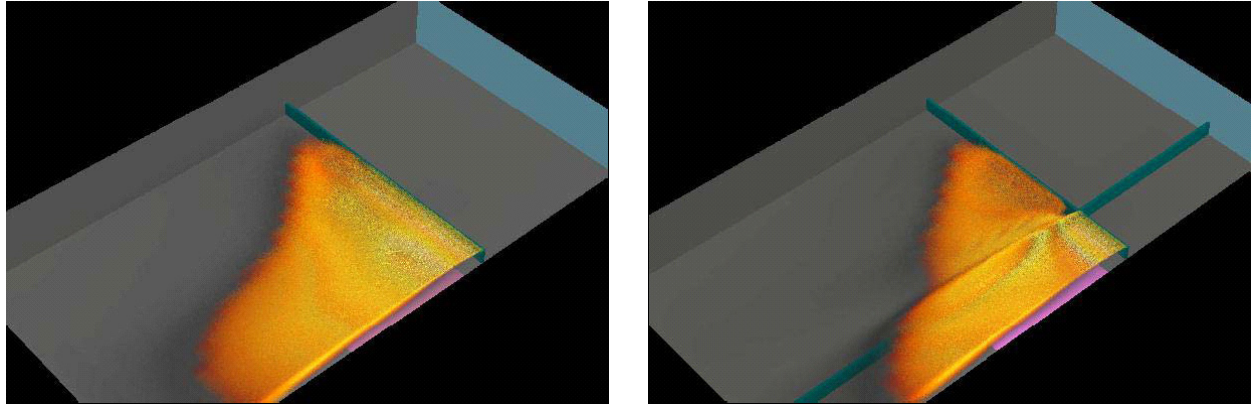


Figure 8-112. Raytracing images of Cases B1 (left) and B2 (right). (Colors as in Figure 8-107. Simulations take advantage of symmetry, and only the calculated half of the domain is shown.)

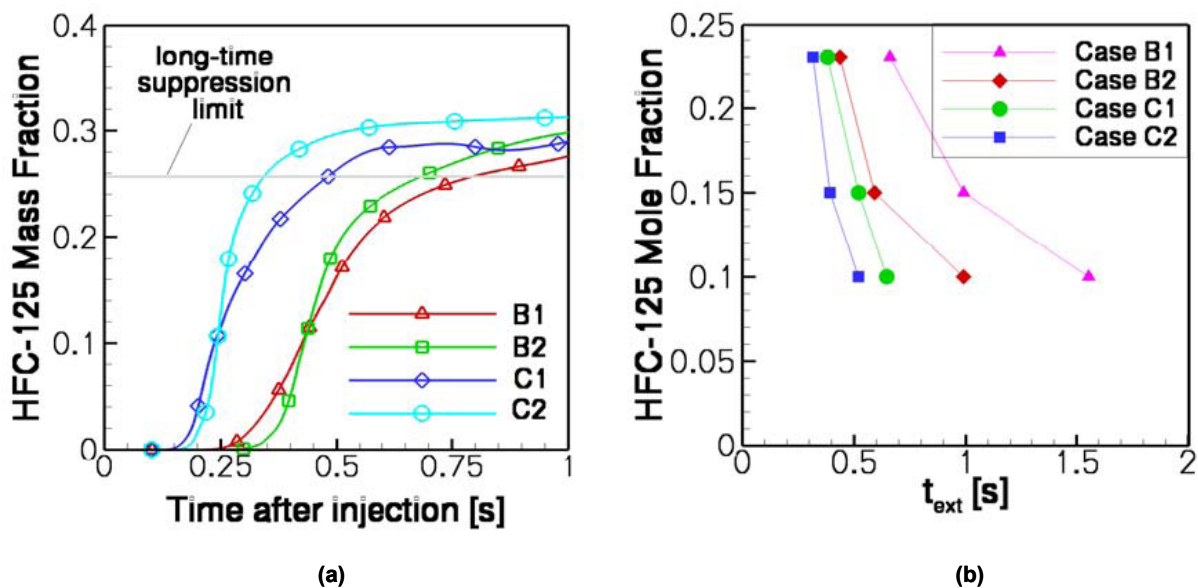


Figure 8-113. (a) Temporal Evolution of HFC-125 Mass Fraction in the Recirculation Zone at a Point 0.012 m above the Lower Surface and 0.05 m behind the Rib along the Centerline. (b) Suppression Times as a Function of HFC-125 Mole Fraction for Cases B1, B2, C1, and C2.

8.5.5 Assessment of VULCAN in Suppressant Distribution in a Full-Scale Nacelle

The flow inside an engine nacelle ground test simulator was studied for the purpose of understanding and optimizing the distribution of suppressant.^{76, 77} One objective of the study was to identify conditions for which suppression would or would not be successful in order to test the ability of VULCAN to discriminate between various scenarios and to provide input on experimental design for full-scale nacelle fire tests. To accomplish this, the distribution of fire suppressant during cold flow (without a fire) was first examined to identify regions of low concentration using VULCAN.

The overall nacelle geometry used in the VULCAN simulations was based on the “Iron Bird” full-scale nacelle simulator (to be described in detail below), which was a mock up of a port engine nacelle. In the absence of fires and suppressant flow, the flow field in the nacelle was dominated by flow through an inlet air scoop located near the front of the nacelle coming up through the nacelle bottom. The inlet air flowed from the inlet across the engine toward the upper aft of the nacelle. For the purposes of the simulations, an air mass flow rate of 1.0 kg/s was used. The inlet air mass flow rates determined the air exchange times, the time over which the mass of air entering and leaving the nacelle equaled the mass of air in the nacelle. For the simulation, the internal volume of the nacelle, neglecting clutter objects, was just over 1.4 m³. This volume gave an air-exchange time of 1.6 s. The inlet cross section was approximately 0.008 m² and the inlet airflow velocity was approximately 150 m/s. This resulted in an inlet Reynolds number of 9×10^5 resulting in strong turbulence even without the clutter-enhanced mixing.

The ground simulator was outfitted with a set of four suppressant discharge nozzles that were found to be sufficient to suppress a fire when 3.2 kg of fire suppressant was discharged.⁷⁸ These are denoted by the numbers 1 through 4 with higher numbers corresponding to nozzles that are located toward the rear of the nacelle (Figure 8-114). Numerical simulations were conducted for suppressant injection through these nozzles into the nacelle in the absence of a fire to obtain information on the distribution through the nacelle.⁷⁶ The suppressant was assumed to enter the nacelle in the vapor phase or to vaporize fast relative to other time scales. The suppressant mass flux for each nozzle was assumed to be proportional to the nozzle area.

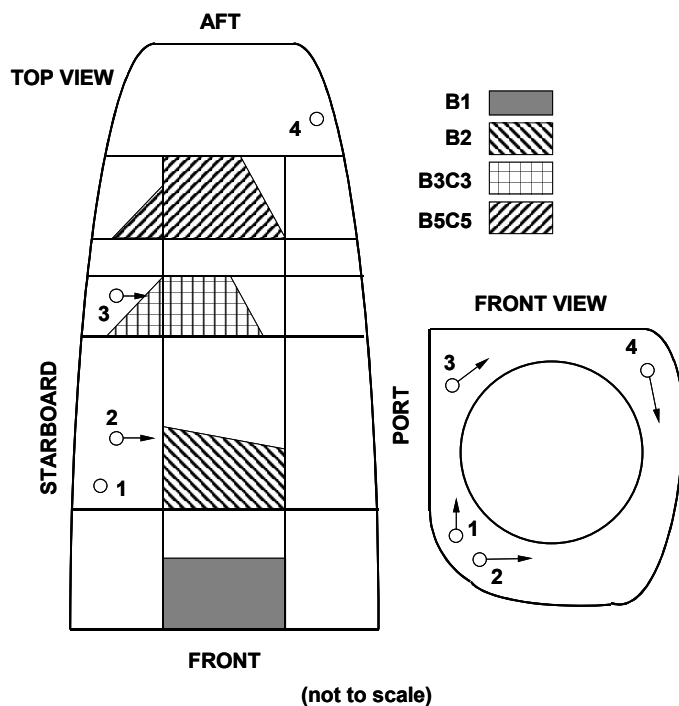


Figure 8-114. Locations of the Suppressant Nozzles and the Pools in the Nacelle Simulator.

The mass fraction of HFC-125 in vertical planes near the nacelle center and near the starboard and port sides are shown in Figure 8-115 at the end of the 3 s suppressant injection period.

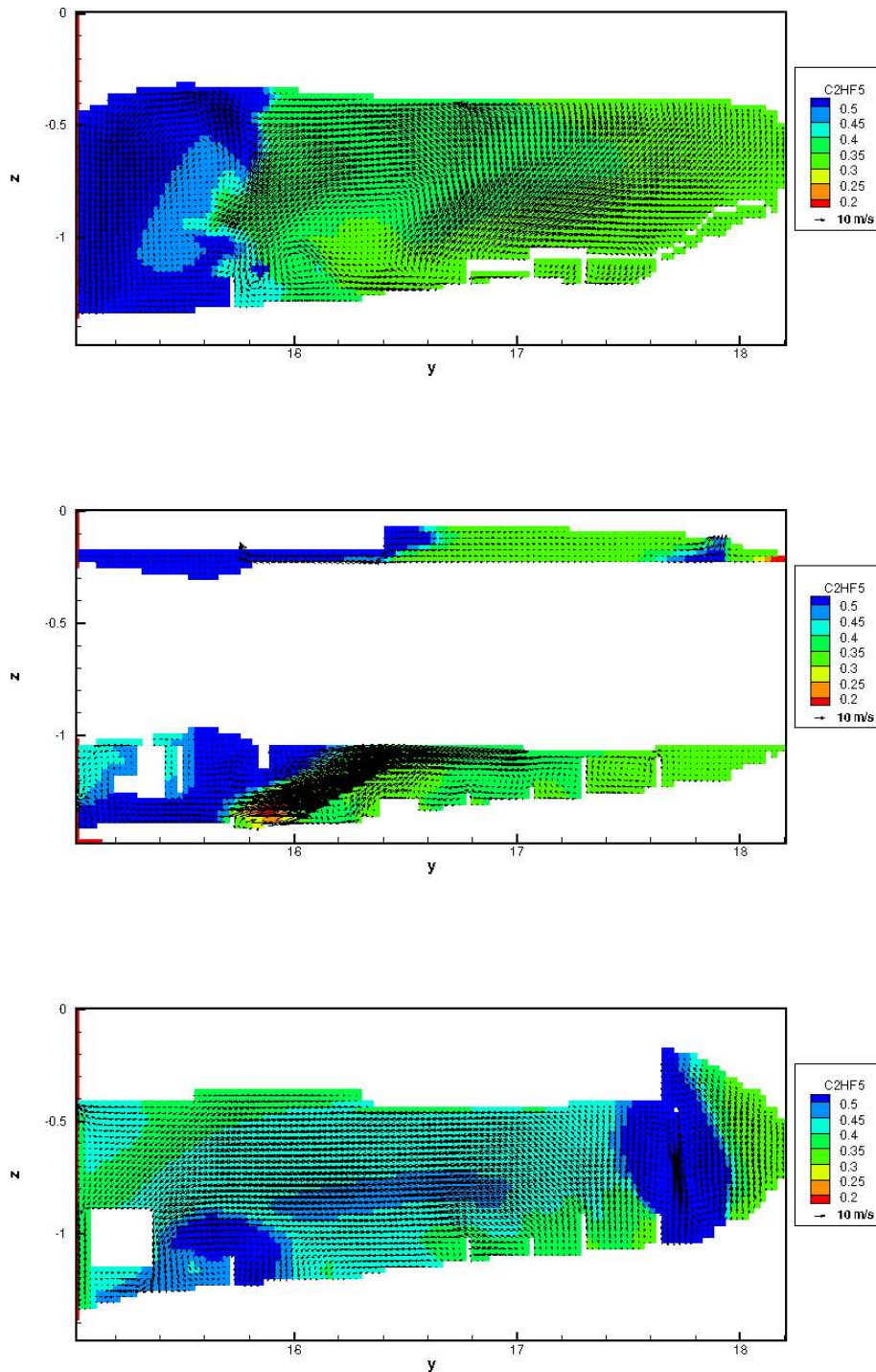


Figure 8-115. Contour Plots of C_2HF_5 at 3.0 s after Start of Suppression Injection in Vertical Planes near Starboard Side (top), near Nacelle Centerline (center), and near Port Side (bottom). (Airflow is 1.0 kg/s, and suppressant flow is 3.2 kg/s over 3 s.)

In these contour plots the computational cells representing the nacelle, the engine, and the clutter are blanked (white). The mass fractions are colored in such a manner that blue and green (cool) colors indicate likely suppression and red (hot) colors indicate that suppression is unlikely. The critical mass fraction for suppression in the absence of intense mixing is somewhat less than 0.3 (closer to 0.25, so that this is a conservative estimate), and so the dividing line for likely suppression can be taken to be the dividing line between yellow-green and green. Depending on the turbulent mixing rates, suppression may occur for lower mass fractions of HFC-125. Velocity vectors are also provided in Figure 8-115 to indicate the general flow direction.

Nozzle 1 is located on the starboard side of the nacelle in the forward section and is directed upward. The suppressant from Nozzle 1 fills the upper forward nacelle and is advected into the lower forward nacelle. Nozzle 2 is located near Nozzle 1 on the starboard side of the nacelle and directed towards the port side beneath the engine and across the top of the inlet airflow. Suppressant from nozzle 2 is dispersed aftward by the inlet jet along the nacelle. Nozzle 3 is located just past the mid-point of the nacelle, in between the second and third ribs, on the upper starboard side of the engine. Suppressant flow is directed at roughly a 45° angle upward across the top of the engine, and the majority of suppressant follows the mean flow forward along the upper nacelle. Nozzle 4 is located on the port side of the engine near the aft of the nacelle just behind the fifth rib. The suppressant is directed downward along the side of the engine in a direction that is counter to the general upward flow toward the upper diamond vent; this recirculation results in oscillations as the injecting gases are turned around by the mean flow.

Distribution of Suppressant throughout the Nacelle

As a measure of sufficient distribution in the nacelle, the portion of the nacelle volume for which the suppressant mass fraction exceeds 30 % has been used for characterization. Even with low-intensity mixing, this amount is generally sufficient for suppression and represents a conservative estimate of suppressibility. Figure 8-116 shows this fraction when the airflow is 1.0 kg/s with varying rates of injection (same mass over different durations). The mass of suppressant to be injected was fixed at 3.2 kg, and the period over which it was released varied from 2 s to 6 s. Shorter injection periods correspond to higher bottle pressures. To the extent that suppressant vaporization is slow, the effective period of injection increases. Figure 8-116 shows that the entire volume is essentially filled for at least one second for injection durations of 3 s or less. For longer periods of injection, the volume is not filled with high concentrations (> 30 %) because suppressant is continually advected out the various vents. The failure to fill the nacelle completely does not indicate that suppression will not occur, but rather reduces the confidence in suppression.

The average peak mass fractions for the simulations shown in this figure are 0.59, 0.51, 0.44 and 0.35. Smaller mass fractions correspond to the longer injection duration. If the turbulent mixing in the nacelle were sufficient to create homogeneity, the mass fraction throughout the nacelle would exceed 0.3 for all of these scenarios. Clearly, inhomogeneities arising from imperfect mixing are significant. This indicates that the CFD analysis can provide significant information on the degree of inhomogeneity. Specifically it can provide an estimate of the volume that fails to meet a criteria such as the one indicated here (suppressant mass fractions exceeding 0.3).

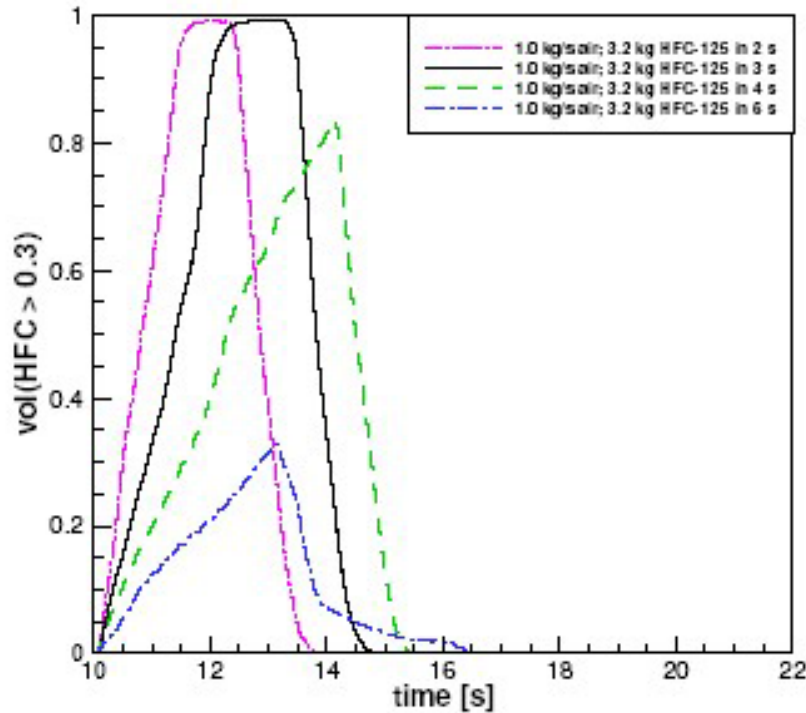


Figure 8-116. Simulation Results of Various Injection Periods.

Influence of Nozzles on Distribution of Agent

Simulations were conducted to ascertain the effect of removing a single suppressant nozzle, while keeping the overall mass of injected suppressant constant at 3.2 kg injected uniformly over 3 s. For these conditions, the nacelle volume in which the fraction exceeds 0.3 is evaluated. These results were compared to those shown for all four nozzles functioning; the nacelle was completely filled, according to this criterion, for the range of flows considered.

In conducting simulations with specific nozzles removed, the mass flow out of the remaining nozzles was kept at the same values used in the previous simulations. This corresponds to an assumption that the pressure driving the suppressant is not affected by the removal of a nozzle and that the nozzle cross-sections have not changed. The duration is thus increased to allow release of the full 3.2 kg of HFC-125.

The volume fraction of the nacelle where the suppressant mass fraction exceeds 0.3 is indicated in Figure 8-117 for an airflow of 1.0 kg/s. In these and other scenarios, it appears that removing Nozzle 3 has no detrimental effect, since the complete volume is indicated as filled, and the duration for which it is filled is increased because of the slightly slower rate of injection using three nozzles. Based on the criteria shown in Figure 8-117, removing Nozzle 4 also has little effect on the sufficient distribution of the suppressant. Note that the lower diamond vent in the nacelle simulator is modeled as essentially blocked, based on observations of the test simulator. Assuming that this vent is not blocked on similar fleet aircraft, the removal of suppressant in the aft region may be substantially faster, making the retention of Nozzle 4 highly desirable. On the other hand, the additional vent in the aft region would mean that a greater portion of the suppressant injected through Nozzle 4 would leave the nacelle rapidly.

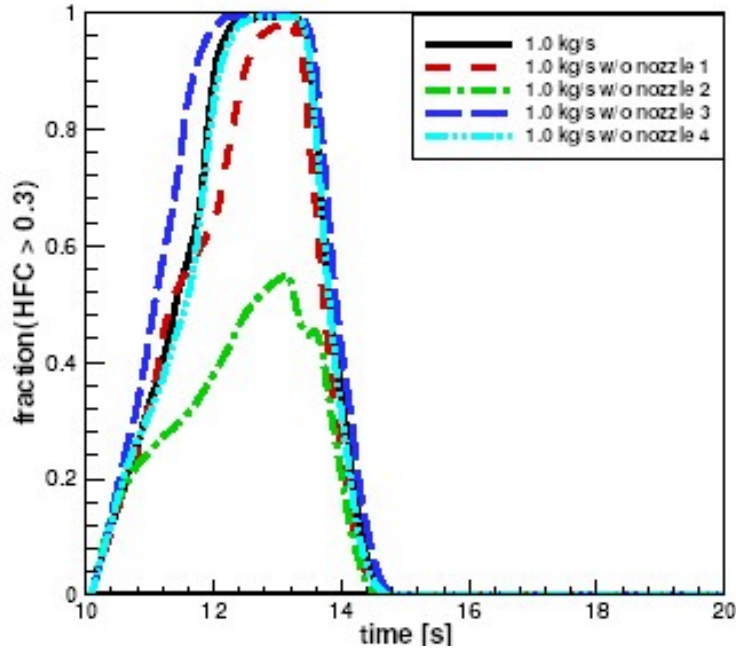


Figure 8-117. Simulation Results Showing the Effect of Nozzles on Agent Distribution.

The removal of Nozzles 1 or 2 does appear to have a significant effect on the distribution of suppressant throughout the nacelle. Suppressant from these nozzles is entrained in the inflow; this entrainment by the air significantly helps distribute suppressant throughout the nacelle.⁶⁷ The distribution of suppressant along the centerline is shown in Figure 8-118 with Nozzle 2 assumed to be capped; this can be compared with the distribution using 4 nozzles. Nozzle 2 is located in the forward starboard area of the nacelle and directed across the lower nacelle outboard. Without Nozzle 2 present, the inlet air jet entrains relatively little suppressant, and this results in little suppressant along the lower nacelle where pool fires might exist. It is clear that Nozzle 2 plays a key role in distributing the suppressant throughout the nacelle as it mixes with the air inlet.

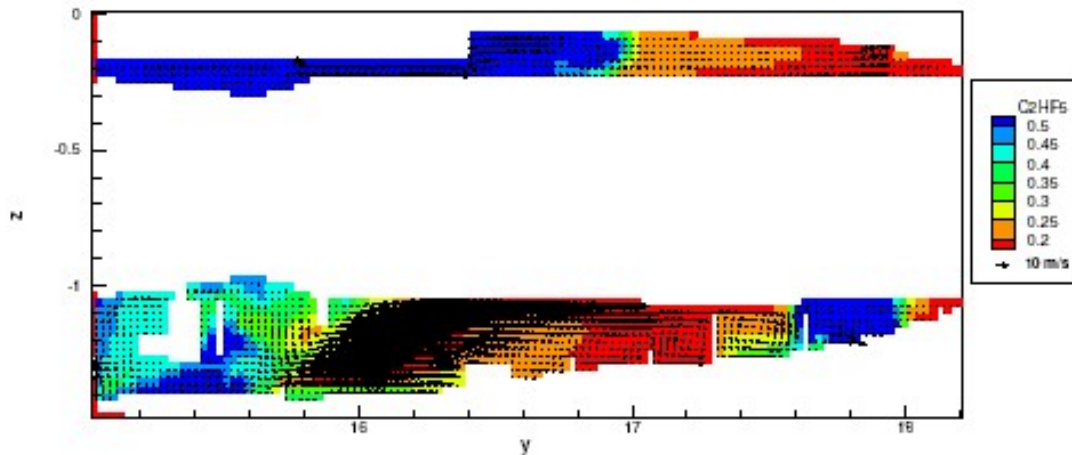


Figure 8-118. Simulated Agent Distribution along the Nacelle Centerline.

8.5.6 Assessment of VULCAN in Pool Fire Suppression in a Full-Scale Nacelle

Pool fires stabilized behind obstructions have been identified as among the most challenging fires to suppress.^{71,72} Obstructions such as structural ribs provide a region of recirculating flow where hot products help stabilize the flame that suppressant is relatively slow to penetrate. In certain scenarios, such as those described in References 54, 66, and 75, the suppressant concentration must be maintained at an elevated level in the flow past the stabilization region for a substantial period of time to ensure that adequate suppressant penetrates the stabilization region.

The approximate locations of the pools used for VULCAN are shown in Figure 8-114. These sections are delineated from the forward to the aft end with increasing numbers as each rib is passed. The letter “B” is applied as a prefix to the pool location to indicate that the pool is located between the two central longerons. These are the only locations where substantial quantities of fuel can be collected. To augment the quantity of fuel, the basin just to the port of that indicated by “B” is sometimes assumed to hold some fuel also; this basin is denoted with the prefix “C”. The pool located at B1 is between the forward end of the nacelle and the first rib. That denoted B2 is located just aft of the first rib; the inlet air flows partially over this pool. The pool denoted B3 is located behind the second rib. The pool denoted B5C5 is located between the fourth and fifth ribs; these are the two larger ribs. The simulations indicate that pool fires at locations B4 and B6 are difficult to stabilize because of the particular predicted circulation. The surface areas of the largest possible pools in each section were measured in the ground-test simulator. Similar pool areas have been used in the simulations; the pool areas are indicated in Table 8-13.

The pools are assumed to be filled with JP-8, and the evaporation rate based on heat feedback to the pool. In general, it is difficult to predict the thermal feedback to a pool from a fire, because these fires are partially advected beyond the pools by the convective flows in the nacelle. It is particularly difficult to determine the evaporation rates without measurements. The uncertainty of the evaporation rate may be as high as 50 %. As a measure of the degree to which fires in different sections spread throughout the nacelle, Table 8-13 also shows the volume over which combustion is occurring and high temperatures exist. Heat release from pool fires B2 and B3C3 is substantially distributed throughout the nacelle by the main air inlet that passes over the fires in these regions.

Table 8-13. Pool Characteristics.

Pool	Area (m ²)	Predicted Evaporation Rate (kg/s)	Volume of Combustion (%)	Volume where $T > 700$ K (%)
B1	0.084	0.0089	5.9	4.6
B2	0.100	0.011	4.6	22
B3C3	0.094	0.0082	5.5	37
B5C5	0.043	0.0043	1.5	5.2

Suppression Using Four nozzles

Suppression was predicted for all pool fires in the nacelle using the four-nozzle configuration and 3.2 kg of suppressant when this mass was injected over 3 s or 4 s. Results of these tests are summarized in Table 8-14.

Table 8-14. Summary of Test Results with Four Nozzles.

Pool	Mass HFC-125 (kg)	Injection Rate (kg/s)	Active Nozzles	Suppression Time (s)
B1	3.2	1.07	1,2,3,4	0.8
B1	2.2	1.07	1,2,3,4	0.8
B2	3.2	1.07	1,2,3,4	0.9
B2	2.2	1.07	1,2,3,4	0.9
B3C3	3.2	1.07	1,2,3,4	1.2
B3C3	2.2	1.07	1,2,3,4	1.2
B3C3	3.2	0.53	1,2,3,4	None
B3C3	3.2	0.64	1,2,3,4	None
B3C3	3.2	0.71	1,2,3,4	None
B3C3	2.2	0.73	1,2,3,4	None
B5C5	3.2	1.07	1,2,3,4	1.8
B5C5	2.2	1.07	1,2,3,4	1.8

To examine the effect of varying the mass of suppressant injected and the rate of injection, a series of additional simulations for fires in pool B3C3 were conducted. When the rate of suppressant injection is reduced to just below 0.75 kg/s, no suppression was predicted in the simulations, although sustained burning would certainly be described as tenuous for these conditions since the fire was restricted to a corner of the pool C3. As the rate of suppressant injection is reduced, the fire stability increases, and at 0.53 kg/s the fire is clearly stabilized, at least near the corner of pool C3. The fire tends to stabilize in this location because the mixing rates are lower, as indicated in the following section. It is noteworthy that the mass of suppressant injected plays little role in determining the occurrence of suppression here. For the two cases with suppressant injection rates of 0.71 and 0.73, the resulting tenuous burning region is very similar. There will be a lower bound in terms of suppressant mass injected over a short period, although this has not been identified here. More significant in practice is the duration over which suppressant will act to inhibit reignition and allow cooling of heated surfaces. Thus the suppressant requirements are likely to be dictated by a combination of the rate required to flood the compartment with a high enough concentration and the mass required to maintain that concentration to inhibit potential reignition sources.

There is one complication that arises with high-boiling point agents, however. For high boiling point agents, the relevant parameter will not be the rate at which liquid suppressant is injected, but rather the rate at which the liquid suppressant vaporizes. The physics of the evaporation process are not captured in the present simulations but will be considered in subsequent simulations.

Though the detailed results are not presented here, suppression is sensitive to heat flux from the fire to the pool. If the heat flux and, hence, the fuel evaporation are reduced by 50 %, suppression is substantially easier for the cases considered in this section. For example, the reduced suppressant injection rates shown in Table 8-14 that fail to suppress the fire in pool B3C3 do succeed in suppressing the fire if the heat flux to the pool is reduced by 50 %. The fire can be completely separated from the fuel source with slower evaporation rates. Similar results are expected if the fuel is cold or if there are substantial heat losses through the nacelle under the pool. While relatively high engine temperatures are expected during operations, temperatures during ground tests may be such that reduced evaporation is experienced.

Suppression with Individual Nozzles Capped

The capping of various nozzles causes inhomogeneities that left certain regions with little suppressant. A series of simulations was conducted where one nozzle was assumed to remain capped. To examine the effects of these inhomogeneities for the majority of these simulations, the flow from each of the other nozzles was maintained at previous values when all nozzles were open, giving a reduced rate for the sum of the three remaining nozzles and an increased duration of injection. Results of these tests are summarized in Table 8-15. For fires in the extreme forward and aft pools, the removal of various nozzles did not alter the prediction of suppression.

Table 8-15. Summary of Test Results with Individual Nozzles Capped.

Pool	Mass HFC-125 (kg)	Injection Rate (kg/s)	Active Nozzles	Suppression Time (s)
B1	3.2	0.83	2,3,4	1.3
B1	2.2	0.83	2,3,4	1.3
B1	3.2	0.74	1,3,4	1.5
B1	2.2	0.74	1,3,4	1.5
B1	3.2	1.07	1,3,4	1.1
B1	3.2	1.07	1,3,4	1.1
B2	3.2	0.83	2,3,4	None
B2	2.2	0.83	2,3,4	None
B2	3.2	0.74	1,3,4	4.6
B2	2.2	0.74	1,3,4	3.2
B3C3	3.2	0.83	2,3,4	1.6
B3C3	2.2	0.83	2,3,4	1.6
B3C3	3.2	0.74	1,3,4	None
B3C3	2.2	0.74	1,3,4	None
B5C5	3.2	0.74	1,3,4	2.4
B5C5	3.2	0.90	1,2,3	1.7

For pool B1 the removal of either Nozzle 1 or Nozzle 2 has little effect beyond delaying the suppression. For pool B5C5, the removal of Nozzle 2 results in an increase in the suppression time because suppressant from Nozzle 2 is entrained in the air and carried back across the ribs surrounding the pool. Without Nozzle 2, the suppression is delayed until suppressant from other nozzles flows around the nacelle to be entrained by the air inlet. The removal of Nozzle 4, which is closest to pool B5C5 and injects suppressant around the aft section of the nacelle, has minimal effect on suppression of this pool because the major flow is under the engine aftward.

For pool B3C3, the removal of Nozzle 1 has little effect other than to delay the suppression. Removing Nozzle 2, however, results in a failure to suppress fires in pool B3C3. As indicated in Figure 8-118, the removal of Nozzle 2 leaves a significant volume directly over the pool B3C3 with little suppressant. Thus, Nozzle 2 is necessary to suppress fires in this region.

For a pool located at B2, Nozzle 1 is critical for suppression. Suppressant from Nozzle 1 is entrained across pool B2 by the air, and in the absence of that nozzle the suppressant's concentrations just over the

pool are too low. Capping Nozzle 2 also leaves a region deficient in suppressant there as well, but the air influx over this region (approaching 100 m/s) is sufficient to extinguish any fire in that region.

As the rate of injection is reduced by a third or more, many volumetric regions of the nacelle do not have sufficient suppressant for all fires. This is caused by inhomogeneities in the concentration, since the average concentrations in the nacelle are sufficient to suppress all fires. Suppression also fails as the rate of injection is reduced by one third or more. The removal of Nozzles 1 and 2 causes substantial inhomogeneities in the distribution of agent. When Nozzle 3 is assumed to be capped, there is no apparent degradation in suppression.

Sensitivity studies in these simulations have disclosed that the pool vaporization rate is very sensitive to fuel temperature, heat losses, details of the geometry, and the momentum associated with injection.

8.6 FULL-SCALE NACELLE FIRE SUPPRESSION TESTS

8.6.1 Experimental Design

Results from the VULCAN pretest simulations (see above VULCAN assessment sections) and simplified analyses helped guide the design of the experimental test plan and matrix for fire suppression tests in a full-scale nacelle. These results estimated the overall concentration of suppressant in the nacelle, the duration of the transients as the concentrations rise and fall, and the magnitude of the distribution of suppressant. A simplified analysis of the relative masses of air and suppressant flowing into the nacelle can provide some guidance on the overall suppressant concentration and the transients. The suppressant mass-injection rate relative to the total injection rate provides a characteristic mean mass fraction within the nacelle, Y_{ss} . The injection must proceed for a long duration for the mean mass fraction to reach this characteristic steady-state value, but the mean mass fraction approaches this value in an exponential manner with an exponential time constant that is proportional to the total nacelle volume divided by the total volumetric influx. This time constant indicates the time scale for transients. In the tests conducted here, it was found that suppression was less sensitive to the total injected mass than it was to the rate of injection.

The VULCAN predictions indicated, and the test results subsequently confirmed, that the overall or average mass fraction of suppressant resulting in fire suppression was substantially greater than the cup burner value, which was $Y_{cb} = 0.28$.⁷⁹ In general, the estimated average fraction required for suppression is on the order of 30 % to 40 % greater than the cup-burner value, according to the VULCAN simulations. A similar excess was required for the tests. The fact that a greater overall mass fraction is required indicates that inhomogeneities are significant. In other words, the suppressant's mass fraction in certain regions of the flow is substantially less than the mean. It is noted that the high rates of mixing present in the nacelle tend to reduce the mass fraction required to suppress the fire. It has been found for HFC-125 that strained laminar flames are indicated to be suppressed at mass fractions as low as 0.16.⁷⁹

One of the primary objectives of the study was to ascertain the predictive capabilities of VULCAN regarding the degree of inhomogeneity in the nacelle. To this end, it was noted that predictions with VULCAN were very successful at reproducing extinction in a geometry where the suppressant was introduced in a uniform manner and the only mixing processes were related to a fire-stabilizing recirculation zone.⁵⁴ The nacelle simulator geometry was appreciably more complicated, and the leading

challenge was expected to be the transport of the suppressant rather than the well-established suppression model itself. In order to evaluate the mixing process for several scenarios, simulations and tests were conducted with different rates of injection and with different nozzle configurations. As an added variable, the air inflow was varied to simulate varying flight conditions. As indicated above, the ratio of the suppressant injection rate to the combined, total mass rates was indicative of the mean of the suppressant mass fractions in the nacelle.

Based on the results of VULCAN model simulations of various test conditions, it was predicted that the suppression would be more sensitive to the rate of injection of agent than to the amount of suppressant, or equivalently the duration of injection. Further, suppression was indicated to be sensitive to the distribution of nozzles about the nacelle. With these results, a test plan was generated in the form of a rule-based sequence of tests. The test sequence was initiated with an approximation of a scenario, which was expected to result in successful suppression. From this point, subsequent tests reduced the effectiveness of that system by either:

- reducing the injection rate by reducing the bottle pressure so that the suppressant's mass fraction was reduced, or
- removing a nozzle so that the distribution of suppressant was less uniform, or
- reducing the mass of suppressant injected for a given bottle pressure so that the peak mass fraction was reduced and held for a shorter duration.

8.6.2 Test Facility

The NAVAIR's full-scale "Iron Bird" nacelle at Navel Air Station (NAS) Patuxent River, Maryland, which is typical of an advanced tactical aircraft, was used for this effort. Figure 8-119 shows the fire test simulator. The air inlet source is seen in the lower left coming up into the bottom of the nacelle. There are two vents in the top: a diamond-shaped vent in the aft, and a balance piston round vent about 1/3 aft of the face. On the front face, there are four exit holes simulating connections from the nacelle to the Airframe Mounted Accessory Drive (AMAD) bay and other parts of the aircraft. These four holes are arrayed around the engine as shown in Figure 8-120.

The flow areas of the top vents, the diamond aft vent and the balance piston vent, are 248 cm² and 22.8 cm² respectively. The ground test simulator is a mock up of a port engine nacelle. Therefore, the port side corresponds to the outboard side of the engine, where air is introduced in flight, and the starboard side corresponds to the inboard side of the engine. The nacelle is roughly 3.18 m long. The width and height vary significantly along the length, but are contained within a region 1.45 m high and 1.15 m wide. Coordinates are measured from a reference point on the top starboard side of the simulator test fixture so that all vertical coordinates are negative while other coordinates are positive.

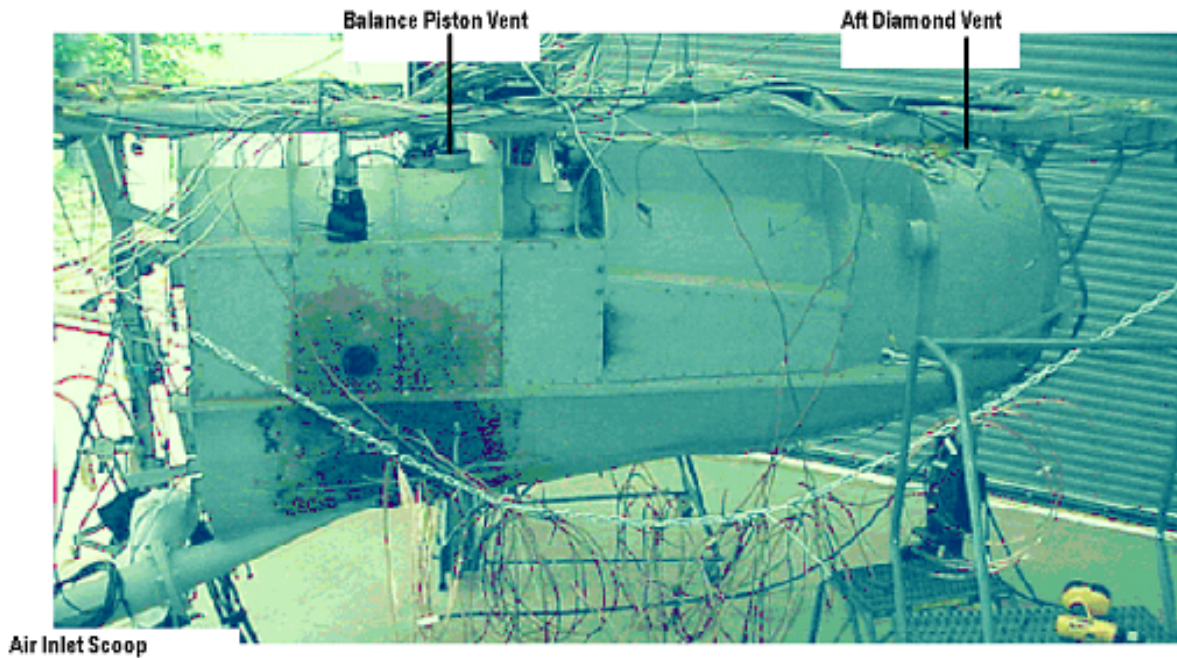


Figure 8-119. Ground Test Nacelle 'Iron Bird' Simulator.

In conjunction with the rearward taper of the airframe, the nacelle is generally tallest and widest near the forward end, narrowing towards the aft. At various sections, there are larger cavities around the engine sides and top with additional space for air circulation. The lower nacelle surface slopes smoothly up from the forward to the aft, crossed by five ribs of varying heights. There are roughly four longerons running along the lower nacelle surface. The two central longerons end about 0.6 m before the aft end. The engine, a hollow cylinder in the ground simulator, extends from the forward to the aft of the nacelle. The engine diameter is nominally 0.77 m with a slight narrowing over the front 0.61 m to a minimum diameter of 0.62 m. From 0.81 m aft to the aft end of the nacelle, the engine is uniformly 0.77 m in diameter.

The outer surface of the engine is generally smooth, although various clutter items are attached as described below. In addition to the ribs and longerons, the most significant clutter is located near the forward end of the nacelle. It is dominated by a gearbox assembly located from 0.1 m to 0.75 m behind the forward end and primarily below the engine. The gearbox assembly is a collection of several parallelepiped and cylindrical objects of varying sizes that obstruct the flow in the large space between the engine and the lower nacelle in the vicinity of the air inlet scoop. Additional large parallelepiped clutter objects are located along the engine, particularly on the port side as far back as 1.5 m behind the forward end. Smaller clutter, primarily tubing and wire bundles, exists along the lower half of the engine across the length of the nacelle. Some of this smaller clutter has been identified as a potential reflight surface because of the relatively low thermal capacity and rapid heating to very high temperatures. The afterburner control vanes at the aft end of the nacelle have not been included in the computational model because the setup (initially) focused on fire scenarios near the forward end of the nacelle.

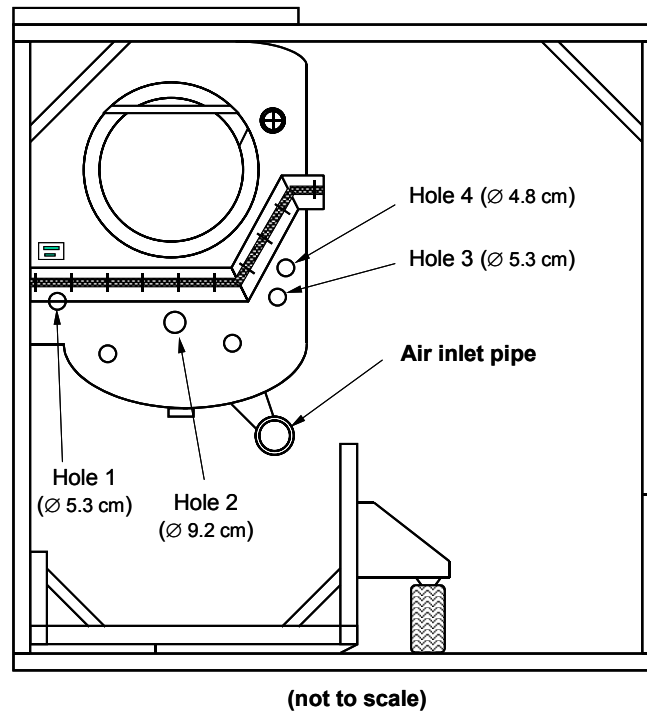


Figure 8-120. Drawing of Front Face of Ground Test Nacelle.

In order to apply realistic boundary conditions for the VULCAN simulations, it was necessary to measure the inlet and outlet flows from the nacelle simulator under ambient conditions without fire. The openings shown in Figure 8-119 and Figure 8-120 are not the geometric ventilation paths. The various ventilation paths, such as the balance piston vent, aft diamond vents (both upper and lower), and AMAD bay ventilation paths in the front, have been "sized" to provide the flow distributions predicted in the airflow analysis conducted by Northrop-Grumman.⁸⁰ The simulator is designed for testing at one flight condition, traveling at 0.55 M (Mach number) at sea level. Given this restriction, three nominal flows were selected to correspond to three major flight conditions: high-speed, high-altitude cruise, loiter, and precision approach. These flows are 0.96 kg/s, 0.68 kg/s, and 0.57 kg/s, respectively. The air is supplied from a centrifugal compressor driven by a gas turbine. The inlet flow is measured using a calibrated turbine meter. There is adequate straight pipe, according to ASME Standards,⁸¹ and a flow straightener between the compressor and the turbine meter. Likewise, there is adequate straight pipe downstream of the turbine meter, and downstream of the 45° elbow, there is an Etoile swirl-removing conditioner in the straight pipe leading to the nacelle. The supply air pressure was measured with a water manometer immediately downstream of the turbine meter. The air effluxes were measured at each of the outlets separately under steady state. The air temperatures in the nacelles were measured with thermocouples at four locations, one on each side and near each end of the nacelle. The airflow out the aft diamond vent was measured with a pitot rake. The airflow in the other outlets was measured with a calibrated vane anemometer and stopwatch. Air pressures in the nacelle were measured at three locations using an inclined water manometer. All airflow data were corrected to ambient conditions at the time of test in order to determine the mass balance.

The nominal mass flow of air was set on the control console by setting the speed of the gas turbine driving the blower. There was some small variation in flow, less than 6 %, with a period of many seconds resulting from the gas turbine-mounted controls. During the test run at each rate, at least four readings were observed from each thermocouple and manometer. Considerably more data were recorded from the turbine meter. The vane anemometer, which was used for all air efflux measurements, except that from the aft diamond vent on top, was equipped with a mechanical totalizer. Consequently, a stopwatch was used to record the period of observation in order to obtain the average flow. The pitot rake and its converging ductwork came equipped with an electronic data output of its own, and the readout that was selected was that of volumetric flow at atmospheric conditions. Its period of observation was about 1 min, and two such observations were recorded for each test condition. All data were observed and recorded manually in view of the steady-state conditions. The automatic data acquisition system is designed for capturing transient fire events in the nacelle simulator and, therefore, would generate far more data than were required for this test. All data were averaged to provide a mean for each steady state. The observations could not be made simultaneously, and since there was some long-period variation in the flow, this introduced an additional uncertainty.

The proportional distribution of air effluxes remained nearly constant throughout the range of inlet flows and, therefore, the actual mass flows are nearly proportional to the total inflow. There were several surprising observations during the tests. The first was that there was no perceptible flow in or out of the bottom aft vent. It could be that the very fine mesh screen (≈ 50 /cm) which covered this vent was clogged with soot and rust particles or that the flow pattern inside the nacelle was directed away from this vent by the interior ribs. The second was the rather large variation, proportionately speaking, in the average pressures measured inside the nacelle, the range being greater than the mean. The third observation was a highly asymmetric velocity profile across the top aft vent. Most of the flow was exiting from the port side of the diamond; the velocity out the starboard side was measured with the vane anemometer to be ≈ 20 % of that out the port side. The pitot rake apparatus was designed to observe an overall average of that efflux collected by the converging duct.

The only corrections made to the pretest VULCAN model were the fact that no flow from the aft bottom vent and the actual, measured vent areas were used instead of their previous estimates. In retrospect, the only assumption which had any consequence was that of a uniform pressure throughout the interior of the nacelle simulator. As mentioned above, these large variations were unexpected, and they contributed significantly to the differences between the actual flow distribution at the boundaries and those predicted. It was predicted that half the flow would exit from the top aft vent. In fact, closer to two-thirds of the flow exited at that location. Consequently, the model predicted about 6.5 % more flow leaving via the Balance Piston Valve and 8.5 % more by the four AMAD vents in the front bulkhead. The test predictions of the model as adjusted for the actual vent areas are shown in Table 8-16.

In discussing the agreement between model and test in the total flow and average pressures, the test was a calibration of the nacelle simulator. In constructing the model, it was assumed that the balance piston vent and aft top vent would behave as parallel orifices and that the AMAD vents would behave more like nozzles. A weighted average of these coefficients of discharge was predicted to be 0.733. By actual test and calibration, it was determined that the effective coefficient of discharge equals 0.614. This value implies that all the vents behave essentially as sharp-edged orifices. This value of the coefficient of discharge correlates very well within the published data for the vent Reynolds number range, during test, of 1680 to 6800, for which the coefficient is 0.613 to 0.605, respectively.⁸¹

Table 8-16. Comparison of Predicted vs. Measured Pressures and Flows.

Inflow (kg/s)	Predicted Pitot Pressure (Pa)	Measured Pitot Pressure (Pa)	Measured Average Nacelle Pressure (Pa)	Predicted Average Nacelle Pressure (Pa)	Bias Ratio
0.92	145.2	93.0	380.6	380.4	-0.00041
0.65	71.4	53.7	181.6	187.3	0.03151
0.52	47.1	too small	118.2	123.6	0.04570

8.6.3 Test Matrices and Decision Tree

The test plan and test matrices were made to correspond to VULCAN simulations previously run to predict the test results. Twenty-five fire tests were conducted in the NAVAIR ground nacelle simulator to validate VULCAN simulations. This simulator was equipped with a four-nozzle suppressant distribution system. JP-8 pool fires (see Table 8-13 for pool areas) were considered in a variety of locations in the nacelle where the collection of fuel was likely, and both the suppressant flow and the overall air flow through the nacelle were varied to simulate a wide range of operating conditions. Tests were run also for reduced air flow. However, because of limitations on the rate of injection imposed by the HFC-125 vapor pressure, it was not possible to reach a condition where suppression failed at lower air flows. That was in agreement with the predictions that for lower airflows the overall mass fraction of agent for the attainable injection rates was always sufficient to extinguish the fires. The effects of varying the inhomogeneities were also investigated by capping individual nozzles.

The planning for the tests and the computer simulations resulted in the following test matrices with decision tree:

In test sequences 1 through 5, there are 11 to 14 tests indicated with no repeats.

1. First sequence: Pools in B1, B2, and B3C3. Airflow: 1 kg/s. All nozzles. Vary the suppressant injection rate. (3 tests)
 - a. Standard suppressant injection rate.
 - b. If 1.a. suppressed, 50 % injection rate.
 - c. If 1.b suppressed, 25 % injection rate. End.
 - d. If 1.b fails to suppress, 75 % injection rate. End
 - e. If 1.a fails to suppress, 150 % injection rate.
 - f. If 1.e suppressed, 125 % injection rate. End.
 - g. If 1.e fails to suppress, 200 % injection rate. End.
 - h. General procedure: Given the results of a test, with the first test nominally at the standard injection rate, successful suppression will lead to a 50 % reduction in the rate of injection and failed suppression will lead to a 50 % increase. A possible sequence of injection rates (suppression results) would be “std” (suppress), “50 %” (fail), “75 %” (?). If the second test had resulted in suppression, then the final injection rate would be “25 %.”

2. Second sequence: Cap Nozzle 2. Airflow: 1 kg/s. (2 or 3 tests) 4 are listed
 - a. If 1.a. fails to suppress, try with pool B3C3 only. Standard injection rate.
 - b. Pools in B1, B2, and B3C3. Standard injection rate.
 - c. If 2.b. is suppressed, try reduction in suppressant injection for 2.b (only pool B3C3). Suggest intermediate injection rate from Sequence 1.
 - d. If 2.a suppressed, try reduced suppressant rate for all pools that gave suppression in the first sequence.
3. Third sequence: Cap Nozzle 1. Airflow: 1 kg/s. (2 or 3 tests)
 - a. If 3.a. fails to suppress, try with pool B2 only. Standard injection rate.
 - b. Pools in B1, B2, and B3C3. Standard injection rate.
 - c. If 3.b. is suppressed, try reduction in suppressant injection for 3.b (only pool B2). Suggest the intermediate injection rate from Sequence 1.
 - d. If 3.a suppressed, try reduced suppressant rate for all pools that gave suppression in the first sequence.
4. Fourth sequence: Cap Nozzle 3. Air standard injection rate. (1 or 2 tests). Pools in B1, B2 and B3C3. Use lowest injection rate where suppression succeeded in the first sequence if this differs from standard injection rate.
 - a. 75 % injection rate.
 - b. 50 % injection rate.
5. Fifth sequence: Repeat first sequence with airflow at 0.5 kg/s. (3 tests). This sequence might best be done before capping any nozzles to help map out the operation space.
 - a. 50 % injection rate.
 - b. 75 % injection rate.
6. Repeat tests in all sequences that bracket suppression.
7. Tests with reduced masses of agent (70 %, 43 %, and 32 %). Airflow: 1 kg/s.
8. Tests with 100 % agent at reduced injection rate. Airflow: 0.75 kg/s.
 - a. Minimum injection rate of agent.
 - b. Slightly lower airflow; 0.73 kg/s.

Suppressant injection rate was defined as “standard” for the standard rate of injection nominally used in the qualification tests, “50 %” for half that rate of injection, “75 %” for $\frac{3}{4}$ that rate, etc. The procedure for changing the suppressant injection rate was to change the bottle pressure with a fixed suppressant mass. If any set of the pool fires were unstable, the air flow was reduced. When capping nozzles, the agent flow for a given bottle pressure was reduced somewhat. The bottle pressures led to suppression without the inhomogeneities caused by removing nozzles.

8.6.4 Actual Test Program

As the tests progressed through the decision tree and matrices, the sequence of tests was modified to adjust to the findings, in particular the seeming dependence of the success of extinguishments on the agent injection rate of the agent. As a result, the enumeration of Test Series 7 and 8 above were changed to Test Series 5 and 1 below. Series 8 was a repeat of certain tests in Series 1 (e.g., 8b = 1b). The actual path was:

1. First sequence: Pools in B1, B2, and B3C3. Airflow: 1 kg/s. All nozzles. Vary the suppressant injection rate. (3 tests)
 - a. Standard suppressant injection rate.
 - b. If 1.a. suppressed, 50% injection rate.
 - c. If 1.b fails to suppress, 75% injection rate.
 - d. Repeated b and c for replication assurance.
2. Second sequence: Cap Nozzle 2. Air flow: 1 kg/s.
 - a. Try with pool B3C3 only. 75% injection rate.
 - b. Pools in B1, B2, and B3C3. 75% injection rate.
 - c. If 2.b suppressed, 50% suppressant rate for pool B3C3.
 - d. Standard injection rate.
3. Third sequence: Cap Nozzle 1. Air flow: 1 kg/s.
 - a. Pools in B1, B2, and B3C3. 50% injection rate.
 - b. Pools in B1, B2, and B3C3. 75% injection rate.
 - c. Pools in B1, B2, and B3C3. 75% injection rate and 0.75 kg/s air flow.
 - d. Pool B3C3 only. 75% injection rate.
 - e. Pool B1 only. 75% injection rate.
4. Fourth sequence: Cap Nozzle 3. Air flow: 1 kg/s.
 - a. Pools in B1, B2, and B3C3. 75% injection rate.
 - b. Pools in B1, B2, and B3C3. 50% injection rate.
5. Fifth sequence: Reduced mass of agent and airflow 1 kg/s.
 - a. 50% injection rate.
 - b. 75% injection rate.
6. Repeat tests in all sequences that bracket suppression.
7. Reduce agent mass. Airflow: 1 kg/s
 - a. 69% of agent and standard injection rate.
 - b. 69% of agent and 75% injection rate.

- c. 43 % of agent and standard injection rate.
 - d. 32 % of agent and 116 % standard bottle pressure.
8. Test with 100 % agent at reduced injection rate. Airflow: 0.75 kg/s
- a. Minimum agent injection rate.

8.6.5 Instrumentation

Supply airflow measurement was made using a 15.24 cm turbine meter (Sponsler Co., Inc., Model SP6-CB-PH7-C-4X, S/N 130619). When calibrated in water, the meter had an relative uncertainty of $\pm 0.75\%$. Temperature measurements were made using 21 type K thermocouples with an uncertainty of $\pm 1\text{ }^{\circ}\text{C}$. Two digital stopwatches with an uncertainty of less than 0.1 s over 15 min period were used for time measurements. Fuel quantities for the pools were metered using graduated cylinders with an uncertainty of $\pm 5\text{ mL}$. Four video cameras were used to record the existence of fire and its extinguishment inside the nacelle. Other instruments included a dead weight tester from Druck Co. with a range of (0 to 71) MPa and an uncertainty of $\pm 0.02\text{ MPa}$, a pressure gage from NoShok with a range of (0 to 7.1) MPa and an uncertainty of $\pm 0.04\text{ MPa}$, and a pressure transducer from Patriot Gage Co. with a range of (0 to 20.7) MPa and an uncertainty of $\pm 0.1\text{ MPa}$.

8.6.6 Test Procedure

These tests focused on extinguishing JP-8 pool fires contained by structural ribs and longerons along the lower nacelle surface. Prior to the testing, the bottom of the nacelle was lowered and the spaces between the ribs were sealed from their normal drain holes so that each could become a container for fuel. In the tests, three pools (Figure 8-114) were used: B1, B2 and B3 (or B3C3, indicating that the pool crossed one longeron). Prior to the tests, measured quantities of water were added to each pool, and the dimensions of the resulting pools were recorded to document the surface area of each pool as a function of liquid contained in the pool.

In most of the tests, all three pools were ignited because this provided the strongest fire source. In several tests, only the first or third pool was used in conjunction with fewer agent-distribution nozzles in order to assess the spatial distribution of the agent in both the VULCAN model and the real nacelle. The burning rate and the nacelle temperatures were observed to be substantially lower when a single pool was burned, as predicted in the VULCAN pretest simulations.

The mass of agent to be used in each test was measured by the difference over the tare of the empty bottle on a calibrated scale. HFC-125 was the agent used in all tests. The rate of injection was controlled by the nitrogen pressure in this bottle, and three rates of injection were targeted by setting the bottle pressure to one of three values: 3.55 MPa, a rate roughly 75 % of standard design, 1.9 MPa, and a rate roughly 50 % of the standard 0.85 MPa. At these ambient temperatures the vapor pressure of HFC-125 was about 0.85 MPa so that no nitrogen charge was added for the lowest pressure and rates. Nitrogen is somewhat soluble in this agent, and consequently the fire-suppression agent in these tests was a mixture of both HFC-125 and nitrogen; the latter was ignored in the VULCAN simulations. The suppressant bottle discharges downward so that the initial discharge is driven by the nitrogen pressure, which drops adiabatically as liquid agent is displaced from the bottle. At an intermediate pressure, the rate of pressure change slows; this is associated with agent discharge driven largely by the boiling of the agent or the

dissolved nitrogen. For the lowest bottle pressure there is no nitrogen-driven stage. The last stage of the discharge is gaseous agent and nitrogen flowing from the bottle together. The pressure profiles from several tests, using all of the nozzles, are shown in Figure 8-121. The discharges from the two tests denoted 1a(21) and 1a(25) are essentially the same conditions, as are the four tests denoted 1b(21), 5d(25), 8a(26) and 1b(26). The scatter in these pressure profiles is indicative of uncertainties attributable to, for example, ambient temperature changes that may heat the bottle during the few minutes that the test is being set up. Such uncertainties were estimated to be roughly $\pm 10\%$.

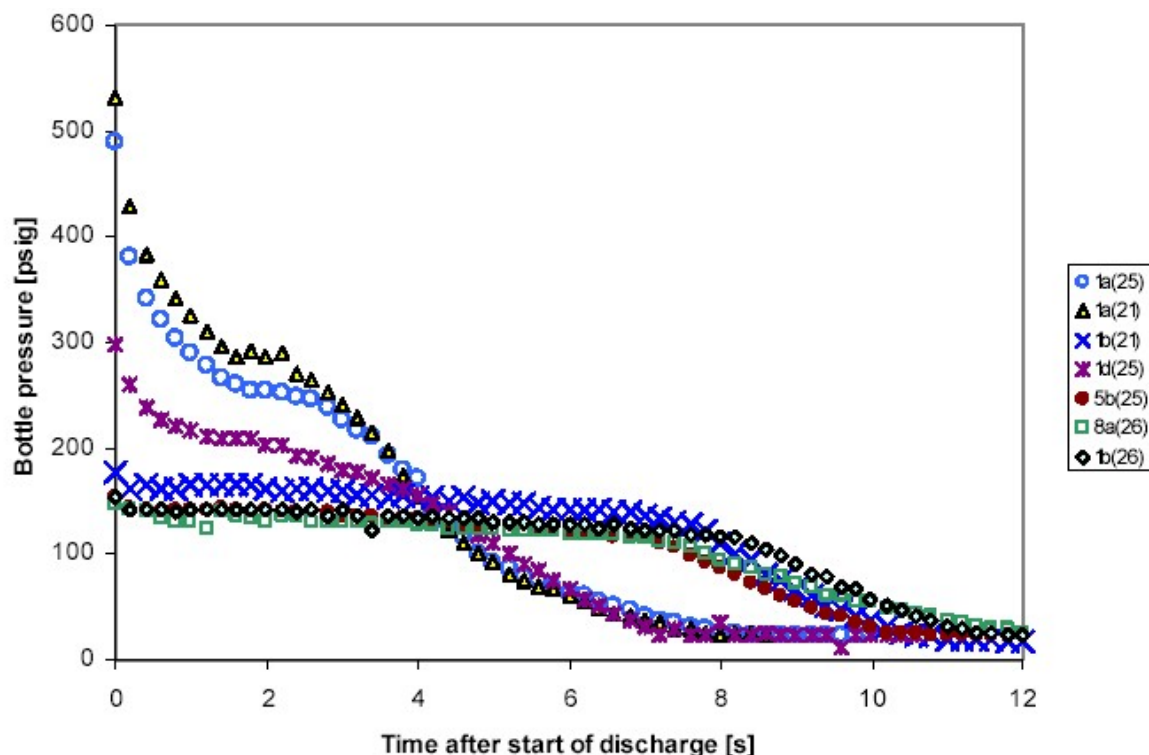


Figure 8-121. Transient Bottle Pressure during Discharge for Various Initial Pressures with Nozzles Discharging a Total of 3.2 kg of HFC-125.

Once the bottle was filled, it was installed into the distribution piping on the nacelle, and its manual safety valve was opened. Predetermined quantities of fuel were poured from graduated cylinders into the pools chosen for each test. At the end of each test, the remaining fuel was drained from each pool so that the amount consumed could be accounted; these data, along with the elapsed time of the test, gave an estimate of the heat-release rate during the test.

Igniting the pools of JP-8 fuel at ambient temperatures was challenging. The bottom of the nacelle was warmed with hot air to enhance the volatility of the fuel and to reduce heat losses. A minimum airflow from the blower at idle was established to provide sufficient air for combustion. An electric igniter was inserted over each pool in turn while a more volatile fuel, pure ethanol, was sprayed onto the pool. Once the pool ignited, it required about 30 s to begin vigorously burning. After all pool flames had been established, the airflow was ramped up to the predetermined rate, either 1 kg/s or 0.5 kg/s, according to the turbine meter. This steady flow was maintained for about 15 s to 30 s before the agent was released. The elapsed period of burning was recorded with stopwatches as well as by the digital data acquisition system.

This system also recorded the signals from the array of 21 thermocouples in the nacelle. The indicated temperatures did not attain steady state over the duration of the fires. Four video cameras recorded the views inside and outside the nacelle, from which elapsed times for extinguishment were extracted.

After each release of agent, a reduced airflow was maintained to cool the nacelle and remove potentially inflammable vapor. Then the remaining fuel was collected and measured in the graduated cylinders.

For the tests in which a nozzle was removed by capping the end, the sequence was repeated also by lowering the bottle pressure until suppression failed. The general sequence for changing the injection rate was to reduce the injection rate by 50 % if the previous attempt succeeded and to increase the injection rate back to 75 % of the standard rate if the previous attempt failed to extinguish. The lowest attainable injection rate was 50 % of the nominal designed rate, so this process results in bracketing the suppression in proximity to 100 %, 75 %, and 50 % of normal injection rates. The nominal bottle pressures corresponding to these tests were 0.84 MPa, 1.9 MPa, and 3.55 MPa. While these were relatively wide margins, the available resources did not allow for additional tests to narrow these bands. The tests actually conducted are summarized in Table 8-17.

Table 8-17. Summary of Full-Scale Tests Conducted.

Test Indicator*	Air Inflow (kg/s)	Pools	Nozzles	Suppressant Mass (kg)	Bottle Pressure (MPa)	Target Suppressant Discharge Rate (kg/s)
1a (25)	0.91	All	All	3.18	3.55	1.1
1a (21)	0.91	All	All	3.18	3.55	1.1
1b (21)	0.91	All	All	3.18	0.84	0.5
1d (25)	0.91	All	All	3.18	1.83	0.8
5b (25)	0.46	All	All	3.18	1.83	0.8
5d (25)	0.46	All	All	3.18	0.84	0.5
7a (26)	0.91	All	All	2.20	3.16	1.1
7d (26)	0.91	All	All	2.20	1.86	0.8
8b (26)	0.68	All	All	3.18	0.83	0.5
1b (26)	0.91	All	All	3.18	0.9	0.5
2d (27)	0.91	B3C3	No Nozzle 2	3.18	3.55	0.7
2b (27)	0.91	All	No Nozzle 2	3.18	1.9	0.6
2d (27)	0.91	All	No Nozzle 2	3.18	3.55	0.7
2a (27)	0.91	B3C3	No Nozzle 2	3.18	1.9	0.6
3d (27)	0.91	All	No Nozzle 1	3.18	1.9	0.6
3b (27)	0.91	All	No Nozzle 1	3.18	3.55	0.8
3c (28)	0.68	All	No Nozzle 1	3.18	1.9	0.6
3e (28)	0.91	B1	No Nozzle 1	3.18	1.9	0.6
3d (28)	0.91	B3C3	No Nozzle 1	3.18	1.9	0.6
4a (28)	0.91	All	No Nozzle 3	3.18	1.9	0.6
4b (28)	0.91	All	No Nozzle 3	3.18	0.84	0.4
7c (28)	0.91	All	All	1.36	3.55	1.1
7d (28)	0.91	All	All	1.02	4.14	1.1

Note: Variations from the baseline conditions, apart from bottle pressure, are indicated in bold face.

* The alpha-numeric indicates the test conditions described in the Actual Test Program. The number in the parentheses is the date when the tests was conducted.

8.6.7 Test Results and Comparisons to Simulations

The tests are enumerated in Table 8-18 in chronological order; these test numbers will be used in the discussion that follows. In addition to VULCAN, simulations were also performed using FDS and FPM to predict the results of the fire tests. Figure 8-122 and Figure 8-123 show the nacelle configurations used in the FDS and FPM simulations, respectively. The rectilinear shape of the nacelle simulator is the result of the Cartesian coordinate system used in FDS and FPM.

Table 8-18. Comparison of Fire Test Results and Pretest Simulations.

Test Plan		Fire Test		VULCAN	FPM	FDS
Test Number	Alpha-numeric Designator	Measured Time to Extinguish (s)	Agent Injection, Rise Time (s)	Predicted Time to Extinguish (s)	Predicted Time to Extinguish (s)	Predicted Time to Extinguish (s)
2	1a	Out in 1.3 s	6.8	1.1 (e)	2.0	2.0
3 & 12	1c	Accelerated burning	10.0	Marginal out	Not out	Not out
5	1d	Out in 5.2 s	7.0	1.9 (e)	2.0 to 3.0	2.6
6	5d	Out, no data	No data	1.9 (e)	1.0 to 2.0	2.6
7	5b	Out in 4.4 s	9.5	Out	1.0	< 5.0
8	5a	Out >6.3 s	4.4	1.9 (e)	< 3.0	1.9
9	5b	Out in 4.85 s	5.0	n/av	1.0	3.0
10 & 11	8b	Out in 2.3 s	9.6	n/av	< 2.0	3.6
13	2a	Out in 11.2 s	6.5	Not out	Not out	6.5
14	2d	Not out	10.4	Not out	Not out	> 4.0
15	2b	Out in 28.9 s	7.2	3.4 (e)	Relight > .6	7.0
16	2c	Not out	9.3	Not Out	2.0 to 3.0	13.0
17	3a	Not out	10.8	Not out	Not out	Not out
18	3b	Out in 6.0 s	5.6	1.5 (e)	7.0	18.6
23	4b	Not out	13.8	n/av	2.0	19.5
24	7a	Out in 3.9 s	3.8	n/av	4.0	16.8
25	7b	Out in 1.8 s	2.4	n/av	3.0, relight @ 6.0 ?	18

Table 8-18 also shows a condensation of all tests for which simulations were available. The primary observations therein include whether or not the fire was extinguished, the model predictions, the period of agent injection, and an estimate of the observed times-to-extinguish versus the predictions. These latter required interpretive judgment and the application of “rules of thumb” unique to each simulation program to decide when extinction was complete. Similarly, for the actual fire test data, while the injection period was acquired, the link between the recording video and the data-acquisition system had failed, unbeknownst to the test engineers. Consequently, the synchronization of the visual data to the agent-injection transient was not available during post-processing. The time of extinction was clearly observable with an uncertainty of ± 0.1 s, but the initiation of mixing the agent could be observed only by a sudden increase in the intensity of the fire. The uncertainty of this observation is estimated to be ± 2 s.

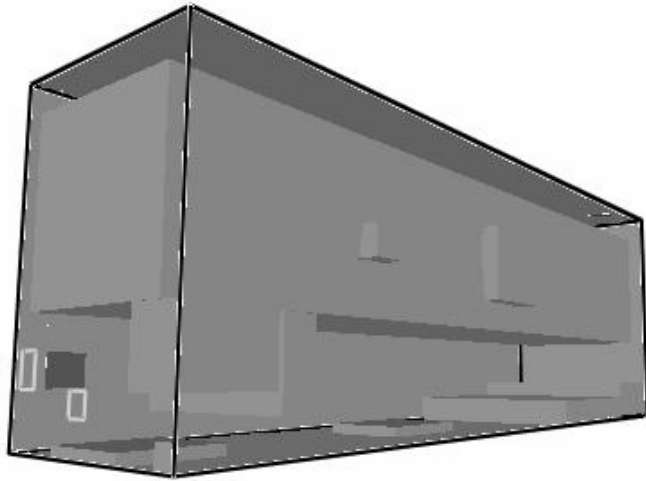
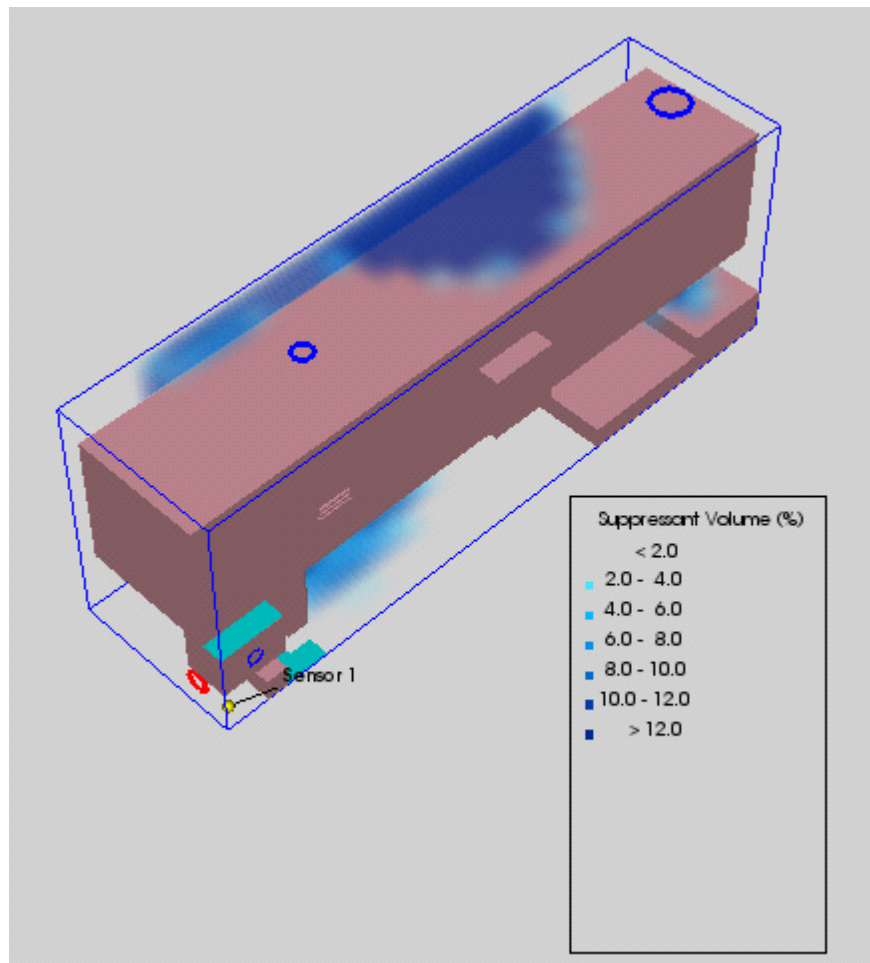


Figure 8-122. Nacelle Configuration Used in FDS Simulations.

Figure 8-123. Nacelle Configuration Used in FPM Simulations.



Test 2 was the “standard” test arrangement. It used the full bottle pressure, the full mass of agent, and all the discharge nozzles and all the discharge locations that were used to qualify the system. As expected and predicted, the fires were extinguished.

In Test 3, the rate of injection was reduced to the minimum, which was the vapor pressure of HFC-125, pre-calculated to be about 50 % of the standard rate. For replication, this test was repeated a few days later, as Test 12. What was observed seemed to be accelerated burning. At this lowest rate of injection, flames came shooting out of every opening in the test nacelle, and the fires did not go out. From the video records and personal observations, it seemed that the injected agent only served to stir up the gases in the nacelle in such a way as to promote better mixing. In consequence, a much more intense fire resulted until the end of the injection period.

The only difference between Tests 5 and 6, which were otherwise a replicate pair, was the order in which the pools were filled. Normally (and in Test 5) they were filled from the front (B1) aft. In Test 6 they were filled front, back, and then middle last, in order to control for loss by evaporation during the period of filling. The reason for this change was the observation that more fuel disappeared from the middle pool than from the other two. There was no change in the test result, and this confirmed observations both during the test and from the viewing the video records that the airflow in the nacelle blew the fuel out of the second pool (B2) in visible drops toward the flame front over the pool B3C3. In both these tests, the agent was injected at about 75 % of the standard rate; in both cases the fires were extinguished.

In Test 7, a proportionality question was investigated. Here, the injection rate was again set at about 50 % of standard, but the airflow also was reduced by half. Even with the extended injection period, the fires were extinguished promptly. In this test, the concentration of agent in the ventilating airflow was identical to that of Test 2, and the obvious conclusion may be drawn. Following this test, the question arose whether or not the vigorous airflow itself was a major factor in “blowing out” the fires. In this test, the pool B3C3 was filled to the standard 2 L, and after the fire was established and stable there, the airflow was increased to the standard rate. The observed result was the most vigorous blow-torch seen, and it was concluded that range of airflows in these tests were insufficient to “blow out” the fires.

Test 8 was the first to investigate the possibility of using less agent; the mass of agent was reduced to 2.2 kg. Using the standard airflow and injection rates, again the fires were extinguished promptly, as in Test 2. Test 9 was identical, except that the injection rate was reduced to about 75 %. As in Test 5, the fires again were extinguished, proving that the “standard” mass of agent was more than sufficient to extinguish these pool fires.

In Tests 10 and 11, the question of proportionality was investigated further. In this replicate pair, the airflow was reduced to 75 % and the injection rate to 50 % (the minimum). In terms of agent concentration relative to airflow, these tests were similar to Test 5, and in the end the result was the same. However, visual observations of the test showed that it took perceptibly longer to extinguish under these conditions, which indicated that the edge of the extinction envelope was near.

In some tests, the standard, successful distribution system of four nozzles discharging the agent was degraded by capping one nozzle at a time and discharging the agent into the nacelle through the remaining three. In Tests 13 through 16, Nozzle 2, which discharged athwart near the front of the nacelle, was capped. In Tests 16 through 21, Nozzle 1, which discharged upwards at the same location as Nozzle 2,

was capped. In Tests 22 through 23, Nozzle 3 was capped. Nozzle 4 was so remote from the fires, toward the aft, outboard end of the nacelle, that it was never altered.

Test 13 was conducted to verify fire-modeling predictions on the effect of poor distribution of agent. Nozzle 2 discharged athwart under the engine. It was predicted by two out of three simulations that this pool fire would not be extinguished, since the only pool fueled and enflamed was B3C3. This was a configuration which was close to the edge of the extinction envelope. The injection rate was set at 75 % of standard, as in Test 5, except in this case the critical nozzle was capped, and only one pool instead of three was used. In fact, the fire did finally go out, but it took more than 11 s to extinguish.

In Test 14, all three pools were lit, and the injection rate was reduced to about 50 %. The model predictions were the same for this case as for Test 13, but this time the fires were not extinguished. This means that FDS, which predicted correctly for Test 13, gave the only “wrong” result this time. In conclusion, it seems that when the models predict different outcomes, the edges of the actual extinction envelope are nearby.

To illustrate how close to the edge of the extinction envelope these tests were, Test 15 replicated Test 13, except that all three pools were lit. In this case, the fires were extinguished. However, the elapsed time to extinction was abnormally long, almost 30 s. Perhaps the greater mass of products of combustion acted to suppress the fires further.

The varied outcomes of the three prior tests led to conducting Test 16, in which only one pool, B3C3, was lit, and the injection rate was reduced to about 50 %. In this case, all three models predicted extinction, and the fires did indeed go out.

In the next series of tests the original, logical sequence was followed with Nozzle 1 capped. As before, in Test 17 the injection rate was set at 50 %, and all three models correctly predicted the outcome. Likewise, in Test 18 the same configuration was set except that the injection rate was set to 75 %. In this test also, all three models correctly predicted the same outcome of extinguishment.

The next three tests, all with Nozzle 1 capped, are not shown in Table 8-18. Test 19 established an airflow of 75 % of standard and an injection rate at 75 %, and even with Nozzle 1 capped the fires were extinguished. This one presented an equivalent proportion of agent to airflow as if both were standard. In Test 20, only pool B1 was enflamed, and with standard airflow and a 75 % injection rate, that fire was extinguished, but with difficulty because it took several seconds to go out. This test was similar to Test 13 except for which pool was fueled. In the same manner, Test 21 was similar to Test 13 including that the fire was in pool B3C3 only, but in this case the fire did not go out. No simulations of these tests were done.

Nozzle 3 was capped in Tests 22 and 23; otherwise Test 22 was a replicate of Test 5, and Test 23 was a replicate of Test 3. For these configurations, Nozzle 3 made no difference: the two tests in each pair had the same outcomes. The fires in Tests 5 and 22 were extinguished; the fires in Tests 3 and 23 did not. The injection period of Test 23 was the longest of any test. A simulation in VULCAN was not run; FPM predicted extinguishment, as did FDS, but again note the elapsed time before extinction, which indicates that this test also approached the edge of the envelope.

All the tests conducted with less agent were successful in extinguishing the fires in all three pools. Standard conditions were set for all these tests. The first instances were reported above for Tests 8 and 9. In Test 24, the mass of agent was reduced to 1.36 kg, and the bottle was at standard pressure. In Test 25, the mass of agent was reduced to 1.02 kg, and the bottle pressure was increased to 4.14 MPa to increase the rate of injection. All fires were promptly extinguished. The most likely deduction may be that the rate of injection is the most important factor in extinguishing fires.

The 25 tests were conducted to explore the edges of the extinguishment envelope for this ground nacelle simulator. Two of these tests were conducted to determine whether or not fires could be stabilized in individual pools (B1 and B3). It was demonstrated that these pools could sustain a fire, which agreed with VULCAN simulations, although the VULCAN simulations indicated that the stability of fires in individual pools was sensitive to heat losses. Specifically, if the heat losses associated with conduction through the pool to the nacelle were 50 % of the heat flux to the pool (essentially reducing the vaporization rate by 50 %), then certain pools, not employed in the present series of tests, could fail to sustain fires. In the test, it was necessary to apply heat sources (heat lamps) to the nacelle under the pools to minimize heat losses just to get the fires stabilized, and this lends support to the VULCAN observations.

Of the remaining tests, two were replicates of the first two tests in order to gain confidence in the results; in each replicate pair, the results were identical. Because of the vapor pressure of HFC-125 and the inability to light or stabilize fires in certain pools, some pretest VULCAN simulations could not be investigated. Consequently certain tests were run without pretest simulations. However, across a similar range of parameters, these results were in agreement with the trends of the VULCAN simulations.

Ideally, the pressure data shown in Figure 8-121 could be used to determine the actual suppressant discharge rate to a level of accuracy similar to the accuracy of the inlet airflow meter. During the post-test data processing, this was done by calculating the adiabatic discharge of liquid agent from the bottle and assuming that the flashing and two-phase flow occurred at the throats of the nozzles, as reported in Smith et al.⁸² However, during the tests the discharge rate had to be estimated. For this purpose, discharge rates identical to those in the VULCAN simulations were employed. Specifically, with all nozzles discharging, the 3.2 kg of HFC-125 was presumed to discharge uniformly over 3 s, 4.5 s, and 6 s for bottle pressures of 3.55 MPa, 1.9 MPa, and 0.85 MPa. The discharge rate was presumed to be reduced in accordance with the reduction in the total nozzle area when nozzles were capped. The assumption of constant discharge rates in the VULCAN model would be a source of disagreement with the test results. This uncertainty in the rates varies over the duration of the injection period, and the errors in the estimates provided here are likely to be greatest in the earliest fraction of a second and during the latter periods. If the rate of suppressant injection were averaged over the significant few seconds, say the first 2 s to 3 s of the injection process, the uncertainties are on the order of $\pm 15\%$.

The results of the tests employing all nozzles are shown in Figure 8-124. Blue bars represent successful extinction, while red bars represent a failure to suppress the fire. In all of these cases, the VULCAN predictions were in agreement with the test results.

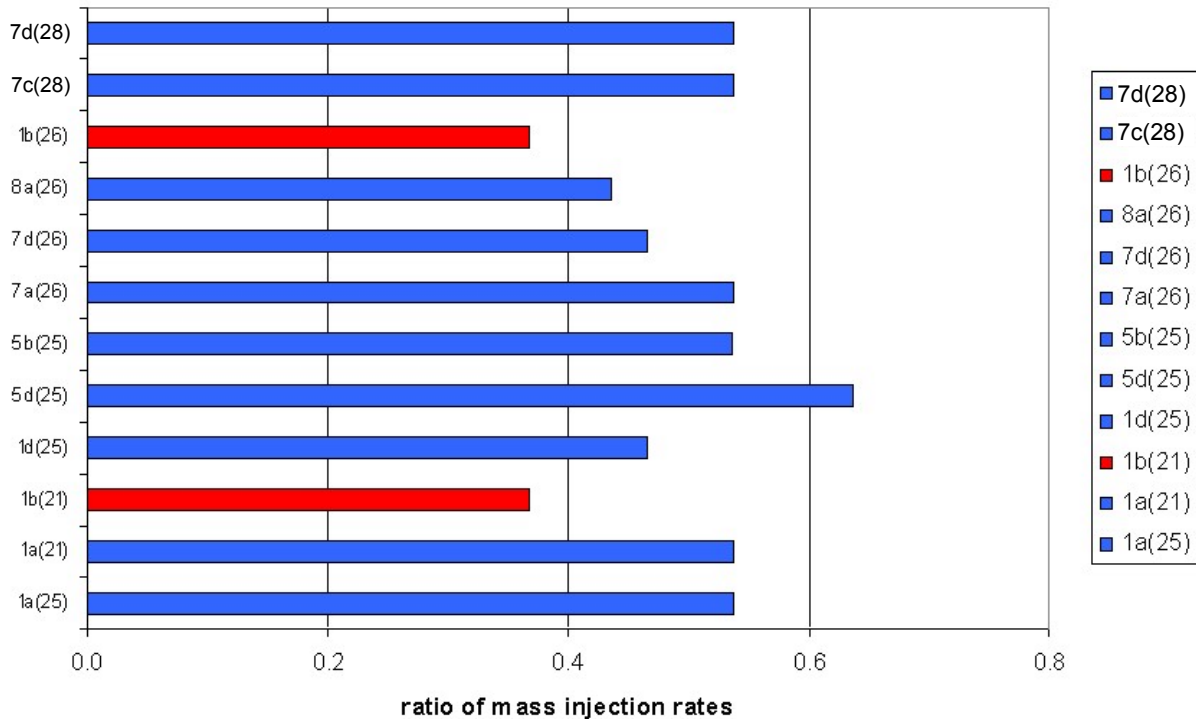


Figure 8-124. Results of Tests with All Nozzles Used.

The results of tests with labels starting in “1”, “5”, or “8” correspond to baseline cases using approximately 3.2 kg of suppressant at varying bottle pressures and airflows. This series can be viewed as varying the ratio of the suppressant mass injection rate to the total (air + suppressant) mass influx. Suppression is observed to fail when this ratio is below (approximately) 0.4 ± 0.04 . Where the airflow is greatest and the bottle pressure is lowest, the total uncertainty is estimated to be $\pm 19\%$. For reduced airflows (0.68 kg/s) or increased bottle pressures (1.82 MPa), suppression was always successful. That the ratio of injection rates exceeds the cup burner mass fraction⁴ by a factor of 1.4 (0.4/0.28) probably indicates the degree of inhomogeneous agent distribution in the system.

In Figure 8-124, the four tests with labels starting “7” are where the mass of suppressant was reduced from 3.2 kg to 2.2 kg, 1.4 kg, and 1 kg. All of these tests resulted in successful suppression of the fire. In each of these cases, the rate of injection was close to that for the designed conditions. It was estimated that the bulk of the suppressant was injected in 3 s for 3.2 kg, in 2 s for 2.2 kg, and in 1 s for 1 kg to 1.7 kg, which reinforced the importance of the ratio of injection rates. The VULCAN simulations were conducted only with 3.2 kg and 2.2 kg of agent, and these simulations agreed with the tests. No VULCAN simulations were run for agent masses less than 2.2 kg.

Figure 8-125 summarizes results for which one of the four nozzles was capped. Blue bars represent successful extinction, while red bars represent a failure to suppress the fire. In all of these cases, the VULCAN predictions were in agreement with the test results. Green bars indicate cases where suppression was successful in the tests but was indicated to fail in the VULCAN simulations.

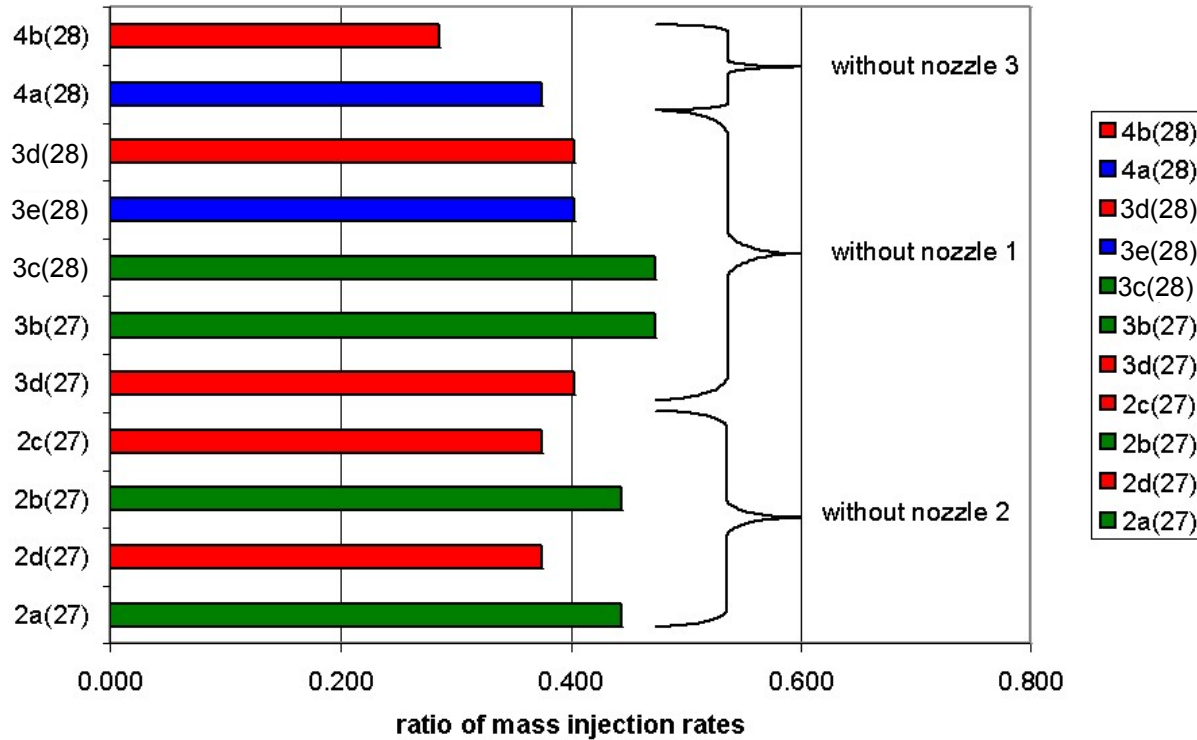


Figure 8-125. Results of Tests with One Nozzle Capped.

Capping a nozzle has two effects. First, the total nozzle area is reduced so that, for the same bottle pressure, the suppressant injection rate is reduced proportionally. The second effect of capping a nozzle is to increase the inhomogeneity of the distribution inside the nacelle. Greater inhomogeneity requires a greater ratio of injection rates to achieve successful suppression. VULCAN simulations predicted that higher inhomogeneity would result by capping either Nozzle 1 or Nozzle 2, but not Nozzle 3.

The results of tests, with Nozzle 3 capped, are indicated by the labels with the prefix “4” at the top of Figure 8-125. The ratio where suppression fails trended toward lower values than with all nozzles. Whether or not the degree of inhomogeneous distribution actually decreased and performance of the system increased by capping Nozzle 3, should not be concluded based on the present results, even if implied by the tests. Nozzle 3 injected suppressant into the upper nacelle, far from any of the pool fires. For this reason, a reduced concentration of suppressant in the upper nacelle may not have influenced agent effectiveness at the locations of the fires. The uncertainties in the suppressant injection rate and the lack of replicate tests do not allow definitive conclusions to be drawn. Tests where Nozzle 1 was capped are indicated with the prefix “3” in Figure 8-125. In some tests only specific pools were ignited in order to find the locations where fires failed to be extinguished (Table 8-17). The tests where all pools were ignited are 3b, 3d, and 3c. In these cases, there was a difference between the VULCAN results and the tests. The VULCAN simulations predicted a failure to suppress the fire in test 3b, although the fire was extinguished in the tests. (The VULCAN prediction for 3c was not actually run, but extrapolated.) Reducing the injection rate to a ratio 20 % less led to a successful prediction, as in case 3d. VULCAN tended to predict failure to suppress before it actually occurred. This may be because the mixing rate within the VULCAN simulation erred on the low side. In highly cluttered areas bounded by walls, the current clutter model did not account properly for enhanced mixing near the wall. Clutter models may

improve these predictive capabilities, but the fact that the VULCAN predictions tended to be conservative, with a safety factor on the order of 20 %, is preferred and acceptable. In terms of the ratio of the mass injection rates, the tests indicated a critical value between 0.4 and 0.45, a statistically insignificant increase over the 0.4 (± 15 %) found in tests employing all nozzles. The VULCAN predictions indicated that the critical ratio of mass injection rates was between 0.45 and 0.55. Tests 3e and 3d, in which only pools B1 and B3 were filled, were done to ascertain the regions of the inhomogeneous agent distribution that led to failed suppression. The results indicate that low concentrations occur in the vicinity of pool B1 but not pool B3, which agrees with the VULCAN simulations. The ability of VULCAN to identify regions where fires cannot be suppressed is very useful.

The results of tests for which Nozzle 2 was capped are indicated by the labels with the prefix “2” in Figure 8-125. As with the previous examples, the VULCAN simulations indicated a failure to suppress at the higher injection rates because of a reduced homogeneity of agent distribution. Test results showed that the failure to suppress occurred at the next decrement in the injection rate, the same as when Nozzle 1 was capped. This likewise indicates a 20 % safety factor relative to the VULCAN simulations. The failure to suppress when either nozzle is capped occurs at a ratio of injection rates again spanning 0.4, the same as in the tests with all nozzles. VULCAN simulations capping Nozzle 2 did indicate greater inhomogeneity in the fire region.

The pretest VULCAN simulations correctly predicted the success or failure of extinction in nearly all cases. In only two cases were there disagreements between the VULCAN predictions and the test results. In both of these cases, when either of the two forward nozzles was capped, the test results found that the fires were suppressed using a bottle pressure 25 % lower than the VULCAN simulations had predicted. This indicates that the VULCAN simulations were somewhat conservative in their predictions of the mixing in the forward nacelle region.

8.7 IMPROVED TRANSPORT OF WATER TO FIRES

8.7.1 Background

As noted in Chapter 1, initially the NGP research was directed at the full range of weapons systems in which halon 1301 systems had been installed. Water sprays or mists were (and are) viable alternatives for some of those platforms. Accordingly, the NGP supported efforts aimed at improving the efficiency of getting water sprays or mists to the fires. In particular, two techniques for improving water droplet transport to fires will be described and discussed: (1) electrically charged water mist and (2) a self-atomizing form of water.

8.7.2 Electrically Charged Water Mist

Background

It is well known that hydrocarbon flames contain electrical charges because of the process of chemiionization.⁸³ In chemiionization, flame radicals react to form electrons and positive ions at temperatures much lower than those required for thermal ionization. In a normal flame, both positive and negative ions (primarily formed by electron attachment) are formed in addition to the electrons. The high mobility of the electrons results in the outer region of the flame being negatively charged by the electrons

and the bulk of the flame region being positively charged by the preponderance of positive ions. Much of what is known about flame ionization has been learned from studies of premixed flames^{83,84,85,86} although some diffusion flame studies have been conducted.⁸⁷

For real fuels and real fires (almost always diffusion flames) there are a number of considerations which could lead to either increases or decreases in the flame ionization, but these cannot be quantified at this time. For example, real fuels contain impurities (e.g., metals) which can greatly increase the ion concentration. On the other hand the formation of soot particles in cooler regions of a fire act as sites to which electrons will attach. This keeps the negative charge closer to these regions of the fire than would occur if the electrons were free to diffuse away on their own. Thus, electron attachment may reduce the charge separation (at least in the fire plume) that normally makes flames appear to be positive.

While it cannot be certain which effects will dominate in real fires, there is no doubt that diffusion flames in air behave as though they are positively charged since they are strongly pulled by negatively charged objects.^{88, 89}

The application of an external electric field in the vicinity of the flame results in the motion of electrons and negative ions towards the positive electrode and the motion of positive ions in the opposite direction towards the negative electrode. More momentum is generally exchanged by collisions between the positive ions and the neutral gas molecules as compared to the momentum exchanged by collisions with the negative species dominated by electrons. This momentum exchange results in the production of an ionic wind⁹⁰ which is a flow towards the negative electrode. This ionic wind is responsible for the large flame displacements reported above, and the effect has been used to control blowoff stability,⁸⁹ which can be increased or decreased depending on the orientation of the electrodes that produce the electric field. These effects can be produced with extremely low electrical power levels, on the order of 10^{-2} % of the power released during combustion.

There are several different scenarios in which electric charging of the water mist droplets can interact with real fires. A negatively charged droplet approaching the vicinity of the fire will repel electrons and negative ions, and there will be an attraction between the negatively charged droplets and positive ions.

To distinguish whether the charged mist droplets move toward the flame or the flame moves towards the droplets, the overall mass of water mist per unit volume in a spray based on assumed droplet velocities was computed and compared it to the density of air under the assumption of a water application rate of $(1 \text{ to } 2) \text{ L}/(\text{min}\cdot\text{m}^2)$, which is considered to be sufficient to extinguish a heptane pool fire.⁹¹ For example, the mass of the water mist droplets contained in a unit volume is 1.3 % of the mass of air in the same volume for a water flux of $1 \text{ L}/(\text{min}\cdot\text{m}^2)$ and a droplet velocity of 1 m/s. The water density relative to air varies proportionately with the water flux and inversely with the droplet velocity. The effective mass per unit volume of the ions was taken as the density of the air since the ions pull the air or other flame gases along with them when they move.

The mass of liquid water per unit volume can vary from a small to a moderate fraction of the mass of the flame gases per unit volume depending on the velocity of the droplets and the temperature of the gases. Of course, the actual droplet flux, and thus the liquid water mass, is decreased if the droplets are evaporating as they approach the flame. Thus, if the water flows are low and/or the droplets experience a great deal of evaporation near the flame, the droplet mass is low compared to that of the ions and the air that contains them so that the droplets can move towards the flame.

Without a mechanism for charge removal, charge would build up and retard the attractive motion between the negative mist and the positive flame gases. This removal can be accomplished if there is an electrical ground in the vicinity of the fire. In many cases the circuit is closed by a conducting floor or wall in contact with the electrical ground. This would be the case for a fire on a ship deck or on metal shelving.

The voltage drop, ΔV , across a surface is given by

$$\Delta V = \frac{\rho t I}{A} \quad (8-51)$$

where ρ is the volume resistivity of any insulating layer such as paint, t is the thickness of the insulating layer, I is the total electrical current and A is the total surface area available through which current passes to ground. Because the currents involved in droplet charging are so small, and the surface area available for current flow to ground through floors and walls is so large, the voltage drop caused by current flow through wall or deck paint should be small. For aircraft applications such as fire extinguishment in engine nacelles, the surfaces are generally not painted so that there is no problem in obtaining a good electrical ground.

Even if the fire's net positive charge is small, the fire can still be a relatively better electrical conductor than the surrounding air due to the presence of charges in it. Thus, the droplets will still try to ground themselves through the fire, and the excess charge that they carry will eventually proceed to an earth ground near the base of the fire.

In addition to water droplets being individually drawn to the flame ions, the presence of a large number of charged droplets results in electrostatic repulsion between the droplets. An electrical ground allows a steady state current composed of the droplet charges to be established under the action of this self-repulsion. The current path could be composed of droplets striking the floor or wall, droplets evaporating and the electrons they carry either passing directly to ground or attaching to a molecule which travels to ground under the influence of the charge induced electric field. Positive ions could move toward the droplets and neutralize them, leaving a net negative charge composed of the fire's electrons and negative ions which are discharged through the electrical ground near the fire's base.

The presence of cooler soot particles in the upper regions of a fire plume may act as sites for flame electron attachment. Repulsion of the negatively charged droplets by the negatively charged soot particles, could be beneficial from the point of view that those droplets might not be swept away by high velocity plume gases. If those droplets are redirected to lower velocity regions outside of the main plume, then they might be pulled in closer to the base of the flame by the positive flame ions or the presence of a surface electrical ground. In any case there are a number of possible situations in which electrical charging will cause water mist to come into closer contact with reacting flame gases.

Safety considerations present only a small concern with the droplet charging method used in this work because the currents involved in mist charging are extremely small. In this program two power supplies were used: a high voltage (15 kV) unit which is not capable of delivering any significant current (200 μ A) and a lower voltage (5 kV) unit which can deliver 10 mA. The first unit is safe and the second unit can be made safe by installing current limiting resistors. While this is not life threatening in itself, any significant shock could be distracting or disorienting in an emergency situation. The only way such a shock could occur is by direct contact with the charged electrode. For this reason it is recommended that the high voltage electrodes be physically shielded to prevent direct contact with them.

Two references of particular interest for the present study are those of Patterson et al.,⁹¹ performed at the New Mexico Engineering Research Institute (NMERI), and Gottuk et al.,⁹² performed at Hughes Associates, Inc. Patterson et al.⁹¹ obtained a large database on uncharged mist extinguishment of heptane pool fires in a well-controlled test chamber environment. Gottuk et al.⁹² compared fire extinguishment of heptane pool fires with and without electric charging.

Patterson et al.⁹¹ used water mist to extinguish 5.08 cm diameter heptane pool fires in a 1.07 m × 1.07 m × 2.06 m chamber. Following establishment of the fire for 30 s, the chamber was closed so that there was no further ventilation once the mist was turned on. In spite of their great care in achieving a uniform water flux over their chamber and the absence of ventilation currents, their data exhibits a tremendous amount of variability in extinguishment time as a function of water flux (Figure 8-126), especially for low values of the flux. The curve shown is a cubic fit to the extracted data.

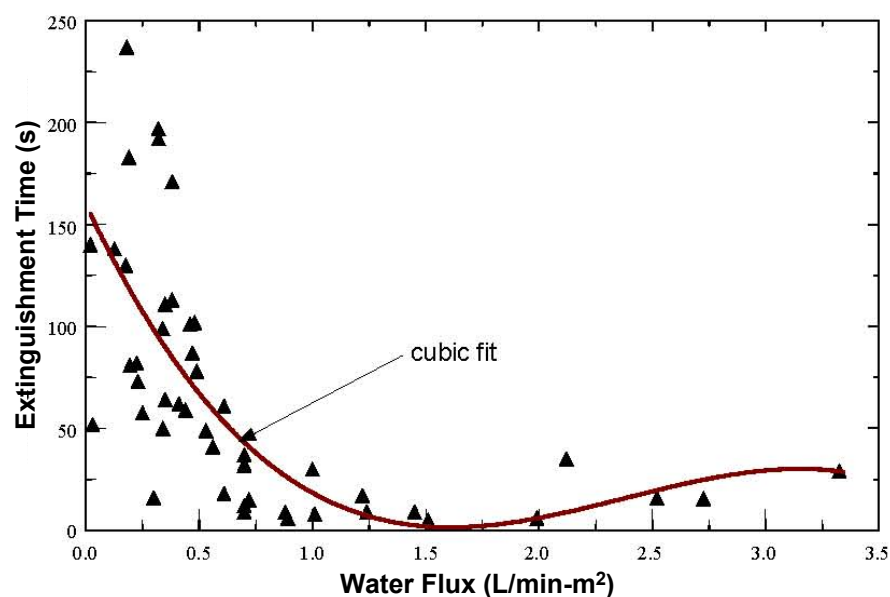


Figure 8-126. Extinguishment of Heptane Pool Fires by Uncharged Water Mist.⁹¹

Gottuk et al.⁹² studied the effects of electric charging of water mists on extinguishment of heptane fuel fires. A single mist nozzle was used in an open environment to extinguish a heptane fire in a 10 cm diameter pan. Water was collected to determine the water flux in the same size pan as used for the fuel. Gottuk et al.⁹² arbitrarily selected the criterion that a fire was considered to be extinguished if the extinguishment occurred within 20 s after application of the water flow. They reported that this was a useful criterion for their experiments on the basis that fires that were not extinguished in that time were never extinguished, except for one case with electrical charging in which extinguishment occurred in 34 s. Results were reported as groups of the number of cases in which a fire was extinguished out of the number of tests within a range of water collection rates for a given voltage.

Table 8-19 reproduces the fire extinguishment results that appear in Table 3 of the report of Gottuk et al.⁹² in the units of water flux used by Patterson et al.⁹¹ Their table shows three ranges of water mist flux and the fraction of the tests in which a fire was extinguished for each flux.

Table 8-19. Effectiveness of Charged Water Mist Expressed as Percent of Successful Pool Fire Extinguishments.⁹²

	Water Application Rate (L/min-m ²)		
	5.0 to 5.9	6.0 to 6.4	6.5 to 7.0
Uncharged (0)	0/0	6/13 (46 %)	9/10
+ Charged	0/3	2/6 (33 %)	0/3
- Charged	0/9	3/4 (75 %)	0/0

For the lowest water flux range, no fires were extinguished by the charged sprays; thus no improvement from the charging could have been seen. For the highest water application rate, the positively charged spray was significantly less effective than the uncharged sprays.

It is difficult to draw a conclusion for the middle range of water application rates. A change of a single test result for either type of charged spray gives results that are similar to the uncharged spray tests. It would take more extensive tests in this range to reveal a real effect.

Gottuk et al.⁹² concluded that no significant increase in fire extinguishing capability resulted from charging the water sprays and that the most notable effect of charging the spray was spray divergence, resulting in lower water application rates to the fire. Gottuk et al.⁹² were also concerned with the safety of the electrical system. However, their observation that charging makes the mist spread out could actually be beneficial, since small uncharged droplets have short horizontal stopping distances which determine how far they can spread from the centerline of a spray nozzle. Charged droplets produce a force on each other that can disperse them to greater horizontal distances. Without charging, extremely high pressures would be needed, or there would have to be an array of a great number of nozzles to achieve a wide distribution of fine water mist spray.

For the NGP, Berman and coworkers⁹³ at AeroChem Research Laboratories carried out exploratory research to further assess whether electrical charging of water mist could substantially reduce both the time and the amount of water required to extinguish a small pool fire by taking advantage of the electrical properties of flames. The specific objectives of the study were to:

- compare the motion of charged and uncharged water mist droplets near a flame
- determine the reduced time for fire extinguishment due to electric charging of the water mist. The current program addressed ceiling sprinkler extinguishment of compartment fires, and the same principles should hold for aircraft engine nacelle fires. The main technical problem encountered was achieving a uniform distribution of water mist over a significant surface area both with and without charging. Promising results were obtained despite this difficulty, which may be correctable with additional work.

Experimental Set-up

The fire test chamber used for the experiment is shown in Figure 8-127. The chamber had a steel frame, polycarbonate walls, and a metal flame hood at its top that leads to a duct flow booster exhaust fan. The chamber plan view dimensions were 1.2 m × 1.2 m, and the viewable height through the Lexan window was about 1.8 m. The bottom of the chamber was open with a vertical height of at least 0.3 m, around the periphery of the bottom of the chamber for fresh air to enter. A horizontal beam located about 0.5 m

above the bottom of the sidewalls was used to mount all of the burners and fuel pans. A translating beam located 0.13 m above the fuel pan held the water collection pans used to determine the water distribution. The translating beam was moved out of the way when fire extinguishment tests were performed. The booster fan was at its half point power position for all extinguishment tests. The chamber's metal structural elements, the flame hood, the spray nozzles, the water pipes, the fuel pans, and the water collection pans were all electrically grounded.

Water Droplet Motion Due to Charging

The hypothesis of this project was that there is an attraction between the negatively charged droplets and the positively charged flame. The first step was to verify that the droplets were being charged and to estimate the magnitude of the charging effect and the corresponding induced motion. Once this was established, tests were performed to detect additional motion of the charged droplets near the flame.

Estimates of Electric Charging and Field Effects

Initial tests were implemented to determine the electric forces on charged droplets in terms of their motion near a grounded metal screen. A Cone Jet TX-1 hollow cone nozzle was chosen to observe the attraction of the charged mist to grounded objects and fires. It was expected that the droplets dispersed in the hollow cone pattern would be easier to track compared to a solid cone spray nozzle. The characteristics of the TX-1 are given in Table 8-20.

Table 8-20. Hollow Cone Nozzle Characteristics.

TX-1 Hollow Cone Nozzle				
Pressure (kPa-g)	206	275	344	412
Mean volume diameter (μm)	108	101	97	93
Flow rate (L/min)	0.056	0.063	na	0.095
Total spray angle (degree)	na	54	na	na

Charging was produced by an inductive principle in which an electric field is established between a positively charged ring and three grounded wire tips in a pitchfork configuration formed by three soft copper wires that were twisted to form a single basic wire shaft (see Figure 8-128). The positive ring induces electron emission from these grounded wires, and these electrons attach to the droplets. The process is aided by the fact that the electric field also aligns polarized droplets so that the positive ends of droplets point toward the grounded wires. The proximity of a positive end of a nearby droplet produces extra field strength to remove additional electrons from the wire. From principles stated by Kelly,⁹⁴ the charges will distribute themselves among the available droplets.

This electrode configuration was typically operated between 5 kV to 15 kV with a Gamma High Voltage Research Inc. dc power supply. This power supply delivered 1 kV output for each 1 V input so that it could be operated with batteries or the low voltage dc normally found in fire control systems (typically 24 V). At 15 kV many droplets tended to head back toward the grounded nozzle body. The maximum effective spreading of the spray pattern occurred at around 10 kV.

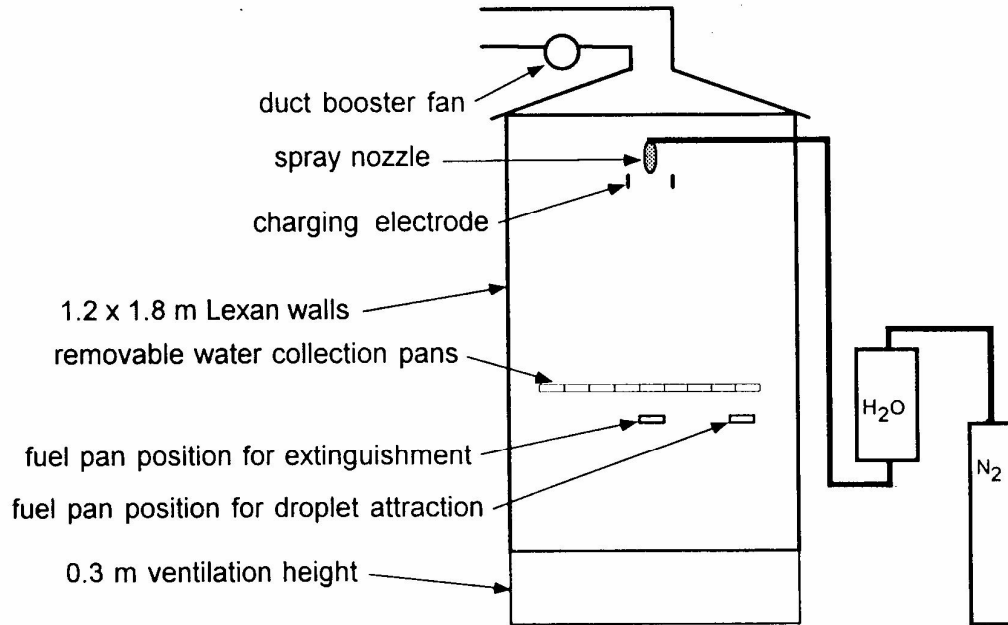


Figure 8-127. Schematic Sketch of Fire Test Chamber. Metal chamber structure, water nozzle, fuel pan, and water collection pans are all electrically grounded.

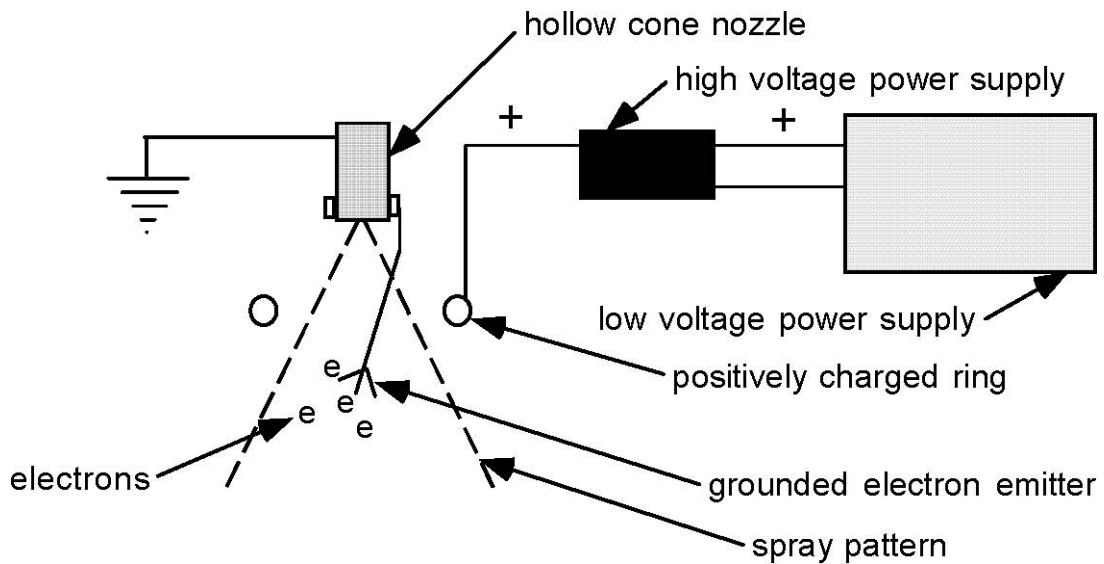


Figure 8-128. Electron Induction Electrode.

The metal screen was positioned vertically and displaced about 13 cm away from the nozzle centerline (see Figure 8-129). Applications of 5 kV to 15 kV to a positive inductive electrode showed that the droplets from the TX-1 hollow cone nozzle were strongly attracted to the screen. Moving the grounded electrodes as a whole to different locations in the spray, e.g., directly underneath the nozzle or off to the side, did not seem to make a big difference in the charging effect. Because the droplets traveled nearly horizontally towards the screen, the electrostatic force on them due to their charge and the electric field generated by the bulk of the charged droplets greatly exceeded the net gravitational force on them.

Estimate of the amount of droplet charging can be obtained by assuming that the ratio of the horizontal component of the droplet velocity to its vertical component is the same as the ratio of the droplet's horizontal electrical force to its gravitational force.

$$\frac{F_{\text{electrical}}}{F_{\text{gravitational}}} = \frac{V_{\text{horizontal}}}{V_{\text{vertical}}} \quad (8-52)$$

This relation is valid if the droplet velocities are based on either of two extreme physical limits: (1) the two accelerating forces are equal to the corresponding component of the droplet drag force or (2) the drag is small compared to the accelerating forces.

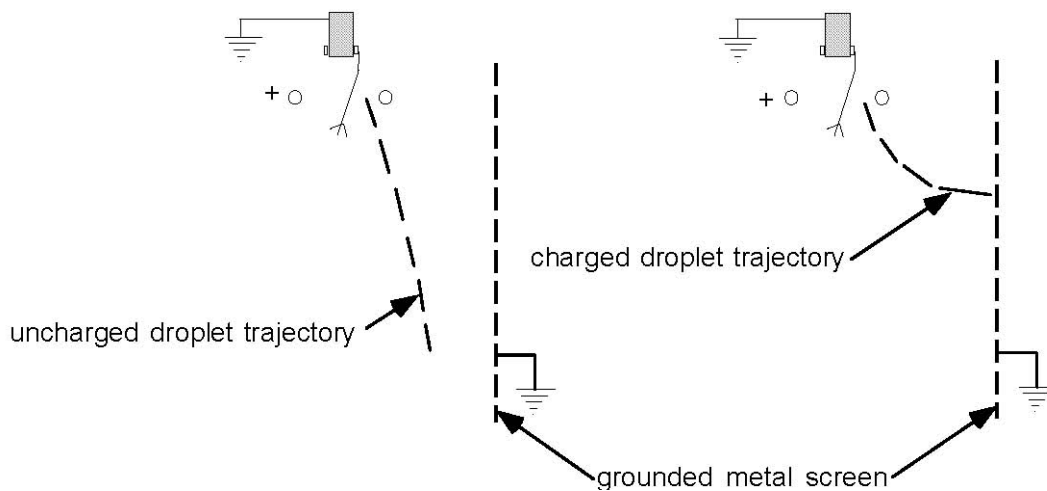


Figure 8-129. Attraction of Charged Droplets to Grounded Metal Screen.

The ratio of the forces is

$$\frac{F_{\text{electrical}}}{F_{\text{gravitational}}} = \frac{3q_d E}{4\pi R_d^3 \rho_d g} \quad (8-53)$$

where q_d is the electrical charge on a droplet, R_d is the droplet diameter, E is the electric field strength, ρ_d is the droplet density, and g is the gravitational acceleration. An important characteristic droplet charge value is the Rayleigh limit droplet charge q_{Rayleigh}^{95} , defined as

$$q_{\text{Rayleigh}} = \sqrt{64 \epsilon_0 \sigma \pi^2 R_d^3} \quad (8-54)$$

where ϵ_0 is the free space electrical permittivity constant and σ is the droplet's surface tension. The droplet will break up into smaller ones if the droplet charge exceeds $q_{Rayleigh}$. For this case, $q_{Rayleigh}$ is around 4×10^7 electrons per droplet. It is common practice to describe the actual droplet charge as a percent of the Rayleigh limit charge. Thus, 1 % of the Rayleigh limit still corresponds to 4×10^5 electrons.

The electric field is determined by the distribution of all the charged droplets and the positioning of the high voltage electrode and all the grounded surfaces. Since the charge distribution is not known, it is not possible to determine E without making some important assumptions and additional computations. However, the product of $q_d E$ can be estimated from Equation 8-53, and some possible combinations of q_d and E can be compared.

Using Equation 8-52 to describe the force ratio and writing q_d as a percent of the Rayleigh limit value, the electric field vector in volts/meter is

$$E = 71,970 \frac{V_{vertical}}{V_{horizontal}} \frac{1}{\%q_{Rayleigh}} \quad (8-55)$$

It is difficult to estimate the velocity ratio since it is so large, and it varies at different locations. If the ratio is arbitrarily set at 100 and the droplets are charged to 1 % of the Rayleigh limit, then $E = 7.197 \times 10^6$ V/m, which is more than twice the breakdown voltage value for air of 3.0×10^6 V/m. Thus, a droplet charging value of 3 % to 4% (with a correspondingly lower value of E) would not be unreasonable. Gottuk et al.⁹² estimated that the charging in their case was 4 % for a spray with a similar droplet size. By rearranging Equation 8-55 to solve for percent of Rayleigh charge as a function of E , the estimate for the percent charging increases if the electric field strength is lower and decreases if the velocity ratio is lower.

Attraction of Droplets to Flames

Tests were performed with the same positive inductive electrode and TX-1 hollow cone nozzle with flames positioned off to the side of the nozzle centerline instead of a metal screen. First, a small propane diffusion flame was positioned a little over 0.30 m from the centerline of the nozzle (see Figure 8-130). Application of a 15 kV voltage changed the droplet trajectories from a vertically downward direction to a nearly horizontal orientation directed towards the base of the diffusion flame.

Similar tests were instituted for pool fires in a 9 cm diameter pan using heptane in one case and methanol in a second. While there was a noticeable increase in the spray angle due to charging, the trajectories did not display the large horizontal motion observed for the propane diffusion flame and appeared to be more continuously vertical near the fire. Charging seemed to increase the amount of water reaching the pool fire, but this may be due to the effect of self-repulsion which would increase the diameter of the region covered by the spray.

There are indeed differences between the gas diffusion and pool flames. The heptane flame produces more soot particles which can attach electrons after the particles cool. The methanol flame is not expected to produce chemiions.

Estimates can be made for the electric field and charging using the velocity ratio in Equation 8-55, typically on the order of 0.5. If the charging level is the same as in the case of attraction to a metal ground, then the electric field will be on the order of a hundred times weaker relative to the estimates

made in the previous section. In making these estimates, one should be aware that air currents, which have not been accounted for, will also have an effect on the velocity components.

Fire Extinguishment Tests

Extinguishment time as a function of water flux with and without electric charging for a different nozzle and nozzle arrangement, a different size fire, and a different chamber was obtained in the present study. The fire extinguishment study by Gottuk et al.⁹² in an open environment pointed out the importance of charging in changing the water flux. For this reason, almost all measurements of extinguishment time, both with and without charging, were either immediately preceded or followed by a measurement of the water collected at the location of the fuel pool pan.

10 cm Diameter Pool Fire

Much effort was needed to develop a spray system that would provide a uniform distribution of water over a diameter of 1 m, ten times the diameter of the 10 cm diameter fuel pans to be used. A special consideration was that droplets carrying the same sign of electrical charge would tend to repel each other. The effect of the self-repulsion would be to produce spreading of the droplets and reduce the water flow per unit area.

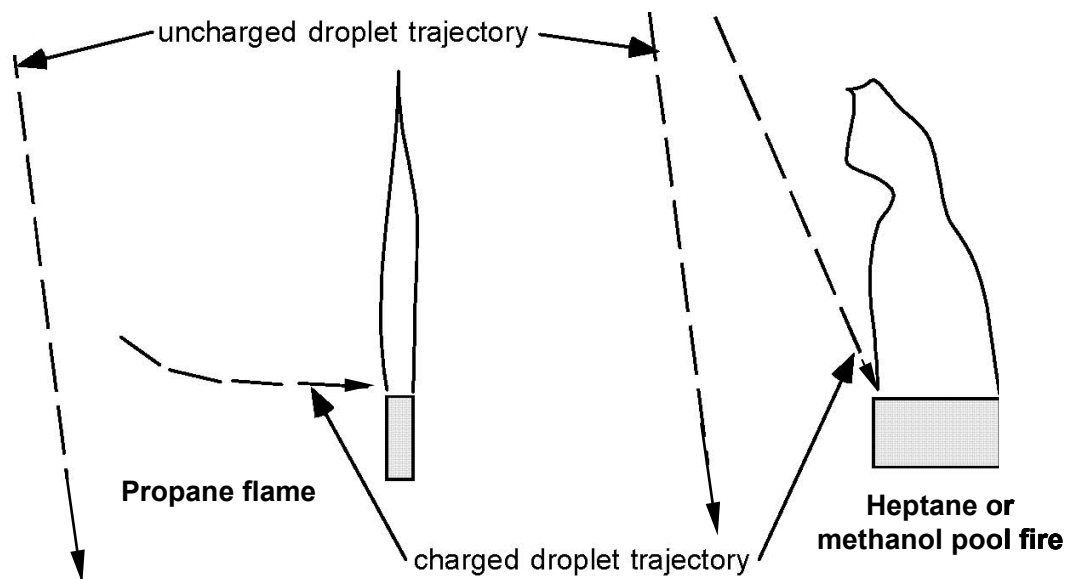


Figure 8-130. Motion of Charged Droplets near Fires.

A single nozzle assembly called the 7N, recommended by Spraying Systems, Inc., was used for the experiments (see Figure 8-131). The 7N assembly, which held 7 individual hollow cone nozzles, had a single 2.54 cm water pipe connection which fed one central nozzle and six outer nozzles at a constant radius from the center one. The axes of the outer nozzles were canted away from the centerline. The manufacturer asserted without specific size measurements that the droplets from the individual nozzles crossed paths so that a somewhat uniform spray was produced. Following the manufacturer's guidelines, the operating range was limited to between 687 kPa and 1031 kPa. A water feed system was designed

and assembled with the water pressurized by nitrogen from a regulated high pressure cylinder to cover the range of pressures to be used with the 7N nozzles.

It was expected that different sized nozzles might be needed to cover the range of conditions for the tests. Based on a preliminary test of fire extinguishment with a single nozzle, 0.095 L/min nozzles were selected for the 7N assembly. The plan was to install the 7N assembly with 0.095 L/min nozzles, observe its fire extinguishment performance with and without charging, and purchase one or more additional 7N assemblies with the appropriate flow capacity nozzles to cover the range of testing. Thus, in all cases the overall geometry would remain unchanged whether or not the droplets were electrically charged or the water flow rates were to be changed by replacement of the 7N assembly or individual nozzles. The water flow per unit area would be controlled by varying the water pressure and changing the nozzles. There was little change in droplet diameter in going up or down one size in nozzle flow capacity.

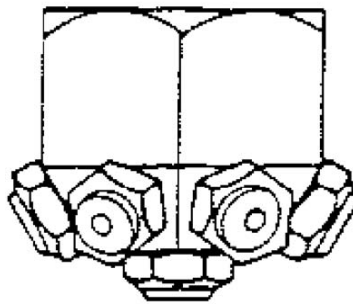


Figure 8-131. 7N Seven Hollow Cone Nozzle Setup.

Since extinguishment times with the 0.095 L/min nozzles were found to be short, a lower capacity 7N supplied with seven 0.063 L/min nozzles was obtained to cover the range of lower flow rates and longer extinguishment times. The characteristics of the 7N system with 0.095 L/min nozzles are given in Table 8-21 and those of the 0.063 L/min 7N system are given in Table 8-22.

Table 8-21. High Flow Capacity Seven Nozzle Assembly.

7N – 1.5 Seven Hollow Cone Nozzle Assembly			
Pressure (kPa-g)	687	859	1031
Mean volume diameter (μm)	69	62	59
Flow rate (L/min)	1.060	1.174	1.287
Spray coverage diameter (m)	0.76	0.76	0.76

Table 8-22. Low Flow Capacity Seven Nozzle Assembly.

7N – 1 Seven Hollow Cone Nozzle Assembly			
Pressure (kPa-g)	687	859	1031
Mean volume diameter (μm)	59	57	55
Flow rate (L/min)	0.680	0.794	0.869
Spray coverage diameter (m)	0.61	0.61	0.61

Charging the spray from the 7N nozzles was challenging because of the close proximity of the nozzles to each other. In a more typical setting in which water was supplied separately to a number of individual nozzles, rather than an assembly, it would be relatively easy to assure that the droplets from each nozzle were charged using an individual charging electrode. For the 7N, a single circular large diameter charging electrode was positioned coaxially around the 7N assembly.

A 3.8 cm wide strip of wire screening material was rolled into a circular hoop and fastened on the inside of an 0.2 m diameter ring made of copper tubing (see Figure 8-132). The orientation of the screening material was vertical. It was hoped that this would decrease water collection on the screening and large droplet formation. This strip produced electron emission from both the top and bottom rows.

The cut screen mesh provided approximately 250 sharp points on the top and the same number on the bottom of the electrode to charge the droplets from the outer set of six nozzles with the 7N grounded. The question was if the center nozzle mist would become charged. The rationale was that since the outer and central nozzle sprays crossed over, some charged outer nozzle spray would find its way to the center of the system, and some inner nozzle spray would move out and become charged due to its proximity to the charged outer nozzle droplets. In addition, earlier tests using the inductive approach with grounded wires as the electron source indicated that the ability to charge droplets was not strongly linked to the position of those electrodes.

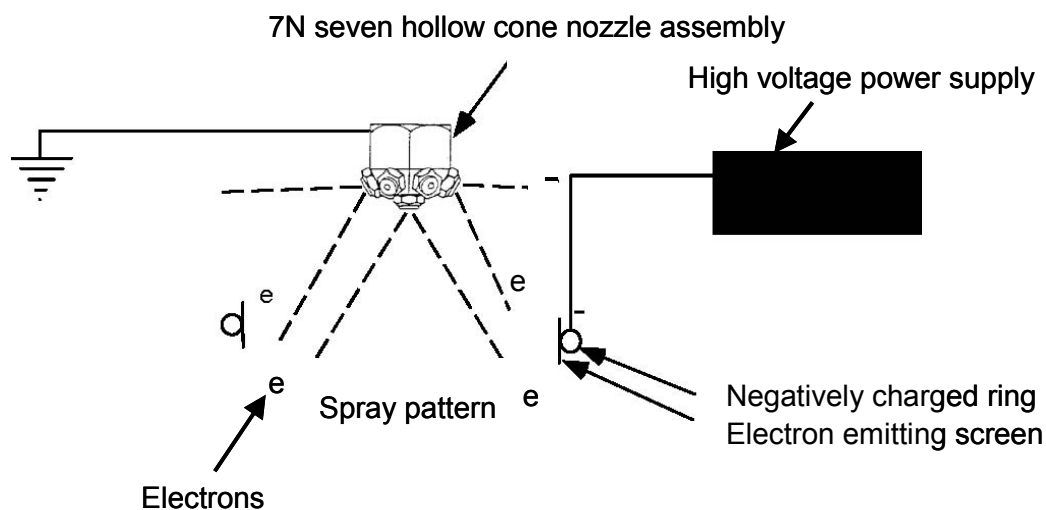


Figure 8-132. Spray Charging Set-up.

One might think of an individual multiply-charged droplet near an uncharged droplet as an inductive source of electrons in the sense of inductive wire electrodes. Thus, an uncharged droplet will become polarized when it passes close to a charged droplet. The positive end of a polarized droplet will become aligned with the negatively charged droplet. The additional electric field strength associated with this alignment will result in the transfer of electrons from the charged to the uncharged droplet. In this way, it was hypothesized that a cascade effect could transfer electrons from regions of charged to regions of uncharged droplets. Despite precautions, some large drops formed on the strip electrode and dripped off, but they did not fall into the fuel pan and thus did not affect fire extinguishment. These larger drops were less susceptible to the effects of airflow induced by the ventilation fan or the fire plume. In a more

realistic environment with individual chargers for each nozzle, dripping would not be expected to be important.

Water flux uniformity tests were made using nine 10 cm diameter pans to collect the water (these were identical to the pan used to hold the fuel for the pool fire). These were placed side by side on a beam that could be slid on a rail into position above the fuel pan, and then be moved easily out of the way when fire extinguishment tests were performed. This array of collection pans was about 13 cm above the plane of the fuel pan, and the entire array of pans spanned a distance of 0.9 m.

With all seven of the 0.095 L/min nozzles installed in the 7N, the flow was quite peaked with its maximum off slightly from the centerline of the nozzle (Figure 8-133). Note that Spraying Systems, Inc. asserted that the spray was uniform over a diameter of 0.75 m if the assembly was more than 0.9 m above the collection plane. Thus, the assembly did not operate as anticipated. It was unclear whether this pattern was characteristic of all 7N assemblies or whether it was influenced by the particular chamber in which it was installed. When the 0.2 m diameter multiple nozzle design electrode ring was placed around the nozzle, the spray pattern appeared to be more symmetric, but was still peaked. Dripping from the electrode contributed significantly to the water collected on either side of the main peak at ± 10 cm from the centerline. While these drops did have a major effect on the water collection, they did not appear to play any significant role relative to fire extinguishment because the water they carried did not interact with the fire and did not splash the fuel surface.

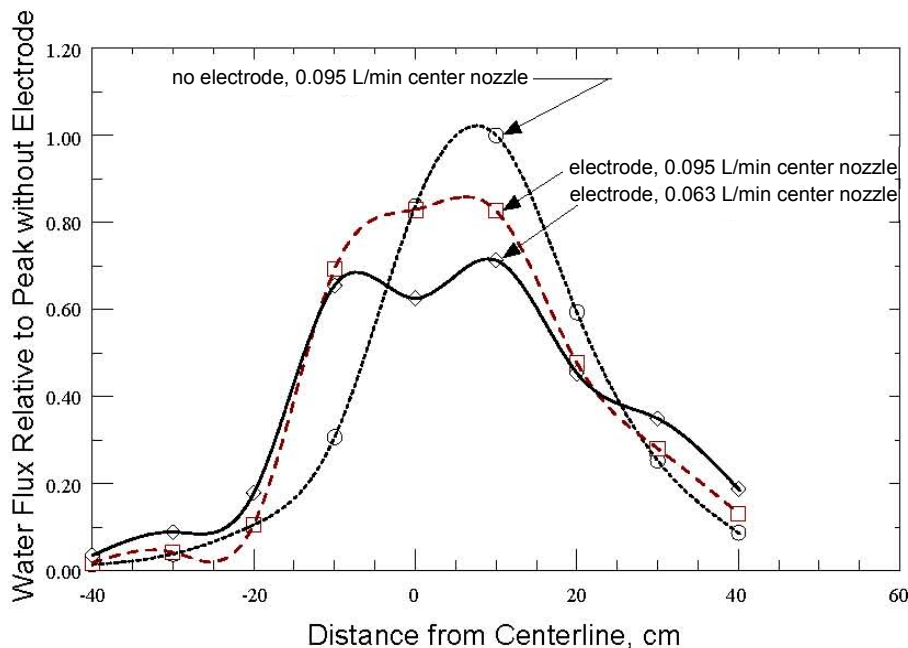


Figure 8-133. Effect of Center Nozzle Size on 7N Nozzles Water Flux.

Plugging the center nozzle produced a fairly uniform water flow distribution. In this case, the spray patterns of the 6 remaining nozzles appeared to project further out radially so that the walls of the chamber became wet at a greater height above floor than had been experienced before. It thus appeared that the central nozzle played an important role in determining the spray patterns of the other six nozzles.

Possibly, air entrained by the central nozzle affected the airflow environment that the other nozzle sprays experienced. Unfortunately, the water flux without the center nozzle flow was too small to extinguish the fire being studied. For this reason, a compromise was reached to replace the center nozzle with a 0.063 L/min capacity nozzle and to retain the six other 0.095 L/min orifices in the 7N assembly. This did not produce any dramatic change in the water distribution (Figure 8-133), but it did allow a pressure to be set to provide extinguishment times in a good range for the measurements.

The water flux distribution of the 7N nozzles with the 0.063 L/min center nozzle is shown in Figure 8-134 when the electrode is uncharged and at -5kV. Charging reduces the center water flux and increases that at the edges of the spray pattern slightly. These changes are much less than those observed by Gottuk et al.⁹² for a single nozzle. In the case of the 7N nozzles, charging of the outer portion of the spray makes those droplets spread out in all directions, and the outer spray droplet charge density restricts the spread of the inner charged spray.

Experiments to determine the effect of mist droplet charging on the extinguishment of a heptane pool fire were performed in the test chamber. The water spray system consisted of an electrically grounded 7N nozzle containing a central 0.063 L/min nozzle and six circumferential 0.095 L/min nozzles located 1.1 m above the pool fire. A 0.2 m diameter electron emission charging electrode, described previously, was placed coaxially around the water spray system centerline and located about 10 cm below the bottom of the nozzle assembly.

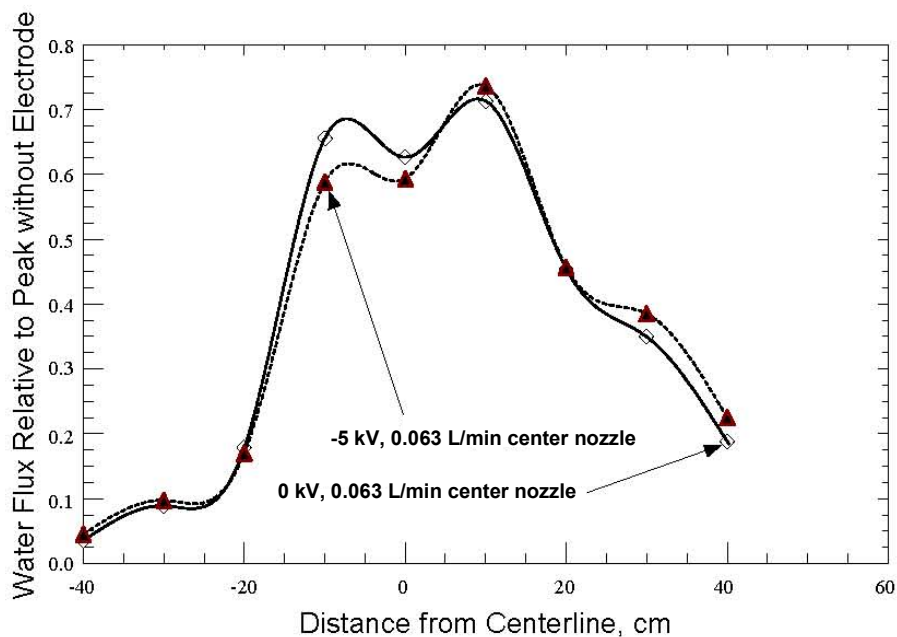


Figure 8-134. Effect of Electrical Charging on Water Flux Distribution of the 7N Nozzles with the 0.063 L/min Center Nozzle.

Heptane was poured into a 10 cm diameter, 2.8 cm tall seamless and electrically grounded tin pan until the fuel level was 0.8 cm from the open end. The fuel was ignited and the fire was allowed to burn for 3 min in order to develop a steady state structure. A water flow at pressures between 687 kPa and 1031 kPa was supplied to the 7N nozzles immediately following the initial heating period. Measurements

of extinguishment time were made separately with and without dc electric field charging of the mist. Water flow measurements were made both with and without dc electric field mist charging by replacing the fuel pan with a water pan of the same size as the fuel pan and the nine pans used previously for water distribution measurements.

Since some previous tests had found large effects with low voltage charging, the tests began with voltages on the order of -1 kV and -2 kV at 1031 kPa. Measurements were then continued at -5 kV at this pressure as well as at pressures of 687 kPa and 859 kPa.

Frequent water flow measurements were needed since it was clear that the water flux at a fixed nozzle pressure varied. These variations develop due to changing airflow patterns in the chamber or deposits found in the nozzle, in spite of the use of a 2 μm filter in the water line.

Extinguishment time is plotted in Figure 8-135 as a function of water flux with and without electric charging. Because the voltage level at 1031 kPa did not produce a clear trend for values between -1 kV and -5 kV, all of the charged mist data is plotted together for these experiments. The voltage was maintained at -5 kV for all of the other droplet charging cases. At the higher flows, it does not appear that there is an effect of electric charging. However, electric charging did produce major improvements over the performance of uncharged droplets in the lower water flux range. As the flux was lowered without charging, a flow was reached where significantly greater times were needed to extinguish the fires. The curves can be interpreted as showing a decreased extinguishment time at constant water flux or reduced water flux to achieve a given extinguishment time. This behavior would be beneficial in cases where the water supply for fire extinguishment is limited. It was speculated that the extinguishment time with charging would also increase if the water flux were lowered much more. Data were not taken for smaller fluxes with this nozzle because the water collection values were inconsistent for pressures below 687 kPa.

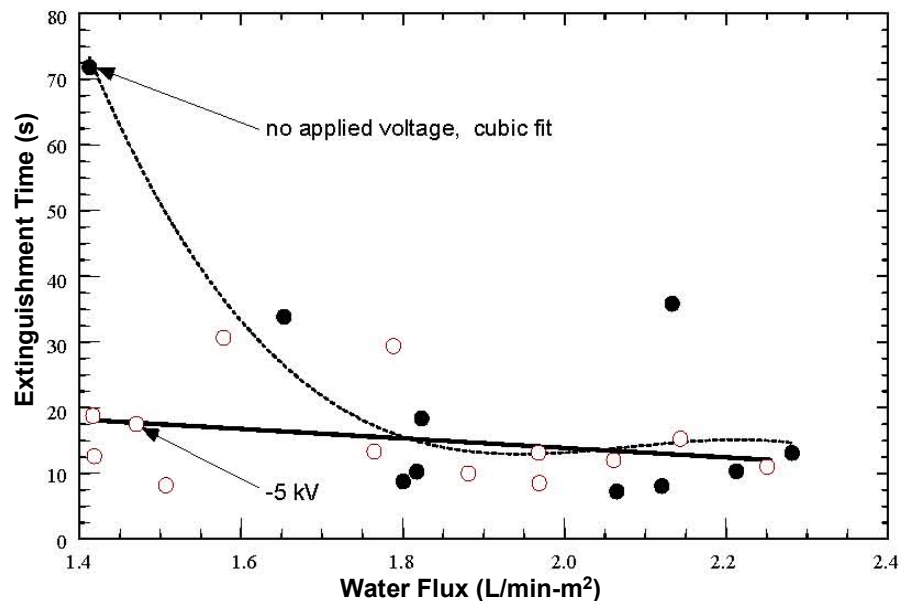


Figure 8-135. Initial Data on Effect of Electrical Charging for a 10 cm Diameter Heptane Pool Fire.

The nozzle and electrode were removed, cleaned, and then reinstalled after the above initial set of data had been analyzed to obtain a second set of data. In the new tests, the water collected in the single pan directly below the nozzle increased due to charging, which was different from other observations including the previously mentioned water flux distribution measurements recorded in Figure 8-134. These new data points were added to those previously displayed in Figure 8-135, and the total data set is presented in Figure 8-136. The trend of rapidly growing extinguishment time with decreasing water flux is not as apparent for the uncharged case as in Figure 8-135. For this reason, linear fits to both the charged and uncharged data sets are displayed in Figure 8-136. Again, there is little difference in extinguishment time due to charging when that time is generally small at the higher water fluxes, but the uncharged case still has extinguishment times that are significantly higher, by a factor of nearly 2, than the charged case in the low water flux regime where extinguishment times are larger. The standard deviation of the uncharged data is nearly twice that of the charged results. Thus, the complete set of data still indicates improvement in extinguishment due to charging, even though the validity of the additional data was questionable because of the higher water collection.

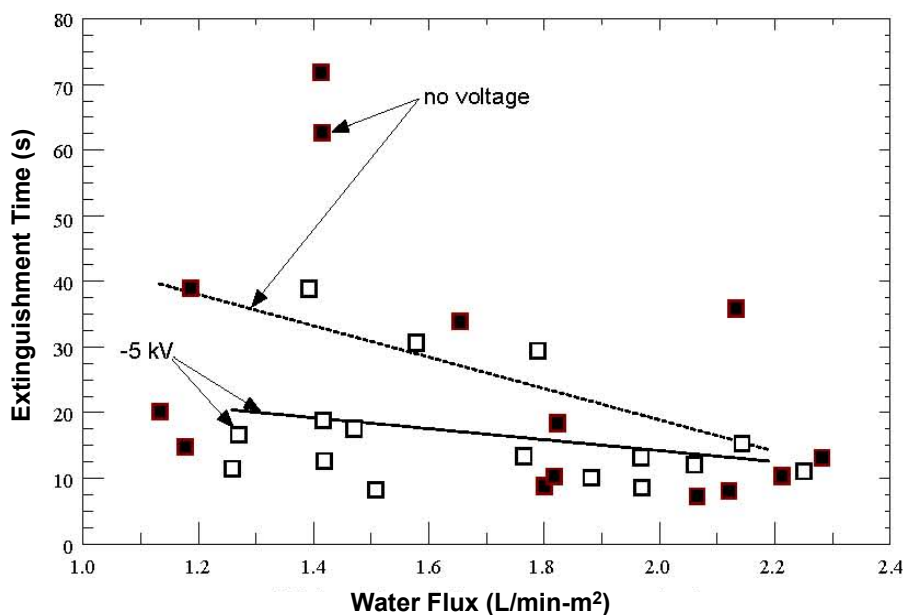


Figure 8-136. All Electrical Charging Data for a 10 cm Diameter Heptane Pool Fire.

5 cm Diameter Pool Fire

Because of difficulties in holding the 7N nozzle water flow constant in the water collection pan and the possibility that the center nozzle mist might not be receiving as much charging as the outer nozzle mist, it was decided to perform additional work with a single water mist nozzle and a smaller, 5 cm diameter, fuel pan. More repeatable water collection rates and more effective charging of the mist were expected with the single nozzle. The smaller fuel pan was chosen to maintain the ratio of the spray diameter to the pan diameter much larger than unity.

The lowest flow solid cone from Spraying Systems, Inc. nozzle was the TG-0.3 whose flow characteristics are given in Table 8-23. A coverage area for the TG-0.3 nozzle was not given in the

specifications. However, the spray visually appeared to be relatively uniform over a diameter of 0.25 m to 0.30 m at a distance of 0.7 m from the nozzle. Based on this observation, the ratio of the spray diameter to pan diameter was between 5 and 6.

A new electrode for these tests consisted of a wire screen with a 8.9 cm diameter circle cut out of its center. The cut inside edges of the screen formed the array of wires that emit electrons (Figure 8-137). This screen was positioned horizontally with its center point coincident with the spray nozzle centerline. It was secured to the circular ring electrode that had been used in the positive inductive electrode system discussed previously (Figure 8-128). With the nozzle grounded, an easily visible spreading of the spray pattern was observed with the application of -3 kV. This spreading was increased considerably when the voltage was increased to the maximum value of -5 kV.

Table 8-23. Solid Cone Nozzle Characteristics.

TG-0.3 Solid Cone Nozzle				
Pressure (kPa-g)	206	275	344	412
Mean volume diameter (μm)	250	210	180	160
Flow rate (L/min)	0.195	0.233	N/A	0.277
Total spray angle (degree)	51	54	N/A	59

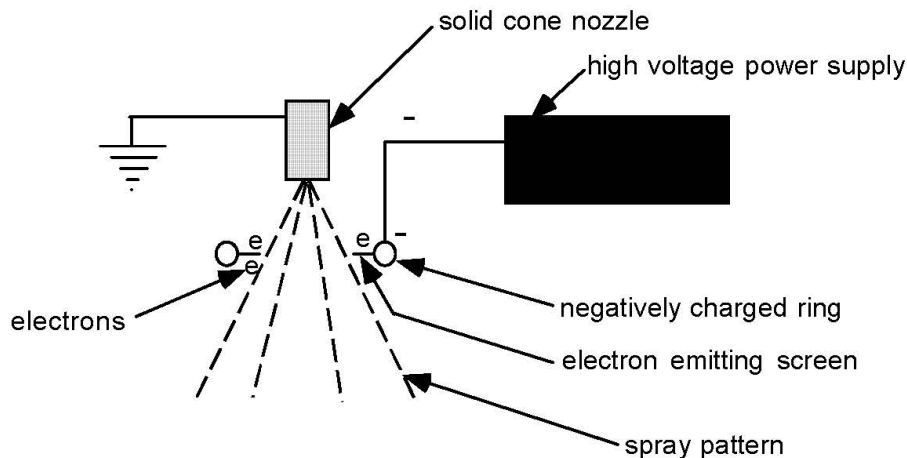


Figure 8-137. Schematic of Single Nozzle Electron Emission Electrode.

Heptane was poured into a 5 cm diameter, 1.6 cm tall seamless and electrically grounded tin pan until the fuel was 0.6 cm from the open end (this is almost the same diameter as used in the study of Patterson et al.⁹¹). The fuel was ignited, and the fire was allowed to stabilize for 1 minute. Water flow at pressures between 206 kPa and 412 kPa was supplied to the TG-0.3 nozzle immediately following the preheat period. Measurements of extinguishment time were made separately with and without dc electric field charging of the mist. In most cases the extinguishment time measurements were followed by water flux measurements in a separate 5 cm diameter pan that was identical with the fuel pan and was placed in the holder that supported the fuel pan.

The distance between the nozzle and the fuel pan was set as 0.7 m. Extinguishment time was then measured as a function of the water flux collected in the 5 cm diameter pan at zero voltage and at -5kV.

When the electrode was charged, there was a considerable decrease in the water flux collected in the pan because of mist spreading. Thus, the nozzle was operated at a higher pressure when charging was applied to obtain the same range of collected water flux rates that had been obtained at lower pressures without charging.

The results plotted in Figure 8-138 show that the expected rise in extinguishment time for the charged case occurred at a lower level of water flux than for the uncharged case. The solid line is a linear fit of the three water flux points for the charged case. A dashed line with the same slope is shifted to the right of the solid line to indicate the general upward trend for the uncharged case. This confirms the general trend seen for the 10 cm diameter fuel pan fire, which also found improved extinguishment with charging. As it was noted for the 10 cm case, the extinguishment times were significantly shorter with charging for the low water flux range in which the uncharged extinguishment times began to grow.

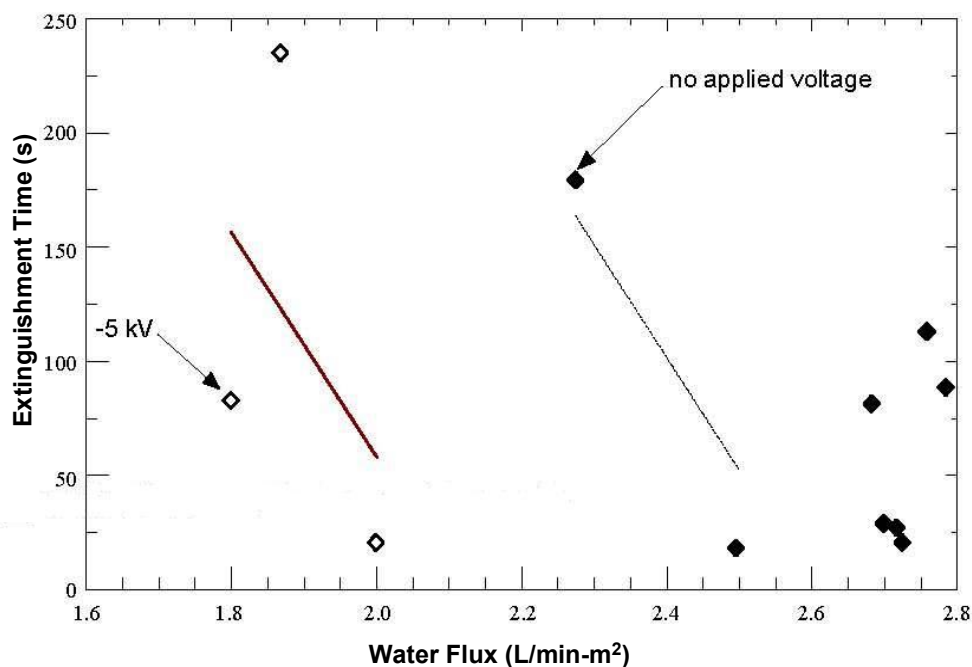


Figure 8-138. Effect of Electrical Charging on Extinguishment for a 5 cm Diameter Heptane Pool Fire.

Discussion of Results

The present results are compared with other data obtained by Patterson et al.⁹¹ and Gottuk et al.⁹² The fitted curve results of Patterson et al.,⁹¹ the fitted data shown in Figure 8-136, and the trend lines in Figure 8-138 are plotted together in Figure 8-139. The experiments of Gottuk et al.⁹² occurred for water flux rates that were more than twice those treated in current experiments and thus outside of the range of Figure 8-139. Patterson et al.⁹¹ did not consider charging, and their data show the general feature of the rise in extinguishment time as water flux is reduced beyond some point and substantiates the present observations of a rapid rise in extinguishment time for the case without charging. Note that the results of the experiments using high water fluxes (small extinguishment time) closely follow the data of Patterson

et al.⁹¹ Although they were careful to establish uniform water flux, and they did not have additional air motion due to ventilation, their extinguishment time data are at least as scattered as the present data. The apparent randomness appears to be inherent to this kind of problem, and it appears that the water flux is a rational basis for comparing and interpreting extinguishment results when using water mists.

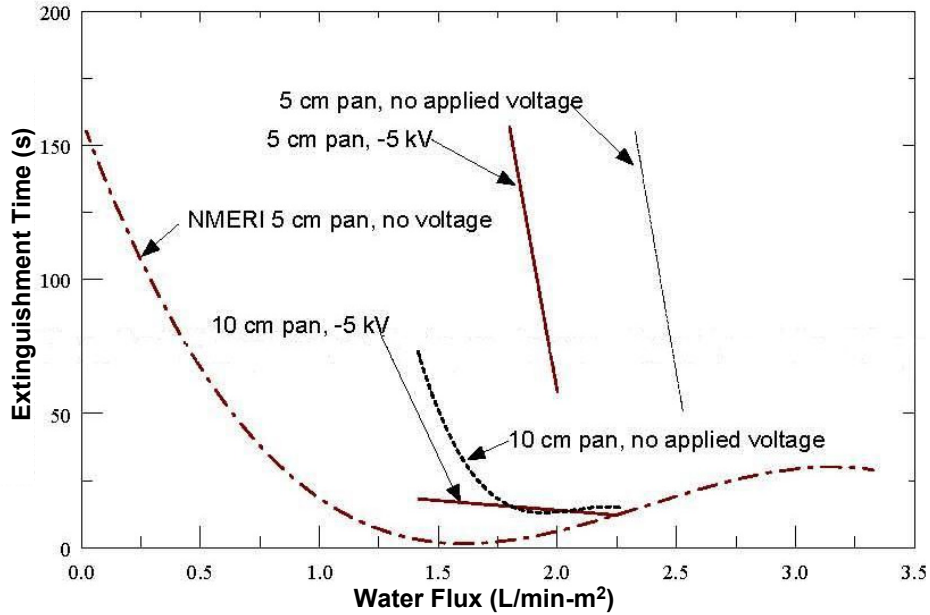


Figure 8-139. AeroChem 5 cm and 10 cm and NMERI 5 cm Heptane Extinguishment Data. Hughes Associates, Inc. 10 cm tests ranged from (5 to 7) L/(min m²).

It was also found that charging the mist reduced the water flow directly under the single TG-0.3 nozzle to around 75 % of its value without charging. The data of Gottuk et al.⁹² show a reduction to around 85 %. For the multiple nozzle configuration, the reduction of the water flux directly below the nozzle assembly was much smaller, being about 95 % of the uncharged value. In addition, the increases due to charging at large distances were also small as seen in Figure 8-134.

Two possible reasons for the small reduction in water flux below the nozzle assembly compared to the single nozzle case are that: (1) the repulsive forces due to charged droplets at larger diameters restrained the tendency of the smaller droplets to spread and (2) an insufficient amount of charge was available to the multiple nozzle spray, and in particular the central portion of the spray, to grossly affect its geometry. This is not a major concern, as it simply indicates the need for a more effective charging electrode for the 7N nozzle.

The current results confirm the conclusion of Gottuk et al.⁹² that charging produces a large amount of spreading in the mist distribution for single nozzles. It is clear that charging applied to an array of single nozzles will enable the use of greater spacing between the nozzles while achieving as uniform a spray pattern as in the case without charging. This is of particular concern for small droplets which are hard to disperse transversely due to their high aerodynamic drag. The electrostatic forces help to spread them out more evenly.

The present results clearly show that application of negative charging to water mist reduces the extinguishment time when the water flux is at its lowest effective values. Within this range the water flux needed to attain a given extinguishment time is also reduced. This is true for both the 5 cm and 10 cm heptane fuel fires and two different nozzle and charging systems. For the 10 cm fire data in Figure 8-136, the variability in extinguishment time, expressed as the standard deviation, was reduced at low values of water flux.

The question of the effect of charging on the total amount of water, Q , per unit floor area needed to extinguish a fire requires some further discussion. Q is equal to the product of the water flux, f , and the extinguishment time t_{ext} so that

$$Q = f t_{ext} \quad (8-56)$$

and it has the dimensions of a length (or thickness). Patterson et al.⁹¹ refer to Q as the “de novo thickness.”

Ways in which reductions in Q can be categorized include: (1) a reduction in the flux, f , at constant extinguishment time, t_{ext} , (2) a reduction in the extinguishment time, t_{ext} , at a constant value of flux, f , and (3) an absolute maximum reduction of Q for some combination of t_{ext} and f . The first two cases are readily seen by comparing curves with and without charging in Figure 8-139 for either fixed f or t_{ext} .

To better understand the condition for an absolute maximum reduction in Q , note that the case of constant Q from Equation 8-56. corresponds to

$$t_{ext} = \frac{Q}{f} \quad (8-57)$$

so that in a plot of extinguishment time vs. water flux, $t_{ext} \rightarrow \infty$ as $f \rightarrow 0$ and $t_{ext} \rightarrow 0$ as $f \rightarrow \infty$. Since the NMERI data in Figure 8-139 remains finite as $f \rightarrow 0$, this data actually shows a trend of decreasing Q for small f , although the absolute minimum Q occurs for an intermediate value of f close to 1.5 L/min-m². The fitted curve of the NMERI data corresponds to increasing values of Q for large f since t_{ext} levels out in that range.

For the AeroChem data in the case of no charging, t_{ext} appears to grow without limit in Figure 8-139 for both the 5 cm and 10 cm fires for finite f so that Q will become infinite as f decreases. Charging allows a much smaller flux f of water to be used to achieve extinguishment in the same time. Here the reduction in Q due to charging can be accomplished in a limited range of f at the same t_{ext} (Figure 8-139). For the 10 cm case, there is insufficient data to make any statement about how small a value of f can be used to minimize Q .

Gottuk et al.⁹² argue that one can simply increase the flux f to achieve the same effect as charging. This may be a simple alternative in the single nozzle, well-ventilated case, but there are broader ranges of f in different problems over which electric charging has a beneficial effect. Increasing f (without significant reductions in extinguishment time) is the wrong approach in a halon replacement program to minimize the weight of the fire suppressant. Therefore, work should focus on increasing the effectiveness of the technique so that smaller values of f will be capable of extinguishing a fire.

Although the effects of ventilation and uniformity cannot be fully separated, a shift appears to be occurring in the AeroChem tests relative to the Hughes Associates, Inc. data to move the extinguishment time curves to lower water flux values and to reduce the magnitude of their slope. Because of this, it is anticipated that conditions such as those reported in Figure 8-126 for unventilated chambers and highly uniform water flux will yield significant reductions in extinguishment time t_{ext} when charging is applied. In that case t_{ext} would be greatly reduced for low f so that Q could be reduced both in the absolute case and for the same extinguishment time according to Equation 8-56.

Implications for Use

Although there seems to be a potential benefit to electrically charged a water mist to extinguish a small pool fire, the locations of in-flight engine nacelle fires and the highly cluttered nature of an engine nacelle preclude further development of this technique. Essentially, all those surfaces act as grounding plates. Thus, one could expect that some fraction of the droplets will be attracted to the clutter and will pool on the surfaces. Furthermore, it is not clear whether a high voltage field would interfere with the aircraft avionics at a critical time when the pilot is undertaking emergency measures to fight the fire and perhaps to maintain readiness for survival. However, these limitations may not apply to other potential applications.

8.7.3 A Self-Atomizing Form of Water

Background

For the NGP, Lyon⁹⁶ explored the potential use of gas hydrates as another approach to generating water mist and efficiently dispersing it throughout the space to be protected. The hydrate is a loosely bound complex of a host gas and a number of water molecules. It is only stable under high pressure. Thus, when released from its storage container, the ejected droplets of the complex would ideally travel some distance and violently break into water droplets and molecules of the host gas. These would then disperse rapidly from these numerous virtual sources. This is an analog to the flashing observed for halon 1301, HFC-125, and other low boiling point fluids.

The hydrates can form in either of two structures. In both of these structures, the essential unit is a pentagonal dodecahedron of water molecules, the gas molecule occupying the space in the center of the dodecahedron. This structure owes its stability to the fact that each of the twenty apices is occupied by an oxygen atom bonded to four hydrogen atoms at close to tetrahedral angles, i.e. it maximizes hydrogen bonding.

In the type I structure there are 2 smaller and 6 larger cavities for every 46 water molecules. For type II there are 16 smaller cavities and 8 larger cavities for every 136 water molecules. The type II hydrate forms only with gas molecules that are too large for the cavities in the type I structure. While the number of cavities has a definite stoichiometry, the extent to which gas molecules occupy those cavities can vary over a significant range. Furthermore mixed hydrates with two or more different types of gas molecules filling the cavities can readily be formed. For the case of a mixed hydrate of a large molecule such as CHCl_3 and a small molecule such as CO_2 , the large molecule occupies some of the large cavities and none of the small cavities while the small molecule occupies some of both.

At 0 °C, a pressure of 1.3 MPa is necessary to form the CO₂ hydrate from pure water. With increasing temperature, the CO₂ pressure needed to form the hydrate increases. At 9.9 °C, 4.39 MPa is needed and at greater temperatures, no hydrate can be formed by CO₂ alone. Mixed hydrates containing substantial amounts of CO₂ can, however, be formed at higher temperatures by using a second gas with a hydrate forming ability greater than CO₂.

There were no published reports as to what happens when a gas hydrate is suddenly depressurized. It is, however, interesting to note that water under extreme pressure can form 5 solid phases in addition to the familiar ice. One of these, ice III, is blue. While ice III is thermodynamically stable only at pressures in excess of 206 MPa, it can be cooled to liquid nitrogen temperature, and then be depressurized. At 0.101 MPa and very low temperature, ice III is metastable. It can last for an extended period of time if kept cold, but it disintegrates into a fine powder of ordinary ice on contact with anything warm.

From a thermodynamic viewpoint, the decomposition of a CO₂ hydrate offers two quite different cases. The heat of forming a CO₂ hydrate from gaseous CO₂ and liquid water is almost exactly the same as the heat for forming ice from the water. Thus, if a pure CO₂ hydrate at an initial temperature below 0 °C were adiabatically depressurized, it would become unstable with respect to decomposition to ordinary ice and gaseous CO₂ with very little temperature change occurring during this decomposition. This case would appear to be quite similar to the case of ice III in which considerable metastability was possible, i.e., both involve the conversion of one solid to another without the formation of a liquid phase.

If, however, the initial temperature were greater than 0 °C, the hydrate would become unstable with respect to adiabatic decomposition to gaseous CO₂ and a mixture of liquid water and ice, the temperature falling during the decomposition to 0 °C. Since the liquid water can act as a catalyst for the conversion of the solid hydrate to ordinary ice, the hydrate seems less likely to be metastable in this case.

The goals of this project were to determine whether hydrates are capable of delayed self-atomization and that they are consequently potentially useful as replacements for halons in fire fighting.

Experimental Procedures

Sample Preparation

0.5 L stainless steel sample bombs which were equipped with 0.635 cm ball valves were used to prepare CO₂/water mixtures which were converted to hydrate. To prepare these mixtures, the sample bomb was weighed, distilled water was transferred into it, and it was reweighed. It was then attached to a vacuum line and evacuated briefly to remove air. The sample bomb valve was then closed, and the bomb was connected to a CO₂ cylinder that was equipped with a dip leg. After liquid CO₂ was added to the bomb, it was reweighed and placed in a refrigerator to convert the CO₂/water mixture to hydrate.

Video Camera Studies

During tests the sample cylinders were held vertically with the valve pointed down. A length of 0.635 cm OD stainless steel tubing on the outlet of the ball valve bent to a right angle or to a U shape was attached to the outlet end of the ball valve. This allowed the discharge to be directed vertically downward or upward. A video camera was used to record what occurred. During subsequent analysis of the videotape, the discharge time was measured with a stopwatch while playing the tape at slow speed. Playing speed

was measured by comparing stopwatch readings with time as recorded on the tape by the video camera's clock. Distances were measured on the tape using a reference length.

Candle in the Wind Experiments

Figure 8-140 shows the experimental setup used in this series of tests. In this setup, a 2.22 cm diameter candle was placed inside a transparent plastic tube, 61 cm long by 10.2 cm in diameter. The top of this plastic tube was connected to a blower while the bottom was filled with vertical 10.2 cm long Pyrex tubes, 6 mm OD and 4 mm ID. The blower was used to pull a flow of air through this tube at a rate of 3.54 L/s, i.e. at a velocity of 43.6 cm/s. The small Pyrex tubes served as flow straighteners.

While the bulk of this airflow was vented, some of it was extracted by a sample pump and sent first through a rotameter then to a Fuji NDIR CO₂ meter, which monitored the CO₂ content of the gases exiting the blower. For comparison experiments with halon 1211, the sample was passed through a bed of an oxidation catalyst at 800 °C (CuO on high surface area alumina) to convert the halon to CO₂. Previous studies have shown that this catalyst is quite efficient for oxidizing halons.

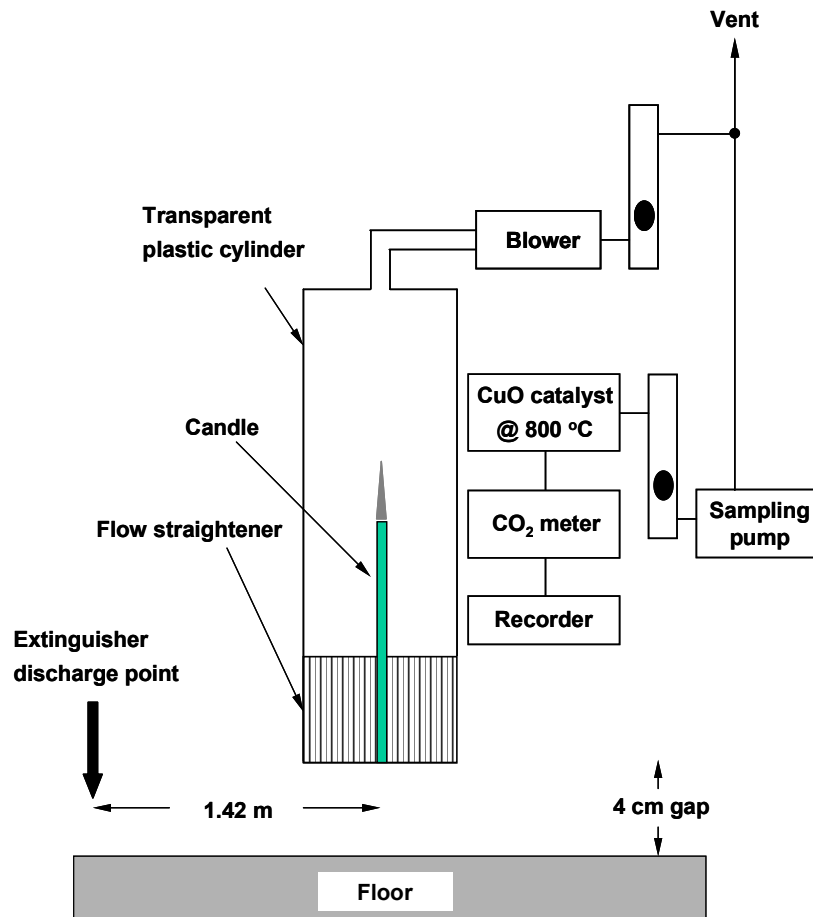


Figure 8-140. Experimental Setup for Testing the Relative Effectiveness of Fire Extinguishing Agents.

Test with an Obstructed Fire

The experimental setup shown in Figure 8-141 was used in the extinguishment tests with an obstructed fire using a single burst discharge of the agent. The following procedure was used: a paper wick and 75 cm³ of diesel fuel were placed in the 6 cm cup. After igniting the wick, the fire was allowed to burn for 3 min, the ball valve was opened, and the result observed.

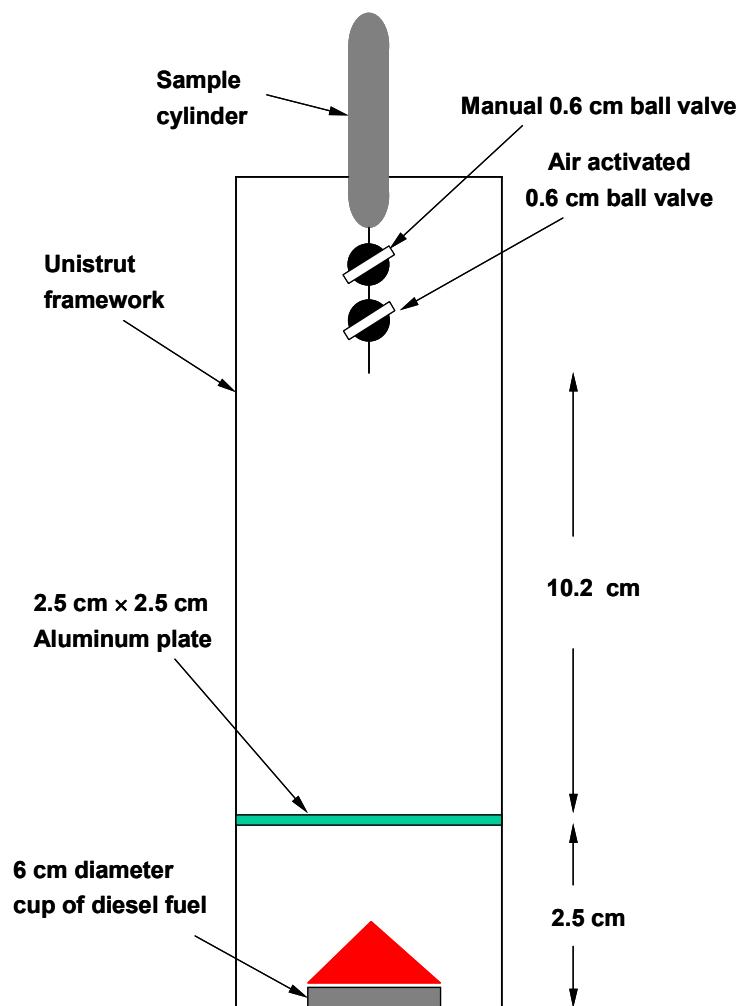


Figure 8-141. Experimental Setup for Testing Agents Against an Obstructed Flame.

Ambient Pressure Recovery of Hydrates

To recover CO₂ hydrate, a 2.54 cm OD stainless steel tube with fittings on its ends was used instead of the 0.5 L sample bomb. Hydrate was prepared as above, but then the sample was cooled to -15 °C, depressurized, the fittings were undone, and the hydrate removed. To prepare and recover C₃F₈ hydrate, the same procedure was used, except that the preparation was done in a Fischer-Porter glass sample bomb.

Discharge Characteristics of CO₂ Hydrate

Samples in which the ratio of CO₂ to water was low enough to leave a significant portion of the water unconverted to hydrate had reasonably satisfactory discharge characteristics, i.e., when the ball valve was opened the hydrate/water mixture was discharged in a more or less continuous flow. Samples in which the ratio of CO₂ to water was high enough to leave little or no water unconverted did not show satisfactory discharge characteristics, i.e., when the ball valve was opened the hydrate was discharged in discontinuous spurts.

Results

Visual Observations

A blank experiment was done with 400 mL samples of water in 1000 cm³ sample bombs pressurized with He at 10.3 MPa. This produced a spray jet with a 0.35 s discharge time, 5 m tall and roughly 15 cm wide at its peak. The droplets formed by this jet showed a readily observable settling rate indicating that they were relatively coarse. Qualitatively similar behavior was observed with helium pressurizations at 6.87 MPa and 3.78 MPa. At 1.57 MPa helium pressurization, however, the discharge resembled that of a common garden hose with little or no atomization.

For a solution of 0.2 mass fraction of CaCl₂ in water saturated with CO₂ at ambient temperature and 5.81 MPa, the spray jet pattern was clearly different, 3 m tall and 50 cm wide. The droplets formed by this jet did not show an observable settling rate, indicating that a desired fine mist was formed.

For samples of CO₂ hydrate/water mixture with an initial pressurization of 1.51 MPa, the discharge was similar in length and width to that of the sample which was pressurized with helium to 1.57 MPa, but the discharge produced a mist with no observable tendency to settle.

Candle Flame Results

Experiments were conducted using the setup illustrated in Figure 8-140 to determine the threshold for extinguishing candle flames by CO₂, halon 1211, and fine mists generated by CO₂ hydrate/water mixtures. The results in Figure 8-142 and Figure 8-143 show that these experiments gave a threshold for CO₂ between 6.8 volume % and 7.1 volume % and a threshold for halon 1211 between 1.57 volume % and 1.74 volume %. No thresholds were determined for fine mists generated by the CO₂ hydrate/water mixtures since under all conditions tested these mists were not able to extinguish the candle flame.

In another experiment, a red laser beam was sent through the transparent plastic cylinder. Initially the beam was invisible, but scattering from particles of Ca(OH)₂ (20 μm to 40 μm size) in the plastic cylinder made the beam evident.

The Obstructed Flame Results

Three tests were done with CO₂ hydrate/water mixtures, and in all three tests the obstructed flame was not extinguished.

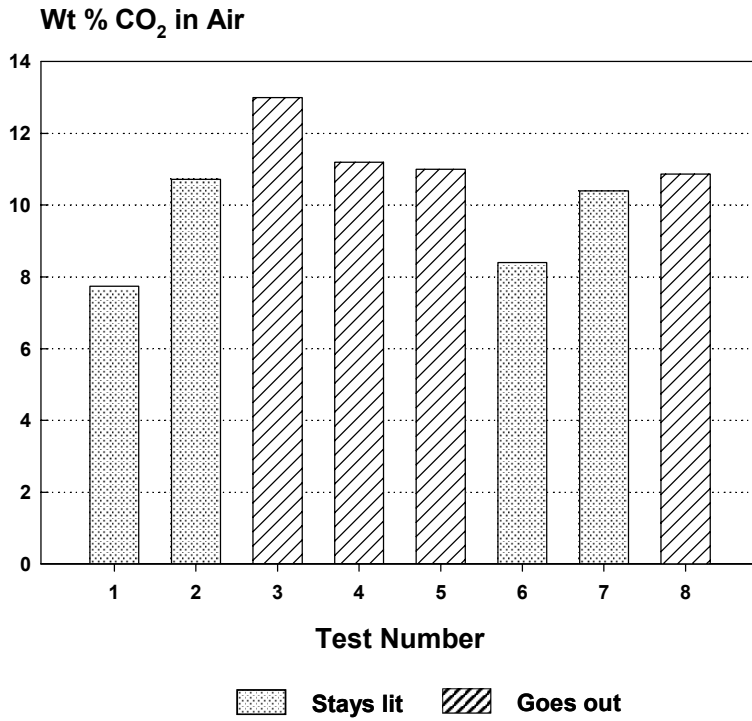


Figure 8-142. Extinction of a Candle Flame by CO₂.

Cylinder cross section = 84 cm²
 Updraft = 44 cm/s

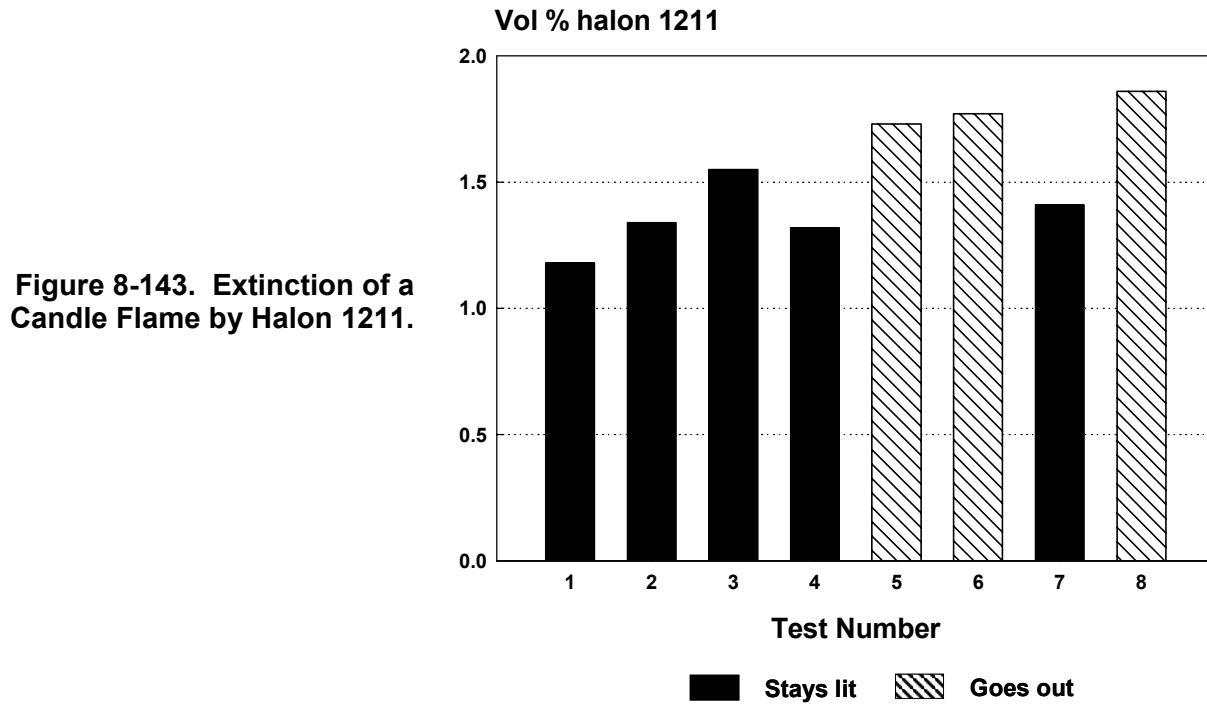


Figure 8-143. Extinction of a Candle Flame by Halon 1211.

Cylinder cross section = 84 cm²
 Updraft = 44 cm/s

Observations on Hydrate Samples Recovered at Ambient Pressure

Samples of the CO₂ hydrate looked very much like ice. When they were placed on the surface of a hot plate (surface temperature of 260 °C), they acted much as did samples ice, i.e., they melted and boiled with little or no wetting of the surface. A sample of the CO₂ hydrate placed on an ambient temperature aluminum plate initially melted with bubbling but without producing mist, then suddenly exploded. After the explosion, some fragments of the sample remained on the aluminum plate. They melted with bubbling but without further explosion. A sample of the C₃F₈ hydrate placed on an ambient temperature aluminum plate melted without explosion or mist production but with bubbling and a continuous snapping sound.

Discussion

Metastability of Gas Hydrates

As discussed above, gas hydrates might be effective firefighting agents if they were to undergo delayed self-atomization, which in turn might occur if the hydrate were metastable at ambient pressure. One might expect that metastability would or would not lead to self-atomization depending on the circumstance. If a particle of hydrate is traveling through the air at a high velocity, its surface is subject to high shear. As that surface begins to convert to liquid water and gaseous carbon dioxide, any bubbles forming will be broken into fine droplets. Thus for a hydrate particle in flight metastability seems likely to lead to atomization. For a particle at rest, however, the situation is less clear. If the particle can store sufficient strain energy for self-atomization, then it might do so. If the stored strain energy is not this large, it could still be sufficient to cause the hydrate particle to explode into coarse fragments or make snapping sounds as it melts. While the observations with the recovered hydrate samples are consistent with these expectations, the only thing they unambiguously show is that the hydrates are capable of metastability.

Analysis of Visual Observations

Different spray forming mechanisms exist when a liquid is discharged through a hole at various flow rates. The spray regime map depends on the Ohnesorge and Weber numbers (see Faeth⁹⁷). The results of calculations for the experiments done with water pressurized with helium were consistent with the observation that samples with helium pressurizations of 10.31 MPa, 6.87 MPa, and 3.78 MPa atomized. Samples pressurized with helium to 1.57 MPa, which was observed not to atomize, were calculated to be in the wind-induced range (Faeth⁹⁷).

The theory of spraying presented in Faeth⁹⁷ does not consider the possibility that the liquid being sprayed may contain a dissolved gas. Given that helium is only very slightly soluble in water, it is not surprising that the experiments with helium pressurized samples were quite consistent with this theory. The solubility of CO₂ in water at 21 °C and 5.81 MPa is, however, 34 cm³ STP gas per cm³ of liquid. The decrease in height, the increase in width and the fact that the droplets did not show observable settling are all consistent with the assumption that the discharge produced coarse droplets which the dissolved CO₂ subsequently or concurrently atomized into fine mist.

There is, however, the problem that droplets of fine mist are far more readily visible than an equal mass of coarse droplets. While the visual observations indicate that spray water saturated with CO₂ at high pressure does indeed produce fine mist, they do not reveal how efficiently this happened.

Since the discharged hydrate/water mixture occurred in the wind induced region, had a similar appearance to the helium pressurized discharge in this region, but still produced a mist that showed no observable settling, the indication of the visual observations is that after a delay the hydrate atomized itself into a fine mist. Here again, however, the data do not indicate how efficient the atomization was.

Fire Extinguishing Tests

In a previous research project, the ability of water saturated with CO₂ at high pressure to extinguish fires was examined.⁹⁸ While the results showed that this was indeed an effective way of extinguishing fires, the mechanism for extinguishing the fires was not clear. Perhaps the fine mist produced by the CO₂ saturated water extinguished the flame by cooling it or perhaps the jet of CO₂/mist was simply blowing out the flame.

Both sets of experiments reported above were designed to avoid this ambiguity. In both cases the flame was protected from the discharge of the hydrate so that mist from the hydrate arrived in the general vicinity of the flame, but without momentum from the discharge to carry it into the flame itself. Under this condition, the mist from the hydrate was not effective for extinguishing the flame.

While the reasons for this failure are not completely clear, two possibilities are obvious. The present results suggest that CO₂ hydrate does undergo delayed self-atomization but they do not show the efficiency of this process. If the efficiency of mist production is poor, the hydrate will not be an effective extinguishing agent. Secondly, there is the question of the velocity at which the mist enters the flame. Droplets of mist have a diffusion coefficient that is very close to zero. For an ideal diffusion flame this would give them a near zero velocity of approaching the flame and for a real diffusion flame the velocity would be quite low. As the above analysis shown, fine mist might be ineffective in this situation.

The goal of this research was to ascertain whether gas hydrates, especially CO₂ hydrate, could undergo delayed self-atomization and whether this property would make them potentially useful replacements for the halons. While the data indicate the former, the latter now appears to be a remote possibility. Accordingly, further research along this line was not pursued.

8.8 SUMMARY OF LESSONS LEARNED

- Fluid storage in a bottle determines the initial conditions for subsequent discharges into piping distribution systems. Fluid storage problems pertain to thermodynamic vapor-liquid phase equilibrium calculations, which in most cases are straightforward.
- For multi-phase pipe flow calculations, the FSP code is capable of calculating the pressure history and discharge flow rates similar to the measured data. The code is able to pick up the qualitative behavior associated with the release of dissolved gas as the delivery system undergoes rapid depressurization during the discharge of the suppressant agent. The code is very flexible in being able to model different piping systems via user input, and it offers the user many options in developing an appropriate input model to describe the physical system. Because of these characteristics, the code appears to be a viable tool for analysis or design of

suppressant delivery systems. However, the code will only begin the computation if the initial thermodynamic state of the fluid is properly specified by the user. The uncertainties in the model predictions can be attributed to the constitutive relationships for interphase drag and wall heat transfer estimations, the inherent uncertainties in predicting the release rate of dissolved gas, the critical gas bubble radius, and the appropriate discharge coefficients to account for uncertainties in the critical flow model of the code and the geometry of the junction for subcooled liquid, two-phase liquid-vapor, and single-phase vapor. The user should plan to vary these parameters for a specific application and gain understanding of how this would affect the overall time of suppressant discharge.

- Any of the fire simulation programs (VULCAN, FDS, and FPM) investigated in this effort can be used to help design a fire suppression system in practically any space inside an aircraft or ground vehicle. While their application to shipboard spaces was not investigated in this effort, there seems to be no conceptual impediment to such an application, except possibly that the allowable grid sizes might lengthen the computational periods significantly. Each of these software simulations incorporates a slightly different set of assumptions, so that using more than one of them will ameliorate unforeseen effects of the peculiar, embedded assumptions on any particular model. Of the three, only the FPM incorporates a threat-evaluation subroutine which predicts whether or not a fire will be initiated by any of the weapons in its library.
- Any of the fire simulation programs (VULCAN, FDS, and FPM) investigated in this effort can be used to optimize the design of qualification tests which may be required for acceptance of a fire-suppression system for an aircraft or ground vehicle. Such utility allows the planner of tests to focus on those cases for which these simulations show that extinction is marginal, thus reducing the number of tests required to ‘prove’ the system.
- If two or more fire simulation programs agree in the outcome, the tests likely will confirm. If there be disagreement in the predicted outcome from different fire-simulation programs for the same case, then the conditions are approaching the edge of the extinguishment envelope. The simplified chemical analyses incorporated into these fire simulations do not account for nonhomogeneous mixing.
- Because of the strongly oscillatory flow and turbulence inside a typical nacelle, the initial concerns about the adverse effects of clutter on the penetration of suppressants into those spaces have been allayed. The “clutter” enhances the mixing of the suppressant into the flow.
- In full-scale nacelle testing, almost all the predictions of “borderline” extinguishment outcomes were, in fact, extinguished. In other words, the simulation programs used in this effort err on the ‘safe’ side. Simplified homogeneous analysis shows two critical parameters determine successful suppression in nacelles:
 1. Ratio of “suppressant” mass inflow rate to “suppressant plus air” mass inflow rate determines the maximum concentration attainable for “long” injection periods. This ratio should be greater than 0.41 for HFC-125.
 2. The speed of injection is more important than the total mass of agent deployed. Total rate of volumetric displacement by inflowing air plus suppressant determines the elapsed time scale to reach maximum concentrations. (For an F-18 nacelle, air flows are large, so that the time scale to reach maximum concentration is small (< 1 s)). Consequently, if a “wave” of sufficiently high concentration reaches all the potential zones of fire for even a fraction of a second, the fire will be extinguished.

- The temperatures of agent storage bottle, airflow, and nacelle surfaces all play important roles in agent dispersion performance at low temperature applications, especially when the prevailing temperature is below the normal boiling point of the agent. Care should be exercised when extrapolating results from room temperature tests to evaluate agent dispersion performance at low temperatures.
- Neither electrically charged water mist systems nor the use of CO₂ hydrates appear to be promising substitutes for halons.

8.9 REFERENCES

1. Hamins, A., McGrattan, K., and Forney, G., "Unwanted Accelerated Burning after Suppressant Delivery," NIST Special Publication 1004, National Institute of Standards and Technology, Gaithersburg, MD, 2003.
2. Yang, J.C., Cleary, T.G., Vázquez, I., Boyer, C.I., King, M.D., Breuel, B.D., Womeldorf, C.A., Grosshandler, W.L., Huber, M.L., Weber, L., and Gmurczyk, G., "Optimization of system discharge," in Gann, R.G., ed., *Fire Suppression System Performance of Alternative Agents in Aircraft Engine and Dry Bay Laboratory Simulations*, NIST SP 890: vol. I, National Institute of Standards and Technology, Gaithersburg, MD, 1995.
3. Walas, S.M., *Phase Equilibrium in Chemical Engineering*, Butterworth, Boston, 1985.
4. Grosshandler W.L., Gann R.G., and Pitts W.M., eds., *Evaluation of Alternative in-Flight Fire Suppressants for Full-Scale Testing in Simulated Aircraft Engine Nacelles and Dry Bays*, NIST SP 861, National Institute of Standards and Technology, Gaithersburg, MD, 1994.
5. Huber, M.L. and Ely, J.F., "A Predictive Extended Corresponding States Model for Pure and Mixed Refrigerants Including an Equation of State for R134a," *International Journal of Refrigeration* **17**, 18-31, 1994.
6. Yang, J.C., Huber, M.L., Vázquez, I., Boyer, C.I., and Weber, L., "Measured and Predicted Thermodynamics Properties of Selected Halon Alternative/Nitrogen Mixtures," *International Journal of Refrigeration* **20**, 96-105, (1997).
7. Tuzla, K., Palmer, T., Chen, J.C., Sundaram, R.K., and Yeung, W.S., "Development of Computer Program for Fire Suppression Fluid Flow," Report number ITF 2000-1, Vols. I and II, Institute of Thermo-Fluid Engineering & Science, Lehigh University, Bethlehem, PA, September 2000.
8. DiNenno, P.J. and Budnick, E.K. Jr., "Halon 1301 Discharge Testing: A Technical Analysis," National Fire Protection Research Foundation, Quincy, MA, 1988.
9. Pitts, W. M., Yang, J. C., Gmurczyk, G. W., Cooper, L. Y., Grosshandler, W. L., Cleveland, W. G., and Presser, C., "Fluid Dynamics of Agent Discharge", in Grosshandler W.L., Gann R.G., and Pitts W.M., eds., *Evaluation of Alternative in-Flight Fire Suppressants for Full-Scale Testing in Simulated Aircraft Engine Nacelles and Dry Bays*, NIST SP 861, National Institute of Standards and Technology, Gaithersburg, MD, 1994.
10. Elliott, D. G., Garrison, P. W., Klein, G. A., Moran, K. M., and Zydowicz, M. P., *Flow of Nitrogen-Pressurized Halon 1301 in Fire Extinguishing Systems*, JPL Publication 84-62, Jet Propulsion Laboratory, California Institute of Technology, Pasadena, California, 1984.
11. Hirt, C. W., Oliphant, T. A., Rivard, W. C., Romero, N. C., and Torray, M. D., *SOLA-LOOP: A Non-Equilibrium, Drift Flux Code for Two-Phase Flow in Networks*, Report No. L-7659, Los Alamos National Laboratory, Los Alamos, NM, 1979.

12. Gallagher, J., McLinden, M., Morrison, G., and Huber, M., "NIST Thermodynamic Properties of Refrigerants and Refrigerant Mixtures Database (REFPROP), Version 4.0," National Institute of Standards and Technology, Gaithersburg, MD, 1993.
13. Marviken Power Station, "The Marviken Full Scale Critical Flow Tests: Volume 1: Summary Report," NUREG/CR-2671, MXC-301, U.S. Nuclear Regulatory Commission, Washington, DC, 1982.
14. EPRI Report NP-2370, "The Marviken Full-Scale Critical-Flow Tests, Volume 1: Summary Report", Electric Power Research Institute, Palo Alto, CA, 1982.
15. Edwards, A.R. and O'Brien, T.P., "Studies of Phenomena Connected with the Depressurization of Water Reactors," *Journal of British Nuclear Energy Society* **9**, 125-135, (1979).
16. RELAP5 Development Team, "RELAP5/MOD3.2 Code Manuals, Volume 1: Code Structure, Models and Numerical Schemes," U. S. Nuclear Regulatory Commission Report NUREG/CR-5535, 1995.
17. RELAP5 Development Team, "RELAP5/MOD3.2 Code Manuals, Volume 2: User Manual," U. S. Nuclear Regulatory Commission Report NUREG/CR-5535, 1995.
18. RETRAN-03: A Program for Transient Thermal-Hydraulic Analysis of Complex Fluid Flow Systems, EPRI NP-7450, Volume 1, May 1992.
19. TRAC-PF1/MOD2 Code Manual, Los Alamos National Laboratory, NUREG/CR-5673 or LA-1203-M, Volume 1-3, 1992.
20. TRAC-BF1/MOD1 Code Manual: An Advanced Best-Estimate Computer Program for BWR Accident Analysis, Idaho National Engineering Laboratory, NUREG/CR-4356 or EGG-2626, Volumes 1-2, 1992.
21. TRAC-BF1/MOD1 Models and Correlations, INEL, NUREG/CR-4391 or EGG-2680, 1992.
22. GOTHIC Containment Analysis Package Version 5.0, Numerical Applications, Inc., User Manual (NAI 8907-02 Rev. 6), and Technical Manual (NAI 8907-06 Rev. 5), 1995.
23. Taitel, Y.A., Bornea, D., and Dukler, A.E., "Modeling Flow Pattern Transitions for Steady Upward Gas-Liquid Flow in Vertical Tubes," *AIChE Journal* **26**, 345-354, (1980).
24. Mishima, K., and Ishii, M., "Flow Regime Transition Criteria Consistent with Two-Fluid Model for Vertical Two-Phase Flow," NUREG/CR-3338, April 1984.
25. Wallis, G.B., *One-Dimensional Two-Phase Flow*, McGraw Hill, New York, 1972.
26. Chisholm, D., "A Theoretical Basis for the Lockhart-Martinelli Correlation for Two-Phase Flow," *International Journal of Heat and Mass Transfer* **10**, 767-1778, (1967).
27. Zuber, N., Tribus, M., and Westwater, J. W., "The Hydrodynamic Crisis in Pool Boiling of Saturated and Subcooled Liquids," *Second International Heat Transfer Conference*, Paper 27, Denver, 1961.
28. Trapp, J. A., and Ransom, V. H., "A Choked Flow Calculation Criterion for Nonhomogeneous, Nonequilibrium Two-Phase Flows," *International Journal of Multiphase Flow* **8**, 669-681, 1982.
29. Cokmez-Tuzla, A.F., Tuzla, K., and Chen, J.C., "High Speed Thermometry for Detection of Transient Liquid Contact on Superheated Surfaces," in Schooley, J., ed., *Temperature Its Measurement and Control in Science and Industry*, vol. 6, pp. 1173-1177, American Institute of Physics, 1993.
30. Welty, J.R., Wicks, C.E., and Wilson, R.E., *Fundamentals of Momentum, Heat, and Mass Transfer*, 3rd edition, John-Wiley & Sons, New York, 1984.
31. Disimile, P.J., Tucker, J.R., Crosswell, B., and Davis, J.M., "The Transport of Water Sprays past Generic Clutter Elements Found within Engine Nacelles," *Fire Safety Journal* **40**, 65-78, (2005).

32. Presser, C., "Parametric Investigation of Droplet Atomization and Dispersion of Liquid Fire Suppressants," Final Report to DoD SERDP, December 2003.
33. Ghee, T.A. and Keyser, D.R., "Basic Aerodynamic Shapes in a Low-Speed, Highly Turbulent Flow," AIAA-2003-3953, 21st AIAA Applied Aerodynamics Conference, Orlando, Florida, June 23-26, 2003.
34. Hoerner, S.F., *Fluid-Dynamic Drag*, Hoerner Fluid Dynamics, Vancouver, WA, 1965.
35. Fage, A. and Warsap, J.H., "The Effects of Turbulence and Surface Roughness on the Drag of Circular Cylinders," ARC RM 1283, 1930.
36. Schlichting, H., *Boundary Layer Theory*, 7th ed., McGraw-Hill, New York, 1987.
37. Welch, P.D., "The Use of Fast Fourier Transform for the Estimation of Power Spectra: A Method Based on Time Averaging over Short, Modified Periodograms," *IEEE Transactions on Audio and Electroacoustics* Vol. AU-15, June 1967.
38. Yang, J.C., Manzello, S.L., Nyden, M.R., and Connaghan, M.D., "Cold Discharge of CF_3I in a Simulated Aircraft Engine Nacelle," *Proc. Seventh International Symposium on Fire Safety Science*: 715-726 (2003).
39. Gann R.G. (ed.), *Fire Suppression System Performance of Alternative Agents in Aircraft Engine and Dry Bay Laboratory Simulations*, volumes I and II, NIST SP 890, U.S. Department of Commerce, Washington, DC, November 1995.
40. Guesto-Barnak, D., Sears, R., and Simpson, T., "Engine nacelle fire protection using non-ozone depleting fire suppressants," *Proceedings of International Conference on Ozone Protection Technologies*, pp. 515-524, Washington, D.C., October 21-23, 1996.
41. Personal communication to Yang, J.C. from Meserve, W.J., Pacific Scientific, HTL/KIN-Tech Division, Document Number 51750579, Duarte, California, May 2000.
42. DeMore, W.B., Sander, S.P., Golden, D.M., Hampson, R.F., Kurylo, M.J., Howard, C.J., Ravishankara, A.R., Kolb, C.E., and Molina M.J., *Chemical Kinetics and Photochemical Data for Use in Stratospheric Modeling, Evaluation: Number 12*, JPL Publication 97-4, Jet Propulsion Laboratory, California Institute of Technology, Pasadena, California, 1997.
43. Yang, J.C., Cleary, T.G., Huber, M.L., and Grosshandler, W.L., "Vapor Nucleation in a Cryogenic Fluid/Dissolved Nitrogen Mixture during Rapid Depressurization," *Proceedings of the Royal Society of London A* **455**, 1717-1738, (1999).
44. Holen, J., Brostrom, M., and Magnussen, B.F., "Finite Difference Calculation of Pool Fires," *Proceedings of the Combustion Institute* **23**, 1677-1683, (1990).
45. Magnussen, B.F., Hjertager, B.H., Olsen, J.G., and Bhaduri, D., "Effects of Turbulent Structure and Local Concentrations on Soot Formation and Combustion in C_2H_2 Diffusion Flames," *Proceedings of the Combustion Institute* **17**, 1383-1393, (1979).
46. Patankar, S.V. and Spalding, D.B., "A Calculation Procedure for Heat, Mass, and Momentum Transfer in Three-Dimensional Parabolic Flows," *International Journal of Heat and Mass Transfer* **15**, 1787-1806, 1972.
47. Magnussen, B.F., "The Eddy Dissipation Concept," *Proceedings of the Eleventh Task Leaders Meeting*, IEA Working Group on Conservation in Combustion, Lund, Sweden, 1989.
48. Hewson, J.C. and Kerstein, A.R., "Local Extinction and Reignition in Nonpremixed Turbulent $\text{CO}/\text{H}_2/\text{N}_2$ Jet Flames," *Combustion Science and Technology* **174**, 35-66, (2002).

49. Tieszen, S.R., Stamps, D.W., and O'Hern, T.J., "A Heuristic Model of Turbulent Mixing Applied to Blowout of Turbulent Jet Diffusion Flames," *Combustion and Flame* **106**, 442-466, (1996).
50. Meeks, E., Moffat, H.K., Grcar, J.F., and Kee, R.J., "AURORA: A Fortran Program for Modeling Well Stirred Plasma and Thermal Reactors with Gas and Surface Reactions," Sandia National Laboratories Report SAND96-8218 (1996).
51. Curran, H.J., Gaffuri, P., Pitz, W.J., and Westbrook, C.K., "A Detailed Modeling Study of Iso-Octane Oxidation," *Proceedings of the Combustion Institute* **27**, 381-395, (1999).
52. Babushok, V.I., Noto, T., Burgess, D.R.F., Hamins, A., and Tsang, W., "Influence of CF₃I, CF₃Br, and CF₃H on the High-Temperature Combustion of Methane," *Combustion and Flame* **107**, 351-367, (1996).
53. Byggstoyl, S. and Magnussen, B.F., "A Model for Flame Extinction in Turbulent Flow," *Proceedings of the Combustion Institute* **17**, 381-395, (1978).
54. Hewson, J.C., Tieszen, S.R., Sundberg, W.D., and DesJardin, P.E., "CFD Modeling of Fire Suppression and Its Role in Optimizing Suppressant Distribution," 2003, in Gann, R.G., Burgess, S.R., Whisner, K.C., and Reneke, P.A., eds., *Papers from 1991-2006 Halon Options Technical Working Conferences (HOTWC)*, CD-ROM, NIST SP 984-4, National Institute of Standards and Technology, Gaithersburg, MD, (2006).
55. DesJardin, P.E., Nelsen, J.M., Gritz, L.A., and Ghee, T.A., "On the Development of a Subgrid Scale Clutter Model," AIAA-2002-0984, 40th AIAA Aerospace Sciences Meeting and Exhibit, Reno, Nevada, January 14-17, 2002.
56. DesJardin, P.E., Nelsen, J.M., Gritz, L.A., Lopez, A.R., Suo-Anttila, J.M., Keyser, D.R., Ghee, T.A., Disimile, P.J., and Tucker, J.R., "Towards Subgrid Scale Modeling of Suppressant Flow in Engine Nacelle Clutter," 2001, in Gann, R.G., Burgess, S.R., Whisner, K.C., and Reneke, P.A., eds., *Papers from 1991-2006 Halon Options Technical Working Conferences (HOTWC)*, CD-ROM, NIST SP 984-4, National Institute of Standards and Technology, Gaithersburg, MD, (2006).
57. CFD-GUI™, CFD-ACE Structured Flow Solver Manual, Version 5, CFD Research Corporation, Huntsville, Alabama, October 1998.
58. CFD-ACE™, Theory Manual, Version 5, CFD Research Corporation, Huntsville, Alabama, October 1998.
59. Launder, B.E. and Spalding, D.B., "The Numerical Calculation of Turbulent Flows," *Computational Methods Applied to Mechanics and Engineering* **3**, 269-289, (1974).
60. Wilcox, D.C., "A Half Century Historical Review of the $k-\epsilon$ Model," AIAA-91-0615, 29th Aerospace Sciences Meeting, Reno, Nevada, Jan 7-10, 1991.
61. Chien, T. and Smith, A.M.O., *Analysis of Turbulent Boundary Layers*, Academic Press, New York, 1982.
62. Fire Prediction Model, Version 3.1, *Software Analyst's Manual*, Pascal, A.M., SURVIAC Information Analysis Center. Available from Mr. M. Lentz, FPM Model Mgr., 46 OG/OGM/OL-AC 46 OG/OGM/OL-AC, 2700 D. St. Bldg. 1661, WPAFB, OH 45433-7605.
63. McGrattan, K.B., Baum, H.R., Rehm, R.G., Hamins, A., Forney, G.P., Floyd, J.E., Hostikka, S., and Prasad, K., *Fire Dynamics Simulator (Version 3) – Technical Reference Guide*, NISTIR 6783, U.S. Department of Commerce, Washington, DC, November 2002.

64. McGrattan, K.B., Forney, G.P., Prasad, K., Floyd, J.E., and Hostikka, S., *Fire Dynamics Simulator (Version 3) – User’s Guide*, NISTIR 6784, U.S. Department of Commerce, Washington, DC, November 2002.
65. Forney, G.P. and McGrattan, K.B., *User’s Guide for Smokeview Version 3.1 – A Tool for Visualizing Fire Dynamics Simulation Data*, NISTIR 6980, U.S. Department of Commerce, Washington, DC, April 2003.
66. Hamins, A., Cleary T., Borthwick, P., Gorchkov, N., McGrattan, K., Forney, G., Grosshandler, W., Presser, C., and Melton, L., “Suppression of Engine Nacelle Fires,” in Gann, R.G., ed., *Fire Suppression System Performance of Alternative Agents in Aircraft Engine and Dry Bay Laboratory Simulations*, NIST SP 890: vol. II, U.S. Department of Commerce, Washington, DC, 1995.
67. Lopez, A.R., Gritzo, L.A., and Hassan, B., “Computational Fluid Dynamics Simulation of the Air/Suppressant Flow in an Uncluttered F-18 Engine Nacelle,” 1997, in Gann, R.G., Burgess, S.R., Whisner, K.C., and Reneke, P.A., eds., *Papers from 1991-2006 Halon Options Technical Working Conferences (HOTWC)*, CD-ROM, NIST SP 984-4, National Institute of Standards and Technology, Gaithersburg, MD, (2006).
68. Black, A.R., Suo-Anttila, J.M., Gritzo, L.A., Disimile, P.J., and Tucker, J.R., *Numerical Predictions and Experimental Results of Air Flow in a Smooth Quarter-Scale Nacelle*, Sandia National Laboratories Report SAND2002-1319, Albuquerque, New Mexico, 2002.
69. Black, A.R., Suo-Anttila, J.M., Disimile, P.J., and Tucker, J.R., “Numerical Predictions and Experimental Results of Air Flow in a Smooth Quarter-Scale Nacelle,” AIAA-2002-0856, 40th Aerospace Sciences Meeting and Exhibit, Reno, Nevada, January 14-17, 2002.
70. Hirst, R. and Sutton, D., “The Effect of Reduced Pressure and Airflow on Liquid Surface Diffusion Flames,” *Combustion and Flame* **5**, 319-330, (1961).
71. Hirst, R., Farenden, P.J., and Simmons, R.F., “The Extinction of Fires in Aircraft Jet Engines – Part I, Small-Scale Simulation of Fires,” *Fire Technology* **12**, 266-275, (1976).
72. Hirst, R., Farenden, P.J., and Simmons, R.F., “The Extinction of Fires in Aircraft Jet Engines – Part II, Full-Scale Fires,” *Fire Technology* **13**, 59-67, (1977).
73. Hamins, A., Presser, C., and Melton, L., “Suppression of a Baffle-Stabilized Spray Flame by Halogenated Agents,” *Proceedings of the Combustion Institute* **26**, 1413-1420, (1996).
74. Takahashi, F., Schmoll, W.J., Strader, E.A., and Belovich, V.M., “Suppression of a Nonpremixed Flame Stabilized by a Backward-Facing Step,” *Combustion and Flame* **122**, 105-116, (2001).
75. Takahashi, F., Schmoll, W.J., Strader, E.A., and Belovich, V.M., “Suppression Behavior of Obstruction-Stabilized Pool Flames,” *Combustion Science and Technology* **163**, 107-130, (2001).
76. Hewson, J.C. and Keyser, D.R., *Suppression of Pool Fires with HFC-125 in a Simulated Engine Nacelle*, Technical Report SAND2007-3442, Sandia National Laboratories, Albuquerque, NM, 2007.
77. Hewson, J.C. and Keyser, D.R., “Predicting Fire Suppression in a Simulated Engine Nacelle,” 2004, in Gann, R.G., Burgess, S.R., Whisner, K.C., and Reneke, P.A., eds., *Papers from 1991-2006 Halon Options Technical Working Conferences (HOTWC)*, CD-ROM, NIST SP 984-4, National Institute of Standards and Technology, Gaithersburg, MD, (2006).
78. Technical Work Description (TWD) LNV12.01-013, “F/A-18 E/F (HFC-125) Fire Protection System Qualification Test,” Northrop Grumman, El Segundo, California, February 29, 2000.

79. Hamins, A., Gmurczyk, G. W., Grosshandler, W. L., Rehwoldt, R.G., Vazquez, I., Cleary, T., Presser, C., and Seshadri, K., "Flame Suppression Effectiveness", in Grosshandler W.L., Gann R.G., and Pitts W.M., eds., *Evaluation of Alternative in-Flight Fire Suppressants for Full-Scale Testing in Simulated Aircraft Engine Nacelles and Dry Bays*, NIST SP 861, U.S. Department of Commerce, Washington, DC, 1994.
80. Northrop Test Work Description, LN 12.01-011, rev. n/c, "F/A-18 E/F Engine Bay Fire Extinguishing System," 09 July 1997, Contract N00019-92-C-0059, H12-354C-7656.
81. Performance Test Code 19.5-2004, *Flow Measurement*, ASME, New York.
82. Smith, L.T., Murdock, J.W., and Applebaum, R.S., "An Evaluation of Existing Two-Phase Flow Correlations for Use with ASME Sharp Edge Metering Orifices," ASME Paper 76-WA/FM-3, New York, NY, 1977.
83. Calcote, H.F., "Ion Production and Recombination in Flames," *Proceedings of the Combustion Institute* **8**, 184-199, (1962).
84. Wortberg, G., "Ion-Concentration Measurements in a Flat Flame at Atmospheric Pressure," *Proceedings of the Combustion Institute* **10**, 651-655, (1965).
85. Peters, J., Vinhier, C., and Van Tiggelen, A., *Oxidation and Combustion Reviews* (C.F.H., Tipper, Ed.) Elsevier, Amsterdam, Vol. 4, 93, 1969.
86. Calcote, H.F., "Ions and Electron Profiles in Flames," *Proceedings of the Combustion Institute* **9**, 622-637, (1963).
87. Calcote, H.F., Olson, D.B., and Keil, D.G., "Are Ions Important in Soot Formation?," *Journal of Energy and Fuels* **2**, 494-504, (1988).
88. Payne, K.G. and Weinberg, F.J., "A Preliminary Investigation of Field-Induced Ion Movement in Flame Gases and Its Applications," *Proceedings of the Royal Society of London* **A250**, 316-336, (1959).
89. Berman, C.H., Gill, R.J., Keil, D.G., and Calcote, H.F., "Enhanced Soot Radiation Using Electric Fields," AeroChem Final Report TP-466, Gas Research Institute Contract No. 5086-260-1312, 1987.
90. Chattock, A.P., *Philosophical Magazine* **48**, 401, (1899).
91. Patterson, R.A., Brabson, G.D., Schiro, J., and Tapscott, R.E., "Critical Concentration Measurements and Lab-to-Room Scale-Up Water Mist Fire Testing," 1996, in Gann, R.G., Burgess, S.R., Whisner, K.C., and Reneke, P.A., eds., *Papers from 1991-2006 Halon Options Technical Working Conferences (HOTWC)*, CD-ROM, NIST SP 984-4, National Institute of Standards and Technology, Gaithersburg, MD, (2006).
92. Gottuk, D.L., Steel, J.S., Roby, R.J., and Beyler, C.L., "Final Report of Phase II, Energy Fields for Fire Extinguishment," Hughes Associates, Inc., Contract No. F08635-92-C-0015, prepared for Tyndall AFB, 1993.
93. Berman, C.H., *et al.*, "Electrically Charged Water Mist for Extinguishing Fires," Final Report to SERDP NGP, March 1998.
94. Kelly, A.J., "On the Statistical, Quantum, and Practical Mechanics of Electrostatic Atomization," *Journal of Aerosol Science* **25**, No. 6, 1159-1177, (1994).
95. Belan, J. and Harstad, K., "Electrostatic Dispersion and Evaporation of Clusters of Drops of High-Energy Fuel for Soot Control," *Proceedings of the Combustion Institute* **26**, 1713-1722, (1997).
96. Lyon, R.K., "Development of a Self Atomizing Form of Water," Final Report to SERDP NGP, January 1998.

97. Faeth, G.M., "Structure and Atomization Properties of Dense Turbulent Sprays," *Proceedings of the Combustion Institute* **23**, 1345-1352, (1990).
98. Lyon, R.K., Private Communication, Energy and Environmental Research Corporation, Whitehouse, NJ 08888, January 1998.